CORA Cork Open Research Archive
Cartlann Taighde Oscailte Chorcaí

Title	Nonlinear large-deformation modeling of planar compliant mechanisms and model-based design optimization
Authors	Liu, Tinghao
Publication date	2025-12-31
Original Citation	Liu, T. 2025. Nonlinear large-deformation modeling of planar compliant mechanisms and model-based design optimization. PhD Thesis, University College Cork.
Type of publication	Doctoral thesis
Rights	© 2025, Tinghao Liu. - https://creativecommons.org/licenses/by-nc-nd/4.0/
Download date	2026-11-15 13:36:54
Item downloaded from	https://hdl.handle.net/10468/18795



UCC
University College Cork, Ireland
Coláiste na hOllscoile Corcaigh

Ollscoil na hÉireann, Corcaigh
National University of Ireland, Cork



Nonlinear large-deformation modeling of planar compliant mechanisms and model-based design optimization

Thesis presented by

Tinghao Liu

for the degree of

Doctor of Philosophy in Mechanical Engineering

Supervisor: Prof. Guangbo Hao

University College Cork

School of Engineering and Architecture

Head of School: Prof. Jorge Oliveria

2025

No storm lasts forever

Declaration

This is to certify that the work I am submitting is my own and has not been submitted for another degree, either at University College Cork or elsewhere. All external references and sources are clearly acknowledged and identified within the contents. I have read and understood the regulations of University College Cork concerning plagiarism and intellectual property.

Digital signature of the candidate:



Publications and Awards

Journal papers

1. Tinghao Liu, Guangbo Hao*, Jiaxiang Zhu, Pongsiri Kuresangsai, Salih Abdelaziz, and Erich Wehrle. 2024. "Modeling Compliant Bistable Mechanisms: An Energy Method Based on the High-Order Smooth Curvature Model." *International Journal of Mechanical Sciences* 275 (April): 109315. https://doi.org/10.1016/j.ijmecsci.2024.109315. (**This journal paper arises from chapter 3 of this thesis.**)

2. Tinghao Liu, and Guangbo Hao*. 2025. "Comprehensive SCME: A Nonlinear Large-Deformation Modeling Approach for Planar Compliant Mechanisms." *Mechanism and Machine Theory* 213 (October): 106070. https://doi.org/10.1016/j.mechmachtheory.2025.106070. (**This journal paper arises from chapter 4 of this thesis.**)

3. Tinghao Liu, Ming Zhou and Guangbo Hao*. 2026. "A bi-level geometrical optimization framework for tailoring kinetostatic behavior of compliant bistable mechanisms" *Mechanism and Machine Theory* 220 (October): 106338. https://doi.org/10.1016/j.mechmachtheory.2025.106338. (**This journal paper arises from chapter 5 of this thesis.**)

4. Jiaxiang Zhu, Guangbo Hao*, Tinghao Liu, and Haiyang Li. 2023. "Design of an Over-Constraint Based Nearly-Constant Amplification Ratio Compliant Mechanism." *Mechanism and Machine Theory* 186 (April): 105347. https://doi.org/10.1016/j.mechmachtheory.2023.105347.

5. Tinghao Liu, and Guangbo Hao*. 2022. "Design of a Cylindrical Compliant Linear Guide with Decoupling Parallelogram Mechanisms." *Micromachines* 13 (8): 1275. https://doi.org/10.3390/mi13081275.

6. Lujie Wang, Tinghao Liu, Guangbo Hao, Chitta Saha, Lei Liu, TinCong Ye, Zhengmin Zhang, and Ningning Wang*. 2023. "An Electromagnetic Vibration Energy Harvester with Compact Flexure Guide for Low Frequency Applications." *Smart Materials and Structures* 33 (1): 015031. https://doi.org/10.1088/1361-665X/ad1429.

Conference papers

1. Jiaxiang Zhu, Guangbo Hao*, Tinghao Liu, and Haiyang Li. "Design and Nonlinear Analysis of an Overconstraint Based Constant Amplification Ratio Compliant Mechanism." *Proceedings of the ASME 2022 International Design Engineering Technical Conferences and Computers and Information in Engineering Conference*, Volume 7, August 14–17, 2022. V007T07A005. ASME. https://doi.org/10.1115/DETC2022-89555.

2. Tinghao Liu, and Guangbo Hao*. "Precision polishing platform based on a flexure-based constant force mechanism." *euspen's 24th International Conference & Exhibition*, June 2024. https://www.euspen.eu/knowledge-base/ICE24295.pdf.

Oral presentations

1. Tinghao Liu, and Guangbo Hao*. "Model-based design and optimization of compliant zero-force mechanism derived from two bistable mechanisms." *WCSMO-15 World Congress of Structural and Multidisciplinary Optimization*, Cork, 2023.

2. Tinghao Liu, and Guangbo Hao*. "Model-based design and optimization of compliant zero-force mechanism derived from two bistable mechanisms." *2nd Forum for Chinese PhD Students in Ireland*, November 2023.

Poster presentations

1. Tinghao Liu, and Guangbo Hao*. "Precision polishing platform based on a flexure-based constant force mechanism." *euspen's 24th International Conference & Exhibition*, June 2024. https://doi.org/10.13140/RG.2.2.17502.65604.

Awards

1. **Postgraduate Publication of the Year**
   School of Engineering and Architecture, University College Cork
   Tinghao Liu (2025).

2. **HEIDENHAIN Scholarship**
   The European Society for Precision Engineering and Nanotechnology (euspen)
   Tinghao Liu (2024).

3. **Outstanding Volunteer Award**
   The 2nd Forum for Ireland–China PhD Students
   Tinghao Liu (2023).

4. **Compliant Mechanisms Award**
   American Society of Mechanical Engineers (ASME)
   Jiaxiang Zhu; Guangbo Hao; Tinghao Liu; Haiyang Li (2022).

5. **Student Mechanism & Robot Design Competition (2nd place)**
   American Society of Mechanical Engineers (ASME)
   Shiyao Li; Jiaxiang Zhu; Tinghao Liu (2022).

Abstract

Compliant mechanisms achieve motion and force transmission through elastic deformation, offering advantages of compactness, precision, low friction, and structural simplicity. These properties make them attractive for a wide range of applications, including precision engineering, biomedical and surgical devices, aerospace and space systems, and robotics. However, their reliance on large elastic deformations introduces highly nonlinear behavior, which poses significant challenges for accurate analysis and design. Conventional finite element simulations, while reliable, are often computationally expensive and provide limited capability of being applied in structural optimization, whereas over-simplified analytical models may fail to capture the essential nonlinear characteristics. Accordingly, this dissertation aims to further contribute to the development of the field of compliant mechanism design by addressing these key challenges, thereby laying a foundation for future theoretical development and engineering applications. Guided by this mission, the dissertation advances along three mutually reinforcing parts.

First, an energy method based on high-order smooth curvature model (High-order SCME) is proposed, in which high-order Legendre polynomials are employed to approximate curvature and derive bending energy expressions. The model provides low-dimensional, differentiable, and efficient solutions for large-deformation compliant mechanisms, achieving high accuracy with significantly reduced computational cost.

Second, recognizing that high-order SCME method neglects axial deformation, a Comprehensive SCME (CoSCME) method is further developed to resolve this issue. By incorporating axial strain energy and bending-axial coupling into a unified framework, CoSCME enables precise predictions of nonlinear responses across pre-buckling and post-buckling regimes. Its accuracy and generality are validated in scenarios including compresural beams, tensural beams, bistable mechanism, general lumped-compliance beams and initially-curved beams. The modeling results are in strong agreement with the finite element analysis results.

Third, a bi-level optimization framework driven by CoSCME is established for systematic mechanism design. The upper-level optimization aims to achieve mechanism configuration search through genetic algorithms, while the lower-level optimization evaluates kinetostatic behavior using the CoSCME method. This bi-level optimization framework successfully achieves optimal designs such as bistable mechanisms with symmetric switching forces and constant negative-stiffness behavior, thereby broadening the functional landscape of compliant mechanisms.

Together, these contributions deliver not only efficient modeling tools and a practical optimization paradigm but also a unifying framework that bridges theoretical modeling, numerical simulation, and experimental validation. By systematically advancing the smooth curvature modeling approach and extending it into comprehensive and optimization-oriented formulations, this thesis deepens the theoretical understanding of large-deformation mechanics in compliant mechanisms. At the same time, it provides engineering methodologies capable of guiding the design of complex, multi-functional, and programmable compliant systems. Collectively, these outcomes underscore the dual significance of this work: establishing a solid theoretical foundation for compliant mechanism research and enabling practical engineering applications across robotics, biomedical devices, and deployable structures.

Table of Contents

Nomenclature xxiii

1 Introduction 1
- 1.1 Compliant mechanisms . . . 1
- 1.2 Applications of compliant mechanisms . . . 3
  - 1.2.1 Precision engineering and micro/nano systems . . . 3
  - 1.2.2 Biomedical and surgical devices . . . 5
  - 1.2.3 Aerospace and Space Systems . . . 6
  - 1.2.4 Robotics . . . 7
- 1.3 Modeling methods . . . 10
  - 1.3.1 Pseudo-rigid-body model . . . 12
  - 1.3.2 Beam constraint model . . . 13
  - 1.3.3 Elliptic integral solution . . . 14
  - 1.3.4 Smooth curvature model . . . 14
- 1.4 Compliant mechanism optimization . . . 16
  - 1.4.1 Optimization methods . . . 17
  - 1.4.2 Optimization algorithms . . . 21
- 1.5 Motivations . . . 24
- 1.6 Contributions . . . 26
- 1.7 Thesis Organization . . . 28

2 Theoretical Background 31
- 2.1 Strain energy . . . 31
  - 2.1.1 Bending strain energy . . . 32
  - 2.1.2 Axial strain energy . . . 34
- 2.2 Smooth curvature model . . . 35
  - 2.2.1 Curvature function derivation . . . 36
  - 2.2.2 Strain energy derivation . . . 38
  - 2.2.3 Kinematic Derivation . . . 39

3 High-order SCME 43

3.1 High-order smooth curvature model . . . 44
3.2 Constructing Lagrangian function . . . 48
3.3 Case study: modeling compliant bistable mechanism . . . 50
3.4 Implementation procedure . . . 55
3.5 FEA and experimental validation . . . 60
3.5.1 FEA validation . . . 60
3.5.2 Experimental validation . . . 65
3.6 Method comparison . . . 70
3.6.1 Comparison across SCME with distinct orders . . . 70
3.6.2 Comparison across modeling methods . . . 74
3.7 Basic assumptions and limitations . . . 78
3.7.1 Plane kinetostatic modeling . . . 78
3.7.2 Neglection of out-of-plane buckling . . . 78
3.7.3 Neglection of axial, shear and twist strain energy . . . 78
3.7.4 Planar stress assumption . . . 79
3.8 Chapter Summary . . . 79

4 Comprehensive SCME 81
4.1 Formulation of CoSCME . . . 82
4.1.1 Fitting axial deformation with Legendre polynomials . . . 83
4.1.2 Deriving coordinates and deflection angle . . . 85
4.1.3 Formulating the strain energy function . . . 86
4.1.4 Identifying kinetostatic modeling . . . 86
4.1.5 Post-processing . . . 87
4.2 Case studies . . . 89
4.2.1 Case study 1: Compresural beams . . . 94
4.2.2 Case study 2: Tensural beams . . . 97
4.2.3 Case study 3: Bistable mechanisms . . . 100
4.2.4 Case study 4: General lumped-compliance beams . . . 107
4.2.5 Case study 5: Initially-curved beams . . . 114
4.3 Discussion . . . 119
4.3.1 Discussion of Modeling Results . . . 119
4.3.2 Method Comparison . . . 121
4.4 Chapter Summary . . . 122

5 Bi-level optimization framework 125
5.1 Bi-level Optimization Framework . . . 132
5.1.1 Lower-level optimization . . . 134

5.1.2 Upper-level optimization . . . 138
5.2 Case Studies . . . 141
5.2.1 Bistable Mechanism with Symmetric Switching Forces . . . 141
5.2.2 Bistable Mechanism with Approximately Constant Negative Stiffness 148
5.3 Discussion . . . 153
5.3.1 Application Scope . . . 153
5.3.2 Limitations . . . 154
5.3.3 Potential methodological extensions . . . 155
5.4 Chapter Summary . . . 157

6 Conclusion 159
6.1 Conclusion . . . 159
6.2 Future Work . . . 160

Bibliography 163

Appendices 183

A Optimization Results 183
A.1 Convergence history of optimization case study 1 . . . 183
A.2 Convergence history of optimization case study 2 . . . 185

Acknowledgment

This dissertation marks the culmination of a challenging yet rewarding journey, one that would not have been possible without the support, guidance, and encouragement of many people.

First and foremost, I would like to express my deepest gratitude to my supervisor, Prof. Guangbo Hao. Throughout these years, his patience, insightful guidance, and tireless teaching have left an indelible mark on me. Beyond academic supervision, he has imparted invaluable lessons about life and conduct, and his mentorship has profoundly shaped both my scholarly path and personal growth. He often says that life is like a research project: if you approach each step with diligence and perseverance, you will eventually achieve success despite the numerous challenges along the way. It has been an immense honor to have him as my supervisor. In addition, I sincerely thank my external examiner, Simon Henein from École Polytechnique Fédérale de Lausanne, and internal examiner, Dr William Wright from University College Cork, for their valuable comments and constructive suggestions, which significantly improved the quality of this thesis.

I owe heartfelt thanks to my wife, Qingyue Wang, whose unwavering support and companionship have been my greatest source of strength. Our bond has grown deeper through these years, and her encouragement has been an enduring motivation that kept me moving forward. In addition, I am deeply indebted to my parents, Mr. Shankui Liu and Ms. Shufang Qu, and my grandfather, Mr. Jihong Liu, for their unconditional love and constant support. Living overseas for so many years has often meant being unable to take proper care of them, for which I feel great regret, yet their trust and encouragement have always been a steady source of comfort. To all who have accompanied me throughout this journey, I extend my heartfelt gratitude for their encouragement, kindness, and support.

Special thanks go to Mr. Timothy Power, Mr. Michael O'Shea and Mr Paul Conway whose technical expertise and generous assistance as technicians are invaluable to the successful completion of my experimental work.

Finally, I would like to gratefully acknowledge University College Cork, the China Scholarship Council (CSC), and the Horizon 2020 EnABLES TA project for their financial support, without which my doctoral study would not have been possible.

List of Figures

1.1 Bio-inspired compliant mechanisms and their wide-ranging applications. . . 2
1.2 Applications of compliant mechanisms in precision engineering and micro/nano systems. 4
1.3 Overview of compliant mechanism applications in biomedical and surgical devices. Figure adapted from a literature review in [1] 6
1.4 Representative applications of compliant mechanisms in aerospace and space systems. 7
1.5 Representative applications of compliant mechanisms in robotics. 8
1.6 Representative kinetostatic modeling methods for compliant mechanisms. . 12
1.7 Classification of optimization approaches and algorithms for compliant mechanisms. 17
1.8 The flowchart of thesis organization 29

2.1 Illustration of compressive and tensile fibers in beam bending deformation. . 32
2.2 Illustration of stretching and compression of the neutral axis during axial deformation of a beam. 34
2.3 The first six Legendre polynomials $P_0(x)$–$P_5(x)$ defined on the interval $x \in [-1, 1]$. Different colors are used to distinguish polynomial orders. . . 37

3.1 Explanation of local and global coordinate systems, trajectory points, and geometric parameters of compliant beams. 51
3.2 The flowchart of the root-finding algorithm. 58
3.3 Two possible deformation shapes exist in modeling results. 59
3.4 Convergence analysis of FEA simulation via modeling compliant beams with varying numbers of beam elements. 62
3.5 The modeling result comparisons between 5th-order SCME method and FEA simulation result. 63
3.6 The variables and geometrical parameters defined to derive the critical buckling position and force. 64
3.7 Comparison between the modeling result considering linear compensation and FEA simulation. 65

3.8 A prototype with three layers used for experimental validation. 66
3.9 The experiment setup and 3D printed prototype. 68
3.10 Experiment result comparison. 69
3.11 Force-displacement relationship comparison between 2nd-order, 3rd-order, 4th-order and 5th-order SCME method. 71
3.12 Modeling error comparison among 2nd-, 3rd-, 4th-, and 5th-order SCME methods. 73
3.13 Force-displacement relationship comparison between 5th-order SCME method, CBCM, CPRBM, and FEA simulation. 76
3.14 Modeling error comparison among the 5th-order SCME method, CBCM, and CPRBM. 77

4.1 Overview of this chapter. 82
4.2 Terminologies employed in the CoSCME. 83
4.3 Definition of geometric parameters. 91
4.4 Comparison of 2D and 3D FEA simulation results for CBPMs under nonlinear static loading. 93
4.5 Modeling result of fixed-fixed beam and fixed-pinned beam. 96
4.6 Modeling results for BPMs and CBPMs. 100
4.7 Modeling results for the classical translational bistable mechanism. Results are verified by FEA simulations. 103
4.8 Modeling results for the pre-loaded rotational bistable mechanism. 106
4.9 Case study of modeling a general lumped-compliance beam, which is composed of two compliant beams. 112
4.10 Twelve distinct configurations of general lumped-compliance beams. 113
4.11 Case study of modeling a compliant bistable mechanism with initially curved beams. 118
4.12 Convergence analysis of beam shape fitting. 119

5.1 The flowchart of bi-level optimization. 133
5.2 Definition of geometric layout and coordinate systems of lumped-compliance beam. 134
5.3 Forward and backward switching force analysis for conventional distributed-compliance bistable mechanisms. 142
5.4 Optimal design of the bistable mechanism with symmetric switching force. . 146
5.5 Illustration and validation of the optimized mechanism with constant negative stiffness. 152

A.1 Convergence history of the optimization for bistable mechanism with symmetric switching force. 183
A.2 Pareto front obtained from multi-objective optimization for a bistable mechanism with approximately constant negative stiffness. 185

List of Tables

1.1 A comparative analysis of kinetostatic modeling methods for compliant mechanisms is presented. . . . 16

2.1 The weights and quadrature points . . . 41

3.1 The shifted Legendre polynomials . . . 45
3.2 The integration of shifted Legendre polynomials . . . 46
3.3 The values of $F_{\min}$ obtained from FEA simulations when the beam are subdivided into distinct amounts of beam elements. . . . 62
3.4 Configuration for 3D printing . . . 67
3.5 Mechanical properties of tough PLA. . . . 67
3.6 Computational efficiency comparison among SCME methods with distinct orders. . . . 74
3.7 Computational efficiency comparison between different methods. . . . 77

4.1 Overview of case studies covering various application scenarios, all presented in the following section. . . . 90
4.2 The formulations for cosine-shaped and circular-arc beams. . . . 116
4.3 Comparison of different modeling methods for a translational bistable mechanism. . . . 122

5.1 Comparison of single-beam, lumped-compliance, and topology-optimized bistable mechanisms. . . . 128
5.2 Optimization variables and their corresponding symbols. . . . 129
5.3 Switching force ratios of conventional distributed-compliance bistable mechanisms with distinct inclination angles. . . . 143
5.4 Maximum and minimum values of force and displacement obtained from modeling, finite element analysis (FEA), and experimental results, extracted from their respective force-displacement curves. . . . 145
5.5 Comparison of switching forces . . . 147
5.6 Optimization variables and their corresponding symbols. . . . 151

A.1 Optimal solution at each generation for bistable mechanism with symmetric switching force. 184
A.2 Geometric parameters corresponding to each Pareto-optimal solution in the case study of optimizing a bistable mechanism with approximately constant negative stiffness. 185

Nomenclature

z	Distance from the neutral axis (used to locate a fiber)
ρ	Radius of curvature
ds	Arc length for neutral axis ($z = 0$)
s	Position of point on beam
$d\theta$	Infinitesimal increment in the rotation angle
ds^{+z}	Deformed arc length for fiber located at $+z$
ε_{b}	Bending strain
$\omega(s)$	Curvature at point s
u_{b}	Bending strain energy density per unit volume
σ_{b}	Bending stress
E	Young's modulus
U_{b}	Bending strain energy
A	Cross section area
T	Beam in-plane thickness
W	Beam out-of-plane thickness
I	Second moment of area
ε_{a}	Axial strain
σ_{a}	Axial stress
u_{a}	Axial strain energy density per unit volume
U_{a}	Axial strain energy
$P_m(x)$	m-th order Legendre polynomials
$P_n(x)$	n-th order Legendre polynomials
n	Order of Legendre polynomials
ψ_n	n-th order Legendre polynomial
$\alpha_{0,1,2,3\ldots}$	Generalized coordinates for bending deformation
L	Beam length
U	Strain energy

$\alpha^*_{0,1,2,3...}$	Generalized coordinates corresponding to the initial beam curvature
$\phi(s)$	Deflection angle at point s
ϕ_{tip}	Deflection angle at beam tip
x_{tip}	x coordinate of beam tip
y_{tip}	y coordinate of beam tip
x_i	Quadrature points
W_i	Weight assigned to each quadrature point
b	Upper bound of the integration interval for Gauss-Legendre quadrature
a	Lower bound of the integration interval for Gauss-Legendre quadrature
N	Order of shifted Legendre polynomials
$\mathcal{L}$	Lagrangian function
$\mathbf{q}$	Generalized coordinates
λ	Lagrangian multiplier
x_{g}	X coordinate of given tip position
y_{g}	Y coordinate of given tip position
ϕ_{g}	Given tip orientation
X_{L}	X axis of local coordinate system
Y_{L}	Y axis of local coordinate system
O_{L}	Origin of local coordinate system
f_x	Reaction force in the x direction in the local coordinate system
f_y	Reaction force in the y direction in the local coordinate system
m_t	Reaction moment in the local coordinate system
X	X axis of global coordinate system
Y	Y axis of global coordinate system
O	Origin of global coordinate system
F_{x}	Reaction force in the x direction in the global coordinate system
F_{y}	Reaction force in the y direction in the global coordinate system
M_{t}	Reaction moment in the global coordinate system
Δy	Prescribed displacement
N_i	Number of discrete trajectory points
$x_{g,i}$	X coordinate of the i-th given trajectory point in global coordinate system
$y_{g,i}$	Y coordinate of the i-th given trajectory point in global coordinate system
$\phi_{g,i}$	Given tip orientation of the i-th given trajectory point in global coordinate system
$\boldsymbol{\alpha}^*$	Solution of generalized coordinates alpha to the Lagrangian function
$\boldsymbol{\lambda}^*$	Solution of Lagrange multipliers to the Lagrangian function
$\mathbf{J}$	Jacobian matrix

$\mathbf{H}$	Hessian matrix
$\boldsymbol{S}_0$	Guess initial vector in iteration
ξ	A non-zero value for initial guess
$\boldsymbol{S}_k$	The solution at iteration step k
γ	Relaxation factor in iteration
$\boldsymbol{S}_i^*$	Convergenced solution for i-th trajectory point
n_{FEA}	Number of beam elements in FEA
F_{min}	The local minima of force-displacement curve obtained from FEA simulation
P_{cr}	Critical buckling force
F_{ycr}	Component force of critical buckling force along y direction
ΔL	Axial deformation
k	Axial stiffness
Δy_{b}	Critical buckling displacement along y direction
θ_0	Initial inclined angle
θ_0'	Critical buckling angle
F_i	Observed value of force from FEA simulation result
$\hat{F}_i$	Modeling results used for evaluating error
E'	Corrected plate modulus
v	Poisson's ratio
P_s^*	Position of point s on undeformed beam
x_s^*	X coordinate of point s on the undeformed beam
y_s^*	Y coordinate of point s on the undeformed beam
ϕ_s^*	Orientation of point s on the undeformed beam
P_s	Position of point s on deformed beam
x_s	X coordinate of point s on the deformed beam
y_s	Y coordinate of point s on the deformed beam
ϕ_s	Orientation of point s on the deformed beam
$\beta_{0,1,2,3\ldots}$	Generalized coordinates for axial deformation
ΔL_{s}	Accumulated axial deformation from fixed end to P_{s}
ΔL_{tip}	Accumulated axial deformation along entire beam
$\mathbb{R}$	The set of real numbers
$x_{\text{g-tip}}$	X coordinate of given beam tip position
$y_{\text{g-tip}}$	Y coordinate of given beam tip position
$x_{\text{g-mid}}$	X coordinate of given beam middle position ($s = 0.5L$)
$y_{\text{g-mid}}$	Y coordinate of given beam middle position ($s = 0.5L$)
e_n	Normalized relative error

e_b	Width of error band
A_c	Amplification coefficient
e_θ	Artificial rotational offset
e_y	Artificial transnational offset
K	Effective length factor
Δx_{cr}	Critical buckling axial deformation
Δx_{P}	Parasitic movement on x-direction
x_s^{L}	X coordinate of point P_s in local coordinate system
y_s^{L}	Y coordinate of point P_s in local coordinate system
ϕ_s^{L}	Orientation of point P_s in local coordinate system
Δy^*	Preloaded displacement in rotational bistable mechanism
$\mathcal{R}^{\text{A}}$	Local coordinate system for beam A
$\mathcal{R}^{\text{B}}$	Local coordinate system for beam B
$P_{\text{tip-A}}$	Tip position of beam A
$\mathcal{R}^{\text{i}}$	Intermediate coordinate system
x_{fr}	X coordinate of O_{B} in $\mathcal{R}^{\text{i}}$ (Frame parameter, remain constant)
y_{fr}	Y coordinate of O_{B} in $\mathcal{R}^{\text{i}}$ (Frame parameter, remain constant)
θ_{fr}	Deflection angle between $\overrightarrow{x_{\text{B}}}$ and $\overrightarrow{x_{\text{i}}}$
$\mathcal{R}^{i*}$	Undeformed intermediate coordinate system
$\mathcal{R}^{A*}$	Undeformed coordinate system for beam A
$\mathcal{R}^{B*}$	Undeformed coordinate system for beam B
$P^*_{\text{tip-A}}$	Undeformed position of beam tip A
x_i^*	X axis of undeformed intermediate coordinate system
y_i^*	Y axis of undeformed intermediate coordinate system
$P_{\text{tip-B}}$	Beam tip position of beam B
α^{A}	Generalized coordinates α for bending deformation of beam A
β^{A}	Generalized coordinates β for axial deformation of beam A
α^{B}	Generalized coordinates α for bending deformation of beam B
β^{B}	Generalized coordinates β for axial deformation of beam B
T_{B}^{A}	Transformation matrix from $\mathcal{R}^{\text{B}}$ to $\mathcal{R}^{\text{A}}$
$x_{\text{tip-B}}^{\mathcal{R}^{\text{B}}}$	X coordinate of beam B tip in $\mathcal{R}^{\text{B}}$
$y_{\text{tip-B}}^{\mathcal{R}^{\text{B}}}$	Y coordinate of beam B tip in $\mathcal{R}^{\text{B}}$
$\phi_{\text{tip-B}}^{\mathcal{R}^{\text{B}}}$	Deflection angle of beam B tip in $\mathcal{R}^{\text{B}}$
$x_{\text{tip-A}}^{\mathcal{R}^{\text{A}}}$	X coordinate of beam A tip in $\mathcal{R}^{\text{A}}$
$y_{\text{tip-A}}^{\mathcal{R}^{\text{A}}}$	Y coordinate of beam A tip in $\mathcal{R}^{\text{A}}$
$\phi_{\text{tip-A}}^{\mathcal{R}^{\text{A}}}$	Deflection angle of beam A tip in $\mathcal{R}^{\text{A}}$
$x_{\text{tip-B}}^{\mathcal{R}^{\text{A}}}$	X coordinate of beam B tip in $\mathcal{R}^{\text{A}}$

$y_{\text{tip-B}}^{\mathcal{R}^{\text{A}}}$	Y coordinate of beam B tip in $\mathcal{R}^{\text{A}}$
$\phi_{\text{tip-B}}^{\mathcal{R}^{\text{A}}}$	Deflection angle of beam B tip in $\mathcal{R}^{\text{A}}$
$x_{\text{tip-B}}^{\mathcal{R}^{\text{G}}}$	X coordinate of beam B tip in $\mathcal{R}^{\text{G}}$
$y_{\text{tip-B}}^{\mathcal{R}^{\text{G}}}$	Y coordinate of beam B tip in $\mathcal{R}^{\text{G}}$
$\phi_{\text{tip-B}}^{\mathcal{R}^{\text{G}}}$	Deflection angle of beam B tip in $\mathcal{R}^{\text{G}}$
$\mathcal{R}^{\text{G}}$	Global coordinate system
T_{B}^{I}	Transformation matrix from $\mathcal{R}^{\text{B}}$ to $\mathcal{R}^{\text{I}}$
T_{I}^{A}	Transformation matrix from $\mathcal{R}^{\text{I}}$ to $\mathcal{R}^{\text{A}}$
T_{A}^{G}	Transformation matrix from $\mathcal{R}^{\text{A}}$ to $\mathcal{R}^{\text{G}}$
ω^{A}	Curvature of beam A
ω^{B}	Curvature of beam B
$\boldsymbol{\epsilon}$	Euclidean norm of the error vector
x_{g}^{G}	Given x coordinate in $\mathcal{R}^{\text{G}}$
y_{g}^{G}	Given y coordinate in $\mathcal{R}^{\text{G}}$
$\phi_{\text{g}}^{\text{G}}$	Given deflection angle in $\mathcal{R}^{\text{G}}$
σ_{yield}	Yield strength
u	Horizontal coordinate for initially-curved beams
ω_{g}	Given curvature for neutral axis
A_{cos}	Amplitude of the cosine shaped beam
T_{cos}	Period of the cosine shaped beam
f_{cos}	Frequency of the cosine shaped beam
R_{arc}	Radius of the circular arc beam
θ_{arc}	Central angle of the circular arc beam
n_{dp}	Number of distributed points
n_{b}	Number of beam elements used in CBCM and CPRBM
E_{p}	Tip position error
R_s	Switching force ratio
F_{forward}	Forward switching force
F_{backward}	Backward switching force
$P(\mathbf{d})$	Penalty function in optimization objective function
e_s	Relative error
i	Index of lower bound of displacement in constant stiffness region
j	Index of upper bound of displacement in constant stiffness region
Δy_i	Lower bound of displacement in constant stiffness region
Δy_j	Upper bound of displacement in constant stiffness region
F_{yi}	Reaction force corresponding to Δy_i
F_{yj}	Reaction force corresponding to Δy_j

f_k	Reaction force at the k-th displacement point
$\hat{f}_k$	Estimated reaction force on the fitted linear curve at the k-th displacement point

1 Introduction

1.1 Compliant mechanisms

Compliant mechanisms are mechanical systems that achieve motion or force transmission through the elastic deformation of structural components [2]. Unlike traditional mechanisms that rely on rigid links and discrete joints such as hinges or sliders, compliant mechanisms leverage the flexibility of their material to enable continuous, smooth motion. Historically, rigid-body mechanisms have been favored in engineering practice due to their modularity and simplicity in analysis. However, nature offers an alternative design paradigm. Biological systems such as the human heart, insect wings, elephant trunks, and flowering plants demonstrate how compliant behavior enables compact, efficient, and multifunctional motion.

These natural systems have inspired renewed interest in compliant mechanisms. Early human inventions, including the bow, exemplify the use of stored strain energy through structural flexibility. Leonardo da Vinci's mechanical sketches include various compliance-based designs, and the Wright brothers initially controlled flight by warping aircraft wings. These examples underscore the long-standing value of compliance in motion generation. Recent technological advancements have greatly expanded the design space for compliant mechanisms. The emergence of soft robotics has introduced new classes of systems that rely entirely on compliance to interact safely with humans and uncertain environments. Multimaterial additive manufacturing allows for the fabrication of structures with spatially varying stiffness, enabling tailored mechanical responses. Biocompatible and stretchable materials have accelerated the development of wearable and implantable compliant systems, bridging mechanics with biology.

In parallel, computational advancements have made it possible to simulate large deformation behaviors with high accuracy, allowing for the design of highly nonlinear compliant systems. Topology optimization, bio-inspired design algorithms, and artificial intelligence (AI)-guided synthesis frameworks now support the creation of compliant mechanisms with unprecedented complexity and functionality. These tools are critical in fields such as microscale actuation, adaptive structures, and low-power devices, where traditional

mechanisms face limitations. While compliant mechanisms often offer reduced part count, weight savings, and increased reliability, they also pose challenges. The integration of multiple mechanical functions within a deformable body complicates the design process. Nonlinear geometric effects, fatigue behavior, and material creep must be carefully addressed.

Despite these difficulties, the potential advantages in energy efficiency, miniaturization, and multifunctionality make compliant mechanisms a popular research direction across multiple disciplines. The following content briefly reviews the applications of compliant mechanisms in distinct fields, including precision engineering and micro/nano systems, biomedical and surgical devices, aerospace and space systems, and robotics.

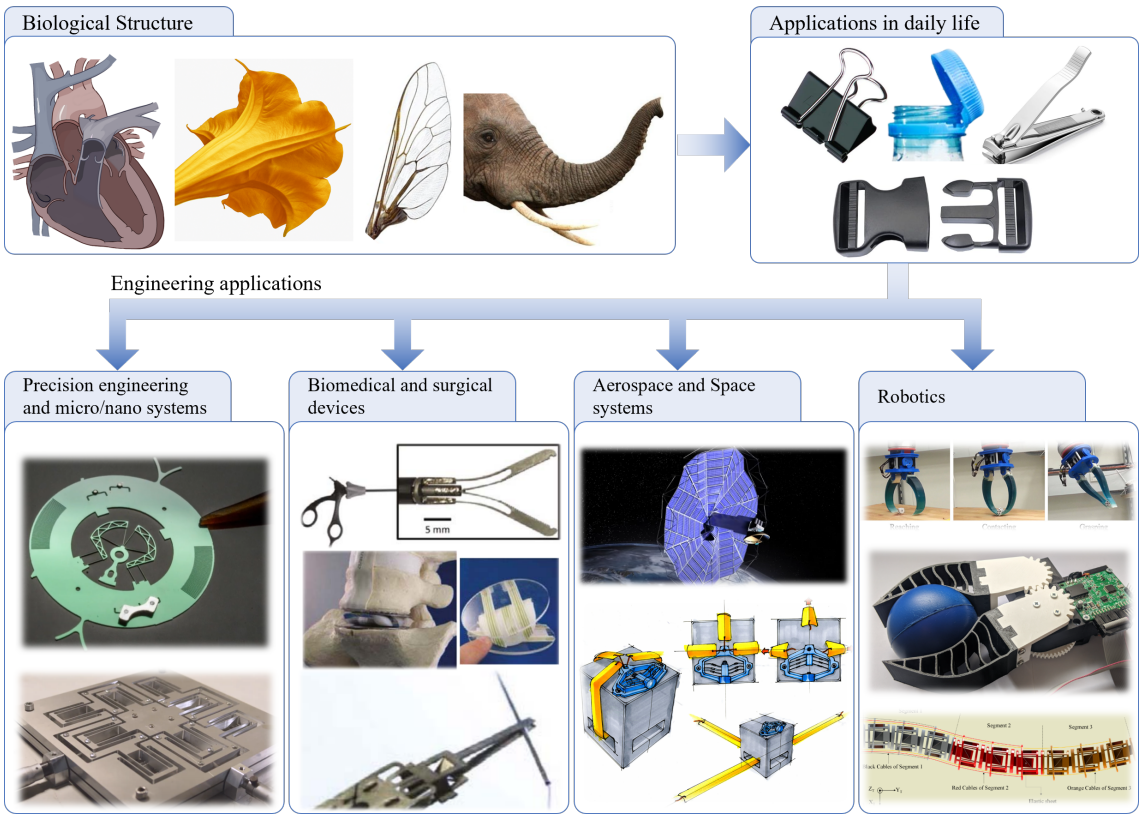


Fig. 1.1.: Bio-inspired compliant mechanisms and their applications. Natural structures such as the heart, flower petals, insect wings, and elephant trunk demonstrate intrinsic compliance, which inspires functional designs in daily objects (e.g., clips, caps, nail clippers, and buckles). These principles are further applied into engineering domains including precision micro/nano systems [3, 4], biomedical and surgical devices [5, 6, 7], aerospace systems [8, 9], and robotics [10, 11, 12], underscoring the versatility of compliant mechanisms.

1.2 Applications of compliant mechanisms

The applications of compliant mechanisms can be classified into distinct categories according to their primary functional objectives and usage contexts. These categories typically include precision engineering and micro/nano systems, biomedical and surgical devices, aerospace and space structures, and robotic systems. Each category is characterized by unique performance requirements and associated challenges. For example, precision and miniaturization in micro/nano devices, biocompatibility and safety in biomedical applications, structural robustness in aerospace, and adaptability in robotics. Despite these differences, all categories benefit from the core advantages of compliance, such as compactness, precision motion, and reduced mechanical complexity. The following sections present representative cases that demonstrate the diverse applications of compliant mechanisms.

1.2.1 Precision engineering and micro/nano systems

Compliant mechanisms are inherently well suited to precision engineering and micro/nano systems due to their jointless characteristic, which eliminates backlash, friction, and lubrication requirements. The transfer of motion through elastic deformation ensures predictable and repeatable displacement at extremely small scales, while structural monolithicity minimizes assembly-induced errors. In precision engineering, these properties are leveraged to achieve sub-micrometer positioning accuracy, high dynamic response, and reduced parasitic motion, which are essential for tasks such as optical alignment, lithography, scanning probe microscopy, and ultra-precision machining. In micro and nanoscale systems, compliant designs facilitate motion amplification, displacement guidance, and integrated sensing/actuation within Micro-Electro-Mechanical Systems (MEMS), enabling compact and multifunctional platforms that cannot be easily achieved using traditional rigid-body joints [13, 14].

In precision engineering, the most representative applications of compliant mechanisms are found in nanopositioning and optical alignment systems. Early research introduced a parallel-kinematic XY stage with symmetric flexure modules [15], achieving both high resonance frequency and low coupling error, which set a baseline for “high stiffness-high speed” designs. This concept was further advanced through the development of a fully decoupled parallel structure [16] that further suppressed cross-axis interference, providing greater margin for control accuracy. For applications requiring large vertical travel, an

integrated Z-stage was proposed [17] that combined displacement amplification, guiding, and decoupling, thereby maintaining stiffness while significantly extending range. In high-precision optical alignment, a compliant remote-center-of-motion stage was designed [18] to reduce lateral errors, particularly suitable for parallel coupling and fiber-optic alignment.

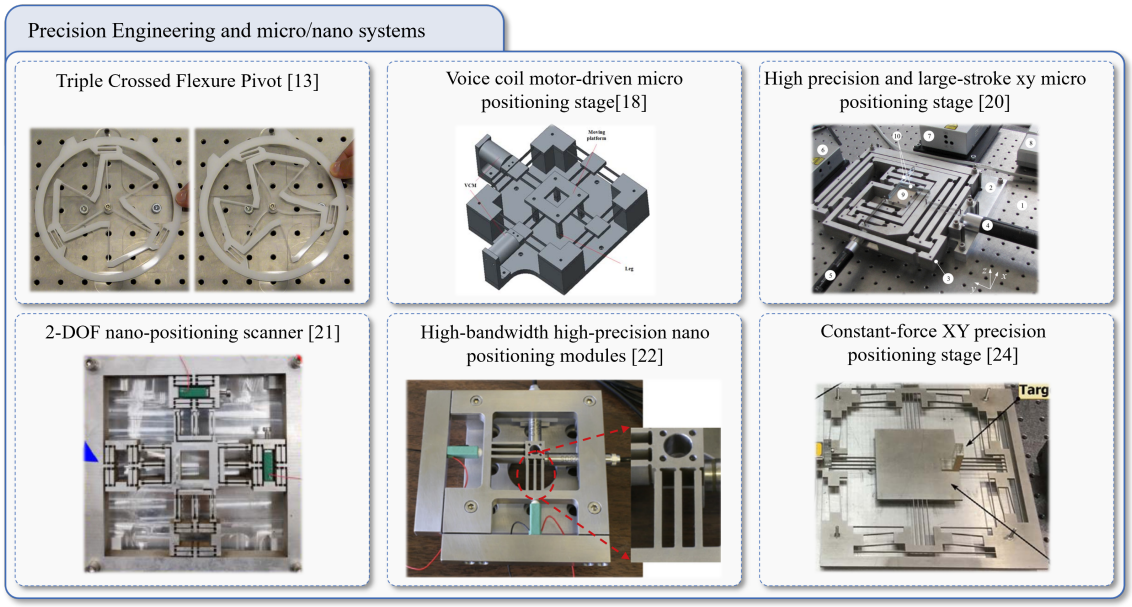


Fig. 1.2.: Applications of compliant mechanisms in precision engineering and micro/nano systems.

From the aspect of actuation, a voice-coil motor with flexure guidance [19] was employed to balance millimeter-scale travel with submicrometer resolution, while more recent work [20] applied multi-level spatial flexure hinges to enhance guiding performance and minimize parasitic motion. The trade-off between travel range and precision was addressed through serially arranged planar flexure guides [21], enabling ±10 mm stroke with high straightness, and through a compound decoupling-guiding scanner [22] that optimized bandwidth and reduced crosstalk. In addition, modular high-bandwidth flexure units [23] were developed for integration into multi-axis platforms.

At the system level, a fully decoupled XYZ parallel nanopositioner [24] resolved both input-output decoupling and integrated amplification challenges, while a constant-force XY stage [25] was introduced to enhance force uniformity in microassembly and contact-based processes. Advances in manufacturability have also played a role, with a monolithic 3D-printed flexure stage [26] achieving sub-100 nm fiber alignment at reduced cost and improved reproducibility. Collectively, these advances establish the fundamental design

pathways through which compliant mechanisms deliver precision, decoupling, and stability in precision systems.

1.2.2 Biomedical and surgical devices

In biomedical and surgical contexts, compliant mechanisms offer compelling advantages due to their monolithic, jointless structures, which inherently reduce tissue trauma, eliminate lubrication and debris, and improve sterilization compatibility. Thomas et al. classified surgical compliant mechanisms into grasping, steering, force transmission, sensing, and implantable or deployable devices, providing a systematic overview of the design strategies and clinical requirements [1]. In addition, Frecker et al. presented a multifunctional compliant mechanism capable of both grasping and cutting, integrating multiple end-effector functions within a single device [27]. Halverson et al. designed a compliant total disc replacement that replicated physiological torque-rotation behavior, offering an alternative to fusion surgery [28]. In addition, a NiTi-based compliant mechanism enabled a 4 mm laparoscopic prototype with two degrees of freedom to deliver over 15 N grasping force for minimally invasive surgery [29]. Compliant mechanisms are also utilized to develop programmable multistable devices for safe surgical puncturing, exemplified by a retinal cannula that decouples puncturing stroke from operator input to prevent overpuncturing [30].

Beyond surgical manipulation, compliant mechanisms have also advanced medical sensing. A study integrated a compliant mechanism to create a biocompatible tip force sensor, enabling real-time measurement with 0.01 N resolution in the 0.1-0.5 N range [31]. Additionally, Kumar et al. utilized topology optimization to fabricate large-deformation compliant devices for controlled tissue strain, demonstrating the adaptability of compliant mechanism based designs for biological experimentation [32]. These studies illustrate that compliant mechanisms provide a unique combination of compactness, multi-functionality, sterility compatibility, and mechanical precision that is difficult to achieve with conventional rigid-body designs.



Fig. 1.3.: Overview of compliant mechanism applications in biomedical and surgical devices. Figure adapted from a literature review in [1].

1.2.3 Aerospace and Space Systems

In aerospace and space systems, compliant mechanisms are leveraged to achieve reliable shape change and deployment with fewer parts, lower mass, and no lubrication, which is critical under harsh environments and tight weight budgets. Distributed-compliance morphing wings replace discrete hinges with selectively compliant internal structures or skins to provide smooth, gap-free camber/twist changes: laboratory-to-flight evidence has shown aerodynamic benefits and robust operation [33, 34]. Compliance can be combined with variable-stiffness or bi-stable laminates to expand attainable shapes and reject loads [35], while corrugated/compliant skins enable large recoverable strains without compromise to load-bearing capability [36]. Passive approaches that exploit elastic instability further demonstrate wing-twist authority without actuators at the control surface scale, highlighting the efficiency potential of compliance-driven morphing wings [37]. In addition, a compliant pivot design for space pointing and scanning mechanisms is proposed, offering minimal parasitic displacement, high angular resolution, and proven long-term durability [38].

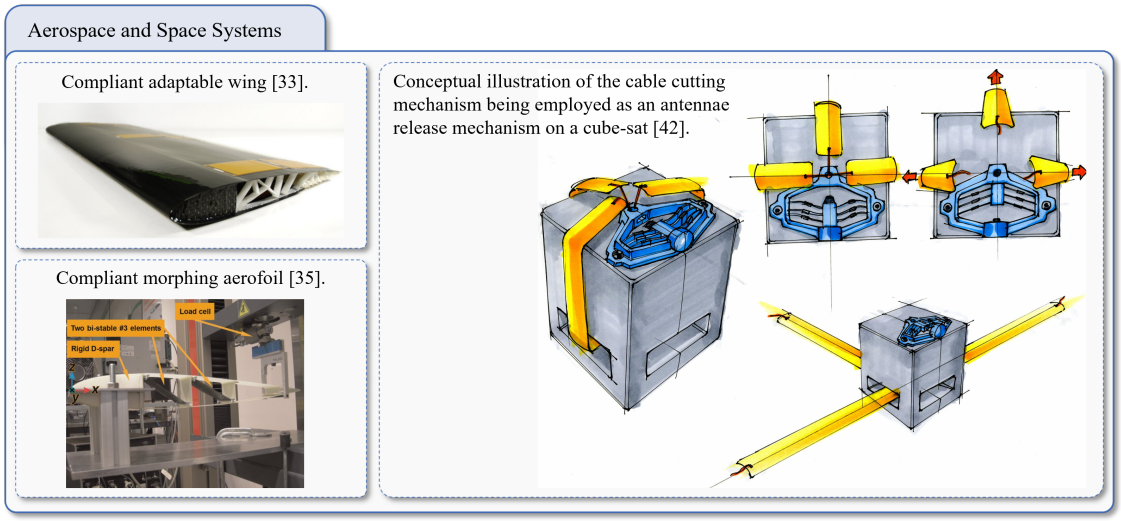


Fig. 1.4.: Representative applications of compliant mechanisms in aerospace and space systems.

For deployable structures in outer space, compliant mechanisms underpin tape-spring hinges and ultrathin composite booms that fold elastically for stowage and self-deploy by releasing stored strain energy, an approach that improves precision and reduces part count relative to traditional hinge-spring trains [39, 40, 41]. Beyond monostable deployments, compliant bi-stable mechanisms (latches, pin-pullers, cutters) have been tailored in space-compatible materials, offering power-free holding states and friction-free releases that enhance reliability of space deployables [42]. At the materials-system interface, aero-structural design methods couple compliant topologies, smart actuation, and control to achieve repeatable morphing under aerodynamic loading, including piezo-composite bi-stable panels configured as wing-shaped elements [43]. Collectively, these studies establish compliant mechanisms as a unifying design route for morphing aerostructures and deployable structures, delivering smooth kinematics, reduced mechanical complexity, and flight-relevant performance.

1.2.4 Robotics

In addition to previous introduced scenarios, compliant mechanisms are also widely used in robotics due to their inherent flexibility, structural simplicity, and precise motion. Recent review studies have summarised the diverse applications of compliant mechanisms across various type of robotics [44, 45, 46, 47, 48]. These applications can be broadly classified into several key directionos. Compliant grippers utilize structural compliance to adaptively grasp objects of varying shapes and fragilities, making them well suited to unstructured

environments. Compliant joints replace traditional bearings or hinges to deliver smooth, backlash-free motion with reduced maintenance [49]. Compliant actuators integrate actuation and structural elements, resulting in compact, lightweight, and energy-efficient motion generation. Compliant sensors exploit deformation-induced responses to measure forces, displacements, or tactile feedback within a structurally integrated design. Compliant end effectors, beyond grippers, encompass tools for cutting, polishing, and manipulation with enhanced contact compliance. Compliant suspension and isolation systems improve stability and safety by mitigating vibrations and absorbing impacts in mobile or aerial robots. Finally, compliant continuum robots employ continuous flexible structures to achieve high flexibility, safety, and adaptability in confined or complex environments. Collectively, these categories demonstrate the critical role of compliant mechanisms in enhancing the performance, safety, and versatility of modern robotic systems.

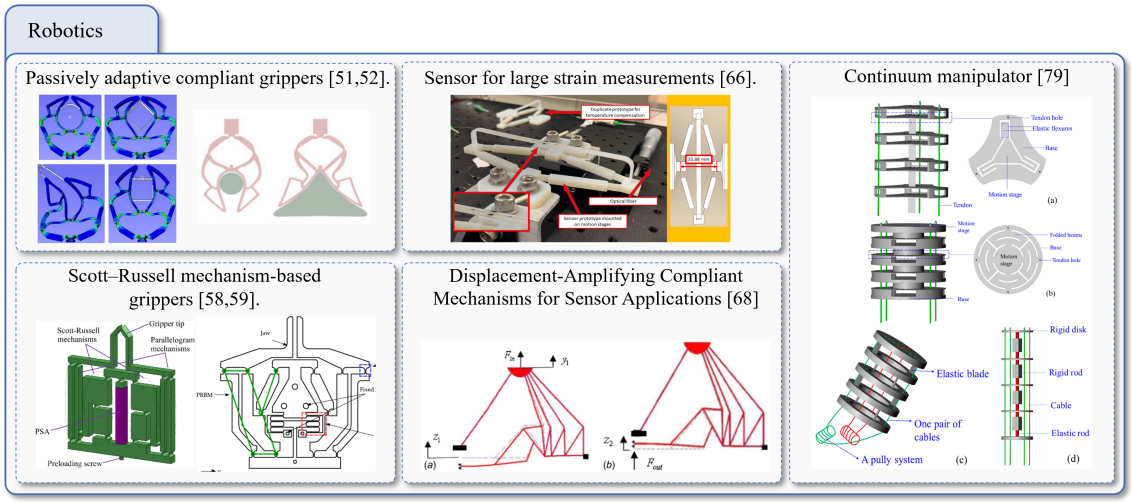


Fig. 1.5.: Representative applications of compliant mechanisms in robotics.

Among these categories, compliant grippers have attracted particular attention for their ability to combine adaptability, precision, and structural efficiency in robotic manipulation tasks. Leveraging the elastic deformation of their structural elements, they can adapt to diverse object shapes, provide protective gripping, and handle delicate items without complex control schemes [50, 51, 52]. Recent developments span constant-force designs for stable grasping performance across varying object sizes [50, 53, 54], multimode jaws enabling multifunctional operation [55, 56], and integrated sensing for position, force, or interaction monitoring [57]. Innovative configurations include mechanisms based on the Scott-Russell linkage [58, 59], distributed-compliance layouts [60], flexure-guided parallel jaw motion [61], and soft composite hinge actuators [62]. Other advancements feature modular systems for micromanipulation [63], variable stiffness implementations via layer

jamming [64], and optimisation-based approaches for grasping unknown or fragile objects [65]. These diverse strategies highlight the versatility and ongoing evolution of compliant gripper technology for addressing the challenges of robotic manipulation.

Beyond their role in compliant grippers, compliant mechanisms have also been extensively integrated into various sensor designs, where their inherent elasticity enables precise force-to-deformation transduction without friction or backlash. Such mechanisms have been utilized in fiber-optic sensing systems to achieve large-strain measurements with high sensitivity and immunity to electromagnetic interference [66]. They have also been exploited in force and weight sensing, where the compliant structure is optimized to enhance measurement accuracy while maintaining mechanical robustness [67]. In addition, displacement-amplifying compliant mechanisms have been systematically evaluated and designed to boost the resolution of sensing elements, enabling the detection of minute displacements and forces in diverse applications [68].

Compliant mechanisms further facilitate the development of multi-range and multi-degree-of-freedom sensing systems. For instance, strain gauge-based force sensors employing compliant structures have been designed with multiple measurement ranges to cover both fine and coarse force detection [69]. At the microscale, compliant mechanisms enable precise measurement of micro/nanoscale planar motions in three degrees of freedom [70], as well as micro-Newton forces through vision-based displacement amplification [71]. Fully decoupled compliant parallel mechanisms have been adopted in multidimensional acceleration sensors to minimize cross-axis interference and improve accuracy [72], while compact three-axis force sensors based on compliant mechanisms have been developed for high-precision manufacturing tasks [73]. These examples illustrate the versatility of compliant mechanisms in sensor applications, offering tailored mechanical responses to meet specific sensitivity, range, and integration requirements.

In continuum robotic systems, compliant mechanisms are widely employed to achieve delicate motion, variable stiffness, and integrated sensing. Mechanical models have been established to capture the complex interactions between compliant joints, tendon actuation, and external forces, providing a foundation for accurate motion prediction and control [74]. Novel designs, such as twin-pivot compliant joints, have been developed and validated to enhance workspace and payload capabilities [75], while additive manufacturing techniques have enabled the fabrication of flexible joints with presettable stiffness tailored for surgical applications [76].

Beyond actuation, compliant mechanisms facilitate intrinsic sensing capabilities, allowing force estimation without dedicated external sensors [77]. Cable-driven manipulators incorporating large open lumens have been realized for minimally invasive procedures, demonstrating both functional integration and application-specific adaptability [78]. Other innovations include double-layer planar springs for achieving high compliance with improved structural support [79] and snake-arm robot architectures interconnected by compliant joints to achieve enhanced maneuverability in constrained environments [80]. Monolithic compliant continuum manipulators have also been demonstrated as proof-of-concept platforms, highlighting the feasibility of integrating actuation, compliance, and sensing into a single structural form [81]. Collectively, these developments showcase the potential of compliant mechanisms to advance the design and performance of continuum robotic systems across medical, industrial, and exploratory domains.

Most of the aforementioned applications rely on beam-based compliant designs, which are widely adopted due to their simplicity and versatility. However, their inherent nonlinear behavior poses significant challenges for accurate analysis. To address this, extensive research has been devoted to the modeling and characterization of beam-based compliant mechanisms. The following section reviews the main modeling approaches that have been developed for this purpose.

1.3 Modeling methods

The broad spectrum of applications of compliant mechanisms, from precision sensing to continuum robotic manipulation, highlights their ability to deliver large, continuous deformations with high repeatability and minimal mechanical complexity. These advantages inherently arise from significant elastic deformation of the structure, often beyond the small-deflection assumptions used in conventional beam or frame theories. In such regimes, pronounced geometric nonlinearity governs the structural response, and accurate prediction of deformation, stress distribution, and force-displacement behavior becomes essential for ensuring reliable performance in demanding applications.

Finite element analysis (FEA) has long been regarded as a powerful and versatile tool for modeling compliant mechanisms under large deformation, providing high-fidelity predictions through numerical discretization. However, its reliance on meshing, substantial computational resources, and case-specific setup can limit its efficiency for iterative design and rapid evaluation. Analytical models, by contrast, offer explicit relationships between

design parameters and mechanical responses, enabling fast performance assessment, sensitivity analysis, and optimization without the computational burden of full-scale simulations. When tailored to capture bending, axial stretching, shear, and torsion in the large-deformation regime, these analytical models serve as an indispensable bridge between conceptual design and high-fidelity numerical validation [82].

Developing analytical models for large-deformation compliant mechanisms presents substantial challenges due to inherent strong geometric and material nonlinearities. The presence of geometric nonlinearities invalidates the linear relationship between displacement and strain, while flexible materials with nonlinear constitutive behavior introduce additional coupling between geometric and material nonlinearities. Furthermore, large deformation processes often involve strongly coupled multi-degree-of-freedom deformation modes, making closed-form solutions particularly difficult to obtain. Addressing these challenges requires analytical formulations that accurately capture the key nonlinear effects while maintaining computational efficiency, thereby supporting the systematic design and optimization of compliant mechanisms for advanced engineering applications.

In prior studies, numerous modeling methods have been proposed for the analysis of compliant mechanisms. These methods can be broadly categorized into four main categories: smooth curvature model (SCM) [83], pseudo-rigid-body model (PRBM) [84], beam constraint model (BCM) [85, 86], and elliptic integral solution (EIS) [87]. The majority of compliant mechanisms have been subjected to modeling, analysis, and optimization using these four fundamental methods and their respective branch methods. The application of these approaches has significantly advanced the development of compliant mechanisms. An in-depth review of the strengths and weaknesses of these methods is presented in the following sections.

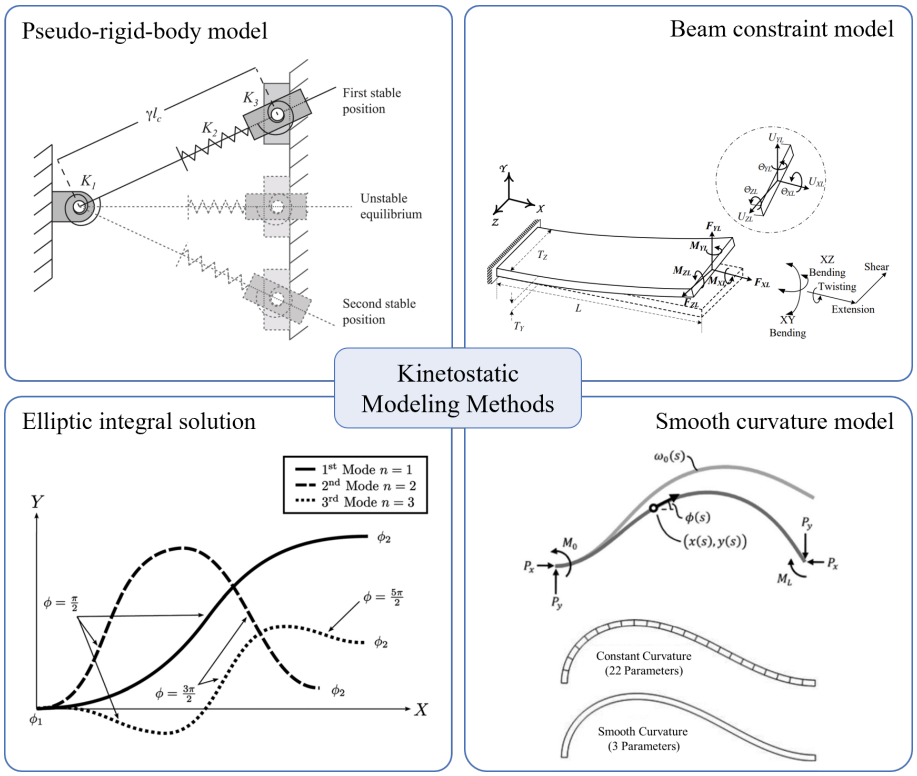


Fig. 1.6.: Representative kinetostatic modeling methods for compliant mechanisms. The pseudo-rigid-body model approximates flexible deformations using rigid links and torsional springs. The beam constraint model captures large deflections through force-moment relations at beam ends. Elliptic integral solutions provide exact analytical descriptions for certain beam configurations, but require discussion on number of inflection points. The smooth curvature model describes the continuous deformation of compliant members with a small number of parameters, offering a balance between accuracy and computational efficiency.

1.3.1 Pseudo-rigid-body model

The pseudo-rigid-body model (PRBM) employs rigid-body components with equivalent force-deflection characteristics to predict system deflection and force-deflection relationships. The 1R-PRBM consists of two rigid links joined at a pin joint and a torsion spring along the beam [84, 88, 89]. However, the approximation error becomes significantly large when the tip inclined angle exceeds a certain bound. The 3R-PRBM was proposed to overcome this weakness, consisting of three revolute joints, each accompanied by a torsion spring [90, 91, 92]. To reduce the complexity and computation time of the 3R-PRBM while increasing the accuracy of the 1R-PRBM, the 2R-PRBM emerged in [93]. To more accurately predict the behavior of compliant beams, the 5R-PRBM and Chained PRBM (CPRBM) have been proposed in recent years [94, 95]. Although PRBM is well-applied

in designing various mechanisms [96, 97, 98], there are still some weaknesses in this modeling method, including unable to obtain accurate deformation shapes, simplified dynamics, and limited accuracy.

1.3.2 Beam constraint model

An alternative modeling approach, the beam constraint model (BCM), provides closed-form solutions for fixed guided beams. The innovation of BCM lies in its capacity to depict the relationships between comprehensive loads and end-displacements, covering both translational and rotational movements, across a wide range, all while maintaining simplicity and accuracy [85, 86]. The Timoshenko BCM (TBCM) expands this framework to account for shear effects, thereby improving prediction accuracy [99, 100]. Furthermore, another modeling technique, the Bi-BCM, involves dividing a fixed-guided beam into two distinct beam elements. The BCM is then independently employed for each beam element and subsequently combined to yield a closed-form load-deflection solution. In this approach, the tip loads are represented as functions of tip deflections. This method particularly excels in modeling compliant beams with a single fixed end, making it well-suited for the analysis of compliant bistable mechanisms [101, 102, 103, 104]. In addition, accurately predicting the effects of significant axial forces presents a challenge for BCM. This challenge was addressed by increasing the order of the BCM [105]. Moreover, a General Lumped-compliance Beam Model (GLBM) was introduced to address modeling challenges posed by complex compliant mechanisms [106]. Moreover, the dynamic beam constraint model (DBCM) addresses nonlinearity in intermediate-deformation compliant mechanisms, aiding kinetostatic and large-amplitude vibration analyses effectively [107].

The BCM and its derivative models, as previously stated, are limited to small deflection assumption, making them unsuitable for modeling compliant mechanisms undergoing large deformation. To tackle this challenge, researchers developed various alternative methods. Chained BCM (CBCM) is proposed for modeling large deflections in both straight and curved compliant beams and mechanisms [108, 109]. It aims to provide a versatile method for efficiently addressing a wide range of large deflection problems in such systems [61, 110, 111, 112, 113]. Besides, chained spatial BCM (CSBCM) was proposed to address the challenge of modeling spatial deflections in compliant mechanisms [114, 115]. While the CBCM and CSBCM methods successfully address the issue of handling large deformations, they introduce increased complexity into the modeling process. This complexity arises from their approach of dividing the beam into multiple sub-beams and applying the BCM to each of these segments. As the number of sub-beams increases,

the computational complexity escalates, and the calculation process starts resembling finite element analysis (FEA). Moreover, these methods are unable to provide specific deformation shapes for compliant beams.

1.3.3 Elliptic integral solution

The elliptic integral solution (EIS) is widely recognized for its accuracy in analyzing large deflections in thin beams within compliant mechanisms [87, 116, 117]. The comprehensive elliptic integral solution (CEIS) also extends the elliptic integral solutions to be suitable for any beam end angle and further considering axial deformation[118]. Within the framework of the EIS method, inflection points consistently constitute a central topic of discussion. These points are characterized by changes in curvature sign on a smooth plane curve, shifting between concave and convex shapes. The number of inflection points plays a pivotal role in the modeling process. Consequently, the modeling process necessitates case specific considerations under different circumstances. This causes an increase in the complexity of the modeling process while simultaneously reducing its universality.

1.3.4 Smooth curvature model

The advent of the smooth curvature model (SCM) has brought the modeling complexity to a lower level, which efficiently describes compliant beams by approximating beam curvature with low-order polynomials [83]. The smooth curvature model and its derived models aim to address the inherent limitations of the previously mentioned methods, which include their restricted applicability to small deformations, complex modeling requirements, lack of consideration for deformation shape, the necessity of inflection point analysis, and suitability only for straight beams.The Multiple SCM (MSCM), an extension of the fundamental SCM which split compliant structure into multiple beam elements and apply SCM to each of the beam element. This method is proficient in modeling intricate, highly compliant mechanisms [119]. Pongsiri et al. integrated the SCM with Lagrange multiplier and Newton-Raphson methods and applied Castigliano's principle of minimum strain-energy, resulting in a novel approach to address the grasp stability problem [120]. This energy method is based on SCM and now referred to as the 2nd-order SCME method.

In addition to the Newtonian methods discussed above, previous studies have established the groundwork for utilizing energy-based methodologies for the kinetostatic analysis

of compliant mechanisms. A previous work has proposed an energy-based method utilizing three commonly used models (BCM, PRBM, and linear Euler-Bernoulli beam model) towards a generalized framework for kinetostatic analysis of planar compliant mechanisms [121]. Besides, another model integrates the screw theory with the energy method for accurate and efficient kinetostatic analysis of general compliant mechanisms [122]. As mentioned earlier in [95], a method combining the energy approach and Chained Pseudo-Rigid-Body Model (CPRBM) is proposed to address the nonlinear contact problem in contact-aided compliant mechanisms. In [123], an energy-based framework is proposed, in which both strain energy and complementary strain energy are integrated into the nonlinear kinetostatic modeling of compliant mechanisms passively. Within this framework, the strain energy and complementary strain energy are expressed using the BCM and integrated through two nonlinear energy theorems, namely Castigliano's first theorem and the Crotti-Engesser theorem.

A comparative analysis is conducted to clarify the strengths of each modeling method, which are summarized in Table 1.1. The high-order SCME and CoSCME methods, both proposed in this thesis, are also included in the comparison to highlight their scope and capabilities relative to existing approaches.

Tab. 1.1.: A comparative analysis of kinetostatic modeling methods for compliant mechanisms is presented. The High-order SCME and CoSCME methods proposed in this thesis are introduced in the following chapters.

	Modeling method	Output			Beam type		Deformation type	
		Deformation shape	Strain energy	Stress	Straight	Curved	Bending	Axial
PRBM	PRBM [84]				✓		✓	
	2R-PRBM [93]		✓		✓		✓	
	3R-PRBM [90, 91, 92]	✓	✓		✓		✓	
	5R-PRBM [94]	✓	✓		✓	✓	✓	
	CPRBM [95]	✓	✓		✓	✓	✓	
BCM	BCM [85, 86]		✓		✓		✓	✓
	TBCM [99, 100]		✓		✓		✓	✓
	3rd-order BCM [105]		✓		✓		✓	✓
	GLMB [106]		✓		✓		✓	✓
	DBCM [107]		✓		✓		✓	✓
	CBCM [108, 109]	✓	✓	✓	✓	✓	✓	✓
	CSBCM [114, 115]	✓	✓	✓	✓	✓	✓	✓
EIS	EIS [87, 116, 117]	✓	✓	✓	✓	✓	✓	
	CEIS [118]	✓	✓	✓	✓	✓	✓	✓
SCM	SCM [83]	✓	✓		✓	✓	✓	
	MSCM [119]	✓	✓		✓	✓	✓	
	SCME [120]	✓	✓	✓	✓	✓	✓	
	High-order SCME [124]	✓	✓	✓	✓	✓	✓	
	CoSCME [125]	✓	✓	✓	✓	✓	✓	✓

1.4 Compliant mechanism optimization

Compliant mechanism optimization refers to the process of systematically improving the geometric configuration, topology, and material distribution of compliant mechanisms to achieve specific performance objectives. Optimization in this context often aims to enhance attributes such as motion precision, force transmission efficiency, energy storage capacity, or multi-functional adaptability, while satisfying constraints related to strength, stability, and manufacturability. Depending on the design requirements, the optimization process can be classified into shape optimization, geometric optimization, and topology optimization, or into single-objective and multi-objective formulations. Common computational algorithms include gradient-based algorithms, genetic algorithms, particle swarm optimization, level-set methods, and topology optimization frameworks, often integrated with analytical models or finite element analysis to ensure accurate modeling of large deflections and nonlinear behavior [126].

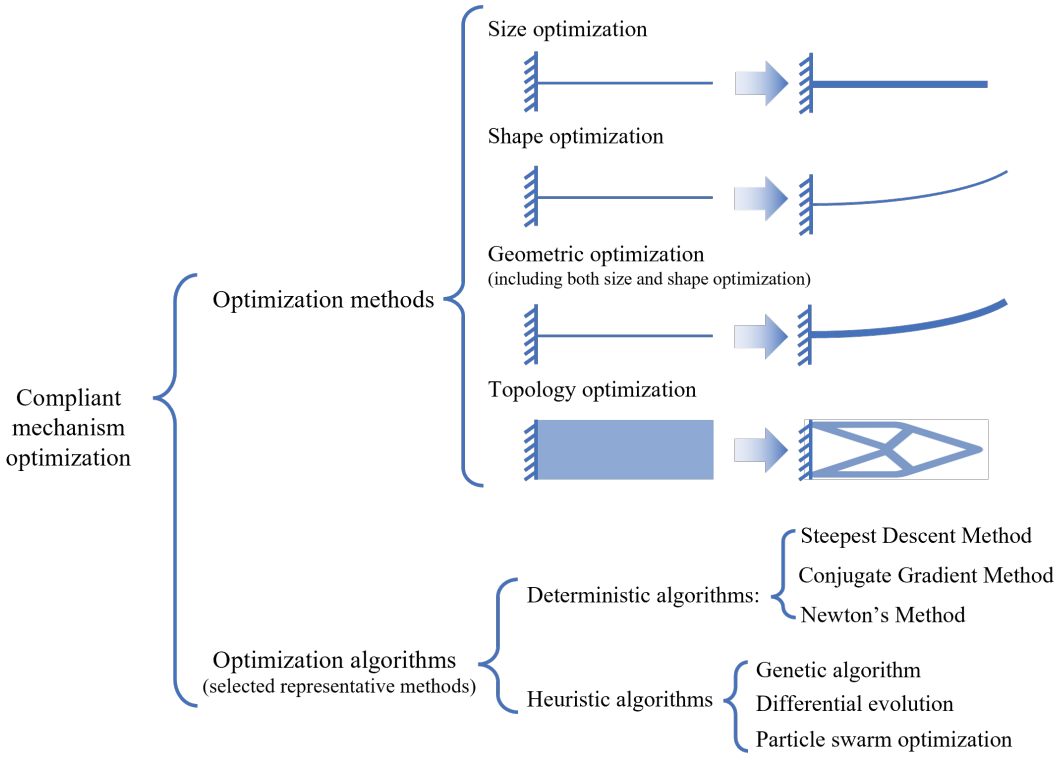


Fig. 1.7.: Classification of optimization approaches and algorithms for compliant mechanisms.

1.4.1 Optimization methods

Optimization methods for compliant mechanisms can be generally classified into four principal categories: size optimization, shape optimization, topology optimization and hybrid optimization methods such as geometric optimization. Size optimization focuses on adjusting dimensional parameters, such as beam length, thickness, width, or cross-sectional radius, while keeping the overall geometry and topology fixed. This approach is straightforward, computationally efficient, and easy to integrate with analytical models, but it offers limited design flexibility. Shape optimization modifies global shape parameters, including curvature distribution, component positioning, and connection angles, without altering the number of components or topology. It provides greater design freedom and can significantly improve kinematic and mechanical performance, although it requires careful parameterization to manage the large design space. Topology optimization operates at the highest level of design freedom by adding, removing, or rearranging structural members to produce entirely new topologies. It can yield highly innovative designs but typically involves high computational costs and post-processing to achieve manufacturable geometries. Hybrid geometric optimization such as geometric optimization combines the principles of size and geometric optimization, simultaneously adjusting dimensional

and geometric parameters within a fixed topology. This method balances computational efficiency with design flexibility, making it well suited for achieving substantial performance improvements while maintaining manufacturability. Each of these approaches offers distinct advantages and trade-offs in terms of design flexibility, computational complexity, and manufacturability, and their selection depends on the desired performance objectives and practical constraints [127, 128, 129].

(a) Size optimization

Size optimization in compliant mechanisms plays a crucial role in fine-tuning key dimensional parameters, such as beam or hinge thickness, width, length, and fillet radius, within a fixed topology to improve performance under operational constraints. Adjusting these parameters can improve displacement amplification, expand the usable workspace, balance input and output stiffness, suppress parasitic motions, reduce peak stresses, extend fatigue life, and optimize dynamic characteristics such as natural frequencies and energy consumption. Compared to geometric or topology alterations, size optimization involves fewer design variables and often allows for analytical derivation, enabling rapid convergence and seamless integration with distinct models.

Although size optimization in compliant mechanisms is less frequently studied as a standalone topic compared to shape or topology optimization, a few notable works have focused primarily on dimensional parameter tuning. Wang et al. optimized the thickness, length, and width of bridge-type flexure hinges to maximize displacement amplification while controlling stress, achieving experimental errors below 6% [130]. Hetrick developed a methodology that, although described as size and shape optimization, is largely driven by dimensional variables such as member length and thickness, incorporating stress constraints to improve durability and flexibility [131]. Similarly, De Bona and Munteanu optimized the neck radius and thickness of micro-fabricated flexural hinges using spline-based notch modeling in a finite-element framework to satisfy both strength and kinematic requirements [132]. These studies demonstrate the value of size optimization for refining compliant mechanism performance within fixed topologies, while also highlighting its relatively modest representation in the literature compared to more widely explored topology or geometric approaches.

(b) Shape optimization

Shape optimization modifies the global geometric parameters of a compliant mechanism, such as component positions and connection angles, without changing the number of components or the overall topology. Compared to size-only optimization, it provides a much broader design space and enables substantial improvements in kinematic performance (such as motion accuracy, displacement amplification, range of motion) and mechanical behavior (such as stiffness distribution, stress concentration reduction, fatigue resistance). This flexibility makes shape optimization a powerful tool for tailoring the force-displacement response, enhancing motion precision.

The concept of obtaining an layout of a structure using frame elements has been referred to as shape optimization of skeletal structures [133]. While early work focused on such skeletal layouts, more recent research has increasingly emphasized determining the optimal boundaries of two- and three-dimensional structures, with numerous innovative methods proposed; a comprehensive review can be found in [134]. Among the various approaches, Zienkiewicz and Campbell [135] defined the nodal coordinates of the finite element model as design variables, a strategy that complicates optimization since arbitrary changes in nodal positions may produce invalid topologies or shapes. To address this, other studies have employed a limited set of key points or master nodes to represent geometric entities [136, 137]. More recently, parametric and feature-based CAD geometric modeling has emerged as a powerful tool, enabling shape control through key dimensions that define the locations of control points. In the context of compliant mechanisms, Hetrick and Kota [138] demonstrated a related approach by varying the coordinates of selected master nodes within a finite element model composed of frame elements to achieve shape variation.

(c) Geometric optimization

Geometric optimization in the context of compliant mechanisms refers to a hybrid design strategy that simultaneously optimizes dimensional parameters (as in size optimization) and global geometric features (as in shape optimization) within a fixed topology. By combining these two levels of control, geometric optimization significantly expands the design space compared to either size-only or shape-only methods, enabling the designer to refine both local stiffness distribution and overall kinematic behavior in a single unified process. This approach allows targeted improvements in performance metrics such as motion amplification, stiffness tailoring, stress reduction, and displacement trajectory accuracy, while maintaining manufacturability and structural integrity.

Several works have introduced geometric optimization strategies for compliant mechanisms that enhance performance through boundary refinement within fixed topologies. One study applies three-dimensional wide-curve representations to refine the spatial geometry of compliant structures, enabling enhanced motion precision and stress distribution without altering the underlying topology [139]. Another methodology employs free-form wide-curve parameterizations to jointly optimize both shape and dimensional attributes of flexure segments, yielding smooth boundaries and improved performance via a compact set of control parameters [140]. Extending this concept, multilayer wide curves have been used to model and optimize multimaterial compliant mechanisms, enabling distinct material zones and geometric control across the structure for tailored stiffness and deformation characteristics [141]. Although specific details of other related approaches, such as multi-objective optimization of linear compliant mechanisms [142] and bend-and-sweep mechanism design [143], are not elaborated here, these studies collectively demonstrate how geometric optimization, particularly through wide-curve parameterization, can significantly expand the design flexibility in compliant mechanism synthesis.

(d) Topology optimization

Topology optimization for compliant mechanisms operates at the highest level of design freedom, allowing the addition, removal, or redistribution of material within a prescribed design domain to achieve a desired function, often without preconceived geometric constraints. Unlike size or shape optimization, which refine existing configurations, topology optimization can generate entirely novel structural layouts capable of achieving specified kinematic or force-displacement responses. This approach enables the synthesis of mechanisms with enhanced performance metrics such as displacement amplification, motion precision, stiffness tailoring, and multi-functional integration. The most common optimization objectives include compliance minimization, mechanical advantage maximization, and output displacement maximization, often under stress, displacement, or frequency constraints. While its design space richness facilitates highly innovative solutions, topology optimization also poses challenges, such as high computational cost, non-unique solutions, and the need for post-processing to convert conceptual layouts into manufacturable geometries.

Topology optimization has been extensively applied to the synthesis of compliant mechanisms, with various formulations targeting different performance criteria. Foundational studies establish continuum-based approaches for compliant mechanism design [144, 145], and reviews have consolidated advances in material distribution methods, objective func-

tions, and computational strategies [144]. Several works address nonlinear elasticity to capture large-deformation effects, improving prediction accuracy and functional performance [146]. Stiffness-targeted formulations aim to achieve prescribed structural compliance or stiffness distribution by adjusting topology while meeting displacement requirements [147]. Multi-objective frameworks have been developed to balance conflicting goals such as maximizing output displacement and minimizing input force or structural volume [148, 149]. Constraint-driven methods explicitly limit stress to improve durability [150] or maintain manufacturability. Evolutionary algorithms offer heuristic search capabilities for conceptual topology generation [151]. Boundary-accurate representations such as the level-set method enable smoother geometries and more precise stress control [152]. Robust optimization frameworks incorporate load uncertainties to ensure stable performance [153]. Applications extend to domain-specific designs, including flapping-wing mechanisms [154], constant-force output devices [155], and planar compliant parallel mechanisms [156]. Additional contributions involve sparse monolithic configurations [157], integrated link and support modeling [158], design-dependent pressure loading [159], and meshless element-free Galerkin formulations for enhanced geometric adaptability [160]. Collectively, these studies demonstrate that topology optimization remains the most powerful generative tool for compliant mechanism synthesis, with a broad spectrum of formulations tailored to performance, robustness, and manufacturing considerations.

1.4.2 Optimization algorithms

Optimization algorithms have become indispensable tools in modern engineering design, enabling systematic and quantitative exploration of high-dimensional design spaces to identify solutions that achieve the best trade-off between performance, cost, and other constraints. By formulating the design task as a mathematical optimization problem, these algorithms provide a structured way to search for optimal or near-optimal configurations, even when intuitive or trial-and-error approaches become impractical due to the complexity of the system. Currently, optimization algorithms can be also broadly classified into deterministic and heuristic approaches, each offering distinct advantages for different classes of problems. Deterministic algorithms rely on exact mathematical rules to guide the search process, producing the same solution when initialized under identical conditions. These methods, such as gradient-based techniques, Newton-type methods, and sequential quadratic programming, typically exploit derivative information to achieve rapid and precise convergence, making them well-suited for smooth and differentiable problems. In contrast, heuristic algorithms incorporate stochastic components inspired by natural phenomena, enabling flexible exploration of complex, multimodal, or non-differentiable

design spaces. Representative examples include evolutionary algorithms, such as the genetic algorithm and differential evolution, and swarm intelligence methods, such as particle swarm optimization and ant colony optimization.

(a) Deterministic algorithms

Deterministic algorithms refer to optimization procedures that follow a well-defined, repeatable sequence of steps, producing identical results when initialized with the same conditions. Their search trajectory is fully determined by the mathematical formulation of the problem, often exploiting gradient or higher-order derivative information to guide the search towards an optimal solution. These methods are particularly effective for smooth, continuous, and differentiable objective functions, where they can achieve rapid convergence with high numerical precision. Representative approaches include but are not limited to the steepest descent method, the conjugate gradient method and Newton's method. Despite their efficiency, deterministic algorithms may converge to local optima in nonconvex landscapes and are sensitive to the quality of the initial guess, making them less robust for highly irregular or discontinuous problems [161, 162].

The steepest descent method, also referred to as the gradient descent method, is a classical iterative optimization approach that updates the solution in the direction of the negative gradient of the objective function, corresponding to the direction of maximum local decrease [163]. A suitable step length is typically determined through line search at each iteration. While originally developed for single-objective unconstrained problems, the method has been extended to handle multicriteria and vector optimization problems by generalizing the descent direction to account for multiple objectives simultaneously [164, 165]. Further developments include hybrid steepest descent schemes that incorporate additional operators, such as projection steps, to address variational inequalities and improve convergence properties [166]. Previous literature reviews indicate that steepest descent methods can be competitive for well-conditioned problems but may converge slowly for ill-conditioned landscapes, motivating adaptive variants and hybridization with stochastic approaches such as random search [167]. These adaptations enhance robustness, broaden applicability, and maintain the conceptual simplicity that has made steepest descent a foundational tool in deterministic optimization.

The conjugate gradient method is another iterative technique for solving large-scale systems of linear equations and unconstrained optimization problems, particularly when the coefficient matrix is symmetric and positive definite [168]. Unlike the steepest descent

method, which may suffer from ill-conditioned problems, the conjugate gradient constructs a sequence of mutually conjugate search directions, leading to faster convergence in at most n steps for n-dimensional problems in exact arithmetic. The method has been extended to the nonlinear conjugate gradient framework, which adapts the direction-update rules to handle general nonlinear optimization problems [169]. Applications also include optimal control problems, where conjugate gradient provides an efficient approach for solving large-scale discretized systems arising from control constraints and partial differential equations [170].

The Newton's method is a classical iterative approach for solving nonlinear equations and optimization problems, based on approximating the objective or residual function with a second-order Taylor expansion and updating the solution using first and second derivative information [171, 172, 173]. In optimization, it achieves quadratic convergence near the optimum when the Hessian is positive definite, and it has been extended to handle multiobjective optimization [174] and problems with constraints through projected and modified Newton schemes [175, 176]. Variants of the method have been applied across disciplines, including decision sciences, education, and nonlinear finite element analysis, often referred to as the Newton-Raphson method in engineering contexts [177, 178]. While Newton's method is powerful, its efficiency depends on accurate derivative information and a good initial guess, and it may require globalization strategies such as line search or trust regions to ensure convergence.

(b) Heuristic algorithms

Heuristic algorithms encompass a broad class of optimization methods that incorporate stochastic elements or problem-specific rules to guide the search process, often drawing inspiration from natural phenomena, social behaviors, or biological evolution. Unlike deterministic algorithms, their search trajectory is not entirely predetermined and can vary across runs even under identical initial conditions, allowing them to explore the design space more broadly and reduce the risk of premature convergence to local optima. These methods do not require derivative information, making them well-suited for complex, multimodal, discontinuous, or non-differentiable objective functions. Representative approaches include genetic algorithms, differential evolution, as well as particle swarm optimization. While heuristic algorithms generally require greater computational effort and may converge more slowly, their flexibility, robustness, and capacity to navigate highly irregular search spaces make them indispensable for challenging real-world engineering optimization problems [179].

The genetic algorithm (GA) is a population-based metaheuristic inspired by the principles of natural selection and genetics. It operates by evolving a set of candidate solutions, referred to as the population, through successive generations in search of improved solutions to the optimization problem. Each candidate solution is encoded as a string of variables, similar to genes in biological systems. Genetic algorithms have been widely applied in mechanical engineering to address complex, nonlinear, and multimodal optimization problems. Applications include compliant mechanism synthesis and design [180, 181], optimal synthesis and balancing of planar and leg mechanisms [182, 183, 184], and cam profile optimization [185]. Genetic algorithms have also been used for composite material optimization [186], structural topology optimization [187], and reduced kinetics mechanism optimization [188]. Broader reviews and studies highlight their role in general mechanical design [189, 190] and evolutionary mechanism design [191], demonstrating their versatility in efficiently exploring large design spaces and accommodating multiple performance objectives.

Differential evolution, proposed by Storn and Price, is a population-based stochastic method for solving continuous, nonlinear, and multimodal problems. It evolves candidate solutions via mutation, crossover, and selection, with mutation achieved by adding the weighted difference between two randomly chosen vectors to a target vector. This algorithm enables adaptive step sizes and effective global search without gradient information. Owing to its simplicity, few parameters, and robustness, it is widely applied in engineering optimization and control tuning, though performance depends on parameter settings and convergence may slow in later stages [192]. Particle swarm optimization, introduced by Kennedy and Eberhart, is a population-based heuristic inspired by the social behavior of flocks and schools. Each particle adjusts its position based on its own best solution and the swarm's best solution, balancing exploration and exploitation. It is simple to implement, requires few parameters, and converges quickly, but may suffer from premature convergence in complex search spaces [193].

1.5 Motivations

Building on the preceding review of compliant mechanisms, their applications, and structural optimization foundations, this thesis is driven by two primary motivations, which are outlined as:

1. **Lack of accurate and highly efficient methods for large-deformation modeling**

   Despite the extensive applications of compliant mechanisms, their modeling remains fundamentally constrained by the persistent trade-off between accuracy and efficiency. Large deflections induce pronounced geometric nonlinearities and strong coupling between bending and axial deformations. Classical models struggle to capture these effects in a unified and tractable manner. Simplified approaches such as the pseudo-rigid-body model provide computational efficiency and intuitive formulations, but at the expense of accuracy, particularly under conditions of large deflection or complex boundary constraints. More advanced formulations, such as the BCM or EIS, improve accuracy but introduce substantial mathematical complexity and a large number of design parameters, which hinder their efficiency and practical applicability. Finite element analysis, although capable of providing highly accurate results across diverse scenarios, is computationally prohibitive for iterative optimization or large-scale parametric studies. Consequently, there exists a clear research gap: the absence of a modeling framework that simultaneously achieves computational tractability, modeling fidelity, and broad applicability to large-deformation compliant mechanisms. Addressing this gap is essential not only for enabling efficient optimization-driven design but also for advancing the theoretical foundations of nonlinear structural mechanics.

2. **Lack of a systematic optimization frameworks for exploring compliant mechanism configurations**

   The design of compliant mechanisms inherently involves multiple, often conflicting, objectives such as stiffness, displacement capacity, energy transmission, and stability. Conventional optimization strategies struggle to address these competing requirements in a systematic way. In particular, heuristic algorithms used in global exploration are prone to local optima, and attempts to improve robustness come at a substantial computational cost. Consequently, existing methods cannot reliably provide scalable and efficient optimization solutions when higher performance or multifunctionality is required. This highlights the gap for advanced optimization strategies that can balance global search capability with convergence efficiency under complex design constraints. In addition, current design frameworks for compliant mechanisms are largely confined to geometric-level parameter tuning within fixed structural layouts. While effective for refining specific shapes, such

approaches inherently restrict the diversity of potential solutions and may overlook unconventional or functionally superior designs. Many emerging applications, such as multi-stable devices, motion amplification, or spatially adaptive systems, demand exploration beyond pre-defined geometries. The lack of systematic configuration search constitutes a significant research gap, restricting the generative capacity of existing design methodologies and limiting innovation in compliant mechanism design..

1.6 Contributions

To address the aforementioned challenges and research gaps, this thesis develops a series of novel modeling and optimization approaches for compliant mechanisms. First, an energy method based on the high-order smooth curvature model (high-order SCME) is proposed to capture large deformations and nonlinear behaviors with improved accuracy while avoiding the excessive complexity of traditional models. Second, the comprehensive energy method based on the smooth curvature model (CoSCME) is introduced to extend applicability and enhance robustness across different classes of compliant mechanisms. Third, a bi-level optimization strategy is formulated to effectively decoupled global configuration exploration and kinetostatic modeling, thereby improving both design efficiency and performance. The detailed motivations for each of these contributions are presented in the following sections.

1. High-order SCME Method

   Conventional smooth curvature models, such as 2nd-order SCME, often lose accuracy when compliant mechanisms undergo large deflections. In such cases, the inability to properly capture the influence of higher-order curvature leads to significant errors in predicting energy and mechanical behaviors. This reveals a theoretical gap, since many complex compliant structures require precise modeling of nonlinear large-deformation responses, but existing frameworks remain inadequate. To address this, the high-order SCME method was developed, which incorporates high-order Legendre polynomials into smooth curvature representations. This allows for a more accurate description of geometric and mechanical characteristics, ultimately improving the modelinng accuracy of nonlinear large deformation. In addition,

owing to the utilization of explicit expressions of gradient formulations, the modeling speed is hundreds of times faster than that of classical methods.

2. Comprehensive SCME Method

   Although the high-order SCME method demonstrates effectiveness in modeling compliant bistable mechanisms, it still suffers from important limitations: the neglect of axial deformation, which reduces accuracy under large-deformation conditions, and its restricted applicability mainly to bistable systems. These shortcomings highlight the need for a more general and accurate modeling framework. To address this, the CoSCME method is developed, which incorporates both bending and axial deformations and explicitly accounts for their coupling effects. The CoSCME achieves higher accuracy and broader applicability across a wide range of planar compliant mechanisms, including compresural beams, tensural beams, bistable mechanisms, general lumped-compliance beams and initially-curved beams.

3. Bi-level Optimization

   To address the lack of systematic optimization in compliant bistable mechanism design, this thesis introduces a bi-level optimization framework that integrates geometry-level parameter tuning with analytical performance evaluation. The optimization aims at tailoring the kinetostatic behavior of compliant bistable mechanisms, which is challenging due to their inherent nonlinear characteristics. Compliant bistable mechanisms are generally designed through distributed compliance, lumped compliance, or topology optimized configurations, each presenting distinct trade-offs in design flexibility, computational cost, and manufacturability. Distributed designs are simple and easy to fabricate but severely limited in tunability, while topology-optimized designs offer maximal freedom at the expense of excessive computational complexity and fabrication difficulty. Lumped compliance mechanisms, by contrast, provide a balanced design space: their intermediate rigid frame expands the number of controllable parameters, supports enhanced stiffness, facilitates integration with actuators or stoppers, and maintains structural clarity for analysis and fabrication. This balance makes them particularly suitable for optimization-driven design. Within the proposed bi-level framework, the upper-level problem adjusts geometric parameters, and the lower-level problem evaluates equilibrium and performance, thereby

enabling systematic tailoring of bistable behavior without resorting to overly complex topological approaches or sacrificing manufacturability.

1.7 Thesis Organization

This thesis is organized into six chapters, each addressing key aspects of the modeling and optimization of compliant mechanisms. The logical flow of this dissertation is illustrated in the form of a flowchart (Figure. 1.8) and is summarized as follows:

Chapter 1 introduces the fundamentals of compliant mechanisms, highlighting their advantages, applications, and the challenges associated with their nonlinear large-deformation behavior. This chapter also critically reviews existing modeling approaches, such as PRBM, BCM, EIS and FEM, and then identifies their limitations, thereby defining the research gaps and outlining the motivations of this work.

Chapter 2 presents the theoretical background, including the detailed derivation process of strain energy and the fundamentals of the smooth curvature model. These two aspects establish the foundation for the kinetostatic models proposed in this thesis.

Chapter 3 proposes the high-order SCME method, which provides an efficient yet accurate approach for capturing the nonlinear behavior of compliant bistable mechanisms. The theoretical formulation, implementation details, and validations against finite element analysis and experiments are presented, followed by discussions on its accuracy and computational benefits.

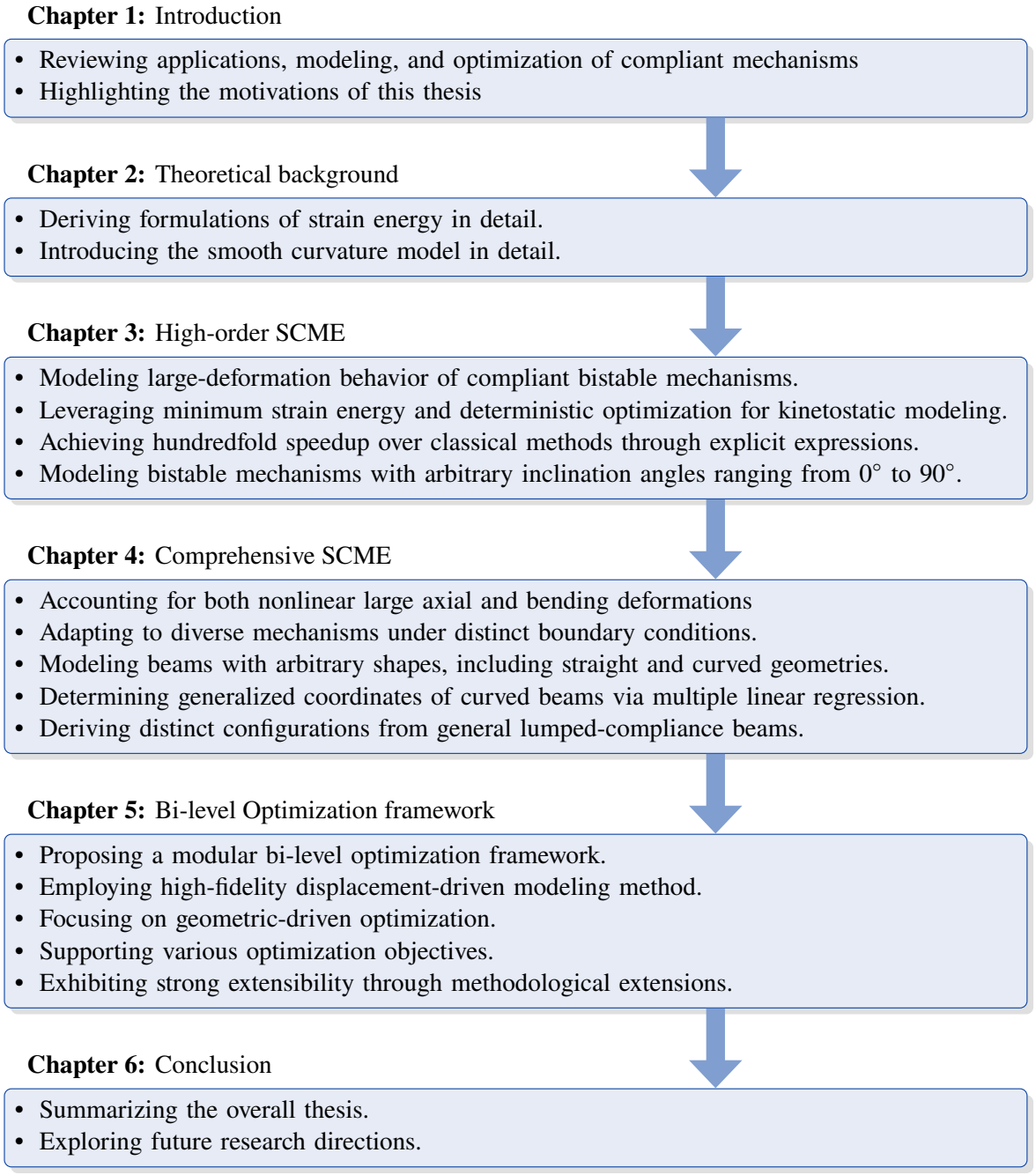


Fig. 1.8.: The flowchart of thesis organization

Chapter 4 introduces the CoSCME method, which incorporates both bending and axial deformations into the modeling process. This enhanced method addresses the limitations of SCME in cases of large axial strains. Its broad applicability to diverse compliant mechanisms is demonstrated through modeling, verification, and comparative studies with FEA.

Chapter 5 presents a bi-level optimization framework for compliant mechanism design. The framework integrates accurate nonlinear modeling with hierarchical optimization strategies

to effectively navigate the trade-offs between performance objectives, computational efficiency, and design feasibility. Two distinct case studies are provided to demonstrate the methodology's robustness and practical utility. The proposed bi-level optimization framework is particularly applied for tailoring the kinetostatic behavior of compliant bistable mechanisms.

Finally, Chapter 6 summarizes the major contributions of the research, reflecting on the advancements in nonlinear modeling and optimization of compliant mechanisms. It highlights the theoretical and practical impacts of the developed SCME, CoSCME, and bi-level optimization framework, and proposes promising directions for future research in compliant systems.

Theoretical Background

2

This chapter provides the theoretical foundations essential for the subsequent developments in this thesis. In particular, it presents the detailed derivations of two fundamental concepts: the strain energy formulation, which serves as the basis for analyzing the deformation and mechanical behavior of compliant mechanisms, and the smooth curvature model, which enables kinetostatic modeling of slender beams.

2.1 Strain energy

In this thesis, all kinetostatic modeling methods are developed on the basis of the minimum strain energy principle. The central idea of these approaches is to determine the equilibrium configuration by identifying the state that minimizes strain energy under prescribed boundary conditions. Consequently, the definition and derivation of strain energy play a fundamental role in these models, serving as the core concept upon which all subsequent analyses are built. To provide a clearer and more intuitive understanding, the following section presents the detailed derivation of the strain energy formulation. These formulations and theories originate from classical mechanics of materials, as documented in [194].

In the present work, the strain energy formulation is restricted to bending and axial components, which are the dominant deformation modes in the considered beam-based compliant mechanisms. The bending strain energy per unit length is governed by the deformed curvature and the initial curvature, leading to an integral form that depends on Young's modulus and the second moment of inertia. From a continuum mechanics perspective, this energy results from strain gradients across the beam thickness due to fiber stretching. In this context, a fiber refers to an infinitesimal material element within the beam that resists deformation mainly through axial loading. In contrast, axial strain energy arises from elongation or compression along the beam neutral line and is expressed in terms of axial strain and cross-sectional area. Other types of strain energy contributions, such as those arising from torsional or warping deformations, local buckling, and lateral-torsional effects, are not taken into account. This simplification allows the modeling framework to remain tractable while still capturing the primary mechanical behavior relevant to bistable mechanism design.

2.1.1 Bending strain energy

In a upward bending beam, the upper fibers are subjected to compression while the lower fibers are in tension. These compressive and tensile strains lead to variations in arc length among fibers located at different distances from the neutral axis. Before deformation, the arc length of any fiber coincides with that of the neutral line (located at $z = 0$). After bending, the beam can be locally approximated as a circular arc, and the arc length of a fiber becomes a function of the radius of curvature. A schematic illustration of compressive and tensile fibers is shown in Fig. 2.1.

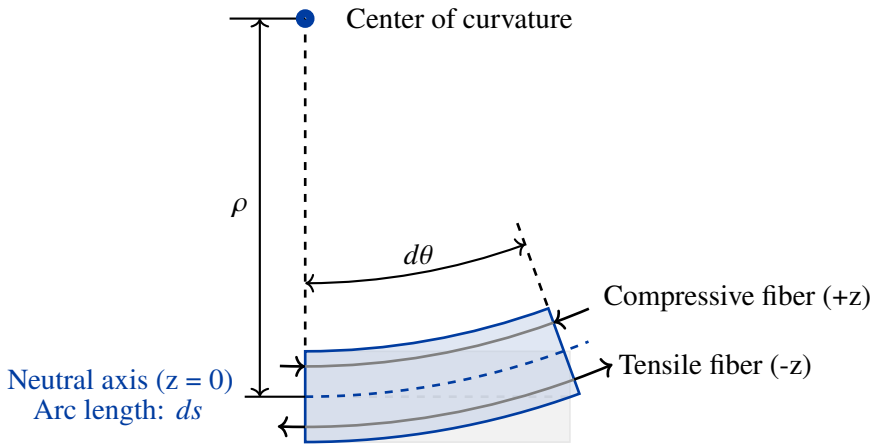


Fig. 2.1.: Illustration of compressive and tensile fibers in beam bending deformation.

In differential geometry, the arc length of a circular segment is expressed as:

$$ds = \rho \, d\theta, \tag{2.1}$$

where ρ is the radius of curvature, and $d\theta$ is the differential change in the tangent angle, measured in radians. It is important to note that $d\theta$ denotes an infinitesimal increment in the rotation angle of the tangent vector along the arc length, and should not be confused with the absolute angle θ at a given point. For the neutral axis ($z = 0$), the arc length element remains $\rho d\theta$. For a fiber located at a distance $+z$ from the neutral axis, the radius of curvature becomes $\rho - z$, resulting in the arc length:

$$ds^{+z} = (\rho - z) \, d\theta. \tag{2.2}$$

In classical mechanics of materials, bending strain is defined as the relative change in length of a fiber with respect to its original (undeformed) length. Under the assumption of pure bending, the neutral axis is strain-free, and its arc length is taken as the reference.

Therefore, the bending strain at a fiber located a distance $+z$ from the neutral axis is given by:

$$\varepsilon_{\mathrm{b}}(s,z) = \frac{(\rho - z)\, d\theta - \rho\, d\theta}{\rho\, d\theta} = -z\frac{1}{\rho} = -z\,\omega(s), \tag{2.3}$$

where $\omega(s) = 1/\rho$ denotes the curvature of neutral line at position s. This leads to the classic result:

$$\varepsilon_{\mathrm{b}}(s,z) = -z\,\omega(s), \tag{2.4}$$

which describes a linear distribution of normal strain across the cross section, with zero strain at the neutral axis and maximum tensile/compressive strains at the outermost fibers. Building upon this strain formulation, the corresponding bending strain energy can be derived by integrating the strain energy density over the cross-section and along the length of the beam. The strain energy density per unit volume is defined as the internal work done per unit volume by the stress through the strain, which can be written as:

$$u_{\mathrm{b}}(s,z) = \int_0^{\varepsilon_{\mathrm{b}}} \sigma_{\mathrm{b}}(\varepsilon_{\mathrm{b}})d\varepsilon_{\mathrm{b}}. \tag{2.5}$$

The current model assumes the material follows Hooke's law, and the material is linear elastic and isotropic. Moreover, material nonlinearity is not taken into account. Thus the stress-strain relationship is:

$$\sigma_{\mathrm{b}}(s,z) = E\varepsilon_{\mathrm{b}}(s,z). \tag{2.6}$$

Substituting Eq. (2.4) and (2.6) into (2.5), the following expression of strain density per unit length of beam can be derived:

$$u_{\mathrm{b}}(s,z) = E\int_0^{\varepsilon_{\mathrm{b}}(s,z)} \varepsilon_{\mathrm{b}} d\varepsilon_{\mathrm{b}} = \frac{1}{2}Ez^2\omega^2(s). \tag{2.7}$$

Integrating the strain energy density over the cross-sectional area A at position s, we can obtain the following formulation:

$$U_{\mathrm{b}}(s) = \int_A u(s,z)dA = \frac{1}{2}E\omega^2(s)\int_A z^2 dA. \tag{2.8}$$

The second moment of area about a given axis (commonly the neutral axis) is a geometric property that describes how the area of a cross-section is distributed with respect to that axis. For a 2D cross-sectional area A, the second moment of area (I) about the horizontal axis is defined as:

$$I = \int_A z^2 dA. \tag{2.9}$$

Thus, substituting Eq. (2.9) into (2.8), we can obtain the following expression of bending strain energy per unit length:

$$U_{\mathrm{b}}(s) = \frac{1}{2} EI\omega^2(s). \tag{2.10}$$

Finally, integrating along the beam length L, the total bending strain energy of the beam is:

$$U_{\mathrm{b}} = \int_0^L U_{\mathrm{b}}(s)ds = \frac{EI}{2}\int_0^L \omega^2(s)ds. \tag{2.11}$$

When modeling an initially curved beam, the initial curvature must be incorporated into the strain energy formulation. The complete expression is:

$$U_{\mathrm{b}} = \frac{EI}{2}\int_0^L (\omega(s) - \omega_0(s))^2\, ds, \tag{2.12}$$

where, $\omega_0(s)$ denotes the curvature function of the beam neutral axis in its undeformed (initially-curved) configuration. The derived expression for bending strain energy characterizes the elastic potential stored in the beam. However, in many practical applications, particularly in cases involving large deformations of compliant beams, axial deformation also contributes significantly to the total strain energy. In the following content, the formulation of axial strain energy arising from longitudinal stretching or compression along the neutral axis is further introduced.

2.1.2 Axial strain energy

Axial elongation and compression along the neutral axis also contribute to the total strain energy of the structure. While the bending strain varies linearly with the distance from the neutral axis, the axial strain is uniform across the cross-section and arises from changes in the axial displacement along the beam. A schematic illustration of arc length change in slender beams is shown in Fig. 2.2.

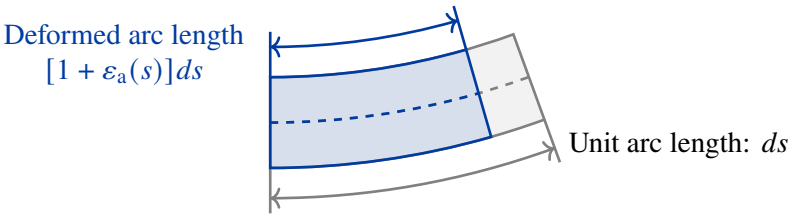


Fig. 2.2.: Illustration of stretching and compression of the neutral axis during axial deformation of a beam.

Under the assumption of linear elasticity, the axial strain at arc-length position s is denoted as $\varepsilon_{\mathrm{a}}(s)$. According to Hooke's law, the corresponding axial stress is:

$$\sigma_{\mathrm{a}}(s) = E\,\varepsilon_{\mathrm{a}}(s). \tag{2.13}$$

The strain energy density per unit volume associated with axial deformation is:

$$u_{\mathrm{a}}(s) = \frac{1}{2}\sigma_{\mathrm{a}}(s)\,\varepsilon_{\mathrm{a}}(s) = \frac{1}{2}E\,\varepsilon_{\mathrm{a}}^2(s). \tag{2.14}$$

To obtain the axial strain energy per unit length, the energy density is integrated over the cross-sectional area A:

$$U_{\mathrm{a}}(s) = \int_A u_{\mathrm{a}}(s)\,\mathrm{d}A = \frac{1}{2}EA\,\varepsilon_{\mathrm{a}}^2(s). \tag{2.15}$$

Then, the total axial strain energy over the entire beam of length L is given by:

$$U_{\mathrm{a}} = \int_0^L U_{\mathrm{a}}(s)\,\mathrm{d}s = \frac{1}{2}EA\int_0^L \varepsilon_{\mathrm{a}}^2(s)\,\mathrm{d}s. \tag{2.16}$$

This expression represents the total energy stored in the beam due to axial deformation. It is widely used in variational formulations and energy-based modeling of flexible structures [195].

2.2 Smooth curvature model

The smooth curvature model was developed as a low-dimensional and accurate representation of large deformation bending of compliant beams to enable computationally efficient modeling of planar robots with flexure-based joints [83]. It is based on the assumption that the curvature of a compliant beam is smooth and can be approximated using low-order polynomial basis functions. By expressing the deformation of the beam as a homogeneous transformation between rigid links, SCM serves as a direct substitute for traditional joint models, allowing accurate and analytical computation of kinematics, Jacobians, and Hessians. With only a few parameters, SCM can faithfully reproduce the deformation, compliance, and buckling behavior of compliant beams under various loading conditions. Originally proposed for robotic applications, this model provides the theoretical foundation for the high-order SCME and CoSCME methods developed in this thesis.

2.2.1 Curvature function derivation

Curvature plays a central role in the modeling of compliant beams, as it directly characterizes beam deformation and can be used to derive the associated bending strain energy. Therefore, parameterizing the curvature function is a meaningful approach for both kinematic and energetic analysis. In the SCM, the curvature profile along the beam neutral axis is approximated using a low-order polynomial basis, which provides a compact and differentiable representation of deformation. Specifically, the curvature function is expressed as a linear combination of orthogonal polynomials. Legendre polynomials are a natural choice due to their smoothness, orthogonality, and closed-form expressions [196]. The standard Legendre polynomials $P_n(x)$ are defined over the interval $[-1, 1]$ and satisfy the orthogonality condition:

$$\int_{-1}^{1} P_m(x)P_n(x)\,dx = 0 \quad \text{for } m \neq n, \tag{2.17}$$

where, the terms $P_m(x)$ and $P_n(x)$ denote the m-th and n-th order Legendre polynomials, respectively. Each $P_n(x)$ is a polynomial of degree n, defined over the interval $[-1, 1]$. The orthogonality condition implies that the inner product (or weighted integral) of any two Legendre polynomials of different orders is zero. This property ensures that the Legendre polynomials form an orthogonal basis for function approximation on the interval $[-1, 1]$. Each Legendre polynomial $P_n(x)$ can be generated recursively using the relation:

$$P_0(x) = 1, \quad P_1(x) = x, \quad P_{n+1}(x) = \frac{2n+1}{n+1}xP_n(x) - \frac{n}{n+1}P_{n-1}(x). \tag{2.18}$$

Alternatively, the first few polynomials can be written explicitly as:

$$\begin{aligned} P_0(x) &= 1, \\ P_1(x) &= x, \\ P_2(x) &= \frac{1}{2}(3x^2 - 1), \\ P_3(x) &= \frac{1}{2}(5x^3 - 3x). \end{aligned} \tag{2.19}$$

Based on the explicit expressions derived above, the first six Legendre polynomials are visualized in Figure 2.3 over the interval $x \in [-1, 1]$. The figure highlights the increasing oscillatory behavior with polynomial order, which underlies their capability to represent higher order deformation modes.

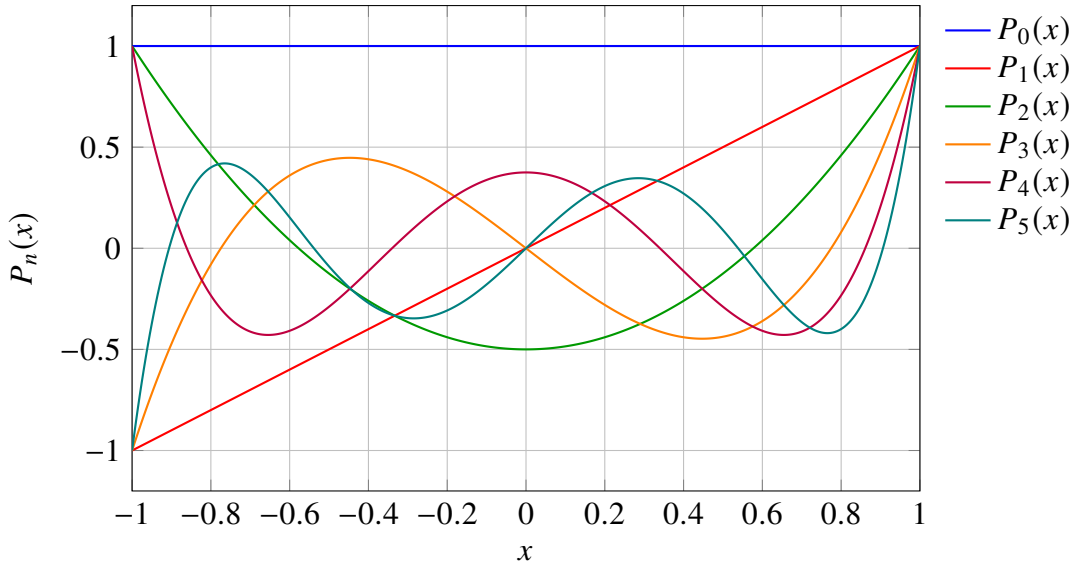


Fig. 2.3.: The first six Legendre polynomials $P_0(x)$–$P_5(x)$ defined on the interval $x \in [-1, 1]$. Different colors are used to distinguish polynomial orders.

To apply these functions to a beam of length L, the domain is shifted from $[-1, 1]$ to $[0, L]$ via a linear transformation:

$$x = \frac{2s}{L} - 1, \tag{2.20}$$

The shifted Legendre polynomials are then defined as:

$$\psi_n(s) = P_n\left(\frac{2s}{L} - 1\right), \tag{2.21}$$

Using this definition, the first few shifted Legendre polynomials become:

$$\begin{aligned}
\psi_1(s) &= P_0\left(\frac{2s}{L} - 1\right) = 1, \\
\psi_2(s) &= P_1\left(\frac{2s}{L} - 1\right) = \frac{2s}{L} - 1, \\
\psi_3(s) &= P_2\left(\frac{2s}{L} - 1\right) = \frac{1}{2}\left[3\left(\frac{2s}{L} - 1\right)^2 - 1\right] = \frac{6s^2}{L^2} - \frac{6s}{L} + 1,
\end{aligned} \tag{2.22}$$

These shifted polynomials form an orthogonal basis over $[0, L]$ and are used in the SCM to express the curvature function as:

$$\omega(s) = \frac{\alpha_1}{L} \cdot \psi_1(s) + \frac{\alpha_2}{L} \cdot \psi_2(s) + \frac{\alpha_3}{L} \cdot \psi_3(s). \tag{2.23}$$

The expanded expression for the curvature is:

$$\omega(s) = \frac{\alpha_0}{L} + \frac{\alpha_1}{L}\left(\frac{2s}{L} - 1\right) + \frac{\alpha_2}{L}\left(\frac{6s^2}{L^2} - \frac{6s}{L} + 1\right), \tag{2.24}$$

where, the coefficients α_1, α_2, and α_3 in the curvature function act as modal parameters that govern the contribution of each corresponding basis function to the overall curvature distribution along the beam. Specifically, they represent the weights associated with the shifted Legendre polynomial basis and collectively define the spatial variation of curvature. From a geometric perspective, these coefficients characterize the deformation mode of the beam. In the context of the smooth curvature model, the vector $\boldsymbol{\alpha} = [\alpha_1, \alpha_2, \alpha_3]^T$ is referred to as a set of generalized coordinates, as it uniquely determines the beam configuration within the reduced-order model. These parameters provide a foundation for analytical formulations of strain energy, beam kinematics, and other physical quantities.

2.2.2 Strain energy derivation

After establishing the curvature distribution in terms of the generalized coordinates $\boldsymbol{\alpha}$, the bending strain energy of the compliant beam is derived within the SCM framework. As shown in Eq. (2.12), by substituting the curvature function given in Eq. (2.24) into the strain energy formulation, the expression can be analytically evaluated as a quadratic form with respect to the generalized coordinates. The strain energy formualtion can be further expressed as:

$$U = \frac{EI}{2}\int_0^L \left(\sum_{i=1}^{3} \frac{\alpha_{i-1}}{L}\psi_i(s)\right)^2 ds. \tag{2.25}$$

Expanding the square results in both square and cross terms:

$$U = \frac{EI}{2}\sum_{i=1}^{3}\sum_{j=1}^{3} \frac{\alpha_{i-1}\alpha_{j-1}}{L^2}\int_0^L \psi_i(s)\psi_j(s)ds. \tag{2.26}$$

Due to the orthogonality of the shifted Legendre polynomials, the following equation can be obtained:

$$\int_0^L \psi_i(s)\psi_j(s)ds = \begin{cases} 0, & i \neq j \\ \int_0^L \psi_i(s)^2\, ds, & i = j \end{cases}. \tag{2.27}$$

The integrals of the cross terms evaluate to zero. As a result, all cross terms vanish, and the strain energy expression simplifies to a sum of squares of the individual coefficients α_i,

each scaled by the squared norm of the corresponding basis function. The expression is further simplified to:

$$U = \frac{EI}{2} \sum_{i=1}^{3} \frac{\alpha_{i-1}^2}{L^2} \int_0^L \psi_i^2(s) ds. \tag{2.28}$$

For the first three shifted Legendre polynomials, the integrals are:

$$\begin{aligned} \int_0^L \psi_1^2(s)\, ds &= L, \\ \int_0^L \psi_2^2(s)\, ds &= \frac{L}{3}, \\ \int_0^L \psi_3^2(s)\, ds &= \frac{L}{5}. \end{aligned} \tag{2.29}$$

Therefore, the final expression for the strain energy becomes:

$$U = \frac{EI}{2L} \left(\alpha_0^2 + \frac{\alpha_1^2}{3} + \frac{\alpha_2^2}{5} \right). \tag{2.30}$$

For the initially curved beam, the expression of strain energy is:

$$U = \frac{EI}{2L} \left(\left(\alpha_0 - \alpha_0^*\right)^2 + \frac{\left(\alpha_1 - \alpha_1^*\right)^2}{3} + \frac{\left(\alpha_2 - \alpha_2^*\right)^2}{5} \right), \tag{2.31}$$

where α_n^* denotes the generalized coordinates defining the initial beam curvature, which is assumed to remain constant.

2.2.3 Kinematic Derivation

Having defined the curvature function $\omega(s)$ as a polynomial parameterized by the generalized coordinates $\boldsymbol{\alpha}$, the smooth curvature model further allows for the derivation of key kinematic quantities such as the tangent deflection angle $\phi(s)$, the tip angle ϕ_{tip}, and the Cartesian tip position $(x_{\text{tip}}, y_{\text{tip}})$. The deflection angle $\phi(s)$ is obtained by integrating the curvature function over the arc length:

$$\phi(s) = \int_0^s \omega(s)\, ds. \tag{2.32}$$

Given the polynomial form of $\omega(s)$, this integration yields a closed-form cubic expression for $\phi(s)$. The formulation of the deflection angle is:

$$\phi(s) = \alpha_0 \frac{s}{L} + \alpha_1 \left(\frac{s^2}{L^2} - \frac{s}{L} \right) + \alpha_2 \left(2\frac{s^3}{L^3} - 3\frac{s^2}{L^2} + \frac{s}{L} \right), \tag{2.33}$$

and the tip angle simplifies to:

$$\phi_{\text{tip}} = \phi(L) = \alpha_0. \tag{2.34}$$

The Cartesian coordinates of the beam tip $(x_{\text{tip}}, y_{\text{tip}})$ are computed by integrating the tangent vector over the beam length:

$$x_{\text{tip}} = \int_0^L \cos\left(\phi(s)\right) ds, \tag{2.35}$$

$$y_{\text{tip}} = \int_0^L \sin\left(\phi(s)\right) ds. \tag{2.36}$$

Since $\phi(s)$ is a nonlinear function of $\boldsymbol{\alpha}$, the resulting integrals are transcendental and generally not solvable in closed form. However, thanks to the smoothness of the curvature profile, numerical integration methods such as Gauss-Legendre quadrature can be employed to accurately and efficiently compute the tip position. Gauss-Legendre quadrature is a numerical integration method widely employed to approximate definite integrals [197]. It relies on the principle of estimating the integral through a weighted sum of function values at specific points within the integration interval. Renowned for its accuracy and efficiency in numerical integration, Gauss-Legendre quadrature finds particular utility in integrating smooth functions over finite intervals. Its applications span diverse disciplines, encompassing physics, engineering, and numerical analysis, where precise numerical integration holds paramount importance. The expression for Gauss-Legendre quadrature is as follows:

$$\int_{-1}^{1} f(x)dx \approx \sum_{i=1}^{i=n} W_i f(x_i), \tag{2.37}$$

where, $f(x)$ is the function being integrated. dx denotes the differential element. $\sum_{i=1}^{i=n}$ represents the sum over the quadrature points. x_i represents the quadrature points within the interval [-1, 1], W_i represents the corresponding weights assigned to each quadrature point. The Legendre polynomials, originally defined on the interval [-1, 1], serve as the foundation for Gauss-Legendre quadrature. However, to apply this quadrature method to a general interval [a, b], a transformation process is required. This transformation involves mapping the original interval [-1, 1] to the desired interval [a, b]. The expression for Gauss-Legendre quadrature on the interval [a, b] can be formulated as:

$$\int_a^b f(x)dx \approx \frac{b-a}{2} \sum_{i=1}^{i=n} W_i f\left(\frac{b-a}{2} x_i + \frac{a+b}{2}\right). \tag{2.38}$$

In the context of the smooth curvature model, the variable is denoted as s/L, where s represents the distance along the curve and L is a length of compliant beam. In this model,

s/L is constrained within the interval [0, 1]. Therefore, for the specific case of integrating over the interval [0, 1], the Gauss-Legendre quadrature can be expressed as follows, where $a = 0$ and $b = L$:

$$\int_0^L f(x)dx \approx \frac{L}{2}\sum_{i=1}^{i=n} W_i f\left(\frac{L}{2}x_i + \frac{L}{2}\right). \tag{2.39}$$

To determine the appropriate number of sampling points for the Gauss–Legendre quadrature, tests with different numbers of integration points were conducted. After observing insufficient accuracy with 5 points, the quadrature order was progressively increased to 7, 8, and up to 10 points, as well as to higher orders such as 15 and 20 points. It was found that the results converged at 10 points, while further increasing the number of points did not noticeably improve accuracy but led to significantly more complicated explicit expressions. Therefore, 10 integration points were selected as a compromise between accuracy and analytical tractability. In the smooth curvature model, when using the Gauss-Legendre quadrature with 10 points to calculate integration over the interval [0, 1], the corresponding weights and quadrature points are listed as follows:

Tab. 2.1.: The weights and quadrature points

n	quadrature point (x_i)	weight (W_i)
1	-0.9739065285171717	0.0666713443086881
2	-0.8650633666889845	0.1494513491505806
3	-0.6794095682990244	0.2190863625159820
4	-0.4333953941292472	0.2692667193099963
5	-0.1488743389816312	0.2955242247147529
6	0.1488743389816312	0.2955242247147529
7	0.4333953941292472	0.2692667193099963
8	0.6794095682990244	0.2190863625159820
9	0.8650633666889845	0.1494513491505806
10	0.9739065285171717	0.0666713443086881

Hence, when we aim to integrate the equations Eq. (2.35) and Eq. (2.36) and subsequently obtain the tip position and orientation, we can employ the Gauss-Legendre quadrature method by substituting the function $f(x)$ with the target trigonometric functions in Eq. (2.35) and Eq. (2.36). By utilizing the appropriate weights and quadrature points, we

can approximate the integral and derive the desired tip position and orientation using Eq. (2.40) (2.41) and (2.42):

$$\phi_{\text{tip}}(\boldsymbol{\alpha}) = \phi(\boldsymbol{\alpha}, L) = \phi_0 + \alpha_0, \tag{2.40}$$

$$\begin{aligned} x_{\text{tip}}(\boldsymbol{\alpha}) \approx L \sum_{i=1}^{10} W_i \cos \Bigg[& \alpha_0 \left(\frac{1}{2}(x_i + 1) \right) + \alpha_1 \left(\frac{1}{4}(x_i + 1)^2 - \frac{1}{2}(x_i + 1) \right) \\ & + \alpha_2 \left(\frac{1}{4}(x_i + 1)^3 - \frac{3}{4}(x_i + 1)^2 + \frac{1}{2}(x_i + 1) \right) \Bigg], \end{aligned} \tag{2.41}$$

$$\begin{aligned} y_{\text{tip}}(\boldsymbol{\alpha}) \approx L \sum_{i=1}^{10} W_i \sin \Bigg[& \alpha_0 \left(\frac{1}{2}(x_i + 1) \right) + \alpha_1 \left(\frac{1}{4}(x_i + 1)^2 - \frac{1}{2}(x_i + 1) \right) \\ & + \alpha_2 \left(\frac{1}{4}(x_i + 1)^3 - \frac{3}{4}(x_i + 1)^2 + \frac{1}{2}(x_i + 1) \right) \Bigg]. \end{aligned} \tag{2.42}$$

The above content summarized the concept of strain energy and the smooth curvature model, outlining their theoretical background and derivation process. However, when applied to complex large-deformation behaviors, the SCM is limited in accuracy. In an earlier stage of this work, the SCM was employed to describe the large deformation of compliant beams. However, based on the modeling results, it was observed that the polynomial fitting adopted in second order formulations cannot adequately capture curves with multiple inflection points, thereby significantly limiting modeling accuracy. This drawback challenges both the applicability and reliability of SCM in advanced design tasks. To overcome this challenge, a high-order SCME approach based on high-order Legendre polynomials has been proposed. This method successfully addresses the deficiencies of the original SCM, enabling accurate modeling of complex large-deformation problems, and has been further applied to the analysis of compliant bistable mechanisms. The following chapter discusses this method in detail and validates its effectiveness.

3 High-order SCME: Modeling Large-deformation Behavior of Compliant Bistable Mechanisms

In this chapter, the energy method based on the smooth curvature model (SCME) and its high order formulations is presented, where the energy method refers to Castigliano's principle of minimum strain energy. This well-established principle indicates that for a structure subjected to external loads and constraints, the equilibrium configuration is achieved when the total strain energy in the structure is minimized [198]. The main content of this chapter has been published in [124]. As a fundamental concept in static analysis, the minimum strain energy is normally used to analyze and design various structures such as beams, trusses, frames, and shells. By minimizing the strain energy, the distribution of stress and deformation shape within these structures under different loading conditions can be determined. Pongsiri et al. integrated the SCM with Lagrange multiplier and Newton-Raphson methods and applied Castigliano's principle of minimum strain-energy, resulting in a analysis approach to address the grasp stability problem [120]. This energy method is based on the 2nd-order SCM and now referred to as the 2nd-order SCME method.

Among compliant mechanisms, compliant bistable mechanisms stand out due to their ability to maintain two distinct stable equilibrium configurations without continuous external energy input. This energy-efficient behavior is especially advantageous in power-constrained environments such as outer space and deep-sea applications [8, 199]. Bistable mechanisms have been widely applied in areas such as energy-absorbing mechanical metamaterials [200, 201], programmable structures [202], and multistable systems [203, 204, 205, 206]. They are also key structural components for deployable structures [207] and mechanical logic devices capable of binary operations [208].

However, the aforementioned 2nd-order SCME method has significant limitations in modeling the large-deformation buckling behavior of compliant beams due to the low fitting accuracy arising from a low-order polynomial basis. This limitation can lead to inaccurate predictions of equilibrium configurations and mechanical responses, particularly

in cases involving strong geometric nonlinearity. This inaccuracy is not characterized by a moderate quantitative error, but rather by a qualitative failure of the model. Specifically, for strongly nonlinear systems such as bistable mechanisms, the second order SCME method fails to capture the existence of multiple stable equilibrium states. Therefore, improving the fitting accuracy is crucial for enhancing the reliability and applicability of the model in practical design scenarios. To address this issue, the SCME method has been enhanced in this study by elevating it from 2nd-order to 5th-order, enabling it to model more intricate buckling behaviors and provide an accurate kinetostatic model for compliant mechanisms. This method is referred to as the high-order SCME method. The high-order SCME method inherits all the advantages of the conventional 2nd-order SCME approach. These advantages encompass the accurate prediction of various aspects, such as bending strain energy, deformation shape, reaction forces, and stress.

A detailed description of the full implementation process is provided, which includes: section 3.1 introducing the high-order smooth curvature model; section 3.2 constructing a Lagrangian function for strain energy minimization; section 3.3 modeling a compliant bistable mechanism as a case study, given its typical geometric nonlinearity, along with a problem description; section 3.4 introducing the Newton-Raphson method as the root-finding algorithm; section 3.5 implementing the high-order SCME in modeling compliant bistable mechanism; section 3.6 validating the model via FEA and experiments; section 3.7 comparing the method with alternatives and across different polynomial orders; and section 3.8 discussing the limitations and underlying assumptions of the current model.

3.1 High-order smooth curvature model

Building upon the foundational 2nd-order SCM introduced in the theoretical background, this work employs a high-order extension, referred to as the high-order SCME method, to improve the accuracy of deformation modeling in compliant mechanisms. While the original SCM captures beam deformation by representing curvature with 2nd-order polynomial approximations, it suffers from limited fitting capability when modeling large deformations or highly nonlinear responses. To address this, the high-order SCME method incorporates higher-degree polynomial basis functions into both the curvature and axial strain representations. This extension allows for greater flexibility in approximating complex deformation profiles while maintaining analytical tractability. This improved fidelity is particularly important for optimization and design tasks where precise control over the equilibrium path and force-displacement characteristics is critical. The curvature

approximation function for the neutral axis in the high-order SCME (5th-order) is given in Eq. (3.1):

$$\omega(\boldsymbol{\alpha}, s) \approx \frac{1}{L}\sum_{n=0}^{n=5}\alpha_n\psi_n(s). \tag{3.1}$$

As described in subsection 2.2.1, the derivation process of the shifted Legendre polynomials is presented in detail. Following this procedure, the expressions of the shifted Legendre polynomials up to the fifth order, along with their integrals, are listed in Table 3.1 and Table 3.2, respectively. In the formulation of the SCME method, the point s is defined on the compliant beam, and thus $s/L = [0, 1]$. The expressions of the shifted Legendre polynomials and their integrals are listed in Tables 3.1 and 3.2.

Tab. 3.1.: The shifted Legendre polynomials

N	Shifted Legendre polynomials
0	1
1	$2\left(\frac{s}{L}\right) - 1$
2	$6\left(\frac{s}{L}\right)^2 - 6\left(\frac{s}{L}\right) + 1$
3	$20\left(\frac{s}{L}\right)^3 - 30\left(\frac{s}{L}\right)^2 + 12\left(\frac{s}{L}\right) - 1$
4	$70\left(\frac{s}{L}\right)^4 - 140\left(\frac{s}{L}\right)^3 + 90\left(\frac{s}{L}\right)^2 - 20\left(\frac{s}{L}\right) + 1$
5	$252\left(\frac{s}{L}\right)^5 - 630\left(\frac{s}{L}\right)^4 + 560\left(\frac{s}{L}\right)^3 - 210\left(\frac{s}{L}\right)^2 + 30\left(\frac{s}{L}\right) - 1$

Tab. 3.2.: The integration of shifted Legendre polynomials

N	Integration of shifted Legendre polynomials
0	$\frac{s}{L}$
1	$\left(\frac{s}{L}\right)^2 - \frac{s}{L}$
2	$2\left(\frac{s}{L}\right)^3 - 3\left(\frac{s}{L}\right)^2 + 1$
3	$5\left(\frac{s}{L}\right)^4 - 10\left(\frac{s}{L}\right)^3 + 6\left(\frac{s}{L}\right)^2 - \frac{s}{L}$
4	$14\left(\frac{s}{L}\right)^5 - 35\left(\frac{s}{L}\right)^4 + 30\left(\frac{s}{L}\right)^3 - 10\left(\frac{s}{L}\right)^2 + \left(\frac{s}{L}\right)$
5	$42\left(\frac{s}{L}\right)^6 - 126\left(\frac{s}{L}\right)^5 + 140\left(\frac{s}{L}\right)^4 - 70\left(\frac{s}{L}\right)^3 + 15\left(\frac{s}{L}\right)^2 - \left(\frac{s}{L}\right)$

Building on this, the full expression of curvature is:

$$\begin{aligned}\omega(\boldsymbol{\alpha}, s) &= \frac{\alpha_0}{L} + \frac{\alpha_1}{L}\left(\frac{2s}{L} - 1\right) + \frac{\alpha_2}{L}\left(\frac{6s^2}{L^2} - \frac{6s}{L} + 1\right) \\ &+ \frac{\alpha_3}{L}\left(\frac{20s^3}{L^3} - \frac{30s^2}{L^2} + \frac{12s}{L} - 1\right) + \frac{\alpha_4}{L}\left(\frac{70s^4}{L^4} - \frac{140s^3}{L^3} + \frac{90s^2}{L^2} - \frac{20s}{L} + 1\right) \\ &+ \frac{\alpha_5}{L}\left(\frac{252s^5}{L^5} - \frac{630s^4}{L^4} + \frac{560s^3}{L^3} - \frac{210s^2}{L^2} + \frac{30s}{L} - 1\right). \end{aligned} \tag{3.2}$$

As explained in the previous chapter, the deflection angle can be derived by integrating the curvature along the beam neutral axis. Thus, based on Eq. (2.32), the full expression of the deflection angle in the high-order SCME method is:

$$\begin{aligned}\phi(\boldsymbol{\alpha}, s) &= \alpha_0 \frac{s}{L} + \alpha_1\left(\frac{s^2}{L^2} - \frac{s}{L}\right) + \alpha_2\left(\frac{2s^3}{L^3} - \frac{3s^2}{L^2} + \frac{s}{L}\right) \\ &+ \alpha_3\left(\frac{5s^4}{L^4} - \frac{10s^3}{L^3} + \frac{6s^2}{L^2} - \frac{s}{L}\right) + \alpha_4\left(\frac{14s^5}{L^5} - \frac{35s^4}{L^4} + \frac{30s^3}{L^3} - \frac{10s^2}{L^2} + \frac{s}{L}\right) \\ &+ \alpha_5\left(\frac{42s^6}{L^6} - \frac{126s^5}{L^5} + \frac{140s^4}{L^4} - \frac{70s^3}{L^3} + \frac{15s^2}{L^2} - \frac{s}{L}\right). \end{aligned} \tag{3.3}$$

After applying Gauss quadrature, the expression for the tip position is approximated as:

$$\phi_{\text{tip}}(\boldsymbol{\alpha}) = \phi(\boldsymbol{\alpha}, L) = \alpha_0, \tag{3.4}$$

$$
\begin{aligned}
x_{\text{tip}}(\boldsymbol{\alpha}) \approx L \sum_{i=1}^{10} W_i \cos \Bigg[& \alpha_0 \left(\frac{1}{2}(x_i+1) \right) + \alpha_1 \left(\frac{1}{4}(x_i+1)^2 - \frac{1}{2}(x_i+1) \right) \\
& + \alpha_2 \left(\frac{1}{4}(x_i+1)^3 - \frac{3}{4}(x_i+1)^2 + \frac{1}{2}(x_i+1) \right) \\
& + \alpha_3 \left(\frac{5}{16}(x_i+1)^4 - \frac{5}{4}(x_i+1)^3 + \frac{3}{2}(x_i+1)^2 - \frac{1}{2}(x_i+1) \right) \\
& + \alpha_4 \left(\frac{14}{32}(x_i+1)^5 - \frac{35}{16}(x_i+1)^4 + \frac{15}{4}(x_i+1)^3 - \frac{5}{2}(x_i+1)^2 + \frac{1}{2}(x_i+1) \right) \\
& + \alpha_5 \left(\frac{21}{32}(x_i+1)^5 - \frac{63}{16}(x_i+1)^5 + \frac{35}{4}(x_i+1)^4 - \frac{35}{4}(x_i+1)^3 + \frac{15}{4}(x_i+1)^2 - \frac{1}{2}(x_i+1) \right) \Bigg],
\end{aligned}
\tag{3.5}
$$

$$
\begin{aligned}
y_{\text{tip}}(\boldsymbol{\alpha}) \approx L \sum_{i=1}^{10} W_i \sin \Bigg[& \alpha_0 \left(\frac{1}{2}(x_i+1) \right) + \alpha_1 \left(\frac{1}{4}(x_i+1)^2 - \frac{1}{2}(x_i+1) \right) \\
& + \alpha_2 \left(\frac{1}{4}(x_i+1)^3 - \frac{3}{4}(x_i+1)^2 + \frac{1}{2}(x_i+1) \right) \\
& + \alpha_3 \left(\frac{5}{16}(x_i+1)^4 - \frac{5}{4}(x_i+1)^3 + \frac{3}{2}(x_i+1)^2 - \frac{1}{2}(x_i+1) \right) \\
& + \alpha_4 \left(\frac{14}{32}(x_i+1)^5 - \frac{35}{16}(x_i+1)^4 + \frac{15}{4}(x_i+1)^3 - \frac{5}{2}(x_i+1)^2 + \frac{1}{2}(x_i+1) \right) \\
& + \alpha_5 \left(\frac{21}{32}(x_i+1)^5 - \frac{63}{16}(x_i+1)^5 + \frac{35}{4}(x_i+1)^4 - \frac{35}{4}(x_i+1)^3 + \frac{15}{4}(x_i+1)^2 - \frac{1}{2}(x_i+1) \right) \Bigg],
\end{aligned}
\tag{3.6}
$$

where x_i denotes the Gauss quadrature points listed in Table 2.1 and corresponds to s/L, defined on the interval $[0, 1]$. Given that both the weights and quadrature points maintain a constant magnitude, it is noteworthy that the tip position and orientation depend exclusively on the generalized coordinates $\boldsymbol{\alpha}$. Furthermore, as derived in subsection 2.2.2, the expression for the strain energy arising from the high-order SCME is given by:

$$
U_{\text{b}}(\boldsymbol{\alpha}) = \frac{EI}{2L} \left(\alpha_0^2 + \frac{\alpha_1^2}{3} + \frac{\alpha_2^2}{5} + \frac{\alpha_3^2}{7} + \frac{\alpha_4^2}{9} + \frac{\alpha_5^2}{11} \right). \tag{3.7}
$$

To summarize, this section establishes all the necessary expressions derived from the high-order SCME method, including the polynomial-based curvature and deflection angle formulations, as well as the Gauss quadrature-based approximation of the tip position and orientation. The strain energy expression has also been obtained in a closed form as a function of the generalized coordinates $\boldsymbol{\alpha}$. These formulations collectively provide a complete mathematical description of the compliant beam's kinematics and energy

characteristics. In the following section, these expressions will be utilized to construct the Lagrangian function, which forms the basis for determining the equilibrium configuration through energy minimization.

3.2 Constructing Lagrangian function

The Lagrange multipliers approach is a classical optimization technique used to determine the local extrema, both maxima and minima, of a function subject to equality constraints [209]. In the context of constrained optimization, this method introduces auxiliary variables, known as Lagrange multipliers, to incorporate the constraint conditions directly into the objective function. The resulting Lagrangian function combines the original objective with the constraint functions, allowing the problem to be treated as an unconstrained one in an augmented variable space.

To find an optimal solution, the Lagrangian must satisfy the necessary conditions for static equilibrium, which include the vanishing of gradients with respect to both the original variables and the Lagrange multipliers. Importantly, the solution must also strictly satisfy all the given equality constraints. In this work, the Lagrangian function is constructed by combining the strain energy expression derived from the high-order SCME method with the geometric constraints imposed at the beam tip. The Lagrange function is expressed in Eq. (3.8):

$$\mathcal{L}(\mathbf{q}, \boldsymbol{\lambda}) = f(\mathbf{q}) + \boldsymbol{\lambda} \cdot \boldsymbol{g}(\mathbf{q}), \tag{3.8}$$

where, $f(\mathbf{q})$ is the objective function, $g(\mathbf{q})$ is the constraint function, $\mathbf{q}$ denotes generalized coordinates. The variables need to be solved are $\mathbf{q}$ and $\boldsymbol{\lambda}$. This function can be explained from an alternative expression: find the maximum or minimum of objective function $f(\mathbf{q})$ when $g(\mathbf{q}) = 0$. In the bending strain energy minimization process, the Lagrangian function is constructed as in Eq. (3.9):

$$\mathcal{L}(\boldsymbol{\alpha}, \boldsymbol{\lambda}) = U_{\mathrm{b}}(\boldsymbol{\alpha}) + \begin{bmatrix} \lambda_1 & \lambda_2 & \lambda_3 \end{bmatrix} \begin{bmatrix} x_{\mathrm{g}} - x_{\mathrm{tip}}(\boldsymbol{\alpha}) \\ y_{\mathrm{g}} - y_{\mathrm{tip}}(\boldsymbol{\alpha}) \\ \phi_{\mathrm{g}} - \phi_{\mathrm{tip}}(\boldsymbol{\alpha}) \end{bmatrix}. \tag{3.9}$$

The constraint equation specifies that the tip position and orientation of the compliant beam should be aligned with the given tip position and orientation $[x_{\mathrm{g}}, y_{\mathrm{g}}, \phi_{\mathrm{g}}]^{\mathrm{T}}$. The formed Lagrangian can be understood as follows: finding the minimum strain energy of the compliant beam when the tip position and orientation is predetermined. When the

objective function reaches its stationary point, indicating a local extreme value, the partial derivatives of each individual parameter are zero. Consequently, the stationary condition can be derived as in Eq. (3.10):

$$\frac{\partial \mathcal{L}}{\partial \boldsymbol{\alpha}} = \frac{\partial \mathcal{L}}{\partial \boldsymbol{\lambda}} = 0. \tag{3.10}$$

By applying the stationary conditions to the Lagrangian function with respect to both the generalized coordinates and the Lagrange multipliers, a system of nonlinear equations is obtained. This system simultaneously satisfies the energy minimization criterion and the imposed geometric constraints. The constructed nonlinear equation system is given as follows:

$$\begin{cases} \dfrac{\partial \mathcal{L}}{\partial \alpha_0} = \dfrac{EI}{L}\alpha_0 - \lambda_1 \dfrac{\partial x_{\text{tip}}}{\partial \alpha_0} - \lambda_2 \dfrac{\partial y_{\text{tip}}}{\partial \alpha_0} - \lambda_3 \dfrac{\partial \phi_{\text{tip}}}{\partial \alpha_0} = 0, \\ \dfrac{\partial \mathcal{L}}{\partial \alpha_1} = \dfrac{EI}{3L}\alpha_1 - \lambda_1 \dfrac{\partial x_{\text{tip}}}{\partial \alpha_1} - \lambda_2 \dfrac{\partial y_{\text{tip}}}{\partial \alpha_1} - \lambda_3 \dfrac{\partial \phi_{\text{tip}}}{\partial \alpha_1} = 0, \\ \dfrac{\partial \mathcal{L}}{\partial \alpha_2} = \dfrac{EI}{5L}\alpha_2 - \lambda_1 \dfrac{\partial x_{\text{tip}}}{\partial \alpha_2} - \lambda_2 \dfrac{\partial y_{\text{tip}}}{\partial \alpha_2} - \lambda_3 \dfrac{\partial \phi_{\text{tip}}}{\partial \alpha_2} = 0, \\ \dfrac{\partial \mathcal{L}}{\partial \alpha_3} = \dfrac{EI}{7L}\alpha_3 - \lambda_1 \dfrac{\partial x_{\text{tip}}}{\partial \alpha_3} - \lambda_2 \dfrac{\partial y_{\text{tip}}}{\partial \alpha_3} - \lambda_3 \dfrac{\partial \phi_{\text{tip}}}{\partial \alpha_3} = 0, \\ \dfrac{\partial \mathcal{L}}{\partial \alpha_4} = \dfrac{EI}{9L}\alpha_4 - \lambda_1 \dfrac{\partial x_{\text{tip}}}{\partial \alpha_4} - \lambda_2 \dfrac{\partial y_{\text{tip}}}{\partial \alpha_4} - \lambda_3 \dfrac{\partial \phi_{\text{tip}}}{\partial \alpha_4} = 0, \\ \dfrac{\partial \mathcal{L}}{\partial \alpha_5} = \dfrac{EI}{11L}\alpha_5 - \lambda_1 \dfrac{\partial x_{\text{tip}}}{\partial \alpha_5} - \lambda_2 \dfrac{\partial y_{\text{tip}}}{\partial \alpha_5} - \lambda_3 \dfrac{\partial \phi_{\text{tip}}}{\partial \alpha_5} = 0, \\ \dfrac{\partial \mathcal{L}}{\partial \lambda_1} = x_{\text{g}} - x_{\text{tip}}(\boldsymbol{\alpha}) = 0, \\ \dfrac{\partial \mathcal{L}}{\partial \lambda_2} = y_{\text{g}} - y_{\text{tip}}(\boldsymbol{\alpha}) = 0, \\ \dfrac{\partial \mathcal{L}}{\partial \lambda_3} = \phi_{\text{g}} - \phi_{\text{tip}}(\boldsymbol{\alpha}) = 0. \end{cases} \tag{3.11}$$

Before proceeding to the next stage, it is necessary to conduct the second partial derivative test [210]. This technique, commonly used in multivariable calculus, is employed to determine whether a critical point of a function corresponds to a local minimum, maximum, or a saddle point. If the Hessian matrix (i.e., the matrix of second-order partial derivatives) is positive definite at the stationary point, it indicates a local minimum. This condition is satisfied when all eigenvalues of the Hessian matrix are positive, implying that the

function curves upward in all directions around the critical point. The Hessian matrix of the Lagrangian function with respect to $\boldsymbol{\alpha}$ is presented in Eq. (3.12):

$$\frac{\partial^2 U_\mathrm{b}}{\partial(\alpha_i)^2} = \begin{bmatrix} \frac{\partial^2 U_\mathrm{b}}{\partial(\alpha_0)^2} & \frac{\partial^2 U_\mathrm{b}}{\partial\alpha_0\partial\alpha_1} & \cdots & \frac{\partial^2 U_\mathrm{b}}{\partial\alpha_0\partial\alpha_5} \\ \frac{\partial^2 U_\mathrm{b}}{\partial\alpha_1\partial\alpha_0} & \frac{\partial^2 U_\mathrm{b}}{\partial\alpha_1^2} & \cdots & \frac{\partial^2 U_\mathrm{b}}{\partial\alpha_1\partial\alpha_5} \\ \vdots & \vdots & \ddots & \vdots \\ \frac{\partial^2 U_\mathrm{b}}{\partial\alpha_5\partial\alpha_0} & \frac{\partial^2 U_\mathrm{b}}{\partial\alpha_5\partial\alpha_1} & \cdots & \frac{\partial^2 U_\mathrm{b}}{\partial\alpha_5^2} \end{bmatrix} = \begin{bmatrix} \frac{EI}{L} & 0 & 0 & 0 & 0 & 0 \\ 0 & \frac{EI}{3L} & 0 & 0 & 0 & 0 \\ 0 & 0 & \frac{EI}{5L} & 0 & 0 & 0 \\ 0 & 0 & 0 & \frac{EI}{7L} & 0 & 0 \\ 0 & 0 & 0 & 0 & \frac{EI}{9L} & 0 \\ 0 & 0 & 0 & 0 & 0 & \frac{EI}{11L} \end{bmatrix}. \tag{3.12}$$

In the resulting diagonal matrix, all eigenvalues are strictly positive and remain constant, as each diagonal entry corresponds to a positive coefficient of the generalized coordinates in the strain energy expression. This definiteness directly reflects the positive curvature of the strain energy function in all directions of the variable space. Consequently, the Hessian matrix is positive definite, and it follows that the stationary point obtained via the Lagrange multipliers method corresponds to a local minimum of the strain energy. This confirms the physical validity and stability of the computed equilibrium configuration.

3.3 Case study: modeling compliant bistable mechanism

Modeling compliant bistable mechanisms under large deformation is particularly challenging due to the presence of strong geometric nonlinearity, especially after buckling occurs. These bistable mechanisms exhibit snap-through behavior, multiple equilibrium configurations, and nonlinear force-displacement responses, which make analytical modeling and numerical simulation considerably difficult [211]. To ensure numerical stability and control the solution path, modeling is often performed in a displacement-driven manner, where a prescribed trajectory is imposed and the corresponding reaction force is derived.

The choice of a bistable mechanism in this study is deliberate. Its inherent strong nonlinearity makes it an ideal benchmark problem for evaluating the capability of advanced modeling approaches. In particular, it serves as an excellent example to showcase the effectiveness of the 5th-order SCME method in capturing large, nonlinear deformations with high accuracy. This section presents the detailed modeling procedure of the compliant bistable mechanism using the 5th-order SCME formulation, highlighting its advantages in handling complex geometries and nonlinear responses.

In preparation for the modeling process, a series of fundamental considerations must be addressed. Firstly, it is essential to establish a well-defined coordinate system that will serve as the foundational reference frame for the following analysis. Subsequently, determining the trajectory of the beam tip is necessary to simulate the movement of the center shuttle. Following these preparations, the modeling of the compliant bistable mechanism is conducted. The following Fig. 3.1 illustrates the definition of local and global coordinate system and also the definition of trajectory points and geometric parameters.

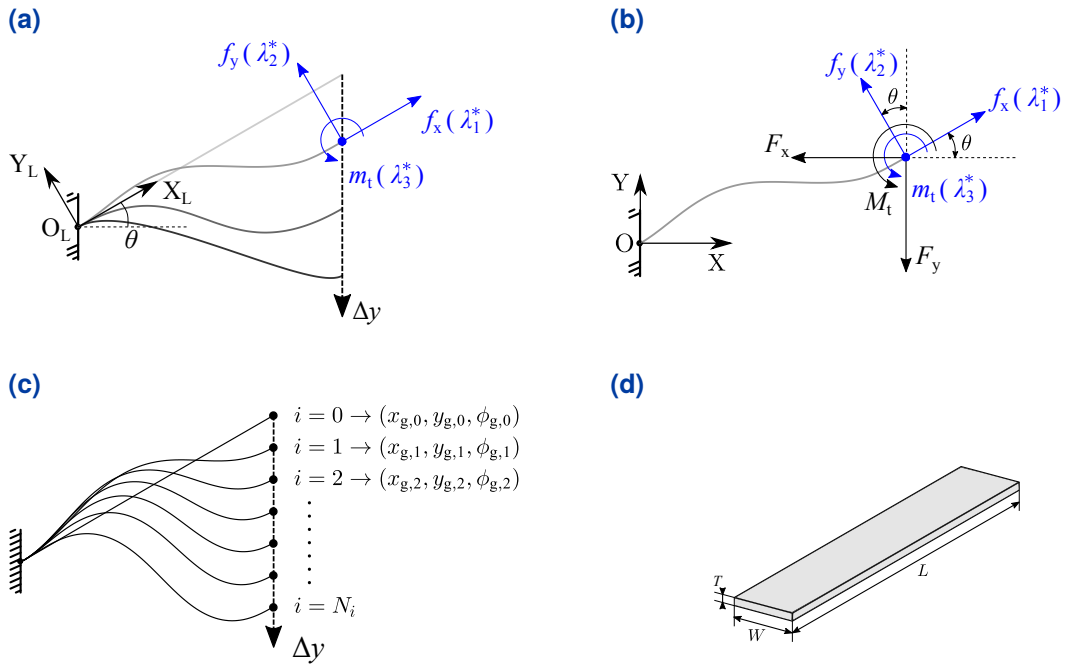


Fig. 3.1.: Explanation of local and global coordinate systems, trajectory points, and geometric parameters of compliant beams.(a) Definition of local coordinate system. (b) Definition of global coordinate system. (c) Definition of discrete trajectory points. (d) Definition of geometric parameters.

In the local coordinate system, the XL axis is aligned with the initial shape of the beam, while the YL axis is perpendicular to the XL axis. The origin, OL, is fixed at the root of the compliant beam. The initial inclined angle of the compliant beam in the global coordinate system is denoted as θ and remains constant throughout the modeling procedure. The forces f_x and f_y, together with the moment m_t, are determined using the Lagrange multiplier method and are defined in the local coordinate framework, with their positive directions indicated by blue arrows. In the global coordinate system, the origin O is also located at the beam root, with the horizontal X axis and the vertical Y axis. The global forces F_x and F_y, as well as the moment M_t, are obtained by transforming the corresponding quantities f_x, f_y, and m_t from the local coordinate system. The positive directions of

forces and moments in the global coordinate system are indicated by black arrows. For the discrete trajectory representation, the overall displacement Δy is discretized into N_i evenly distributed points along the trajectory. The coordinates of the i-th trajectory point are given by $[x_{g,i},, y_{g,i}]$, with the corresponding deflection angle denoted as $\phi_{g,i}$. The geometric parameters, as illustrated in Fig. 3.1, include the beam length L, the in-plane thickness T, and the out-of-plane thickness W.

Following the establishment of both material and geometric properties, the subsequent step involves determining the trajectory of the beam tip. The tip trajectory is defined to move along the negative direction of the Y-axis in the global coordinate system, as shown in Fig. 3.1 (c). The straight trajectory is discretized into finite trajectory points, and the amount of these points is denoted as N_i. The index of these discrete points is denoted as i. The coordinates of each trajectory point in local coordinate system $O_L X_L Y_L$ can be calculated using Eq. (3.13), Eq. (3.14) and Eq. (3.15).

$$x_{g,i} = L - i\frac{\Delta y \sin\theta}{N_i}, \tag{3.13}$$

$$y_{g,i} = -i\frac{\Delta y \cos\theta}{N_i}, \tag{3.14}$$

$$\phi_{g,i} = \theta, \tag{3.15}$$

where, $[x_{g,i}, y_{g,i}, \phi_{g,i}]$ represents the coordinates of i-th given tip poses in the trajectory. Δy is the hypothetical length of trajectory. The inclined angle θ of the compliant beam is initially defined and remains constant in this formulation. In Fig. 3.1 (d), W, T and L represent the out-of-plane thickness, in-plane thickness, and length of the compliant beam, respectively.

Typically, a second-order polynomial, which has been previously used in the modeling of compliant grippers, can effectively approximate a beam with two inflection points [120]. However, when modeling compliant bistable mechanisms, such lower-order polynomials become inadequate due to the complex post-buckling deformations commonly observed in compliant beams. These deformation profiles often exhibit multiple inflection points, exceeding the representational capacity of low-order basis functions. Since the number of inflection points that a polynomial can represent is inherently limited by its order, low-order polynomials lack the flexibility to capture deformation patterns involving a greater number of curvature changes. Therefore, higher-order representations are necessary to accurately model the geometric nonlinearity in bistable systems.

To further model the kinetostatic behavior of the compliant bistable mechanism, the full expression of the Lagrangian function is given as:

$$\mathcal{L}(\boldsymbol{\alpha}, \boldsymbol{\lambda}) = \frac{EI}{2L}\left(\alpha_0^2 + \frac{\alpha_1^2}{3} + \frac{\alpha_2^2}{5} + \frac{\alpha_3^2}{7} + \frac{\alpha_4^2}{9} + \frac{\alpha_5^2}{11}\right) + \begin{bmatrix}\lambda_1 & \lambda_2 & \lambda_3\end{bmatrix}\begin{bmatrix} x_{\mathrm{g},i} - x_{\mathrm{tip}}(\boldsymbol{\alpha}) \\ y_{\mathrm{g},i} - y_{\mathrm{tip}}(\boldsymbol{\alpha}) \\ \phi_{\mathrm{g},i} - \phi_{\mathrm{tip}}(\boldsymbol{\alpha})\end{bmatrix}, \tag{3.16}$$

where, the position constraints are updated in each iteration to correspond to the target beam tip position. Typically, Lagrangian multipliers assume distinct meanings when addressing optimization problems. In the context of modeling compliant beams, it can be assumed that the Lagrange multipliers $\boldsymbol{\lambda}$ represent the applied force and moment at the tip. To verify this assumption, the proof procedure is demonstrated as:

a) Based on Eq. (3.11), the solution ($\boldsymbol{\alpha}^*$and $\boldsymbol{\lambda}^*$) to the Lagrangian function can be treated as a function of $x_{\mathrm{g},i}$, $y_{\mathrm{g},i}$, and $\phi_{\mathrm{g},i}$, denoted as $\boldsymbol{\alpha}^*(x_{\mathrm{g},i}, y_{\mathrm{g},i}, \phi_{\mathrm{g},i})$ and $\boldsymbol{\lambda}^*(x_{\mathrm{g},i}, y_{\mathrm{g},i}, \phi_{\mathrm{g},i})$. The obtained minimum bending strain energy which denoted as $U_{\mathrm{b}}(\boldsymbol{\alpha}^*)$ can be further reformulated as $U_{\mathrm{b}}\left[\boldsymbol{\alpha}^*(x_{\mathrm{g},i}, y_{\mathrm{g},i}, \phi_{\mathrm{g},i})\right]$. The expression of the Lagrange function at the stationary point is reformulated as in Eq. (3.17):

$$\begin{aligned}\mathcal{L}[\boldsymbol{\alpha}^*(x_{\mathrm{g},i}, y_{\mathrm{g},i}, \phi_{\mathrm{g},i}), \boldsymbol{\lambda}^*(x_{\mathrm{g},i}, y_{\mathrm{g},i}, \phi_{\mathrm{g},i}), x_{\mathrm{g},i}, y_{\mathrm{g},i}, \phi_{\mathrm{g},i}] &= U_{\mathrm{b}}\left[\boldsymbol{\alpha}^*(x_{\mathrm{g},i}, y_{\mathrm{g},i}, \phi_{\mathrm{g},i})\right] \\ &= U_{\mathrm{b}}(x_{\mathrm{g},i}, y_{\mathrm{g},i}, \phi_{\mathrm{g},i}),\end{aligned} \tag{3.17}$$

where, the constraint components are eliminated due to $g(x) = 0$ at stationary point.

b) Derive the partial derivative of $U_{\mathrm{b}}(x_{\mathrm{g},i}, y_{\mathrm{g},i}, \phi_{\mathrm{g},i})$ with regard to $x_{\mathrm{g},i}$, $y_{\mathrm{g},i}$, $\phi_{\mathrm{g},i}$ at the stationary point and based on the multivariable chain rule, Eq. (3.18), (3.19) and (3.20) can be obtained as:

$$\begin{aligned}\frac{\partial U_{\mathrm{b}}(x_{\mathrm{g},i}, y_{\mathrm{g},i}, \phi_{\mathrm{g},i})}{\partial x_{\mathrm{g},i}} &= \frac{\partial \mathcal{L}[\boldsymbol{\alpha}^*(x_{\mathrm{g},i}, y_{\mathrm{g},i}, \phi_{\mathrm{g},i}), \boldsymbol{\lambda}^*(x_{\mathrm{g},i}, y_{\mathrm{g},i}, \phi_{\mathrm{g},i}), x_{\mathrm{g},i}, y_{\mathrm{g},i}, \phi_{\mathrm{g},i}]}{\partial x_{\mathrm{g},i}} \\ &= \frac{\cancel{\partial \mathcal{L}}}{\cancel{\partial \boldsymbol{\alpha}}}\frac{\partial \boldsymbol{\alpha}^*}{\partial x_{\mathrm{g},i}} + \frac{\cancel{\partial \mathcal{L}}}{\cancel{\partial \boldsymbol{\lambda}}}\frac{\partial \boldsymbol{\lambda}^*}{\partial x_{\mathrm{g},i}} + \frac{\partial \mathcal{L}}{\partial x_{\mathrm{g},i}}\frac{dx_{\mathrm{g},i}}{dx_{\mathrm{g},i}} + \frac{\partial \mathcal{L}}{\partial y_{\mathrm{g},i}}\frac{\cancel{dy_{\mathrm{g},i}}}{\cancel{dx_{\mathrm{g},i}}} + \frac{\partial \mathcal{L}}{\partial \phi_{\mathrm{g},i}}\frac{\cancel{d\phi_{\mathrm{g},i}}}{\cancel{dx_{\mathrm{g},i}}},\end{aligned} \tag{3.18}$$

$$\frac{\partial U_{\mathrm{b}}(x_{\mathrm{g},i}, y_{\mathrm{g},i}, \phi_{\mathrm{g},i})}{\partial y_{\mathrm{g},i}} = \frac{\partial \mathcal{L}[\boldsymbol{\alpha}^*(x_{\mathrm{g},i}, y_{\mathrm{g},i}, \phi_{\mathrm{g},i}), \boldsymbol{\lambda}^*(x_{\mathrm{g},i}, y_{\mathrm{g},i}, \phi_{\mathrm{g},i}), x_{\mathrm{g},i}, y_{\mathrm{g},i}, \phi_{\mathrm{g},i}]}{\partial y_{\mathrm{g},i}}$$
$$= \cancel{\frac{\partial \mathcal{L}}{\partial \boldsymbol{\alpha}}} \frac{\partial \boldsymbol{\alpha}^*}{\partial y_{\mathrm{g},i}} + \cancel{\frac{\partial \mathcal{L}}{\partial \boldsymbol{\lambda}}} \frac{\partial \boldsymbol{\lambda}^*}{\partial y_{\mathrm{g},i}} + \frac{\partial \mathcal{L}}{\partial x_{\mathrm{g},i}} \cancel{\frac{dx_{\mathrm{g},i}}{dy_{\mathrm{g},i}}} + \frac{\partial \mathcal{L}}{\partial y_{\mathrm{g},i}} \frac{dy_{\mathrm{g},i}}{dy_{\mathrm{g},i}} + \frac{\partial \mathcal{L}}{\partial \phi_{\mathrm{g},i}} \cancel{\frac{d\phi_{\mathrm{g},i}}{dy_{\mathrm{g},i}}}, \tag{3.19}$$

$$\frac{\partial U_{\mathrm{b}}(x_{\mathrm{g},i}, y_{\mathrm{g},i}, \phi_{\mathrm{g},i})}{\partial \phi_{\mathrm{g},i}} = \frac{\partial \mathcal{L}[\boldsymbol{\alpha}^*(x_{\mathrm{g},i}, y_{\mathrm{g},i}, \phi_{\mathrm{g},i}), \boldsymbol{\lambda}^*(x_{\mathrm{g},i}, y_{\mathrm{g},i}, \phi_{\mathrm{g},i}), x_{\mathrm{g},i}, y_{\mathrm{g},i}, \phi_{\mathrm{g},i}]}{\partial \phi_{\mathrm{g},i}}$$
$$= \cancel{\frac{\partial \mathcal{L}}{\partial \boldsymbol{\alpha}}} \frac{\partial \boldsymbol{\alpha}^*}{\partial \phi_{\mathrm{g},i}} + \cancel{\frac{\partial \mathcal{L}}{\partial \boldsymbol{\lambda}}} \frac{\partial \boldsymbol{\lambda}^*}{\partial \phi_{\mathrm{g},i}} + \frac{\partial \mathcal{L}}{\partial x_{\mathrm{g},i}} \cancel{\frac{dx_{\mathrm{g},i}}{d\phi_{\mathrm{g},i}}} + \frac{\partial \mathcal{L}}{\partial y_{\mathrm{g},i}} \cancel{\frac{dy_{\mathrm{g},i}}{d\phi_{\mathrm{g},i}}} + \frac{\partial \mathcal{L}}{\partial \phi_{\mathrm{g},i}} \frac{d\phi_{\mathrm{g},i}}{d\phi_{\mathrm{g},i}}. \tag{3.20}$$

c) At the stationary point, both $\partial \mathcal{L}/\partial \boldsymbol{\alpha}$ and $\partial \mathcal{L}/\partial \boldsymbol{\lambda}$ equal zero. Furthermore, the coordinates $x_{\mathrm{g},i}, y_{\mathrm{g},i}, \phi_{\mathrm{g},i}$ are mutually independent. Hence Eq. (3.18-3.20) can be simplified to:

$$\frac{\partial U_{\mathrm{b}}(x_{\mathrm{g},i}, y_{\mathrm{g},i}, \phi_{\mathrm{g},i})}{\partial x_{\mathrm{g},i}} = \frac{\partial \mathcal{L}}{\partial x_{\mathrm{g},i}} \frac{dx_{\mathrm{g},i}}{dx_{\mathrm{g},i}} = \lambda_1, \tag{3.21}$$
$$\frac{\partial U_{\mathrm{b}}(x_{\mathrm{g},i}, y_{\mathrm{g},i}, \phi_{\mathrm{g},i})}{\partial y_{\mathrm{g},i}} = \frac{\partial \mathcal{L}}{\partial y_{\mathrm{g},i}} \frac{dy_{\mathrm{g},i}}{dy_{\mathrm{g},i}} = \lambda_2, \tag{3.22}$$
$$\frac{\partial U_{\mathrm{b}}(x_{\mathrm{g},i}, y_{\mathrm{g},i}, \phi_{\mathrm{g},i})}{\partial \phi_{\phi,i}} = \frac{\partial \mathcal{L}}{\partial \phi_{\mathrm{g},i}} \frac{d\phi_{\mathrm{g},i}}{d\phi_{\mathrm{g},i}} = \lambda_3. \tag{3.23}$$

d) Castigliano's first theorem indicates that, the first partial derivative of the total internal energy (strain energy) in a structure with respect to any particular deflection component at a point is equal to the force applied at that point and in the direction corresponding to that deflection component. In derivation process, the Lagrangian multipliers indeed represent the first partial derivative of the internal energy. Consequently, it can be proven that the obtained Lagrange multipliers $\boldsymbol{\lambda}$ correspond to the applied forces and moment on the beam tip. Specifically, λ_1, λ_2 and λ_3 denote the applied forces f_{x}, f_{y} and moment m_{t} on the beam tip in the local coordinate system.

The aforementioned procedure is commonly referred to as the interpretation of Lagrange multipliers [212]. Eq. (3.24), Eq. (3.25) and Eq. (3.26) can be employed to transform the reaction force and moment from the local coordinate system to the global coordinate system as:

$$F_{\mathrm{x}} = -f_{\mathrm{x}} \cos\theta + f_{\mathrm{y}} \sin\theta = -\lambda_1^* \cos\theta + \lambda_2^* \sin\theta, \tag{3.24}$$

$$F_{\mathrm{y}} = -f_{\mathrm{x}} \sin\theta - f_{\mathrm{y}} \cos\theta = -\lambda_1^* \sin\theta - \lambda_2^* \cos\theta, \tag{3.25}$$

$$M_{\mathrm{t}} = m_{\mathrm{t}} = \lambda_3^*. \tag{3.26}$$

Determining the applied force on the beam tip is crucial for assessing stress in the modeling of compliant bistable mechanisms. This evaluation is essential to ensure the structural integrity, performance, and safety of these mechanisms. After determining the stationary point, the generalized coordinates are thereby determined, and the curvature of the beam can be easily obtained by substituting the $\boldsymbol{\alpha}^*$ into Eq. (3.2). In addition, the maximum bending stress at point s, occurring at the extreme fiber of the beam (the fiber farthest from the neutral axis), is calculated using the SCME method as given in Eq. (4.10).

$$\sigma_{\mathrm{b}}(s) = \frac{M}{I} \cdot \frac{T}{2} = \frac{EI\omega(s)}{I} \cdot \frac{T}{2} = \frac{ET\omega(s)}{2}, \tag{3.27}$$

where, $\sigma_{\mathrm{b}}(s)$ represent the bending stress at the extreme fiber of compliant beam at point s.

The above content outlines the detailed modeling procedure for the compliant bistable mechanism, including the formulation of the Lagrangian function and the definition of relevant constraints. The following section presents the implementation procedure, which is carried out in MATLAB using a customized Newton–Raphson method tailored for the efficient solution of the nonlinear equilibrium equations.

3.4 Implementation procedure

The minimization of the strain energy function necessitates the use of optimization algorithms. Given that the smooth curvature model is formulated as a continuous function,

deterministic approaches are particularly appropriate, as they ensure reliable performance and offer rapid convergence. In this study, the Newton-Raphson method is adopted to carry out the minimization, owing to its well-established efficiency in solving nonlinear problems through iterative refinement. The Newton-Raphson method starts with an initial guess for the root of the equation and then iteratively refines this guess to approach the actual root. It is based on the idea of using the tangent line approximation to the function at the current guess to find a better approximation for the root. During the process of seeking the minimum bending strain energy, the primary objective is to determine the stationary point of the nonlinear equation system in Eq. (3.11). The root-finding algorithm can be seen from the flow chart in Fig. 3.2. The algorithm proceeds through the following steps:

1. **Preprocessing Step:**
   Before the iteration begins, the analytical expressions of the Jacobian matrix $\mathbf{J}$ and the Hessian vector $\mathbf{H}$ with respect to the optimization variables $\boldsymbol{\alpha}$ and Lagrange multipliers $\boldsymbol{\lambda}$ are derived. These derivatives are essential for evaluating the Newton-Raphson update.

2. **Initialization:**
   An initial guess vector $\boldsymbol{S}_0 = [\boldsymbol{\alpha}, \boldsymbol{\lambda}] = [\pm\xi, 0, 0, \ldots, 0]$ is provided to start the iteration. This vector serves as the starting point for solving the root of the nonlinear system at each target beam tip position.

3. **Iterative Update:**
   At each iteration step k, the Jacobian and Hessian are evaluated using the current estimate $\boldsymbol{S}_k$, and the solution vector is updated via the Newton-Raphson rule:

   $$\boldsymbol{S}_{k+1} = \boldsymbol{S}_k - \gamma \mathbf{J}^{-1}\mathbf{H}$$

   where $\gamma \in [0, 1]$ is a relaxation factor introduced to enhance convergence stability.

4. **Convergence Check:**
   The iteration continues until the norm of the Jacobian (representing the residual of the gradient) falls below a predefined threshold ϵ, indicating convergence.

5. **Saving and Iterating Over Trajectory Points:**
   Once convergence is achieved for a given target beam tip position (indexed by i), the corresponding solution $\boldsymbol{S}_i^*$ is saved. The algorithm then checks whether all trajectory

points have been processed. If not, the solution $\boldsymbol{S}_i^*$ is used as the initial guess for the next target point by setting $\boldsymbol{S}_0 = \boldsymbol{S}_i^*$, and the process is repeated.

6. **Termination:**
   The loop continues until all N_i trajectory points are processed, at which point the algorithm terminates.

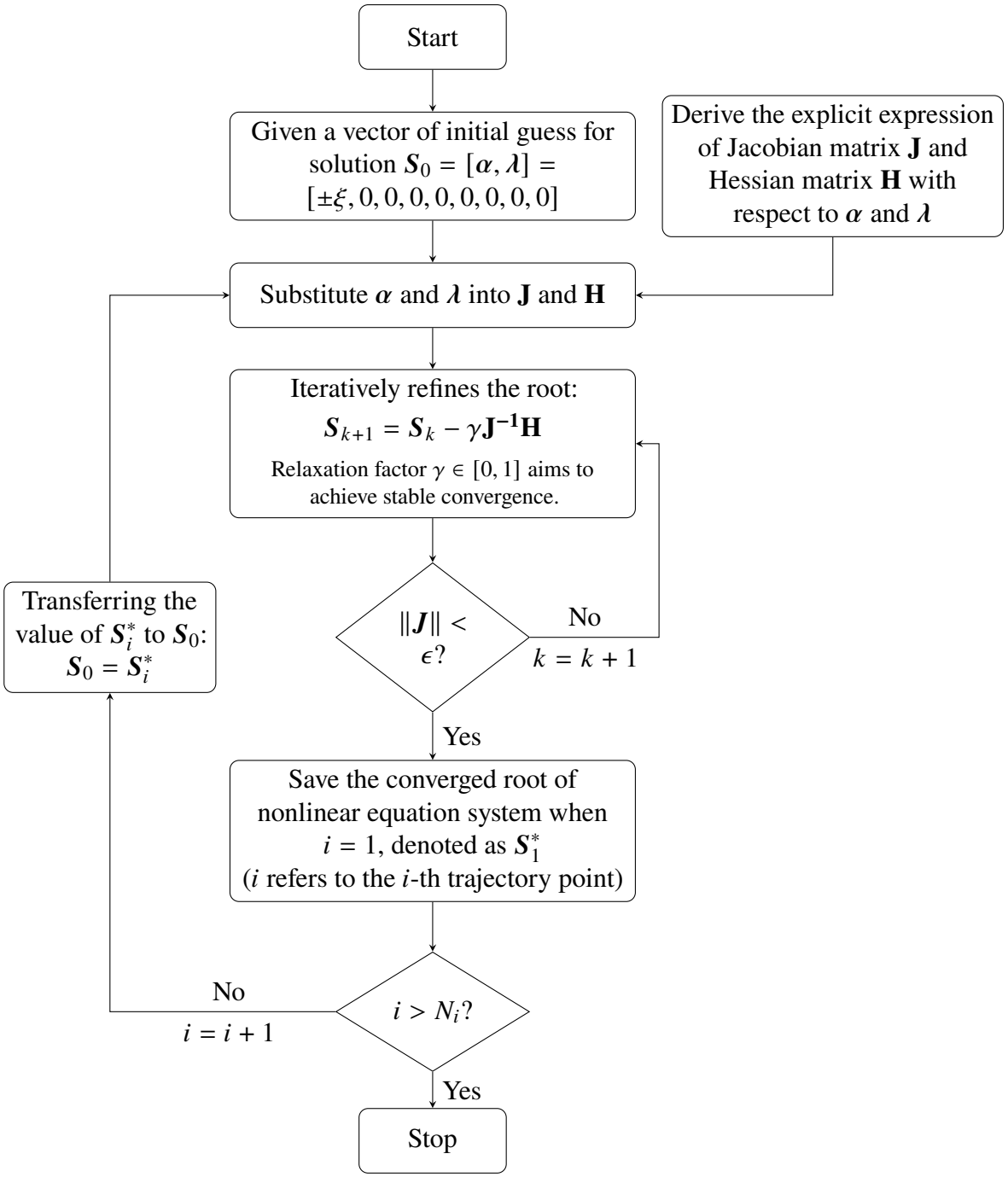


Fig. 3.2.: The flowchart of the root-finding algorithm. Before conducting the iteration, the explicit expressions of the Jacobian matrix $\mathbf{J}$ and Hessian matrices $\mathbf{H}$ need to be derived and used as part of the formulation during the iteration process. Then, the root-finding algorithm begins with a given initial guess S_0. The Newton-Raphson method is then applied to determine the root of the Lagrange function as demonstrated in the flowchart. The iteration stops when the norms of the gradients have converged to the threshold ϵ. Subsequently, the iteration process is applied to each trajectory point sequentially, until the last trajectory point.

When using the Newton-Raphson method, providing an initial guess of the root is vital, which influences the deformation shape as it determines the starting point for the iteration process. The iterative root-finding process relies on updating this initial guess. Notably, choosing an initial guess of zero can entirely lead to matrix singularity, making iteration difficult or impossible and obstructing convergence toward the root of the nonlinear equation system. The distinct deformation shapes, as shown in Fig. 3.3 (a) and (b), do not affect the mechanical characteristics of the mechanism. This problem can also be seen as a multi-solution problem, where a deformation shape corresponds to a valid solution.

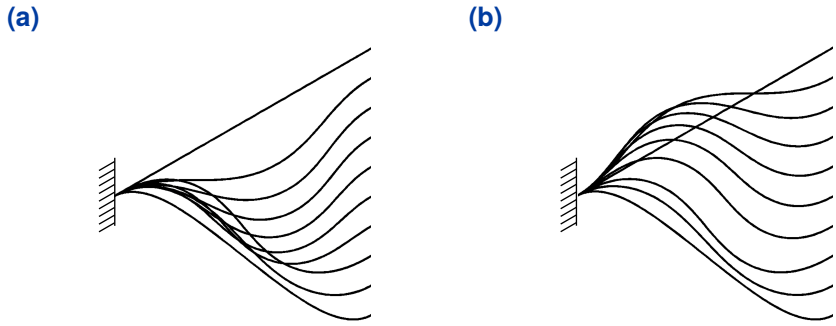


Fig. 3.3.: Two possible deformation shapes exist in modeling results. The distinct deformation shapes are induced by setting the initial guess of the root in the root-finding procedure. The sign of ξ affects the deformation shape (buckling direction). (a) Possible deformation shape A: when a positive ξ is given in initial guess $\boldsymbol{S}_0$. (b) Possible deformation shape B: when a negative ξ is given in initial guess $\boldsymbol{S}_0$.

Moreover, in real-world scenarios, both aforementioned buckling directions are plausible and challenging to predict due to various influencing factors such as manufacturing inaccuracies, load deviation, minor plastic deformations, and surface defect. However, only one buckling direction will be seen usually in a real-word application. Integrating these factors into mathematical models poses a significant challenge. In mechanisms design, achieving a desired deformation shape may involve inducing deformation based on designing an initially-curved small shape or applying small deviation load to the mechanisms. In the proposed SCME method, the specified initial guess set as $\boldsymbol{S}_0 = [\boldsymbol{\alpha}, \boldsymbol{\lambda}] = [\pm\xi, 0, 0, 0, 0, 0, 0, 0, 0]$ effectively meets the requirement of providing an initial guess used to be updated while ensuring that compliant beams deform as intended. The magnitude of ξ would not influence the modeling result.

The implementation procedure of the proposed modeling framework has been detailed in this section, including both the formulation and numerical solution process. In the

following section, modeling results are further validated through FEA simulation and experiment.

3.5 FEA and experimental validation

This section focuses on validating the accuracy of the 5th-order SCME method through FEA simulations and experimental tests. The FEA simulations and experimental tests serves to further ensure the reliability of the proposed 5th-order SCME method. Details on setting up the FEA simulations and experiments are demonstrated in the following content.

3.5.1 FEA validation

The modeling is exemplified through the analysis of an inclined compliant beam with a length of 100 mm and an inclined angle of 20 degrees. This subsection focuses on examining the model by comparing it with FEA simulation results. The FEA simulation is conducted in Strand7 R2.4.4, a powerful commerical FEA simulation software that focuses on addressing complex issues in structural engineering and civil engineering [213]. Its modeling and simulation capabilities enable the accurate simulation and analysis of the behavior of various structures and materials. The procedure of conducting FEA simulation is listed as:

a) Define and subdivide the compliant beam

   This part involves designing the compliant beam with an initially straight shape. The beam length is set at 100 mm, and the inclined angle is designed to be 20 degrees, consistent with the modeling in the SCME method. Initially, the coordinates of the beam ends are defined as $[0, 0, 0]$ and $[100\cos 20°, 100\sin 20°, 0]$. The beam is then created by connecting these two nodes. When applying finite element method, the beams are normally subdivided into finite amount of beam elements (denoted as n_{FEA}). This amount (n_{FEA}) is a key factor influence the convergence and efficiency. The element used for simulation in Strand7 refers to the conventional beam element with six degrees of freedom at each node: three translations and three rotations. The undeformed element is a straight line between the two nodes to which it is connected. The beam carries axial force, torque, shear forces, and bending moments

in its principal planes. For modeling slender beams, the FEA simulation conducted in Strand7 is based on the planar stress assumption.

b) Define the constraint

The constraint is the same as the constraint set in the SCME method. The beam root is fixed, restraining all degrees of freedom, while the other end is set to have movement only along the y-direction. All other degrees of freedom, including rotation along X,Y,Z axes and translational movement along X and Z axes, are fully constrained.

c) Define the mechanical properties of material

For consistency with the SCME method, Young's modulus is set to 2800MPa. As the effect of plate stress is neglected, the Poisson's ratio is not required for subsequent calculations. The beam cross section is identical to that used in the SCME method, with a width $W = 10$ mm and a thickness $T = 0.6$ mm. All sub beams are defined with identical material properties.

d) Conduct nonlinear static simulation

The nonlinear static simulation only considers geometric nonlinearity while ignoring material nonlinearity. In the modeling process, 201 vertical trajectory points are defined to obtain the applied force-displacement relationship along the vertical trajectory. To maintain consistency, the nonlinear FEA is defined with 201 steps, and each step solves for the same equilibrium configuration of the compliant beam as in the SCME method. The solver for nonlinear static simulation is also based on the Newton-Raphson method. The convergence of displacement and force is set to be the same as in the SCME method, which is 10^{-14}. To avoid singularity, the function of the sub-step is applied to obtain a more accurate result when the model is hard to converge.

The accuracy of FEA simulations plays a vital role, as it directly reflects the performance of the high-order SCME method. Increasing the number of elements is critical for improving modeling accuracy; however, an excessively large number of elements significantly reduces computational efficiency. Therefore, a convergence analysis is essential to determine the optimal number of beam elements for FEA simulations.

To investigate the impact of varying the number of beam elements, several FEA simulations were conducted and compared. Convergence was evaluated by examining the variation in the local minimum of F_y, as this point poses the greatest challenge for accurate modeling. Once the force stabilizes around a specified value, the simulation is considered to have converged efficiently. The optimal number of beam elements is then selected based on a trade-off with computational efficiency. The comparison results are shown in Fig. 3.4.

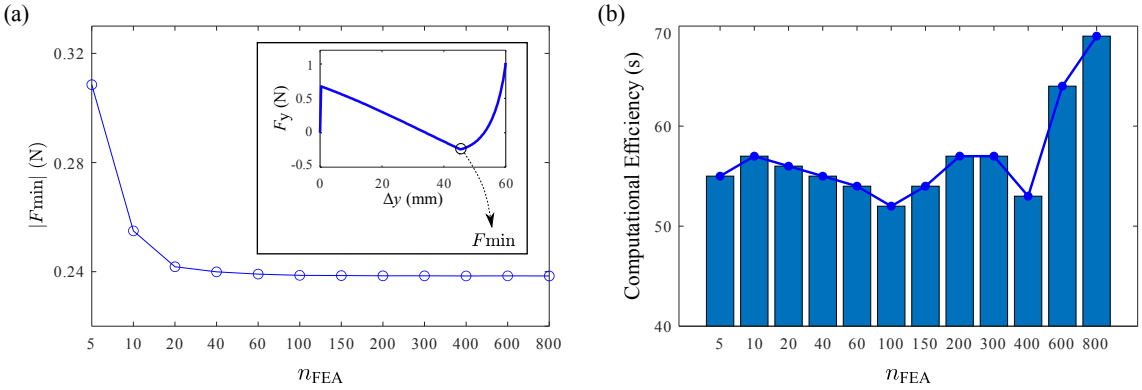


Fig. 3.4.: Convergence analysis of FEA simulation via modeling compliant beams with varying numbers of beam elements. The amount of beam elements varies from 5 to 800. (a) The local minima of the force-displacement curve (F_{min}) obtained from FEA simulations against distinct beam elements. The convergence of the simulation is evaluated by examining whether the magnitude of F_{min} converges. (b) Computational efficiency comparison, which is measured in seconds.

n_{FEA}	$\lvert F_{\text{min}}\rvert$ (N)	n_{FEA}	$\lvert F_{\text{min}}\rvert$ (N)
5	0.308527	150	0.238559
10	0.254951	200	0.238478
20	0.241803	300	0.238479
40	0.239930	400	0.238433
60	0.239110	600	0.238456
100	0.238652	800	0.238423

Tab. 3.3.: The values of F_{min} obtained from FEA simulations when the beam are subdivided into distinct amounts of beam elements.

In Table 3.3, it can be observed that as the number of beam elements exceeds two hundred, the force begins to converge to the fourth decimal place (converging to 0.0001N). Since the FEA simulation result is used as a reference for comparison, a discretization with 200 beam elements is adopted to ensure higher accuracy and reliability. It is also noted from Fig. 3.4 (b) that, the computational efficiency at n_{FEA}=200 is relatively high, however, when $n_{\text{FEA}} = 600$ or $n_{\text{FEA}} = 800$, the computational efficiency decreases significantly.

The procedure for conducting the FEA simulation is outlined above, and the results obtained from the FEA simulation are compared with those from the 5th-order SCME method in Fig. 3.5.

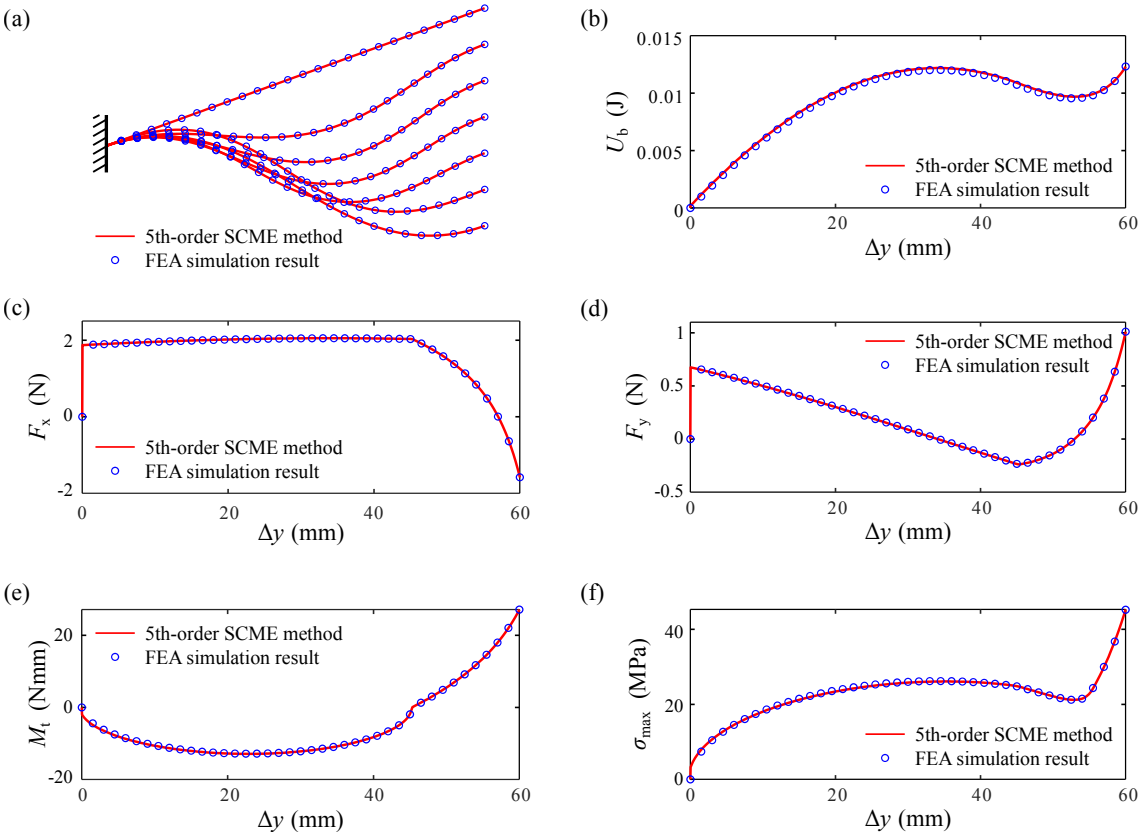


Fig. 3.5.: The modeling result comparisons between 5th-order SCME method and FEA simulation result. The parameters used in modeling and simulation are: L=100mm, θ=20°, E=2800 MPa, W=10mm, T=0.6mm. (a) Comparison of deformation shape. (b) Comparison of bending strain energy U_b. (c) Comparison of F_x (d) Comparison of F_y. (e) Comparison of M_t. (f) Comparison of maximum stress σ_{max}.

As shown in Fig. 3.5, the deformation shapes of the beams exhibit a high degree of similarity. Additionally, in Fig. 3.11, lower order polynomial models fail to accurately capture the large deformation behavior, leading to noticeable deviations from the reference results. Other key aspects, including bending strain energy, applied forces, and moments, also show strong agreement. Further evaluation of compliant mechanisms over a broader range of inclined angles is provided in Section 3.6. Although Fig. Fig. 3.5(d) exhibits a deformation shape similar to that shown in Fig. 3.6, the two figures correspond to different modeling objectives and parameter settings. Fig. 3.6 focuses on validating the proposed linear compensation method using an increased beam thickness to emphasize axial deformation effects, whereas Fig. 3.5(d) assesses the modeling accuracy over the

entire displacement range by comparison with finite element analysis using a thinner beam.

In addition, prior to buckling, the beam experiences linear axial deformation while maintaining its equilibrium configuration. However, once the critical buckling load is reached, the structure loses its stability and the internal stresses are no longer sufficient to balance the applied load. As a result, the structure begins to buckle laterally and its axial stiffness decreases, causing the load to be redistributed throughout the structure. As the high-order SCME method neglects the axial deformation, it cannot directly capture the prior buckling deformation.

To compensate the initial linear deformation occurs before the buckling happened, a nonlinear equation system is set up to solve for the initial buckling position Δy_b. The geometric relationship can be seen from the Fig.3.6.

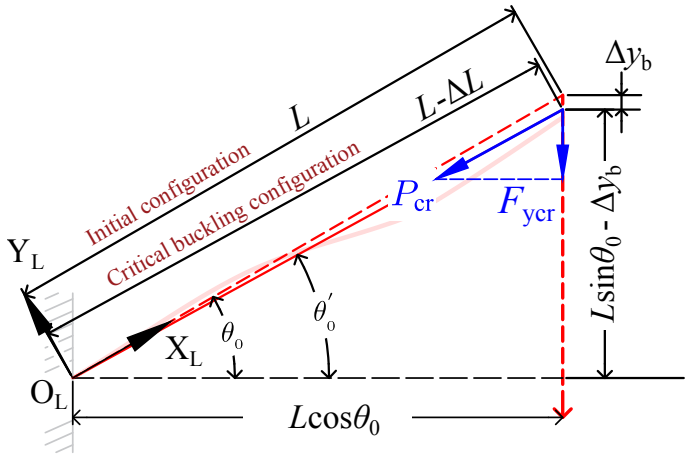


Fig. 3.6.: The variables and geometrical parameters defined to derive the critical buckling position and force. The initial configuration of the beam is represented using the red dashed line. The critical buckling configuration is represented using the red continuous line. The buckled configuration of the beam line is represented using a half-transparent red continuous line.

The critical axial buckling force P_{cr} is dependent on the geometrical shape, material properties, and boundary conditions applied to the compliant beam. When modeling the compliant bistable mechanism, the critical axial buckling force P_{cr} has a component force F_{ycr} along the moving direction. The component force F_{ycr} can be determined through the first point on the force-displacement relationship obtained from the SCME method. By applying the Pythagorean theorem and Hooke's law, a system of two nonlinear equations can be established to solve for the critical buckling position Δy_{b} and the axial deformation

ΔL. The axial deformation ΔL can be calculated by dividing the critical buckling force F_{ycr} by the axial stiffness k, which can be formulated as EA/L; where E represents Young's modulus and A denotes the cross-sectional area of the beam:

$$\begin{cases} \Delta L = \dfrac{P_{\text{cr}}}{k} = \dfrac{PL}{EA\sin\theta_0'} = \dfrac{PL\,(L-\Delta L)}{EA\,(L\sin\theta_0 - \Delta y_{\text{b}})}, \\ (L-\Delta L)^2 = (L\cos\theta_0)^2 + (L\sin\theta_0 - \Delta y_{\text{b}})^2\,. \end{cases} \tag{3.28}$$

To verify the accuracy of this model under small deformation conditions, a case study was conducted on a beam with a length of 100 mm and a thickness of 2 mm. The inclined angle was $\theta_0 = 20°$. The Young's modulus used in this case study is 2800 MPa. The response of the compliant beam is modeled within the range of $\Delta y = [0, 1]$. The comparison between linear deformation compensation and FEA simulation results can be seen from Fig. 3.7. The comparison indicates agreement between the FEA simulation result and linear compensation, demonstrating the feasibility of the approach for determining the critical buckling position and force.

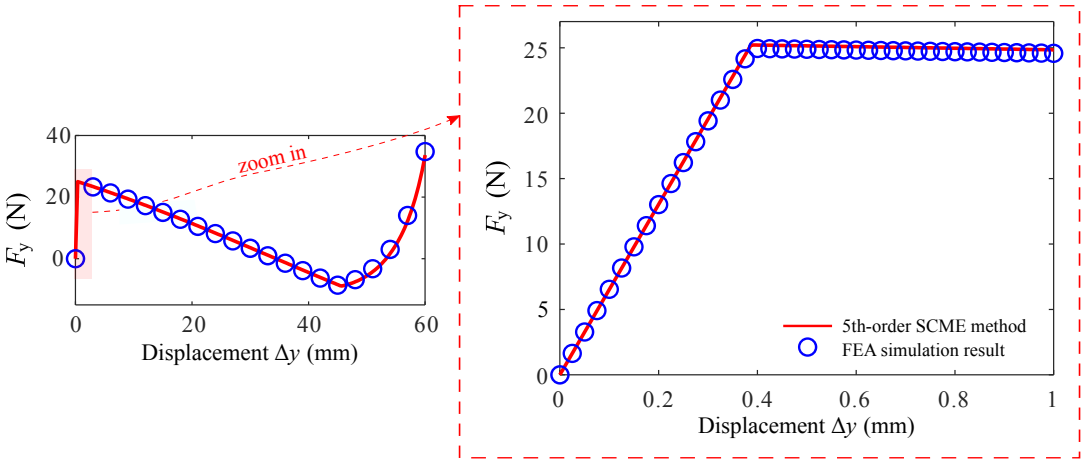


Fig. 3.7.: Comparison between the modeling result considering linear compensation and FEA simulation. The overall force-displacement curve is displayed on the left, while the displacement range [0,1] is zoomed in to provide a clearer visualization of the linear deformation compensation result, as demonstrated on the right.

3.5.2 Experimental validation

In this subsection, the primary objective is to conduct an experiment test aimed at validating the accuracy of the proposed high-order SCME method. Through this empirical

investigation, the emphasis is on providing robust confirmation of the method's accuracy in modeling the applied force and deformation shape.

The designed bistable mechanism for experimental validation is composed of four inclined compliant beams, exhibiting symmetry along the central shuttle with two beams positioned on each side. The inclusion of four beams in the design serves the purpose of mitigating the prevalent issue of rotational imbalance that often encountered in bistable mechanisms that employ only two beams. This mitigation is achieved by constraining the degrees of freedom of the mechanism, thereby ensuring its operation as a single-degree-of-freedom (DOF) mechanism. The shape and dimensions of the 3D model are illustrated in Fig. 3.8.

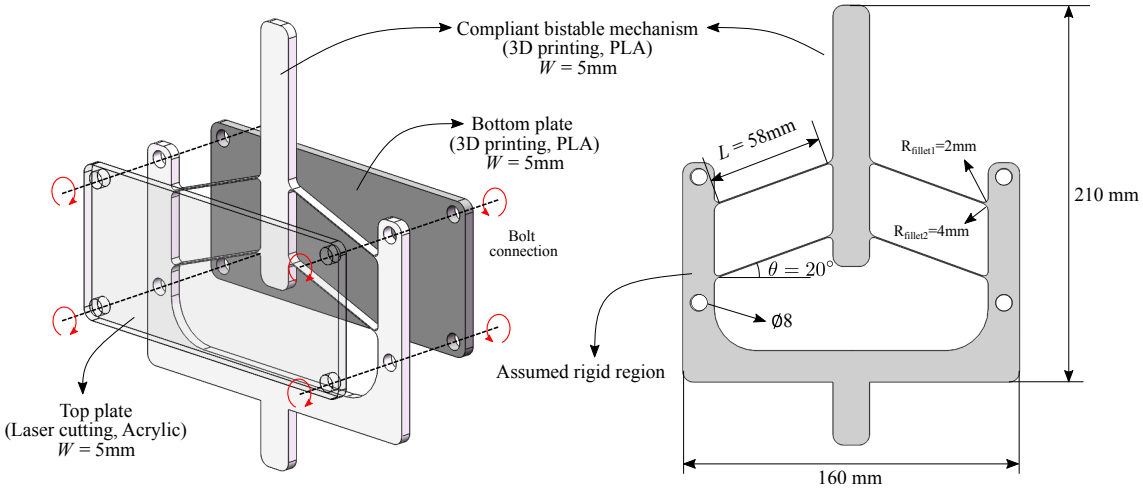


Fig. 3.8.: A prototype with three layers used for experimental validation. The bottom plate and top plate are designed to ensure sufficient stiffness of the rigid components while maintaining the entire mechanism in a relatively compact size. The middle layer is compliant bistable mechanism. Laser cutting is applied to manufacture the top plate, and transparent acrylic material is used to guarantee the visibility of deformation. The geometric parameters of the compliant bistable mechanism can be observed on the right side. Fillets are applied to the roots of beams to avoid stress concentration problems. The beam in-plane thickness T is designed to be 0.8mm.

In the high-order SCME method, it is assumed that the root of the compliant beam is fully fixed. However, during experiments, the root is not fully constrained due to slight deformations within the assumed rigid region and further cause experimental errors. To address this, a three-layer layout is implemented to improve the stiffness of the assumed rigid region. To guarantee visibility of the deformation in the compliant bistable mechanism, the top plate is made from transparent material Acrylic, manufactured using laser cutting machine, while the bottom plate is 3D printed using Tough PLA material in black to enhance contrast and further improve visibility. These three layers are connected via bolt

connections. The center shuttle of the compliant bistable mechanism is designed to be sufficiently long to prevent interference between the mechanism and the testing machine fixture.

The 3D printing process is accomplished using the UltiMaker S3 which is a fused deposition manufacturing device. This budget-friendly desktop 3D printer provides reliable performance and high-quality prints, making it ideal for prototyping. The 3D model is sliced to be further printed in UltiMaker Cura. The printing settings, including the compliant bistable mechanism and bottom plate, can be found in Tab. 3.4.

Tab. 3.4.: Configuration for 3D printing

	Print core	Material	Infill density	Infill pattern	Temperature	Speed	Layer height	Adhesion
Compliant bistable mechanism	AA 0.25	Tough PLA	80%	Grid	210°	60mm/s	0.1mm	Skirt
Bottom plate	AA 0.4	Tough PLA	40%	Grid	210°	60mm/s	0.2mm	Skirt

Tough PLA was chosen as the preferred 3D printing material for compliant bistable mechanism due to its advantageous combination of strength, rigidity, and moderate elasticity. UltiMaker Tough PLA for S series is a technical PLA material with a toughness similar to ABS. The mechanical properties of Tough PLA are listed in Table 3.5, and are obtained from the material properties manual provided by the manufacturer [214]. It is ideal for printing functional prototypes and tooling at larger sizes, without fear of delamination or warping.

Tab. 3.5.: Mechanical properties of tough PLA.

	Young's modulus (MPa)	Yield stress (MPa)	Density (g/cm^3)	Hardness (Shore D)
Tough PLA	2800 (2797±151)	45.3±2	1.22	Shore D 80

The top plate is chosen to be made of transparent acrylic material for visualization purposes. It is cut from an acrylic plate using a laser cutting machine (Laserscript LS1290 Pro) equipped with an 80W CO2 laser. The bed size of the laser cutting machine is 1200 x 900mm. In the cutting process, the speed is set to 5mm/s, and the laser is adjusted to 60% of its maximum power. The resulting top plate exhibits high accuracy compared to the designed model.

The experiment was conducted using the TA HD plus texture analyzer. Texture analysis involves studying how materials change mechanically, such as deforming, breaking, or undergoing other alterations when forces are applied. In this study, the texture analyzer assesses the force-displacement of a compliant bistable mechanism.

The TA HD plus can execute a single DOF movement while maintaining high accuracy in measuring force or displacement. Due to the inherent snap-through behavior in bistable mechanisms, the experiment focuses on a displacement-driven test. The prototype is positioned at the center of the texture analyzer, and displacement occurs from top to bottom. As the displacement increases, the bistable mechanism begins to deform.

The test machine records forces from sensors and to achieve a higher-resolution experimental result, a 50N load cell is chosen for the texture analyzer, with a force sensor resolution of 0.001N. Although the nominal force resolution of the sensor is 0.001 N, the experimentally recorded force values are output with higher numerical precision, reaching up to ten decimal places due to digital acquisition and post processing. The input displacement resolution is 0.001mm. To minimize dynamic effects, the movement speed is set at 0.1 mm/s. The experimental procedure is repeated five times to obtain an average value. The experimental set up can be found in Fig. 3.9.

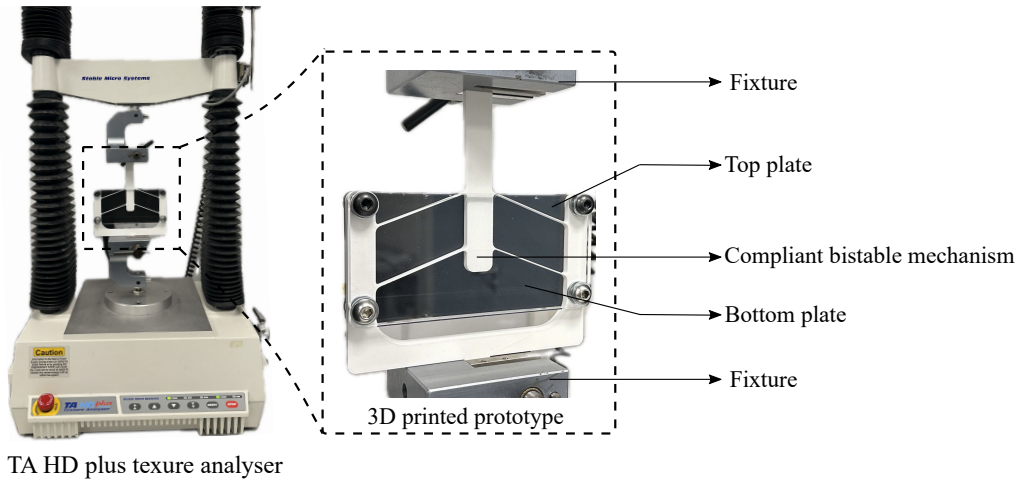


Fig. 3.9.: The experiment setup and 3D printed prototype. The experiment is conducted on the TA HD plus texture analyzer. The 3D printed prototype consists of three layers, including top and bottom plates, which are used to enhance the lateral stiffness. The middle layer is the 3D printed compliant bistable mechanism.

In the experiment, force–displacement data were acquired while the deformation process of the compliant bistable mechanism was simultaneously recorded. The deformation shapes

at displacements of 5 mm, 10 mm, and 15 mm were examined and compared with those predicted by the SCME method, showing a high level of agreement. In addition, the experimentally measured force–displacement response of the compliant bistable mechanism agrees well with both the FEA simulations and the SCME method predictions. These results demonstrate strong consistency between the experimental observations and the predicted mechanical behavior of the mechanism. The comparison of results is shown in Fig. 3.10.

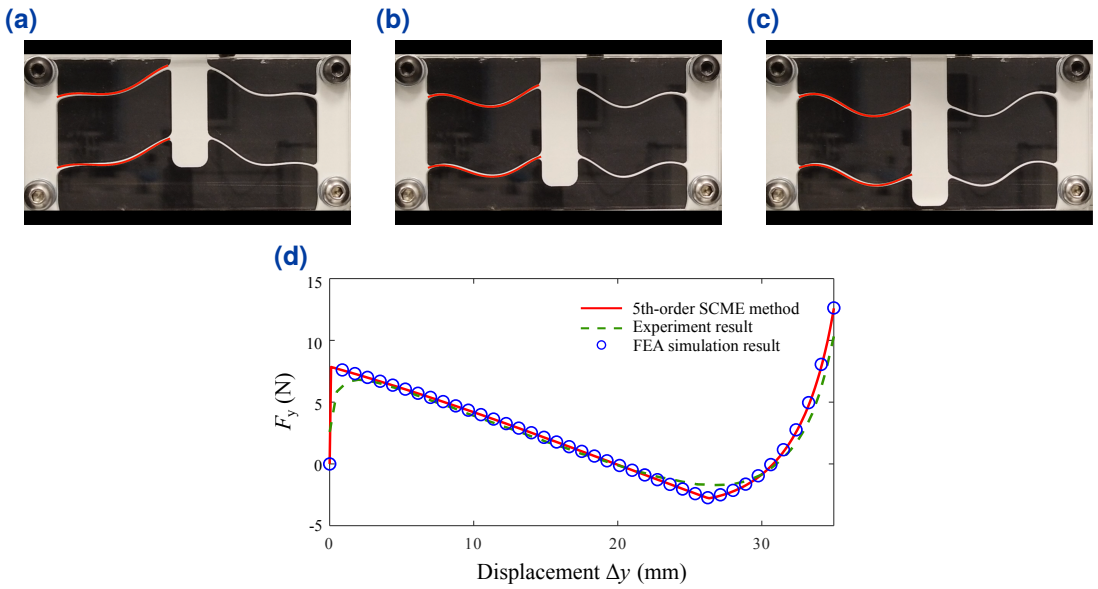


Fig. 3.10.: Experiment result comparison. The red continuous line represents the predicted deformation shape obtained from the SCME method. (a) Deformation shape comparison when Δy = 5mm. (b) Deformation shape comparison when Δy = 15mm. (c) Deformation shape comparison when Δy = 25mm. (d) Force-displacement relationship comparison among the SCME method, experiment, and FEA simulation. Note that the total force obtained through the 5th-order SCME method is four times the force calculated for a single compliant beam. This is because the designed prototype incorporates four beams.

The primary source of error stems from the insufficient rigidity of the support structure in the experiment, where deformation within the rigid region contributes to a flatter experimental force-displacement curve.

3.6 Method comparison

3.6.1 Comparison across SCME with distinct orders

Order of a smooth curvature model is defined as the highest order of Legendre polynomials employed in the curvature representation process. While low-order models offer improved computational efficiency, they fundamentally fail to capture the large deformation behavior of beams. Generally, when dealing with intricate curvature profiles necessitating fitting, selecting a higher-order model is often the preferable choice. This preference stems from the fact that higher-order Legendre polynomials can closely approximate the actual curvature, particularly in cases where curvature exhibits complexity. Although the higher-order model leads to more accurate results, it would cause complex mathematical expression as well.

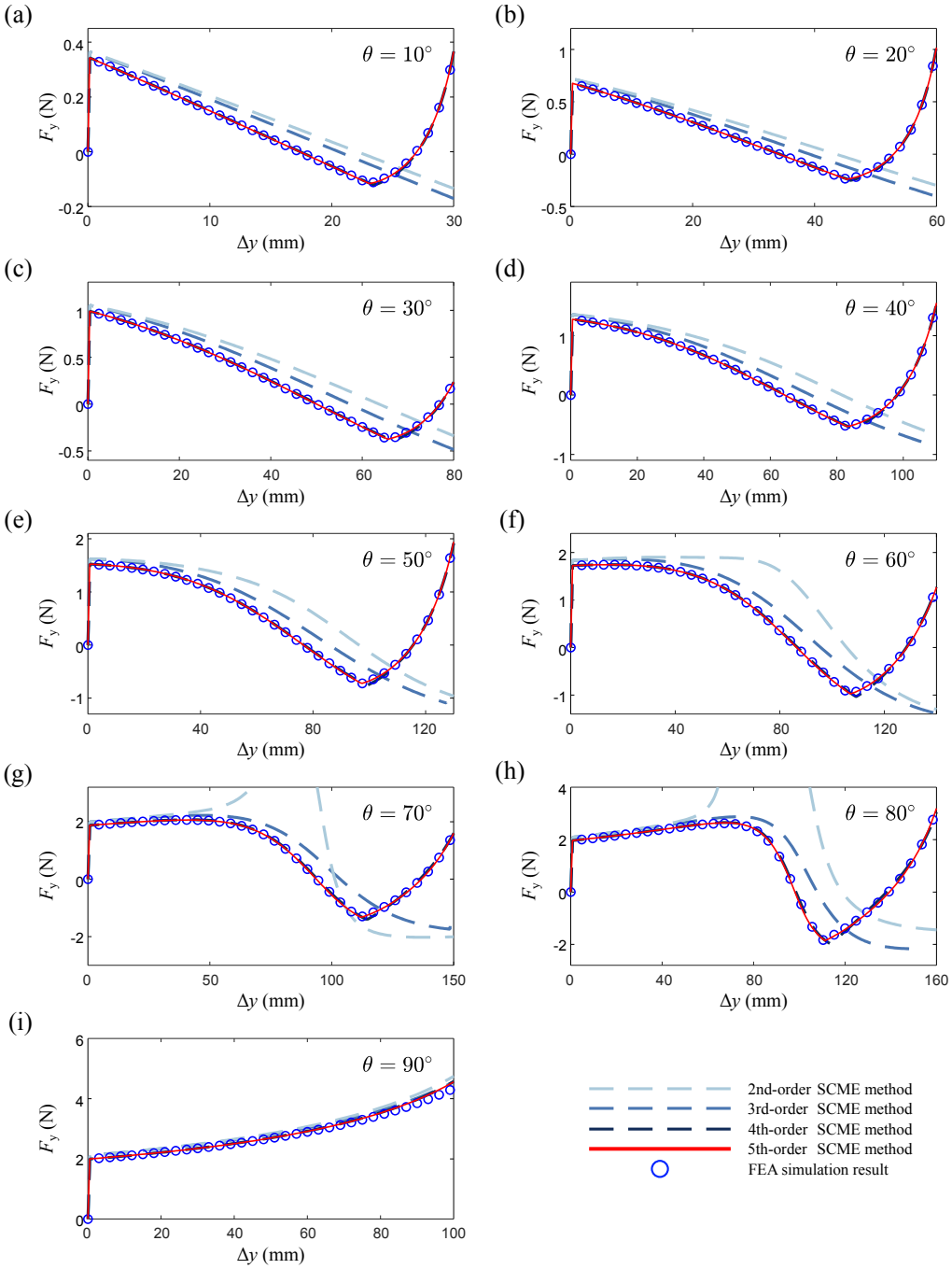


Fig. 3.11.: Force-displacement relationship comparison between 2nd-order, 3rd-order, 4th-order and 5th-order SCME method. The parameters used in modeling and simulation are: L=100mm, E=2800 MPa, W=10mm, T=0.6mm. (a) $\theta = 10°$. (b) $\theta = 20°$.(c) $\theta = 30°$. (d) $\theta = 40°$. (e) $\theta = 50°$. (f) $\theta = 60°$. (g) $\theta = 70°$. (h) $\theta = 80°$. (i) $\theta = 90°$.

The compliant bistable mechanisms, with inclined angles varying from 10 to 90 degrees, are modeled using the 2th-order, 3th-order, 4th-order and 5th-order SCME methods. The modeling outcome demonstrates that the 2nd or 3rd order SCME methods are unable to

capture the nonlinear large deformation behavior and are thus unsuitable for modeling compliant bistable mechanisms. For the 4th-order SCME method, the overall accuracy is high and stable in the interval of angles varying from 0 to 40 degrees. However, when the beam inclined angle exceeds 40 degrees, the accuracy starts to decrease, although it can still accurately predict the force-displacement relationship in the initial region of displacements. When the order of the SCME method is increased to the 5th order, its accuracy would be much higher than the 4th-order SCME method over the full range of incined angles. The modeling results and comparison can be seen in Fig. 3.11.

The modeling error is further assessed using normalized mean absolute error (NMAE) which is a metric used to evaluate the accuracy of models [215]. NMAE is calculated by dividing the MAE by the range of the observation values. NMAE values can range from 0 to 1, with a lower value indicating a better fit. The NMAE can be formulated using Eq. 3.29:

$$\text{NMAE} = \frac{\frac{1}{N_i}\sum_{i=1}^{i=N_i}|F_i - \hat{F}_i|}{\max(F_i) - \min(F_i)}, \tag{3.29}$$

where, F_i represents the modeling results from the various modeling methods; $\hat{F}_i$ represents the observed value, which is the FEA simulation result. N_i denotes the amount of data points, corresponding to the amount of trajectory points. The NMAE has been measured for each SCME method, and the resulting data are demonstrated in Fig. 3.12.

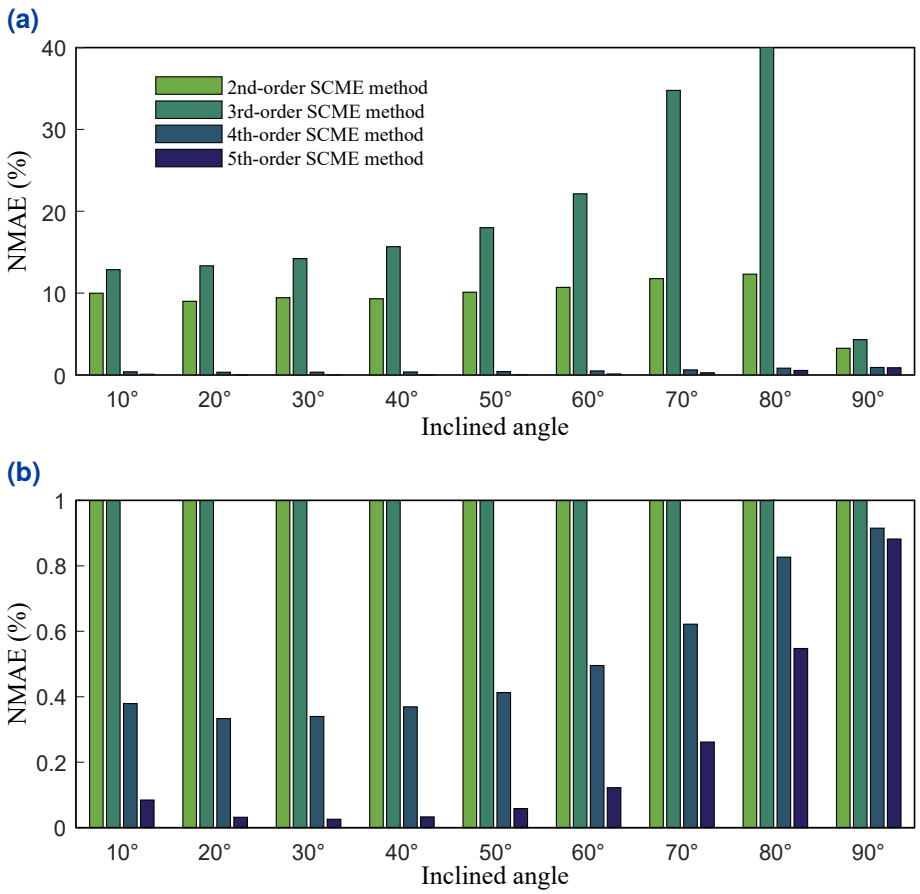


Fig. 3.12.: Modeling error comparison among 2nd-, 3rd-, 4th-, and 5th-order SCME methods. The error is measured using normalized mean absolute error. The comparison result indicates that the 5th-order SCME method is the most accurate. (a) The range of NMAE varies from 0% to 40%. (b) The range of NMAE varies from 0% to 1%.

The 5th-order SCME method has a decreasing accuracy after 40 degree but a stably high accuracy over 0 to 40 degrees. The bar chart in Fig. 3.12 confirms that the 5th-order SCME method is more accurate than the 4th-order in terms of accuracy over the range of angles. Although the NMAE is similar for the 4th order and 5th order SCME methods, the 4th order model exhibits higher accuracy in capturing extreme response values. In particular, differences become more pronounced at critical points such as the extreme minimum force and the displacement at the second stable configuration. These extreme states are key performance indicators in the analysis and design of compliant bistable mechanisms and are therefore of greater practical importance than the average error over the full deformation range. Consequently, despite the increased computational cost, the 5th order SCME model is still adopted to ensure reliable modeling. Overall, as the inclination angle increases, the accuracy decreases across all SCME methods accordingly, including 2nd, 3rd, 4th, and 5th order.

Tab. 3.6.: Computational efficiency comparison among SCME methods with distinct orders when the trajectory has 200 sampling points (N_i = 200).

Inclined angle (θ)	10°	20°	30°	40°	50°	60°	70°	80°	90°	Variable Count
2th-order SCME method	0.054	0.052	0.056	0.058	0.064	0.066	0.068	0.075	0.065	6
3th-order SCME method	0.209	0.052	0.049	0.053	0.051	0.048	0.046	0.022	0.034	7
4th-order SCME method	0.115	0.021	0.018	0.022	0.024	0.022	0.023	0.022	0.018	8
5th-order SCME method	0.075	0.074	0.079	0.081	0.085	0.096	0.105	0.111	0.097	9

The computational efficiency is measured by seconds. The computation is implemented by MATLAB R2022b.

Higher-order SCME methods generally require more computation time compared to lower-order methods. Table. 3.6 compares the computational efficiency of SCME methods at various inclined angles, using a trajectory with 200 sampling points. Table. 3.6 suggests that the 5th-order SCME method can offer the best accuracy without compromising the computational efficiency too much.

3.6.2 Comparison across modeling methods

Performing comparative analysis is crucial when proposing a novel method against existing modeling methods. In this subsection, the SCME method was compared with CBCM[108] and CPRBM[95], focusing mainly on modeling accuracy and computational efficiency.

In the SCME method, bending strain energy is modeled using a constructed continuous function of curvature, where the equilibrium configuration is obtained by minimizing the strain energy. The number of variables depends on the order of SCM, requiring i+3 variables for an i-th order SCM. Additionally, the SCME method provides explicit gradients, significantly speeding up the computation process.

For CBCM, the beam is divided into n elements, and BCM is applied to each element. CBCM can account for axial deformation and bending strain energy, making it better suited for modeling large deflection compliant mechanisms in which the beam undergoing axial deformation. Typically, CBCM accounts for $6n$ variables, encompassing load variables (F_x, F_y, M_t) and displacement variables (X, Y, θ). However, when applying CBCM to model compliant bistable mechanisms, the number of variables to be calculated reduces to $3n$: F_x, F_y and M_t). This is because the displacements are constrained, meaning that X, Y, θ serve as inputs to the model.

CPRBM, used for modeling large-deformation beams, treats each element as a rigid rod with a torsional spring attached to its end. The total strain energy is calculated by summing the strain energy stored in each torsional spring. CPRBM simplifies the modeling process compared to SCME and CBCM because all strain energy formulations are linear. The determination of minimum strain energy is based on an optimization strategy, with the number of variables being the deflection angle of each element. If the beam is divided into n elements, n variables need to be solved.

The compliant beams, with inclined angle ranging from 0 to 90 degrees, are modeled using these three methods mentioned above. Then, the obtained modeling results are compared to provide a clear visualization of modeling accuracy for each method. When modeling the beams with the CBCM and CPRBM, 10 and 20 elements are employed for each model plotting to assess the computational effort and accuracy of these models. The comparison of modeling results is illustrated in Fig. 3.13. These results are obtained separately using the 5th-order SCME method, CBCM, and CPRBM.

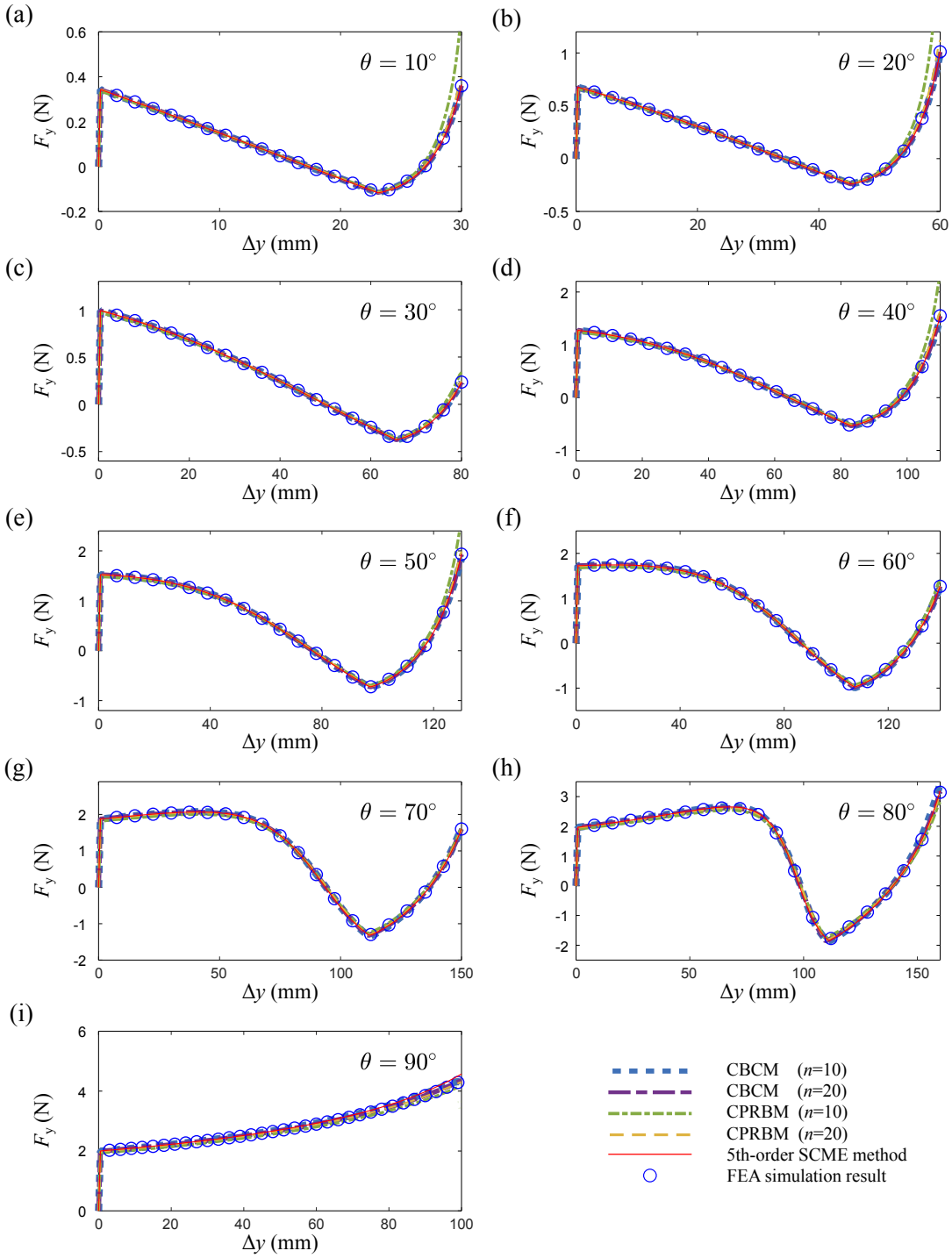


Fig. 3.13.: Force-displacement relationship comparison between 5th-order SCME method, CBCM, CPRBM, and FEA simulation. Ten and twenty beam elements are used in CBCM and CPRBM. The parameters used in modeling and simulation are: L=100mm, E=2800 MPa, W=10mm, T=0.6mm. (a) $\theta = 10°$. (b) $\theta = 20°$.(c) $\theta = 30°$. (d) $\theta = 40°$. (e) $\theta = 50°$. (f) $\theta = 60°$. (g) $\theta = 70°$. (h) $\theta = 80°$. (i) $\theta = 90°$.

The bar errors for each method can be observed in Fig. 3.14.

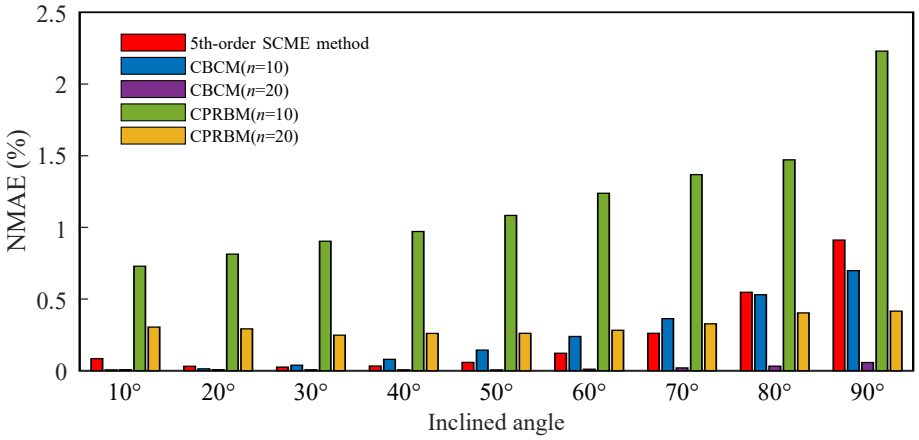


Fig. 3.14.: Modeling error comparison among the 5th-order SCME method, CBCM, and CPRBM. Ten and twenty beam elements are used in CBCM and CPRBM. The inclined angles gradually increase from 10 to 90 degrees.

The computational efficiency is measured by the computation speed of the model codes running on the same computer. The computer utilized for this research comprises a desktop equipped with an Intel Core i7-9700 3.0GHz processor, 32GB of DDR4 RAM, and an AMD Radeon RX 550 graphics card. The MATLAB version is R2022b, operating on Windows 10 enterprise edition. The running time can be seen in Table. 3.7.

Tab. 3.7.: Computational efficiency comparison between different methods when the trajectory has 200 sampling points (N_i = 200).

Inclined angle (θ)	10°	20°	30°	40°	50°	60°	70°	80°	90°	Variable Count
5th-order SCME method	0.075	0.074	0.079	0.081	0.085	0.096	0.105	0.111	0.097	9
FEA simulation	64	66	86	74	68	74	77	69	94	-
CBCM (n=10)	23.166	23.712	24.768	23.614	24.291	25.889	24.267	22.996	21.794	30
CBCM (n=20)	56.013	58.814	59.699	59.712	56.023	59.015	59.462	62.535	56.043	60
CPRBM (n=10)	11.946	11.892	11.794	11.193	11.463	11.497	11.062	10.953	10.934	10
CPRBM (n=20)	20.107	21.451	21.328	20.842	20.646	20.872	21.133	20.773	18.922	20

The computational efficiency is measured by seconds. The computation is implemented by MATLAB R2022b.

The comparison results demonstrate that the SCME method offers the advantage of the fastest modeling speed while maintaining a high level of accuracy. However, while the most accurate method is CBCM with 20 elements, the 5th-order SCME method exhibits a speed advantage of approximately 750 times faster than CBCM (n=20). The modeling speed of 5th-SCME method is fast due to two main reasons: Firstly, there are fewer variables to solve compared to CBCM, CPRBM, and FEA simulations. Secondly, the explicit gradient is provided when applying the Newton-Raphson method to solve for the approximate root. Thus, utilizing the SCME method can significantly reduce the time cost in the design and optimization of compliant mechanisms.

3.7 Basic assumptions and limitations

The limitations of the proposed high-order SCME method are discussed in the following content.

3.7.1 Plane kinetostatic modeling

For kinetostatic modeling, previous methods outlined in the literature have been reviewed, which primarily focus on plane kinetostatics for modeling mechanisms deformed in a 2D plane. Additionally, for specific applications such as MEMS, there is focus on in-plane fabrication and kinetostatics. If investigating out-of-plane deformation becomes necessary, spatial modeling technology should be considered instead of relying solely on plane modeling technology. It is essential to recognize that the current high-order SCME method lacks the capability to model spatial deformation, including spatial twist and bending, thus rendering it inadequate for spatial kinetostatic modeling.

3.7.2 Neglection of out-of-plane buckling

Out-of-plane buckling refers to the buckling behavior that occurs outside the principal deformation plane of a structure. It can result from various factors such as non-axial loads, surface defects in the beam, and material anisotropy caused by uneven material distribution. This type of buckling typically exhibits complex nonlinear characteristics, making accurate prediction challenging using mathematical methods. Many existing modeling approaches simplify analysis and design by disregarding out-of-plane buckling [108, 95, 118]. The assumption of neglecting out-of-plane buckling also applies to the SCME method.

3.7.3 Neglection of axial, shear and twist strain energy

In the process of minimizing strain energy, the optimization process is confined to bending strain energy. When modeling the post-buckling behavior of slender compliant bistable mechanisms, axial strain energy is neglected due to its small magnitude compared to bending strain energy. In the linear deformation stage, axial deformation dominates, and we compensate using Hooke's Law and the Pythagorean theorem. Shear strain energy is accounted for in modeling thick beams but ignored in slender beams. The Timoshenko-Ehrenfest beam theory, commonly used for thick beams, incorporates shear deformation

and bending effects. However, in modeling compliant bistable mechanisms, the shear effect is negligible due to the use of the slender beams. Twist strain energy is not considered in modeling compliant bistable mechanisms, as all deformations are assumed to occur within a single plane, neglecting out-of-plane effects.

3.7.4 Planar stress assumption

In this work, the modeling process relies on the planar stress assumption where the Young's modulus E of the material is adopted, as reported in most papers in the literature [216, 217, 218]. In the planar stress assumption, stress occurs only in the bending plane (XY-plane), and the beam's out-of-plane thickness W is qualitatively assumed to be small enough. Both the proposed high-order SCME method and FEA simulations utilize Young's modulus when modeling compliant bistable mechanisms.

When the out-of-plane thickness W is qualitatively large enough, the planar strain assumption should be considered, where the plate modulus $E' = E/(1-\nu^2)$ is adopted [219, 220]. In the planar strain assumption, the strain perpendicular to the bending plane is negligible.

3.8 Chapter Summary

The development of high-order SCME method offers significant practical implications and contributes to the broader field of compliant mechanism design. The proposed method, which focuses on accurate planar kinetostatic modeling with broad applicability to large deformation beams, offers new opportunities for innovative design. Additionally, the high efficiency of the SCME method, facilitated by utilizing a low-dimensional model (without discretization) and providing explicit expressions of gradients, can save substantial time in optimization processes, potentially reducing costs and increasing productivity.

Beyond its application in modeling compliant bistable mechanisms, the high-order SCME method is also employed to model and design a flexure-based constant force polishing platform, as detailed in [221]. The proposed mechanism provides a stable reaction force over a prescribed displacement range, which helps maintain consistent polishing pressure and improve surface finishing quality. This additional application further demonstrates the suitability of the high-order SCME method for analyzing and designing compliant mechanisms exhibiting large deformation and nonlinear force response.

The novelties of the proposed high-order SCME method are summarized as follows:

(1) **Accurate modeling of strongly nonlinear mechanical behavior**:
This study employs the high-order SCME method for modeling compliant bistable mechanisms, yielding accurate results for all performance characteristics including deformation shapes, forces, strain energy, and stress. Furthermore, these results have been validated through FEA simulations and experimental tests.

(2) **Efficient modeling**:
Benefiting from the continuous smooth curvature model (without discretization), deriving bending strain energy, along with offering an explicit expression of the gradient of Lagrange function during the root-finding process, the SCME method enables quick/efficient modeling. This approach is comprehensively compared with FEA simulations, CBCM, and CPRBM. The comparison results prove that the modeling speed is much quicker without compromising modeling accuracy.

(3) **Applicability in full angle range**:
The high-order SCME method (5th order) is capable of modeling compliant bistable mechanisms with varying inclined angles from 0 to 90 degrees without the need for discretization. This feature simplifies the process of modeling the compliant beams.

The high-order SCME method does not extend the design space itself, but provides a more accurate and robust modeling framework within the existing design space, particularly for compliant bistable mechanisms undergoing large deformation. Moreover, its computational efficiency enables faster design iteration and significantly improves the efficiency of structural optimization. The proposed high-order SCME method enables accurate kinetostatic modeling, providing engineers with reliable insights into the nonlinear behavior of compliant mechanisms, which is essential for performance optimization and reliability assessment in precision engineering applications. Furthermore, the proposed method shows potential for modeling nonlinear energy behavior in lattice based mechanical metamaterials, such as transition wave phenomena. By capturing the complex interactions within these materials, the proposed modeling framework contributes to the development of artificial mechanical metamaterials with programmable properties and functionalities.

4

Comprehensive SCME: Enhanced High-order SCME considering Axial Deformation

Although the high-order SCME has proven effective for modeling compliant bistable mechanisms, it still has several limitations that motivate further development. One major limitation is that the SCME neglects axial deformation, reducing accuracy when beams undergo large axial deformations. While this simplification causes negligible errors in cases of small deformation, it becomes significant under large deformation conditions, resulting in inaccurate predictions of the nonlinear behavior of mechanisms, such as the pre-buckling stage in compliant bistable mechanisms, as discussed previously in Chapter 3. Another limitation is that the SCME has primarily been applied to compliant bistable mechanisms, highlighting its capability to handle strong nonlinearities, but its potential applicability to a broader range of scenarios remains unexplored.

Therefore, this chapter aims to address the limitations of the previous high-order SCME by introducing an enhanced modeling approach termed the Comprehensive energy method based on the smooth curvature model (CoSCME), applicable to diverse planar compliant mechanisms. The CoSCME significantly extends the original SCME by incorporating both bending and axial deformations and explicitly accounts for the coupling effects between these deformation modes by integrating axial elongation into the bending deformation analysis. Both axial and bending deformations are modeled using Legendre polynomial fitting, where curvature is fitted for bending deformation and axial strain for axial deformation. Equilibrium configurations are determined by minimizing the total strain energy within an optimization framework, subject to appropriate boundary conditions. To demonstrate its broad applicability, the CoSCME is applied to various compliant mechanisms, including beams subjected to compresural or tensural displacement loads, translational and rotational bistable mechanisms, general lumped-compliance beams, and initially curved beams. The primary contributions of this work are summarized in Fig. 4.1.

The structure of this chapter is organized as follows: section 4.1 introduces the detailed modeling framework of planar compliant mechanisms using CoSCME, emphasizing its capability to incorporate both bending and axial deformations. Section 4.2 presents various case studies, demonstrating the applicability of CoSCME in modeling different types of compliant mechanisms, including compresural beams, tensural beams, bistable mechanisms, general lumped-compliance beams, and initially curved beams. Section 4.3 conducts detailed discussion on the modeling results and provides an comparison analysis among different modeling methods. Finally, section 4.4 summarize the findings and potential future directions of this work.

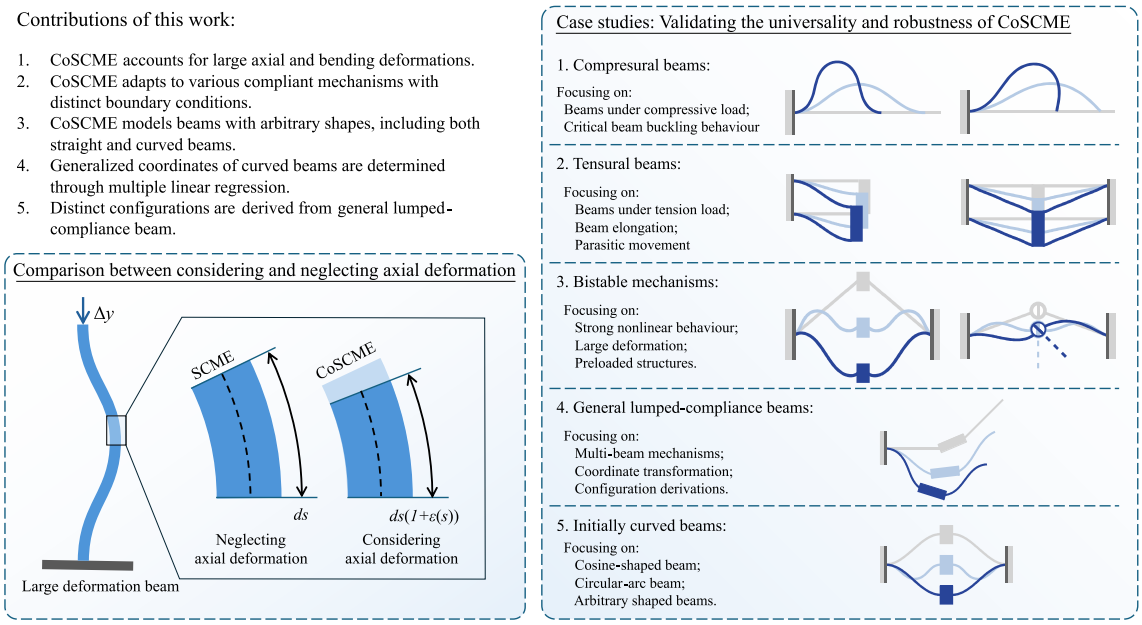


Fig. 4.1.: Overview of this chapter: Proposal of the CoSCME method with additional consideration of axial deformation, enhancing modeling accuracy and comprehensiveness; validation of the universality and robustness of the proposed method through various case studies.

4.1 Formulation of CoSCME

Drawing from the limitations of the high-order SCME method outlined in the previous chapter, enhancing the high-order SCME by incorporating axial strain energy is crucial for expanding its application scenarios. Inspired by the modeling method proposed in [222], which accounted for axial deformation in the modeling process, further enhancements to the high-order SCME are detailed in the following content.

Similarly to fitting the curvature function using shifted Legendre polynomials, as in Eq. (3.2), the axial deformation is also fitted based on Legendre polynomials. Utilizing

Legendre polynomials as a basis offers the advantages of global approximation and possesses orthogonality and normalization properties. Therefore, models based on Legendre polynomials are well-suited for numerical computations. Furthermore, adjusting the order of Legendre polynomial basis provides flexibility in balancing modeling accuracy and computational efficiency.

In the high-order SCME, constraints are applied at the beam tip. In the present modeling methodology, a more general form of position constraint is provided, which applies position constraints to an arbitrary point P_s. The arc length from the fixed end of beam to the point P_s is s. The definition of terminologies can be found in Fig. 4.2. The coordinates and deflection angle of point P_s^* on the initial shape of the beam are denoted as (x_s^*, y_s^*, ϕ_s^*). When adding position constraint to point P_s^*, the compliant beam deforms, and the position and deflection angle of point s are transformed to (x_s, y_s, ϕ_s). When $s = L$, the displacement is exerted on the beam tip. The reaction force is the force generated by the deformed structure to maintain equilibrium configuration. The force/moment derived from CoSCME is the reaction force/moment. When the position constraint is exerted on point P_s, the reaction forces and reaction moment at point P_s are denoted as F_x, F_y, and M_s.

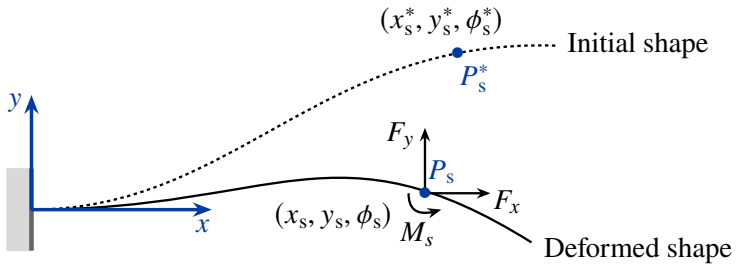


Fig. 4.2.: Terminologies employed in the CoSCME.

4.1.1 Fitting axial deformation with Legendre polynomials

In the previous high-order SCME formulation, the beam curvature was expressed using the generalized coordinates α in conjunction with shifted Legendre polynomials. This approach effectively fits the beam curvature. To further incorporate axial deformation, a similar construction method is applied. Specifically, a new set of generalized coordinates, β, is introduced to construct an expression for the axial strain, maintaining consistency with the formulation used for the beam curvature. To ensure the accuracy and efficiency of the proposed CoSCME, the selection of the appropriate order of polynomials becomes crucial. In previous work [124], the impact of polynomial order on model accuracy was thoroughly examined. The results of this comparison indicated that higher-order models yield greater accuracy. However, the use of higher-order polynomials also introduces

increased complexity in the derivation processes and formulations. As a result, the 5^{th}-order polynomials were determined to be the optimal choice for balancing accuracy and complexity. Similarly, in the present study, the CoSCME method is based on the same modeling foundation as the high-order SCME. Therefore, we adopt the 5^{th} order polynomial for the CoSCME method as well. The axial strain ε_{a} is thus formulated in Eq. (4.1):

$$\begin{aligned}\varepsilon_{\mathrm{a}}(\boldsymbol{\beta}, s) &\approx \sum_{n=0}^{n=N} \beta_n \psi_n(s) \\ &= \beta_0 + \beta_1\left(\frac{2s}{L} - 1\right) + \beta_2\left(\frac{6s^2}{L^2} - \frac{6s}{L} + 1\right) \\ &\quad + \beta_3\left(\frac{20s^3}{L^3} - \frac{30s^2}{L^2} + \frac{12s}{L} - 1\right) \\ &\quad + \beta_4\left(\frac{70s^4}{L^4} - \frac{140s^3}{L^3} + \frac{90s^2}{L^2} - \frac{20s}{L} + 1\right) \\ &\quad + \beta_5\left(\frac{252s^5}{L^5} - \frac{630s^4}{L^4} + \frac{560s^3}{L^3} - \frac{210s^2}{L^2} + \frac{30s}{L} - 1\right),\end{aligned} \tag{4.1}$$

where, $\boldsymbol{\beta}_n$ are generalized coordinates used for formulating axial strain, L is the beam length. The n-th order shifted Legendre polynomials in interval $[0, 1]$ are denoted by $\psi_n(s)$. The accumulated axial deformation of the beam segment from the fixed root to point P_{s} can be derived by integrating the axial strain, denoted as ΔL_{s}. The formulation of this accumulated axial deformation in the beam segment is expressed in Eq. (4.2):

$$\begin{aligned}\Delta L_{\mathrm{s}}(\boldsymbol{\beta}, s) &= \int_0^s \varepsilon_{\mathrm{a}}(\boldsymbol{\beta}, s) ds \\ &= \beta_0 s + \beta_1\left(\frac{s^2}{L} - s\right) + \beta_2\left(\frac{2s^3}{L^2} - \frac{3s^2}{L} + s\right) \\ &\quad + \beta_3\left(\frac{5s^4}{L^3} - \frac{10s^3}{L^2} + \frac{6s^2}{L} - s\right) \\ &\quad + \beta_4\left(\frac{14s^5}{L^4} - \frac{35s^4}{L^3} + \frac{30s^3}{L^2} - \frac{10s^2}{L} + s\right) \\ &\quad + \beta_5\left(\frac{42s^6}{L^5} - \frac{126s^5}{L^4} + \frac{140s^4}{L^3} - \frac{70s^3}{L^2} + \frac{15s^2}{L} - s\right).\end{aligned} \tag{4.2}$$

The accumulated axial deformation along entire beam is denoted as ΔL_{tip}.The formulation is expressed in Eq. (4.3):

$$\Delta L_{\text{tip}} = \int_0^L \varepsilon_{\text{a}}(\boldsymbol{\beta}, s) ds = \beta_0 L. \tag{4.3}$$

The aforementioned content introduces the fitting process of axial strain and accumulated axial deformation. The following sections demonstrate the procedure for incorporating axial deformation into the original high-order SCME, and the approach to dealing with coupling effect between axial and bending strain.

4.1.2 Deriving coordinates and deflection angle

In the original high-order SCME, the coordinates and inflection angle of point s are derived from the integration of beam curvature, as demonstrated in Eqs. (2.34) (2.35) and (2.36). However, when considering axial deformation, the formulations of inflection angle at point s need to be updated by extending the interval of integration from $[0, s]$ to $[0, s + \Delta L_{\text{s}}(\boldsymbol{\beta}, s)]$. Additionally, the integrand needs correction when accounting for the coupling effect among axial and bending deformation. The revised function of deflection angle at point s, based on Eq. (2.32), is formulated in Eq. (4.4):

$$\phi_s(\boldsymbol{\alpha}, \boldsymbol{\beta}, s) = \int_0^{s+\Delta L_{\text{s}}(\boldsymbol{\beta},s)} \omega(\boldsymbol{\alpha}, s) \left[1 + \varepsilon_{\text{a}}(\boldsymbol{\beta}, s)\right] ds, \tag{4.4}$$

where, $\omega(\alpha, s)$ represents the beam curvature as a function of the generalized coordinates α and the position s along the neutral axis. Then the coordinates of point s can be further derived by integrating the inflection angle along the beam. The formulation can be seen as in Eqs. (4.5) and (4.6):

$$x_s(\boldsymbol{\alpha}, \boldsymbol{\beta}, s) = \int_0^{s+\Delta L_{\text{s}}(\boldsymbol{\beta},s)} \cos\left[\phi_s(\boldsymbol{\alpha}, \boldsymbol{\beta}, s)\right] ds, \tag{4.5}$$

$$y_s(\boldsymbol{\alpha}, \boldsymbol{\beta}, s) = \int_0^{s+\Delta L_{\text{s}}(\boldsymbol{\beta},s)} \sin\left[\phi_s(\boldsymbol{\alpha}, \boldsymbol{\beta}, s)\right] ds. \tag{4.6}$$

At this stage, the formulation for the coordinates and deflection angle of point s has been derived. Subsequently, the focus shifts to constructing the formulation of strain energy, which serves as the objective function of optimization.

4.1.3 Formulating the strain energy function

According to the principle of minimum strain energy, the equilibrium configuration is found when the strain energy is minimized. Therefore, to determine the equilibrium configuration, it is necessary to formulate the total strain energy, which encompasses both bending and axial strain energies, and find its minimum value. The formulation of bending strain energy is shown in Eq. (3.7). The axial strain energy U_{a} is formulated in Eq. (4.7) based on the elastic strain theory [223].

$$U_{\mathrm{a}}(\boldsymbol{\beta}) = \frac{EA}{2}\int_0^L \varepsilon_a(\boldsymbol{\beta}, s)^2 ds = \frac{EAL}{2}\left(\beta_0^2 + \frac{\beta_1^2}{3} + \frac{\beta_2^2}{5} + \frac{\beta_3^2}{7} + \frac{\beta_4^2}{9} + \frac{\beta_5^2}{11}\right). \tag{4.7}$$

Hence, the expression of total strain energy is formulated in Eq. (4.8):

$$\begin{aligned} U(\boldsymbol{\alpha}, \boldsymbol{\beta}) = {} & \frac{EI}{2L}\left(\alpha_0^2 + \frac{\alpha_1^2}{3} + \frac{\alpha_2^2}{5} + \frac{\alpha_3^2}{7} + \frac{\alpha_4^2}{9} + \frac{\alpha_5^2}{11}\right) \\ & + \frac{EAL}{2}\left(\beta_0^2 + \frac{\beta_1^2}{3} + \frac{\beta_2^2}{5} + \frac{\beta_3^2}{7} + \frac{\beta_4^2}{9} + \frac{\beta_5^2}{11}\right). \end{aligned} \tag{4.8}$$

4.1.4 Identifying kinetostatic modeling

In this subsection, the strain energy minimization progress is described in the framework of optimization. The objective of the optimization is to find the minimum of the strain energy $U(\boldsymbol{\alpha}, \boldsymbol{\beta})$, in order to determine the equilibrium configuration of the compliant beams. The decision variables in the optimization are the generalized coordinates $\boldsymbol{\alpha}$ and $\boldsymbol{\beta}$. The domain of the decision variables belongs to the set of real numbers $\mathbb{R}$. The constraint of the optimization problem is to ensure that the coordinates and deflection angle of point s are equal to the given coordinates and deflection angle. The optimization process is performed using the *fmincon* function in MATLAB with the *'interior-point'* algorithm, which is well-suited for large-scale nonlinear constrained optimization problems. The solver is configured to ensure efficient computation and reliable convergence. To reduce unnecessary printing and improve computational efficiency, the *display* option is set to *'off'*. The maximum number of function evaluations (*MaxFunEvals*) is set to 1×10^6,

allowing extensive exploration of the solution space. The step tolerance (*StepTolerance*) and optimality tolerance (*OptimalityTolerance*) are specified as 1×10^{-10}, ensuring that the optimization process achieves a satisfactory level of precision in determining the minimum strain energy. The constraint tolerance (*ConstraintTolerance*) is set to 1×10^{-12}, enforcing stringent satisfaction of nonlinear constraints. Analytical gradients are not provided because the complexity of the analytical expressions makes their inclusion inefficient. The mathematical expression of the optimization objective is demonstrated in Eq. (4.9).

$$\begin{aligned} \underset{\boldsymbol{\alpha},\, \boldsymbol{\beta} \in \mathbb{R}}{\text{minimize}} \quad & U(\boldsymbol{\alpha}, \boldsymbol{\beta}) \\ \text{subject to} \quad & x_s^*(\boldsymbol{\alpha}, \boldsymbol{\beta}, s) = x_\mathrm{g}, \\ & y_s^*(\boldsymbol{\alpha}, \boldsymbol{\beta}, s) = y_\mathrm{g}, \\ & \phi_s^*(\boldsymbol{\alpha}, \boldsymbol{\beta}, s) = \phi_\mathrm{g}, \\ & 0 < s \leq L. \end{aligned} \tag{4.9}$$

Then, the generalized coordinates can be determined by solving this optimization problem.

4.1.5 Post-processing

After obtaining the generalized coordinates corresponding to stable configurations, the next step is to post-process the complex nonlinear behavior of compliant mechanisms. This post-processing involves deriving the deformation shape of the slender beam, calculating the corresponding applied force, and determining the bending and axial stresses.

- **Deformation shape**

  Deriving the deformation shape is crucial for visualizing the nonlinear behavior of compliant beams. One straightforward approach to visualize this deformation is by calculating the positions of points along the beam.

  Specifically, deriving the deformation shape requires the prior determination of generalized coordinates ($\boldsymbol{\alpha}$ and $\boldsymbol{\beta}$) relative to the equilibrium configuration. Then, based on Eqs. (4.5) and (4.6), the node positions of each subbeam can be determined. By selecting a sufficient number of points along the beam, the deformation shape

can be represented by connecting these points with straight lines. This allows the neutral line of the deformed compliant beam to be identified. The representation of beam thickness depends on the specific requirements of the analysis.

- **Reaction force**

Aside from interpreting the nonlinear behavior through deformation, another critical aspect is the nonlinear force-displacement relationship. Establishing this relationship is essential in the design and modeling of compliant mechanisms as it allows for accurate prediction of their force-displacement response, ensuring the mechanism functions as intended. This relationship is also key in design parameter optimization to improve overall performance. Furthermore, precise modeling of force-displacement relationship guarantees the controllability and precision of the mechanism, which is crucial for high-precision applications. It also assists in the selection of suitable materials and geometric configurations, facilitating the optimal design of compliant mechanisms that meet specific performance criteria.

When the optimization problem is solved using '*fmincon*', the output includes the values of '*lambda*', which are the Lagrange multipliers obtained from the optimization. These lambda values represent the forces or moments corresponding to the applied constraints, depending on the type of constraint. The interpretation of these Lagrange multipliers has been proved in previous work in [124].

When the beam is subjected to multiple position constraints, the derived forces/moments correspond to each other. For example, if position constraints $(x_{\text{tip}}(\boldsymbol{\alpha}, \boldsymbol{\beta}, L) = x_{\text{g-tip}}, y_{\text{tip}}(\boldsymbol{\alpha}, \boldsymbol{\beta}, L) = y_{\text{g-tip}})$ are applied at the beam tip and another set of position constraints $(x_{\text{mid}}(\boldsymbol{\alpha}, \boldsymbol{\beta}, L/2) = x_{\text{g-mid}}, y_{\text{mid}}(\boldsymbol{\alpha}, \boldsymbol{\beta}, L/2) = y_{\text{g-mid}})$ is applied at the middle of the beam, the obtained lambda values sequentially represent the forces corresponding to each constraint, i.e., $F_{x-\text{tip}}, F_{y-\text{tip}}, F_{x-\text{mid}}, F_{y-\text{mid}}$ at their corresponding positions.

- **Stress evaluation**

The CoSCME accounts for axial deformation, providing an advantage over the original high-order SCME by being capable of deriving axial stress, which allows for better evaluation of the maximum stress and further helps avoid structural failure.

For a beam subjected solely to bending deformation, the maximum stress at point P_s occurs at the outermost fiber of the beam, as shown in Eq. (4.10).

$$\sigma_b(s) = \frac{ET\omega(\boldsymbol{\alpha}^*, s)}{2}, \tag{4.10}$$

where, the beam in-plane thickness is denoted by T. Since the axial strain is considered in the model, the axial/normal stress can be directly evaluated using the linear stress-strain relationship, as shown in Eq. (4.11).

$$\sigma_a(s) = E\varepsilon_a(\boldsymbol{\beta}^*, s) \tag{4.11}$$

Hence, when evaluating the maximum stress for avoiding structural failure, the stress will not exceed the boundary $\sigma_{\max}$ defined in Eq. (4.12).

$$\sigma_{\max} = |\sigma_b(s)|_{\max} + |\sigma_a(s)|_{\max}, \tag{4.12}$$

where, the maximum absolute value of bending stress and axial stress are denoted by $|\sigma_b(s)|_{\max}$ and $|\sigma_a(s)|_{\max}$.

In summary, this section presented the integration of axial strain into the SCME, leading to the development of the CoSCME approach. The construction and solution of the optimization problem were also discussed. Additionally, post-processing methods were introduced to derive the deformation shape, applied forces, and stress. The following section presents several case studies to validate the wide applicability of the CoSCME.

4.2 Case studies

Several representative compliant mechanisms are analyzed and modeled using the CoSCME in this section, which were not studied in the SCME in previous work [124]. By modeling diverse compliant mechanisms, the modeling performance across various application scenarios can be comprehensively assessed. The selected case studies include compresural beams, tensural beams, bistable mechanisms, general lumped-compliance beams, and initially curved beams. These cases exhibit differences in structural complexity and

boundary conditions, allowing for a comprehensive evaluation of the modeling applicability in various scenarios. The structure type, research focus and study objectives of each case study are summarized in Table. 4.1.

Tab. 4.1.: Overview of case studies covering various application scenarios, all presented in the following section. Each case is introduced with its structure type, along with the corresponding research focus and study objectives.

Structure type	Research focus	Study Objectives
Compresural beam	Beams under compressive load; Critical beam buckling;	• Assessing the capability of modeling beams under compressural loads. • Focusing on the critical buckling condition. Modeling results are validated using Euler's critical load.
Tensural beam	Beam under tensural load; Beam elongation; Parasitic movement	• Assessing the capability of modeling beams under tensural loads, including nonlinear reaction, beam elongation and parasitic movement. • Investigating the nonlinear response of basic parallelogram mechanisms and compound basic parallelogram mechanisms.
Bistable mechanism	Strong nonlinear behavior; Large deformation; Preloaded structures	• Demonstrating the capability to capture complex nonlinear responses of bistable mechanisms under large deformations. • Validating the accuracy of CoSCME in predicting snap-through behavior and force-displacement relationships. • Applying the method to analyze the nonlinear behavior of preloaded structures.
General lumped-compliance beam	Multi-beam mechanisms; Coordinate transformation; Configuration derivations	• Exploring CoSCME's ability to model serially connected beams with rigid connections. • Revealing the potential capacity for modeling complex structures involving multiple beams. • Validating the universality and robustness by modeling various distinct configurations of general lumped-compliance beams.
Initially curved beam	Cosine-shaped beam; Circular-arc beam; Arbitrary shaped beam	• Introducing the application of CoSCME in modeling cosine-shaped beams and circular-arc beams. • Proposing a modeling method for arbitrarily shaped beams based on multiple linear regression. • Evaluating and analyzing the fitting accuracy of multiple linear regression results with various amounts of sampling points.

In the following text, all material properties are theoretically assumed and are not specific to any particular material. Since material nonlinearity is not considered, the Young's modulus E is set to 2800 MPa in all subsequent modeling. The Poisson's ratio used in

the modeling is 0.35. For straight beams, the geometric parameters are fixed, with their definitions provided in Fig. 4.3. The geometric parameters for curved beams are redefined in later content.

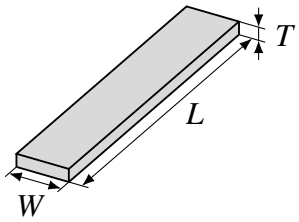


Fig. 4.3.: Definition of geometric parameters: L is the beam length, W is the beam width, and T is the beam thickness. In the following case studies involving initially straight beams, all beams are defined with $L = 100\text{mm}$, $W = 10\text{mm}$, $T = 0.8\text{mm}$.

Besides, the modeling errors are measured by normalized relative error (e_n). This criteria reduces the risk of error amplification caused by singular values in the data. For example, relative errors near zero can be greatly magnified, even when the original error is relatively small. The formulation of normalized relative error is evaluated by Eq. 4.13:

$$e_n = \frac{|F_i - \hat{F}_i|}{\max(\hat{F}_i) - \min(\hat{F}_i)}, \tag{4.13}$$

where, F_i represents the modeling results derived from the CoSCME; $\hat{F}_i$ represents the reference value, which is the FEA simulation result. To further analyze the error distribution, error bands are incorporated into the result figures. The error band is defined as a region surrounding the modeling result. The upper and lower boundaries of the error band (e_b) represent the magnitude of the modeling error in comparison with FEA simulations. The usage of the error band facilitates a clearer visualization of the modeling error distribution. The boundaries of the error band (e_b) are determined using the following Eq. (4.14):

$$e_b = F_i \pm |F_i - \hat{F}_i| \cdot A_c, \tag{4.14}$$

where A_c is the amplification coefficient, introduced to magnify the error and enhance the clarity of error distribution in the plots. The error band is shaded in light blue in the figures, and the amplification coefficient is indicated in each plot.

The FEA simulation was conducted in Strand7 R2.4.4 using the nonlinear static analysis solver, which accounts for geometric nonlinearity while ignoring material nonlinearity.

This solver employs the Newton-Raphson method to iteratively resolve the equilibrium equations. Convergence is defined when the displacement is lower than 1×10^{-10} mm, with the displacement norm tolerance set to 1×10^{-10} mm. The maximum iteration count is 50. To avoid singularities and improve numerical stability, the sub-step function was activated, incrementally scaling the loads to ensure stable convergence.

The 2D simulations are based on a beam element model. As demonstrated in chapter 3, subdividing beam elements into 100 segments ensures results converge to the fourth decimal place, achieving sufficient accuracy. Accordingly, all beams in this study were discretized into 100 segments. Material properties and boundary conditions were tailored to each case study.

To assess the accuracy of these 2D FEA simulations, 3D FEA serves as an ideal benchmark, since it captures spatial deformations and stress distributions more comprehensive. For 3D simulations, geometries were first modeled in SolidWorks and imported into Strand7. The AutoMesh function converted these geometries into solid elements using Quad4 (4-node quadrilateral) elements, with a maximum edge length constraint of 2% of the beam length. Material properties matched those used in the 2D model. Boundary constraints were applied to the beam's end face, and a displacement-driven analysis was performed. The total reaction force was extracted as the sum of nodal forces on the constrained surface. As same with the 2D simulations, the convergence criterion is defined as the displacement being lower than 1×10^{-10} mm.

A comparison between 2D and 3D FEA simulations is conducted, and the results are illustrated in Fig. 4.4. The presented results are obtained from simulating the nonlinear behavior of compound basic parallelogram mechanisms (CBPMs), which were chosen due to their significant axial deformation during the deformation process. A basic introduction to CBPMs can be found in case study 2 in section 4.2.2. All geometric parameters, material properties, and boundary conditions are consistent. Despite some discrepancies between the 2D and 3D simulation results, the errors fall within an acceptable range (with $e_{\mathrm{n}} < 1\%$). Thus, the comparative analysis confirms the reliability of 2D simulations.

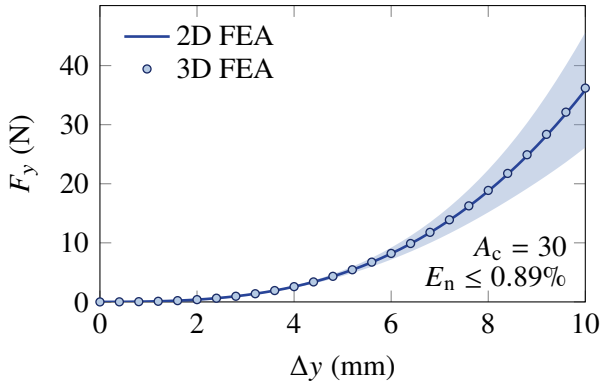


Fig. 4.4.: Comparison of 2D and 3D FEA simulation results for CBPMs under nonlinear static loading. The 2D model uses beam elements with 100 segments per beam, while the 3D model employs Quad4 elements with a maximum edge length of 2% of the beam length. Both models share consistent material properties and boundary conditions.

3D FEA simulations are computationally more expensive than 2D FEA simulations due to several factors. First, 3D simulations involve a higher number of degrees of freedom (DOF) per node, resulting in a larger system of equations to solve. Additionally, accurately capturing 3D geometries requires a finer mesh, which increases the number of elements and nodes, raising both memory usage and computational time. The calculation of element stiffness matrices is also more complex in 3D, demanding more processing power. Furthermore, nonlinearities and longer convergence times contribute to the computational burden, making 3D simulations much more resource-intensive.

When comparing computational efficiency, 2D and 3D simulations show significant differences. Although both simulations use the same number of load steps (50), the computational scale of the 3D simulation is much larger: the number of equations increases from 594 in 2D to 3861 in 3D, and the number of nodes rises from 101 to 1327. This increased complexity results in a significant rise in computational time, with the 3D simulation taking 34.750 seconds compared to only 8.766 seconds for the 2D simulation. Clearly, the 3D simulation is far less efficient due to its higher degrees of freedom and more complex mesh discretization.

Additionally, it is important to note that the proposed CoSCME is based on several key mechanical assumptions. Firstly, the cross-section of a beam remains planar after deformation, with no warping. Secondly, the cross-section stays perpendicular to the beam's neutral axis. Furthermore, any in-plane distortion of the cross-sections post-deformation is disregarded. These assumptions are generally valid for isotropic, homogeneous, slender

beams with simple cross-sections. Besides, the proposed CoSCME is only applicable to slender beams instead of short or thick beams.

Moreover, the CoSCME relies on the plane stress assumption, which states that a solid element, infinitesimal in size, only experiences stress in the x and y directions, parallel to the coordinate axes, while no stress is present in the z direction. When modeling compliant mechanisms using CoSCME, the material adheres to the linear elasticity assumption, i.e. Hooke's law. In linear elasticity, stress and strain share a linear relationship: the material deforms under load and returns to its original shape once the load is removed. In addition, the proposed CoSCME neglects the Poisson effect and thermal effects. Under large deformations, material nonlinearity becomes significant, reducing model accuracy. For materials with nonlinear responses, such as plasticity in metals or hyper-elasticity in rubbers, the stress-strain relationship deviates from linearity, leading to discrepancies in predicted mechanical responses.

In the following case studies, a color representation is used in the deformation plots, where gray represents the initial beam configuration, light blue indicates the intermediate shape, and dark blue signifies the fully deformed state. This representation enhances clarity and facilitates understanding of the deformation behavior. Please refer to the colored PDF version for optimal visualization.

4.2.1 Case study 1: Compresural beams

In this subsection, the proposed CoSCME is used to model two classical beam large deformation behaviors with different end constraint conditions, i.e. the fixed-fixed beam and fixed-pinned beam. Under ideal conditions, a perfectly straight beam subjected only to axial load would deform axially without bending. Nevertheless, beams in real-world scenarios often have initial imperfections due to manufacturing errors and material nonuniformity. These imperfections cause the beam to bend under compressive load. Neglecting these imperfections would prevent the beam from buckling and lead to exclusively axial shrinkage.

Beam buckling is a structural instability phenomenon that typically occurs in slender members, such as beams or columns, under compressive load. Specifically, when the compressive force exceeds the critical load, the beam may suddenly bend or twist instead of continuing to deform axially. When modeling beam buckling behavior, the linear

deformation prior to beam buckling cannot be accurately captured if the model only considers bending deformation while neglecting axial deformation. Hence, the high-order SCME, which considers only bending deformation, fails to accurately capture the pre-buckling behavior and can only model it using linear compensation. Therefore, applying a model that considers both bending and axial deformation is crucial for modeling instability problems. The CoSCME is capable of addressing this challenge efficiently.

To better simulate real-world scenarios, a small artificial offset is introduced into the model to simulate these initial imperfections. These offsets are typically very small but can induce buckling instability under critical loads without significantly altering the post-buckling behavior of beams [224]. For the fixed-fixed beam, the artificial offsets are typically added at the beam tip in the form of deflection angle, denoted as e_θ. Meanwhile, for the fixed-pinned beam, the artificial offset is usually applied to the translational displacement in the y-direction, denoted as e_y. The objective function of the optimization problem when dealing with the buckling problem can be summarized in Eq. (4.15) and Eq. (4.16).

For fixed-fixed beam:

$$\begin{aligned} \underset{\boldsymbol{\alpha},\,\boldsymbol{\beta}\,\in\,\mathbb{R}}{\text{minimize}} \quad & U(\boldsymbol{\alpha},\boldsymbol{\beta}) \\ \text{subject to} \quad & x_s(\boldsymbol{\alpha},\boldsymbol{\beta},s) = L - \Delta x, \\ & y_s(\boldsymbol{\alpha},\boldsymbol{\beta},s) = 0, \\ & \phi_s(\boldsymbol{\alpha},\boldsymbol{\beta},s) = e_\theta, \\ & s = L. \end{aligned} \tag{4.15}$$

For fixed-pinned beam:

$$\begin{aligned} \underset{\boldsymbol{\alpha},\,\boldsymbol{\beta}\,\in\,\mathbb{R}}{\text{minimize}} \quad & U(\boldsymbol{\alpha},\boldsymbol{\beta}) \\ \text{subject to} \quad & x_s(\boldsymbol{\alpha},\boldsymbol{\beta},s) = L - \Delta x, \\ & y_s(\boldsymbol{\alpha},\boldsymbol{\beta},s) = e_y, \\ & s = L, \end{aligned} \tag{4.16}$$

where, Δx is the displacement along x axis. The direction of Δx is marked in Fig. 4.5.

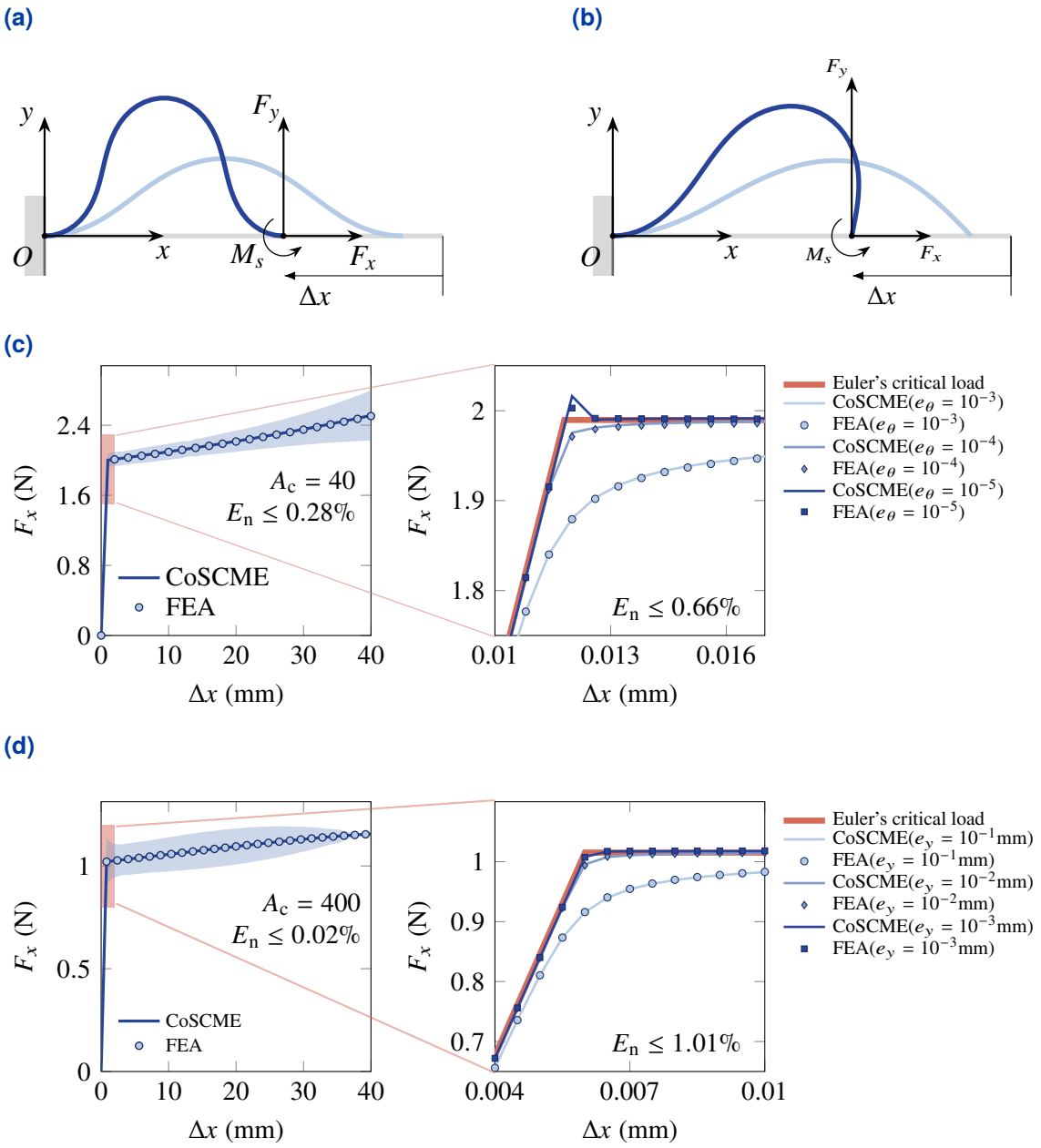


Fig. 4.5.: Modeling result of fixed-fixed beam and fixed-pinned beam. (a) Fixed-fixed beam. (b) Fixed-pinned beam. (c) F_x-Δx curve for fixed-fixed beam. (d) F_x-Δx curve for fixed-pinned beam.

Furthermore, in classical mechanics of materials, Euler-Bernoulli beam theory serves as a important fundamental concept for analyzing the stability and buckling behavior of beams. The expression for the critical buckling load can be simplified as in Eq. (4.17).

$$P_{cr} = \frac{\pi^2 EI}{(KL)^2}, \tag{4.17}$$

where, P_{cr} represents the critical longitudinal compression load. When the applied load exceeds this critical value, the beam begins to buckle. The effective length factor is denoted as K and its value depends on the constraint conditions applied to the beam. For a fixed-fixed beam, K is 0.5, whereas for a fixed-pinned beam, K is 0.7 [225]. Based on the critical buckling load and incorporating with Hooke's law, the critical buckling axial deformation Δx_{cr} can be calculated by solving Eq. (4.18).

$$\Delta x_{cr} = \frac{P_{cr} L}{EA} = \frac{\pi^2 T^2}{12 K^2 L}, \tag{4.18}$$

The critical Euler buckling load serves as a reference to evaluate the accuracy of the proposed CoSCME. Besides, FEA simulation, as a highly accurate numerical modeling approach, is also used to validate the accuracy of the proposed modeling method. The beam tip constraint is set according to the objective function (4.15) and (4.16). The modeling result and accuracy validation can be found in Fig. 4.5. The right part of Fig. 4.5 (c) and (d) zooms in on the results, providing more details around the critical buckling point. As can be found in the result comparison, the modeling results demonstrate remarkable agreement with FEA simulation results when different artificial error e_θ and e_y are applied to the beam tip. In addition, the comparison results demonstrate the capability of accurately modeling the behavior of compresural beams.

As demonstrated in this case study, even minor initial imperfections can lead to variations in structural response, highlighting the influence of geometric deviations (e.g., beam length, thickness, and curvature), material properties, assembly errors, and surface treatment. These imperfections can significantly impact the reliability, fatigue resistance, and overall structural behavior of compliant mechanisms. Given that the functionality of compliant mechanisms relies on elastic deformation, small defects in geometry or material may result in noticeable performance differences. These imperfections are inherently present in real-world fabrication processes and are often difficult to predict. This study focuses on modeling compliant mechanisms under theoretical conditions; therefore, manufacturing imperfections are not considered in the proposed CoSCME.

4.2.2 Case study 2: Tensural beams

Basic parallelogram mechanisms (BPMs) are fundamental compliant components applied in many designs of mechanism. These mechanisms typically consist of two compliant slender beams, with one end fixed and the other end connected to a moving shuttle. BPMs are capable of performing single-direction translational movement while eliminating parasitic

rotational motion due to their unique geometric layout. Consequently, parallelogram mechanisms are commonly used in high-precision x-y translational positioning platforms and guiding mechanisms, as their utilization can minimize the adverse effects of rotational movement. In addition to the rotational parasitic motion, there is another type of translational parasitic motion that is perpendicular to the direction of motion. This parasitic motion can be eliminated by combining two BPMs. The resulting combined structure is known as compound basic parallelogram mechanisms (CBPMs).

For a theoretical scenario that neglects beam axial deformation, the compliant beams in CBPMs are fully constrained and thus cannot deform. Therefore, mathematical models neglecting axial deformation, such as the high-order SCME, cannot be applied to analyze the nonlinear behavior of CBPMs. Consequently, enhancing the original SCME by considering axial deformation is important, as it makes the method more universally applicable to multiple scenarios. The modeling of BPMs and CBPMs can be achieved by modeling single beam with specific position constraints and then linearly superimpose the obtained modeling results according to the amount of flexible beams and layout. The objective function of modeling BPMs and CBPMs are shown in Eq.(4.19) and Eq.(4.20). Due to the neglect of tensile fractures and material nonlinearity in the CoSCME, the beams can theoretically elongate and shrink infinitely.

For basic parallelogram mechanisms (BPMs):

$$\begin{aligned} \underset{\boldsymbol{\alpha},\,\boldsymbol{\beta}\in\mathbb{R}}{\text{minimize}} \quad & U(\boldsymbol{\alpha},\boldsymbol{\beta}) \\ \text{subject to} \quad & y_s(\boldsymbol{\alpha},\boldsymbol{\beta},s) = -\Delta y, \\ & \phi_s(\boldsymbol{\alpha},\boldsymbol{\beta},s) = 0, \\ & s = L \end{aligned} \tag{4.19}$$

For compound basic parallelogram mechanisms (CBPMs):

$$
\begin{aligned}
\underset{\boldsymbol{\alpha},\,\boldsymbol{\beta}\in\mathbb{R}}{\text{minimize}} \quad & U(\boldsymbol{\alpha},\boldsymbol{\beta}) \\
\text{subject to} \quad & x_s(\boldsymbol{\alpha},\boldsymbol{\beta},s) = L, \\
& y_s(\boldsymbol{\alpha},\boldsymbol{\beta},s) = -\Delta y, \\
& \phi_s(\boldsymbol{\alpha},\boldsymbol{\beta},s) = 0, \\
& s = L
\end{aligned}
\tag{4.20}
$$

Modeling results and corresponding FEA validation can be found in Fig. 4.6. The conducted modeling and analysis examine the nonlinear force-displacement relationship of BPMs and CBPMs, the parasitic movement and maximum stress in BPMs, as well as the elongation of a single beam in CBPMs.

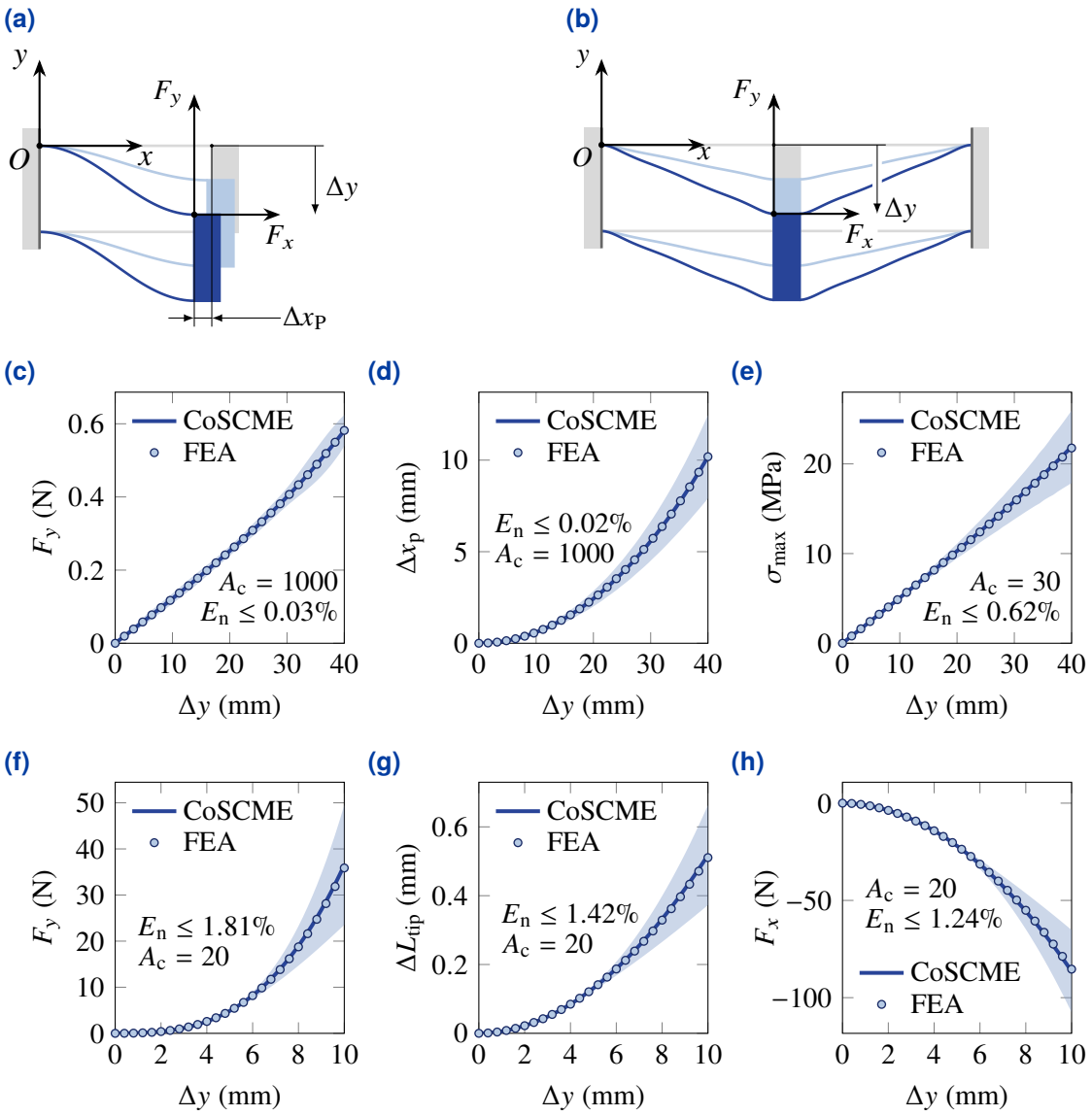


Fig. 4.6.: Modeling results for BPMs and CBPMs. (a) BPMs. (b) CBPMs. (c) F_y-Δy curve for BPMs. (d) Δx_p-Δy curve (parasitic movement of the moving shuttle) for BPMs. (e) σ_{max}-Δy curve for BPMs. (f) F_y-Δy curve for CBPMs. (g) ΔL_{tip}-Δy curve for CBPMs. (h) F_x-Δy curve for CBPMs.

4.2.3 Case study 3: Bistable mechanisms

In this study, the capability of modeling nonlinear large-deformation beams is evaluated through the analysis of compliant bistable mechanisms. The following section introduces the modeling procedure for two types of bistable mechanisms: classical translational bistable mechanisms and pre-loaded rotational bistable mechanisms. The classical translational compliant bistable mechanism consists of multiple symmetrically aligned inclined slender

beams, a center moving shuttle, and fixed supports. When a vertical displacement load is applied to the center shuttle, the inclined beams buckle and start bending. As the displacement increases, the strain energy stored in the mechanism increases until it reaches a local maximum point which is corresponding to a zero-stiffness configuration. After that point, the strain energy starts to decrease. This decrease continues until the mechanism reaches its second stable state, where the strain energy attains a local minimum. Different from classical compliant bistable mechanisms, which primarily focus on translational bistability, the pre-loaded rotational bistable mechanism explores off-axis rotational bistability. A rotatable shuttle is designed to connect two beams and is preloaded to a position where the beam has already buckled. The position of the central shuttle is then fixed, and different rotational loads are applied to the shuttle to investigate the nonlinear relationship between the moment and the rotational angle. Previous experiments have demonstrated that the pre-loaded bistable mechanism indeed exhibits rotational bistability, as shown in [226].

For modeling classical compliant bistable mechanism, the optimization objective function can be expressed as in Eq. (4.21).

$$\begin{aligned} \underset{\boldsymbol{\alpha},\,\boldsymbol{\beta}\,\in\,\mathbb{R}}{\text{minimize}} \quad & U(\boldsymbol{\alpha},\boldsymbol{\beta}) \\ \text{subject to} \quad & x_s^{\mathrm{L}}(\boldsymbol{\alpha},\boldsymbol{\beta},s) = L - \Delta y \sin\theta, \\ & y_s^{\mathrm{L}}(\boldsymbol{\alpha},\boldsymbol{\beta},s) = -\Delta y \cos\theta, \\ & \phi_s^{\mathrm{L}}(\boldsymbol{\alpha},\boldsymbol{\beta},s) = 0, \\ & s = L, \end{aligned} \tag{4.21}$$

where, the x and y coordinate of point P_s in local coordinate system is denoted by x_s^{L} and y_s^{L}. Similarly, the deflection angle at point P_s is ϕ_s^{L}. The angle between the x-axis of local and global coordinate system is θ. In this case study, the angle θ is given by 40°. Applied displacement load is Δy, which is described in global coordinate system. Since the obtained forces (f_x and f_y) are described in the local coordinate system, they have to be converted to the global coordinate system when deriving the modeling results, using Eqs. (4.22-4.23):

$$F_x = f_x \cos\theta - f_y \sin\theta, \tag{4.22}$$

$$F_y = f_x \sin\theta + f_y \cos\theta. \tag{4.23}$$

The definitions of the terminologies used for modeling the compliant translational bistable mechanism are provided in Figure 4.7, along with the modeling results compared to FEA simulations.

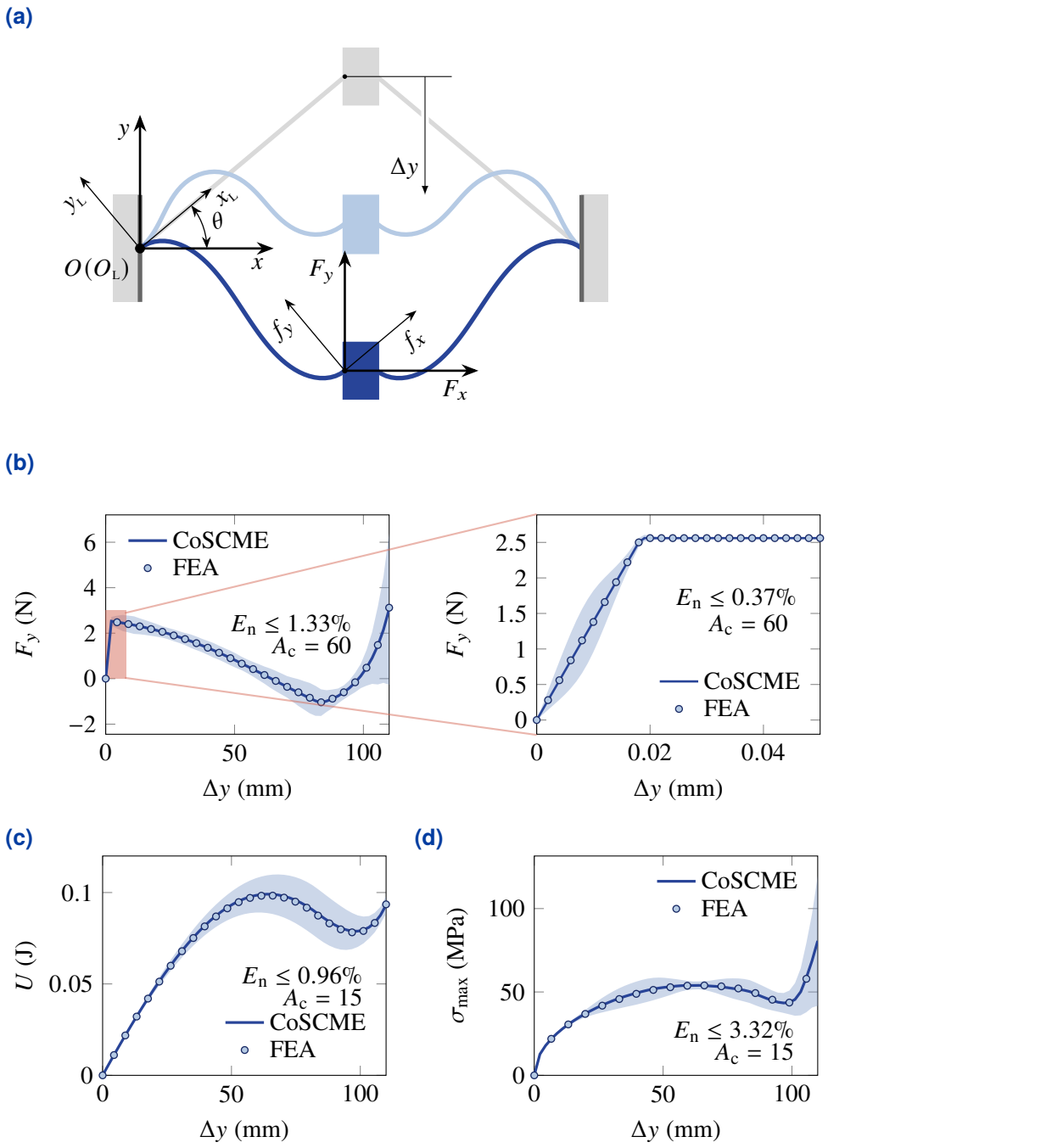


Fig. 4.7.: Modeling results for the classical translational bistable mechanism. Results are verified by FEA simulations. (a) Coordinate systems and terminology used for modeling the classical translational bistable mechanism: Parameters defined in the global coordinate system ($O - xy$) include the displacement exerted on the center shuttle, denoted as Δy, and the reaction forces in the global coordinate system, denoted as F_x and F_y. Parameters defined in the local coordinate system ($O_L - x_L y_L$) include the reaction forces, denoted as f_x and f_y. (b) The force-displacement relationship of the translational bistable mechanism. The figure on the right zooms in on the results, providing more details around the critical buckling point. (c) Energy-displacement curve for translational bistable mechanism. (d) Maximum stress during deformation obtained from both CoSCME and FEA simulation.

For the preloaded rotational bistable mechanism, the modeling process needs to be divided into two steps. The idea of pre-loaded rotational bistable mechanisms originates from previous work in [226]. Step 1 is preloading the stage, and step 2 is applying the rotational load on the center shuttle. The optimization objective function for step 1 can be obtained from Eq. (4.24).

$$\begin{aligned} \underset{\boldsymbol{\alpha},\, \boldsymbol{\beta} \in \mathbb{R}}{\text{minimize}} \quad & U(\boldsymbol{\alpha}, \boldsymbol{\beta}) \\ \text{subject to} \quad & x_s^{\mathrm{L}}(\boldsymbol{\alpha}, \boldsymbol{\beta}, s) = L - \Delta y^* \sin\theta, \\ & y_s^{\mathrm{L}}(\boldsymbol{\alpha}, \boldsymbol{\beta}, s) = -\Delta y^* \cos\theta, \\ & \phi_s^{\mathrm{L}}(\boldsymbol{\alpha}, \boldsymbol{\beta}, s) = 0, \\ & s = L, \end{aligned} \tag{4.24}$$

where, the preloaded displacement is denoted by Δy^*, which remains constant during the modeling process. Similarly, the angle θ serves as a constant in the optimization process. In this case study 3, the value of Δy^* is given by 25mm. After obtaining the preloaded configuration, the step 2 is conducted. Step 2 begins after obtaining the equilibrium stable configuration from step 1, followed by applying rotational load on the central rotatable shuttle. The optimization objective function for step 2 is provided in Eq. (4.25):

$$\begin{aligned} \underset{\boldsymbol{\alpha},\, \boldsymbol{\beta} \in \mathbb{R}}{\text{minimize}} \quad & U(\boldsymbol{\alpha}, \boldsymbol{\beta}) \\ \text{subject to} \quad & x_s^{\mathrm{L}}(\boldsymbol{\alpha}, \boldsymbol{\beta}, s) = L - \Delta y^* \sin\theta, \\ & y_s^{\mathrm{L}}(\boldsymbol{\alpha}, \boldsymbol{\beta}, s) = -\Delta y^* \cos\theta, \\ & \phi_s^{\mathrm{L}}(\boldsymbol{\alpha}, \boldsymbol{\beta}, s) = \Delta\theta, \\ & s = L, \end{aligned} \tag{4.25}$$

where, the rotational angle of center shuttle is denoted by $\Delta\theta$ and it serves as a input variable in the step 2. The existence of rotational bistability is evaluated based on whether there is more than one configuration in which the strain energy reaches a local minimum.

The definitions of the terminologies used for modeling the compliant torational bistable mechanism are provided in Figure 4.8, along with the modeling results compared to FEA simulations. it is demonstrated that the proposed mechanism exhibits rotational bistability. Furthermore, this has been confirmed experimentally in previous work [226]. Additionally, the modeling results for reaction forces, strain energy, and maximum stress are derived and

verified through FEA simulations. A comparison of the results and an explanation of the terminology can be found in Fig. 4.8.

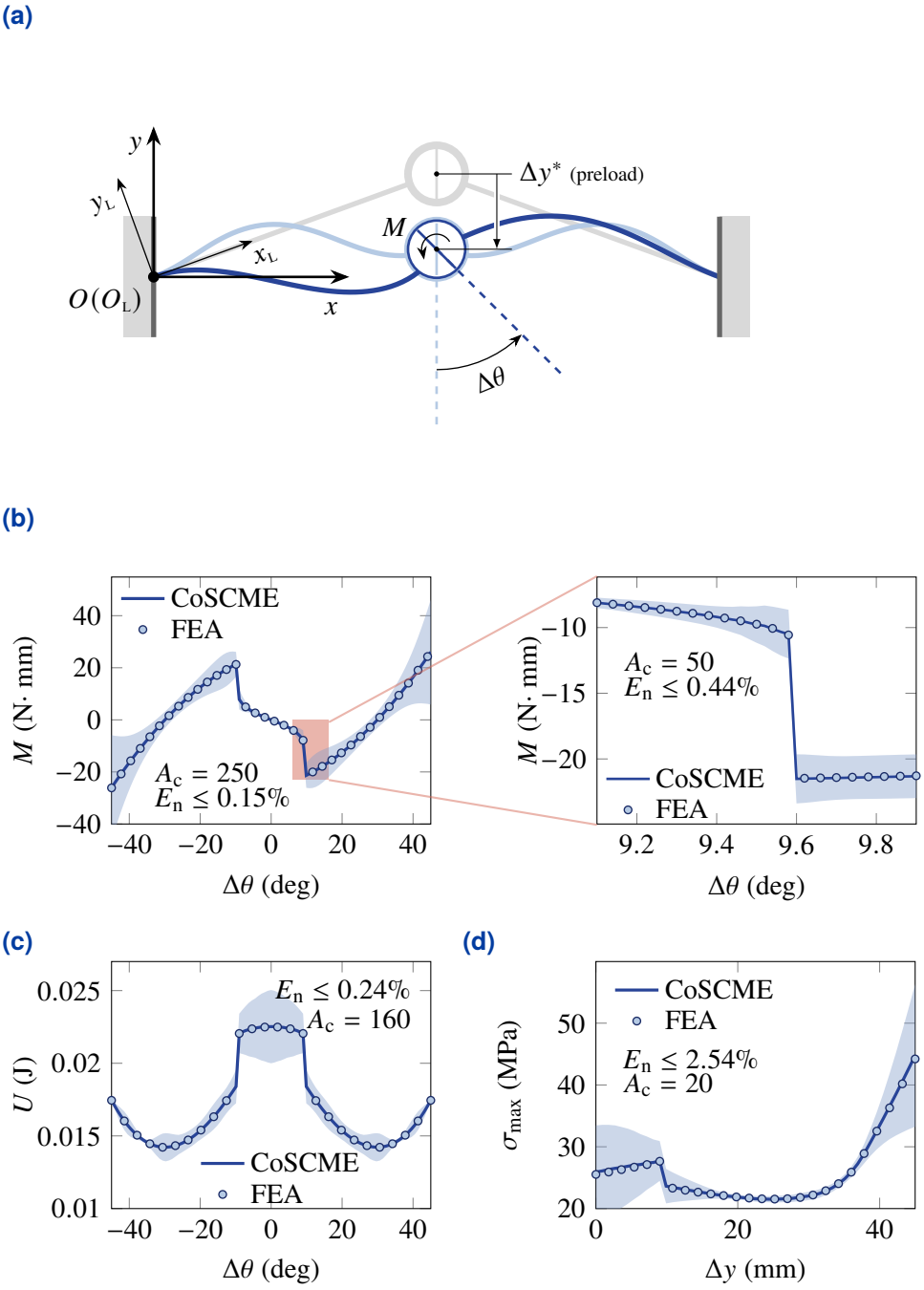


Fig. 4.8.: Modeling results for the pre-loaded rotational bistable mechanism. Results are verified by FEA simulations. (a) Coordinate systems and terminology used for modeling the preloaded rotational bistable mechanism. The mechanism is preloaded by applying a translational displacement Δy^* (25 mm) to the center rotatable shuttle. After preloading, the position of the moving shuttle is fixed, while allowing it to rotate. The rotation angle of the center shuttle is denoted by $\Delta\theta$. The positive direction of $\Delta\theta$ is defined in Figure. The angle between the x-axis of the local and global coordinate systems is 20° in this case study. (b) The moment-angle relationship of the preloaded rotational bistable mechanism. The figure on the right zooms in on the results, providing more details around the snap through behavior. (c) Energy-rotation curve for preloaded rotational mechanism. (d) Maximum stress during deformation for the preloaded rotational bistable mechanism.

4.2.4 Case study 4: General lumped-compliance beams

Numerous designs of compliant mechanisms consist of multiple interdependent beams connected by rigid blocks, which is known as general lumped-compliance beams [106]. Therefore, modeling a single beam is insufficient for comprehensively investigating the nonlinear response of these beam-based mechanical systems. The previously proposed high-order SCME is limited by its reliance on single-beam models, making it applicable only to mechanisms with a single beam or symmetric beams. In this work, the CoSCME successfully addresses this limitation and is applied to model general lumped-compliance beams. This is achieved by incorporating the planar transformation matrix into the modeling process, constructing a mechanical system with two distinct beams, and then finding the minimum strain energy for this system to determine the equilibrium configuration.

Similar to the modeling of single compliant beams, the kinetostatic modeling of general lumped-compliance mechanisms also relies on the principle of minimum strain energy, as mentioned earlier. It is worth noting that this method can be expanded to model more complex mechanism configurations with a finite number of beams by establishing a similar optimization framework. In this subsection, a simple example with only two compliant beams is presented for clarity. The modeling steps are outlined as follows:

(1) Establishment of coordinate systems:

Establishing coordinate systems is crucial when modeling general lumped-compliance beams, as it clarifies the geometric relationships between each beam. For the case study demonstrated in Fig. 4.9 (a), two coordinate systems $\mathcal{R}^{\mathrm{A}} - O_{\mathrm{A}}x_{\mathrm{A}}y_{\mathrm{A}}$ and $\mathcal{R}^{\mathrm{B}} - O_{\mathrm{B}}x_{\mathrm{B}}y_{\mathrm{B}}$ are defined to describe the beam deformation. Besides, an intermediate coordinate system $\mathcal{R}^{i} - P_{\mathrm{tip-A}}x_i y_i$ is defined to describe the geometric layout between coordinate system $\mathcal{R}^{\mathrm{A}}$ and $\mathcal{R}^{\mathrm{B}}$, where, $P_{\mathrm{tip-A}}$ denotes the tip position of beam A. The position of O_{B} in the coordinate system $\mathcal{R}^{i}$ is $(x_{\mathrm{fr}}, y_{\mathrm{fr}})$, which remains constant during deformation, demonstrating the rigid connection between the two beams. Similarly, the angle θ_{fr}, which denotes the deflection between $\overrightarrow{x_{\mathrm{B}}}$ and $\overrightarrow{x_i}$, remains constant as well. In this specific case study, the value of x_{fr}, y_{fr} and θ_{fr} are defined as in Eq. (4.26):

$$\begin{aligned} x_{\mathrm{fr}} &= 100\cos(22.5^{\circ})\ mm \\ y_{\mathrm{fr}} &= 100\sin(22.5^{\circ})\ mm \\ \theta_{\mathrm{fr}} &= 45^{\circ} \end{aligned} \tag{4.26}$$

During the deformation process, the positions and orientations of the coordinate systems $\mathcal{R}^i$ and $\mathcal{R}^{\mathrm{B}}$ within the fixed-to-ground coordinate system $\mathcal{R}^{\mathrm{A}}$ change along with the tip position $P_{\mathrm{tip-A}}$ of beam A. The coordinate systems for initially undeformed coordinate system are denoted by $\mathcal{R}^{i*} - P^*_{\mathrm{tip-A}} x^*_i y^*_i$ and $\mathcal{R}^{\mathrm{B}*} - O^*_{\mathrm{B}} x^*_{\mathrm{B}} y^*_{\mathrm{B}}$.

(2) Formulation of position constraints:

In the previously defined coordinate systems, $\mathcal{R}^{\mathrm{A}*}$ is designated as the fixed-to-ground reference coordinate system. Therefore, to derive the expression for beam tip constraints, all deformations and deflections must be transformed and described within the framework of $\mathcal{R}^{\mathrm{A}*}$. Before conducting the coordinate transformation, the beam tip position $P_{\mathrm{tip-B}}(x^{\mathrm{B}}_{\mathrm{tip}}, y^{\mathrm{B}}_{\mathrm{tip}})$ of beam B in the coordinate system $\mathcal{R}^{\mathrm{B}}$ is formulated as in Eqs. (4.27-4.28):

$$x^{\mathcal{R}^{\mathrm{B}}}_{\mathrm{tip-B}}(\boldsymbol{\alpha}^{\mathrm{B}}, \boldsymbol{\beta}^{\mathrm{B}}, L_{\mathrm{B}}) = \int_0^{L_{\mathrm{B}}+\Delta L_{\mathrm{s}}(\boldsymbol{\beta}^{\mathrm{B}}, L_{\mathrm{B}})} \cos\left[\phi_s(\boldsymbol{\alpha}^{\mathrm{B}}, \boldsymbol{\beta}^{\mathrm{B}}, L_{\mathrm{B}})\right] ds, \tag{4.27}$$

$$y^{\mathcal{R}^{\mathrm{B}}}_{\mathrm{tip-B}}(\boldsymbol{\alpha}^{\mathrm{B}}, \boldsymbol{\beta}^{\mathrm{B}}, L_{\mathrm{B}}) = \int_0^{L_{\mathrm{B}}+\Delta L_{\mathrm{s}}(\boldsymbol{\beta}^{\mathrm{B}}, L_{\mathrm{B}})} \sin\left[\phi_s(\boldsymbol{\alpha}^{\mathrm{B}}, \boldsymbol{\beta}^{\mathrm{B}}, L_{\mathrm{B}})\right] ds, \tag{4.28}$$

where, $x^{\mathcal{R}^{\mathrm{B}}}_{\mathrm{tip-B}}$ and $y^{\mathcal{R}^{\mathrm{B}}}_{\mathrm{tip-B}}$ denotes the beam tip coordinates of beam B in the coordinate system $\mathcal{R}^{\mathrm{B}}$. The generalized coordinates $\boldsymbol{\alpha}^{\mathrm{B}}$ and $\boldsymbol{\beta}^{\mathrm{B}}$ are used to model the beam curvature and beam axial strain. The tip deflection of beam B can be formulated as in Eq. (4.29):

$$\phi^{\mathcal{R}^{\mathrm{B}}}_{\mathrm{tip-B}}(\boldsymbol{\alpha}^{\mathrm{B}}, \boldsymbol{\beta}^{\mathrm{B}}, L_{\mathrm{B}}) = \int_0^{L_{\mathrm{B}}+\Delta L_{\mathrm{s}}(\boldsymbol{\beta}^{\mathrm{B}}, L_{\mathrm{B}})} \omega(\boldsymbol{\alpha}^{\mathrm{B}}, L_{\mathrm{B}}) \left[1 + \varepsilon_{\mathrm{a}}(\boldsymbol{\beta}^{\mathrm{B}}, L_{\mathrm{B}})\right] ds, \tag{4.29}$$

where, $\phi^{\mathcal{R}^{\mathrm{B}}}_{\mathrm{tip-B}}$ denotes the beam tip deflection of beam B in the coordinate system $\mathcal{R}^{\mathrm{B}}$. A planar transformation matrix $T^{\mathrm{A}}_{\mathrm{B}}$ is formulated in Eq. (4.30) to transform all the coordinates from $\mathcal{R}^{\mathrm{B}}$ to $\mathcal{R}^{\mathrm{A}}$.

$$T_{\mathrm{B}}^{\mathrm{A}} = \begin{bmatrix} \cos\left(\phi_{\mathrm{tip-A}}^{\mathcal{R}^{\mathrm{A}}} + \theta_{\mathrm{fr}}\right) & -\sin\left(\phi_{\mathrm{tip-A}}^{\mathcal{R}^{\mathrm{A}}} + \theta_{\mathrm{fr}}\right) & x_{\mathrm{tip-A}}^{\mathcal{R}^{\mathrm{A}}} + x_{\mathrm{fr}} \\ \sin\left(\phi_{\mathrm{tip-A}}^{\mathcal{R}^{\mathrm{A}}} + \theta_{\mathrm{fr}}\right) & \cos\left(\phi_{\mathrm{tip-A}}^{\mathcal{R}^{\mathrm{A}}} + \theta_{\mathrm{fr}}\right) & y_{\mathrm{tip-A}}^{\mathcal{R}^{\mathrm{A}}} + y_{\mathrm{fr}} \\ 0 & 0 & 1 \end{bmatrix}, \tag{4.30}$$

where, $x_{\mathrm{tip-A}}^{\mathcal{R}^{\mathrm{A}}}$, $y_{\mathrm{tip-A}}^{\mathcal{R}^{\mathrm{A}}}$ and $\phi_{\mathrm{tip-A}}^{\mathcal{R}^{\mathrm{A}}}$ denotes the beam tip position and deflection in the coordinate system $\mathcal{R}^{\mathrm{A}}$. They are formulated in Eq. (4.31):

$$\begin{aligned} x_{\mathrm{tip-A}}^{\mathcal{R}^{\mathrm{A}}}(\boldsymbol{\alpha}^{\mathrm{A}}, \boldsymbol{\beta}^{\mathrm{A}}, L_{\mathrm{A}}) &= \int_0^{L_{\mathrm{A}}+\Delta L_{\mathrm{s}}(\boldsymbol{\beta}^{\mathrm{A}}, L_{\mathrm{A}})} \cos\left[\phi_s(\boldsymbol{\alpha}^{\mathrm{A}}, \boldsymbol{\beta}^{\mathrm{A}}, L_{\mathrm{A}})\right] ds, \\ y_{\mathrm{tip-A}}^{\mathcal{R}^{\mathrm{A}}}(\boldsymbol{\alpha}^{\mathrm{A}}, \boldsymbol{\beta}^{\mathrm{A}}, L_{\mathrm{A}}) &= \int_0^{L_{\mathrm{A}}+\Delta L_{\mathrm{s}}(\boldsymbol{\beta}^{\mathrm{A}}, L_{\mathrm{A}})} \sin\left[\phi_s(\boldsymbol{\alpha}^{\mathrm{A}}, \boldsymbol{\beta}^{\mathrm{A}}, L_{\mathrm{A}})\right] ds, \\ \phi_{\mathrm{tip-A}}^{\mathcal{R}^{\mathrm{A}}}(\boldsymbol{\alpha}^{\mathrm{A}}, \boldsymbol{\beta}^{\mathrm{A}}, L_{\mathrm{A}}) &= \int_0^{L_{\mathrm{A}}+\Delta L_{\mathrm{s}}(\boldsymbol{\beta}^{\mathrm{A}}, L_{\mathrm{A}})} \omega(\boldsymbol{\alpha}^{\mathrm{A}}, L_{\mathrm{A}}) \left[1 + \varepsilon_{\mathrm{a}}(\boldsymbol{\beta}^{\mathrm{A}}, L_{\mathrm{A}})\right] ds, \end{aligned} \tag{4.31}$$

After deriving the expression of transformation matrix, the tip position of beam B can be formulated as in Eq. (4.32):

$$\begin{bmatrix} x_{\mathrm{tip-B}}^{\mathcal{R}^{\mathrm{A}}}(\boldsymbol{\alpha}^{\mathrm{A}}, \boldsymbol{\alpha}^{\mathrm{B}}, \boldsymbol{\beta}^{\mathrm{A}}, \boldsymbol{\beta}^{\mathrm{B}}, L_{\mathrm{A}}, L_{\mathrm{B}}) \\ y_{\mathrm{tip-B}}^{\mathcal{R}^{\mathrm{A}}}(\boldsymbol{\alpha}^{\mathrm{A}}, \boldsymbol{\alpha}^{\mathrm{B}}, \boldsymbol{\beta}^{\mathrm{A}}, \boldsymbol{\beta}^{\mathrm{B}}, L_{\mathrm{A}}, L_{\mathrm{B}}) \\ 1 \end{bmatrix} = T_{\mathrm{B}}^{\mathrm{A}} \begin{bmatrix} x_{\mathrm{tip-B}}^{\mathcal{R}^{\mathrm{B}}}(\boldsymbol{\alpha}^{\mathrm{B}}, \boldsymbol{\beta}^{\mathrm{B}}, L_{\mathrm{B}}) \\ y_{\mathrm{tip-B}}^{\mathcal{R}^{\mathrm{B}}}(\boldsymbol{\alpha}^{\mathrm{B}}, \boldsymbol{\beta}^{\mathrm{B}}, L_{\mathrm{B}}) \\ 1 \end{bmatrix}. \tag{4.32}$$

In terms of the beam tip deflection of beam B in the coordinate system $\mathcal{R}^{\mathrm{A}}$, the formulation can be obtained from Eq. (4.33):

$$\phi_{\mathrm{tip-B}}^{\mathcal{R}^{\mathrm{A}}}(\boldsymbol{\alpha}^{\mathrm{A}}, \boldsymbol{\alpha}^{\mathrm{B}}, \boldsymbol{\beta}^{\mathrm{A}}, \boldsymbol{\beta}^{\mathrm{B}}, L_{\mathrm{A}}, L_{\mathrm{B}}) = \phi_{\mathrm{tip-A}}^{\mathcal{R}^{\mathrm{A}}}(\boldsymbol{\alpha}^{\mathrm{A}}, \boldsymbol{\beta}^{\mathrm{A}}, L_{\mathrm{A}}) + \theta_{\mathrm{fr}} + \phi_{\mathrm{tip-B}}^{\mathcal{R}^{\mathrm{B}}}(\boldsymbol{\alpha}^{\mathrm{B}}, \boldsymbol{\beta}^{\mathrm{B}}, L_{\mathrm{B}}) \tag{4.33}$$

At this stage, the formulation of optimization constraint function has been derived. The next step is to derive the objective function, which is to minimize the strain energy for the entire system.

(3) Formulation of strain energy:

In the framework of using the energy method to solve static problems, the optimization objective is to minimize the total strain energy in the mechanical system. Therefore, to model the nonlinear behavior of general lumped-compliance beams, it is essential to derive the expression for the total strain energy U^{Total} in the system, as formulated in Eq. (4.34):

$$\begin{aligned}
U^{\text{Total}}(\boldsymbol{\alpha}^{\text{A}}, \boldsymbol{\alpha}^{\text{B}}, \boldsymbol{\beta}^{\text{A}}, \boldsymbol{\beta}^{\text{B}}, L_{\text{A}}, L_{\text{B}}) &= U^{A}(\boldsymbol{\alpha}^{A}, \boldsymbol{\beta}^{A}, L_{\text{A}}) + U^{B}(\boldsymbol{\alpha}^{B}, \boldsymbol{\beta}^{B}, L_{\text{B}}) \\
&= \frac{EI}{2L_{\text{A}}}\left(\left(\alpha_0^{\text{A}}\right)^2 + \frac{\left(\alpha_1^{\text{A}}\right)^2}{3} + \frac{\left(\alpha_2^{\text{A}}\right)^2}{5} + \frac{\left(\alpha_3^{\text{A}}\right)^2}{7} + \frac{\left(\alpha_4^{\text{A}}\right)^2}{9} + \frac{\left(\alpha_5^{\text{A}}\right)^2}{11}\right) \\
&+ \frac{EAL_{\text{A}}}{2}\left(\left(\beta_0^{\text{A}}\right)^2 + \frac{\left(\beta_1^{\text{A}}\right)^2}{3} + \frac{\left(\beta_2^{\text{A}}\right)^2}{5} + \frac{\left(\beta_3^{\text{A}}\right)^2}{7} + \frac{\left(\beta_4^{\text{A}}\right)^2}{9} + \frac{\left(\beta_5^{\text{A}}\right)^2}{11}\right) \\
&+ \frac{EI}{2L_{\text{B}}}\left(\left(\alpha_0^{\text{B}}\right)^2 + \frac{\left(\alpha_1^{\text{B}}\right)^2}{3} + \frac{\left(\alpha_2^{\text{B}}\right)^2}{5} + \frac{\left(\alpha_3^{\text{B}}\right)^2}{7} + \frac{\left(\alpha_4^{\text{B}}\right)^2}{9} + \frac{\left(\alpha_5^{\text{B}}\right)^2}{11}\right) \\
&+ \frac{EAL_{\text{B}}}{2}\left(\left(\beta_0^{\text{B}}\right)^2 + \frac{\left(\beta_1^{\text{B}}\right)^2}{3} + \frac{\left(\beta_2^{\text{B}}\right)^2}{5} + \frac{\left(\beta_3^{\text{B}}\right)^2}{7} + \frac{\left(\beta_4^{\text{B}}\right)^2}{9} + \frac{\left(\beta_5^{\text{B}}\right)^2}{11}\right)
\end{aligned} \tag{4.34}$$

(4) Definition of optimization objective function:

The position constraint and objective formulation have been previously derived. At this stage, the objective function of the optimization problem will be clarified, which involves minimizing the total strain energy when the tip of beam B is aligned with a specified position and deflection angle. In the case sudy demonstrated in Fig. 4.9 (a), the beam length L_{A} and L_{B} are the same and given by $L = 100\text{mm}$. Based on this case study, the formulation of the objective function can be seen in Eq. (5.7):

$$\begin{aligned}
&\underset{\boldsymbol{\alpha},\, \boldsymbol{\beta} \in \mathbb{R}}{\text{minimize}} \quad U^{\text{Total}}(\boldsymbol{\alpha}^{\text{A}}, \boldsymbol{\alpha}^{\text{B}}, \boldsymbol{\beta}^{\text{A}}, \boldsymbol{\beta}^{\text{B}}, L_{\text{A}}, L_{\text{B}}) \\
&\text{subject to} \quad x_{\text{tip}-\text{B}}^{\mathcal{R}^{\text{A}}}(\boldsymbol{\alpha}^{\text{A}}, \boldsymbol{\alpha}^{\text{B}}, \boldsymbol{\beta}^{\text{A}}, \boldsymbol{\beta}^{\text{B}}, L_{\text{A}}, L_{\text{B}}) = L_{\text{A}} + x_{\text{fr}} + L_{\text{B}}\cos(\theta_{\text{fr}}) + t\Delta x,
\end{aligned} \tag{4.35}$$

$$y^{\mathcal{R}^{\mathrm{A}}}_{\mathrm{tip-B}}(\boldsymbol{\alpha}^{\mathrm{A}}, \boldsymbol{\alpha}^{\mathrm{B}}, \boldsymbol{\beta}^{\mathrm{A}}, \boldsymbol{\beta}^{\mathrm{B}}, L_{\mathrm{A}}, L_{\mathrm{B}}) = y_{\mathrm{fr}} + L_{\mathrm{B}} \sin(\theta_{\mathrm{fr}}) + t\Delta y,$$
$$\phi^{\mathcal{R}^{\mathrm{A}}}_{\mathrm{tip-B}}(\boldsymbol{\alpha}^{\mathrm{A}}, \boldsymbol{\alpha}^{\mathrm{B}}, \boldsymbol{\beta}^{\mathrm{A}}, \boldsymbol{\beta}^{\mathrm{B}}, L_{\mathrm{A}}, L_{\mathrm{B}}) = \theta_{\mathrm{fr}} + t\Delta\theta,$$

where, t serves as a normalized scale parameter to describe the deformation process. This is necessary because distinct type of displacement loads are exerted on the tip of beam B, and to comprehensively describe the deformation of a general lumped-compliance beam, the normalized scale parameter is adopted. The range of t is from 0 to 1.

The above content comprehensively demonstrates the modeling procedure for a general lumped-compliance beam with two sub-beams. The used terminologies are explained in Fig. (4.9) (a). In this case study, displacement loads along the x_{A}-direction ($\Delta x = -30$) and y_{A}-direction ($\Delta y = -120$), as well as a rotational load ($\Delta\theta = -45°$), are simultaneously applied to the tip of beam B. The modeling results are shown in Fig. (4.9) (b), which is verified by FEA simulation.

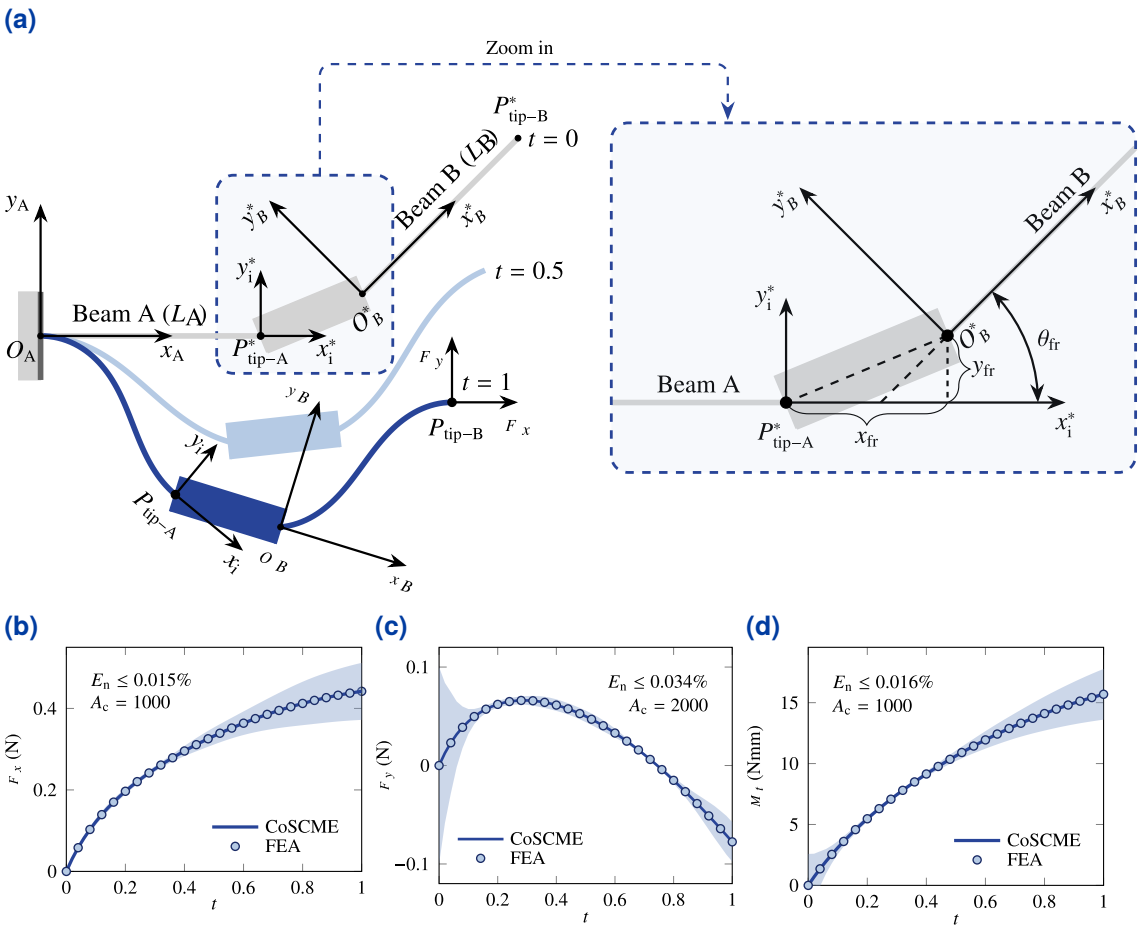


Fig. 4.9.: Case study of modeling a general lumped-compliance beam, which is composed of two compliant beams. A displacement load and a rotational load are applied to the tip of beam B. The deformation result is derived from the modeling using the CoSCME. (a) Terminology used for modeling the general lumped-compliance beam. The deformation process is described using the parameter $t \in [0, 1]$. Coordinate systems are defined in the figure, and all the coordinate systems for the initially undeformed configuration are marked with $*$. (b) Modeling results obtained from the CoSCME and FEA simulations, including reaction forces along the x- and y-directions, and the tip reaction moment M_t.

By systematically adjusting the key frame parameters (x_{fr}, y_{fr}, and θ_{fr}), twelve distinct configurations of general lumped compliance beams were obtained, as illustrated in Fig. 4.10. Each configuration exhibits a unique combination of compliance and stiffness, effectively covering a broad range of design scenarios and practical applications.

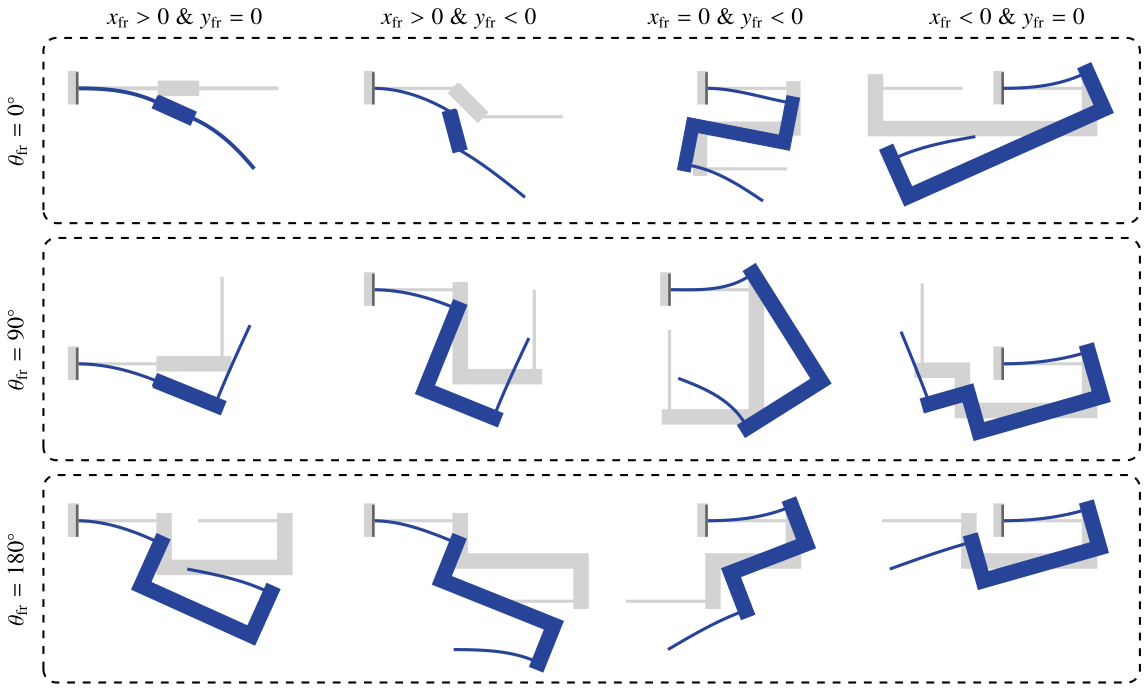


Fig. 4.10.: Twelve distinct configurations of general lumped-compliance beams. These beams are developed by adjusting frame parameters (x_{fr}, y_{fr}, and θ_{fr}), which is inspired by the position-space-based compliant mechanism reconfiguration approach. The undeformed configurations are represented in grey, while the deformed configurations are shown in blue. The deformations are obtained from modeling results of the CoSCME. A vertical displacement load is applied to all of these general lumped-compliance beams, with the tips of each beam B free to rotate.

The obtained configurations not only serve to illustrate the versatility of the position-space-based design approach [227, 228], but also validate the universality and robustness of the proposed CoSCME. The ability to model various configurations demonstrates that this approach is not restricted to a single type; rather, it can reliably predict the nonlinear behavior of compliant mechanisms under different conditions. This adaptability emphasizes the method's applicability to diverse design requirements.

Furthermore, the analysis of these configurations provides valuable insights into design optimization. By evaluating different combinations of parameters, we can identify those that yield superior performance in practical applications, thereby establishing quantitative criteria for the optimal design of compliant mechanisms. This capability not only enhances the precision of structural design but also contributes to the development of lightweight, high-performance engineering structures.

4.2.5 Case study 5: Initially-curved beams

The above case studies primarily investigate the nonlinear behavior of initially-straight compliant beams. The adopt of initially-curved beams in compliant mechanisms offers several distinct advantages over initially-straight beams. These include a wider range of mechanical behaviors under loading conditions and a more uniform distribution of stresses. Consequently, initially curved beams have been extensive applied in the design of compliant mechanisms [229, 230, 109]. The proposed CoSCME is well-suited for modeling initially-curved beams, offering an approach that accurately captures their nonlinear, large-deformation behavior under various loading conditions.

Modeling initially-curved beams requires consideration of their initial shape and formulating its curvature using constant generalized coordinates $\boldsymbol{\alpha}^*$, as mentioned in [231]. The comprehensive formulation of bending strain energy can be found in Eq. (4.36).

$$U_{\mathrm{b}} = \int_0^L \frac{EI}{2} \left(\omega\left(\boldsymbol{\alpha}, s\right) - \omega^*\left(\boldsymbol{\alpha}^*, s\right)\right)^2 ds, \tag{4.36}$$

where, the curvature function of initially-curved beam is denoted by $\omega^*\left(\boldsymbol{\alpha}^*, s\right)$, which is shown in Eq. (4.37):

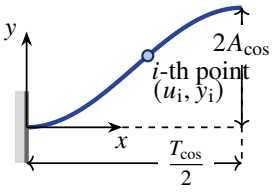
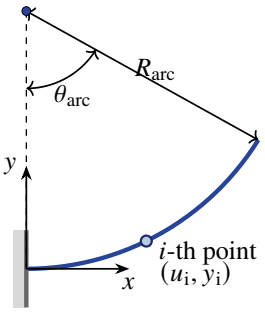
$$\begin{aligned}
\omega^*(\boldsymbol{\alpha}^*, s) \approx & \frac{1}{L} \sum_{n=0}^{n=N} \boldsymbol{\alpha}_n^* \psi_n(s) \\
= & \frac{\alpha_0^*}{L} + \frac{\alpha_1^*}{L}\left(\frac{2s}{L} - 1\right) + \frac{\alpha_2^*}{L}\left(\frac{6s^2}{L^2} - \frac{6s}{L} + 1\right) \\
& + \frac{\alpha_3^*}{L}\left(\frac{20s^3}{L^3} - \frac{30s^2}{L^2} + \frac{12s}{L} - 1\right) \\
& + \frac{\alpha_4^*}{L}\left(\frac{70s^4}{L^4} - \frac{140s^3}{L^3} + \frac{90s^2}{L^2} - \frac{20s}{L} + 1\right) \\
& + \frac{\alpha_5^*}{L}\left(\frac{252s^5}{L^5} - \frac{630s^4}{L^4} + \frac{560s^3}{L^3} - \frac{210s^2}{L^2} + \frac{30s}{L} - 1\right),
\end{aligned} \tag{4.37}$$

where, the generalized coordinates used for formulating initially curved curvature functions are denoted as $\boldsymbol{\alpha}_{\mathrm{n}}^*$. The amount of generalized coordinates depends on the highest order of polynomials. These generalized coordinates $\boldsymbol{\alpha}_{\mathrm{n}}^*$ are used to describe the initial shape, which

means their values are constant during the iteration process. Therefore, these constants need to be determined before performing the numerical iteration.

Typically, continuous curves are used to describe the neutral line of an initially curved beam. Common shapes for initially curved beams for compliant mechanisms include cosine-shaped curves and circular arcs. These shapes can be described using mathematical expressions. The formulations for cosine-shaped beam and circular-arc beams are listed in Table 4.2. For the cosine-shaped beam, the shape is defined by a half-period cosine curve with period $T_{\cos}$, amplitude $A_{\cos}$ (an absolute value), and frequency $f_{\cos}$. For the circular-arc beam, the shape is described by the radius R_{arc} and the radian of circular θ_{arc}. These parameters are indicated in the beam shape diagrams. For the i-th evenly distributed point on the beam, the x coordinate is denoted by u_{i} and the arc length from the beam root to i-th point is denoted by s_{i}. The goal of evenly distributing points on the beam is to set the curvature described by the function, $\omega^*(\boldsymbol{\alpha}^*, s_{\text{i}})$, equal to the given curvature, $\omega_{\text{g}}(u_{\text{i}})$, at i-th evenly distributed points, i.e., $\omega^*(\boldsymbol{\alpha}^*, s_{\text{i}}) = \omega_{\text{g}}(u_{\text{i}})$. Increasing the number of distributed points (n_{dp}) on the beam contributes to a more accurate result for the initial generalized coordinates ($\boldsymbol{\alpha}^*$). Notably, when calculating the x coordinate for the i-th point in cosine-shaped beams, the equation provided needs to be solved to obtain the value of u_i.

Tab. 4.2.: The formulations for cosine-shaped and circular-arc beams include shape functions, beam length, curvature, and the x-coordinates of evenly distributed points along the beam arc(denoted as u_i).

Beam type	Beam Shape	Formulations
Cosine-shaped beams		Shape function: $y(u) = -A_{\cos}\cos(2\pi f_{\cos}\cdot u) + A_{\cos}, \left(u \in \left[0, \frac{T_{\cos}}{2}\right]\right).$ Beam length: $L = \int_0^{\frac{T_{\cos}}{2}} \sqrt{1 + (2\pi f_{\cos}A_{\cos})^2 \sin^2(2\pi f_{\cos}u)}\, du.$ (Curvature: $\omega_g(u) = \frac{4\pi^2 f_{\cos}^2 \lvert A_{\cos}\cos(2\pi f_{\cos}u)\rvert}{\left(1 + 4\pi^2 A_{\cos}^2 f_{\cos}^2 \sin^2(2\pi f_{\cos}u)\right)^{3/2}}.$ The i-th point: $\int_0^{u_i} \sqrt{1 + (2\pi f_{\cos}A_{\cos})^2 \sin^2(2\pi f_{\cos}u)}\, du - \frac{L}{n-1} = 0.$
Circular-arc beams		Shape function: $y(u) = R_{\text{arc}} - \sqrt{R_{\text{arc}}^2 - u^2}, (u \in [0, R_{\text{arc}}]).$ Beam length: $L = R_{\text{arc}}\theta_{\text{arc}}.$ Curvature: $\omega_g(u) = \frac{1}{R_{\text{arc}}}$ (constant). The i-th point: $u_i = R_{\text{arc}}\sin\left(\frac{i\theta_{\text{arc}}}{n_{\text{dp}} - 1}\right).$

Due to the low-dimensional nature of the proposed CoSCME model, accurately fitting the initial shape of the beam using polynomials presents challenges. Hence, the multiple linear regression method is employed to better determine the generalized coordinates used for describe initial shape. By setting up an overdetermined system of equations and using the least squares method, the desired initial generalized coordinates can be determined. The setup of multiple linear regression equations is mainly based on: $\omega_g\left(x_i\right) = \omega^*\left(\boldsymbol{\alpha}_n^*, s_i\right)$ and can be transformed into the standard linear regression matrix form as in Eq. (4.38):

$$\boldsymbol{\omega_g} = \frac{1}{L}\boldsymbol{\psi}\boldsymbol{\alpha}^* + \boldsymbol{\epsilon}, \tag{4.38}$$

where, the $\boldsymbol{\epsilon}$ denotes the error between given value and calculated value. The expanded form is shown in Eq. (4.39):

$$\begin{bmatrix} \omega_g(x_1) \\ \omega_g(x_2) \\ \vdots \\ \omega_g(x_n) \end{bmatrix} = \frac{1}{L} \begin{bmatrix} \psi_0(s_1) & \psi_1(s_1) & \psi_2(s_1) & \psi_3(s_1) & \psi_4(s_1) & \psi_5(s_1) \\ \psi_0(s_2) & \psi_1(s_2) & \psi_2(s_2) & \psi_3(s_2) & \psi_4(s_2) & \psi_5(s_2) \\ \vdots & \vdots & \vdots & \vdots & \vdots & \vdots \\ \psi_0(s_n) & \psi_1(s_n) & \psi_2(s_n) & \psi_3(s_n) & \psi_4(s_n) & \psi_5(s_n) \end{bmatrix} \begin{bmatrix} \alpha_0^* \\ \alpha_1^* \\ \alpha_2^* \\ \alpha_3^* \\ \alpha_4^* \\ \alpha_5^* \end{bmatrix} + \begin{bmatrix} \epsilon_1 \\ \epsilon_2 \\ \vdots \\ \epsilon_n \end{bmatrix}. \tag{4.39}$$

Then, the least squares method is applied to solve for this multiple linear regression problem. The principle of the least squares method is to find a vector $\boldsymbol{\alpha}^*$ that minimizes the Euclidean norm of the error vector $\boldsymbol{\epsilon}$, as expressed in Eq. (4.40).

$$\underset{\boldsymbol{\alpha}^* \in \mathbb{R}}{\text{minimize}} \ \|\boldsymbol{\epsilon}\|^2 = \underset{\boldsymbol{\alpha}^* \in \mathbb{R}}{\text{minimize}} \left(\sqrt{\sum_{m=1}^{m=n} \epsilon_m^2} \right)^2 = \underset{\boldsymbol{\alpha}^* \in \mathbb{R}}{\text{minimize}} \left(\boldsymbol{\omega}_\mathbf{g} - \frac{1}{L} \boldsymbol{\psi} \boldsymbol{\alpha}^* \right)^T \left(\boldsymbol{\omega}_\mathbf{g} - \frac{1}{L} \boldsymbol{\psi} \boldsymbol{\alpha}^* \right) \tag{4.40}$$

After expanding the sum of squared errors, take the partial derivative with respect to $\boldsymbol{\alpha}^*$. Then, set the resulting partial derivative to zero since the derivative is zero at the minimum value. The matrix $\boldsymbol{\psi}^T \boldsymbol{\psi}$ is invertible, thus, directly use Eq. (4.41) can successfully obtain the value of $\boldsymbol{\alpha}^*$.

$$\boldsymbol{\alpha}^* = (\boldsymbol{\psi}^T \boldsymbol{\psi})^{-1} \boldsymbol{\psi}^T \boldsymbol{\omega}_\mathbf{g} \tag{4.41}$$

After determining the values of initial generalized coordinates $\boldsymbol{\alpha}^*$, the shape of the initially curved beam is defined. At this stage, it is feasible to apply the CoSCME to model the initially curved beam and derive the modeling results. To validate the proposed modeling approach for the initially curved beam, the method is applied to a classical case: modeling a compliant bistable mechanism with cosine-shaped beams. The modeling result can be found in Fig. 4.11. The geometric parameters used for describing this cosine-shaped beam is: $T = 180\text{mm}$, $A = 25\text{mm}$.

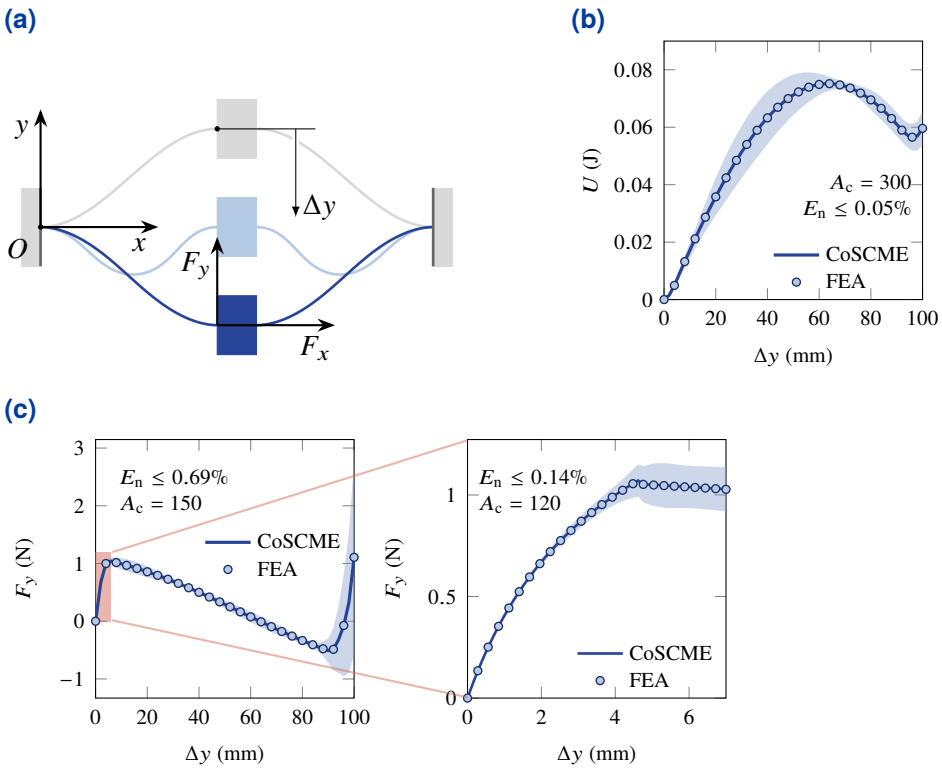


Fig. 4.11.: Case study of modeling a compliant bistable mechanism with initially curved beams. (a) Deformation results of the compliant bistable mechanism. The coordinate system, displacement direction, and reaction force are shown in the plot. (b) The strain energy curve during deformation. All results are validated by FEA simulations. The geometric parameters used describing this cosine-shaped beam is: $T = 180$mm, $A = 25$mm. (c) The modeling result of reaction force F_y. The figure on the right shows a zoomed-in result for more detail.

Although the CoSCME has been proven to have high modeling accuracy, the beam shape fitting accuracy has not yet been investigated. The most important factor that affects the fitting accuracy is the number of sampling points. Hence, a convergence analysis is conducted by evaluating the relationship between fitting accuracy and different numbers of sampling points. The convergence results can be seen in Fig. 4.12. The results prove that the fitting becomes more accurate when more sampling points are adopted in the fitting process. The error is simplified by evaluating the tip position error (E_P). Additionally, the convergence criterion is defined by the position error, which must be less than 0.01% of the half period (90 mm) to be considered converged, specifically requiring it to be below 0.009 mm for this analysis. The values that meet the convergence criteria are highlighted in red. A position error of 0.0087 mm was achieved in the convergence analysis using 100 sampling points. Consequently, 100 sampling points were determined to be optimal, providing a good balance between fitting accuracy and complexity.

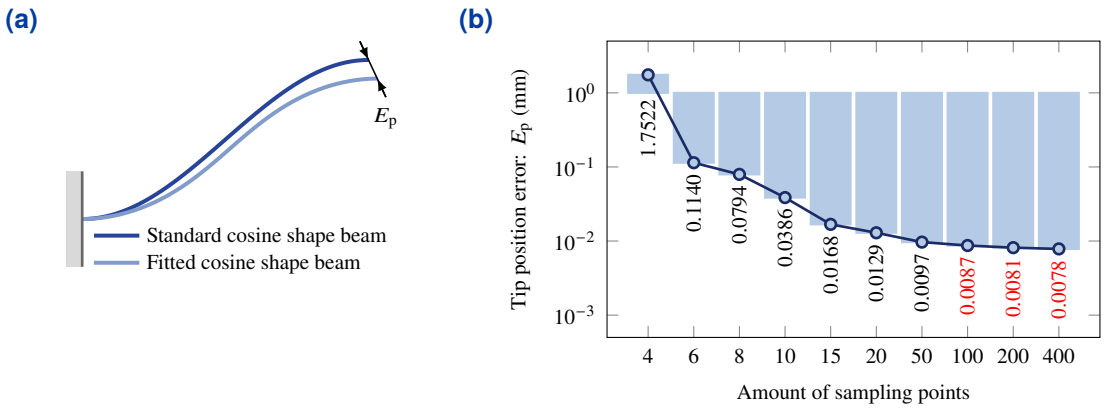


Fig. 4.12.: Convergence analysis of beam shape fitting. (a) Error comparison between the standard and fitted cosine-shaped beams. (b) Convergence analysis results.

Theoretically, any shape of an initially curved beam can be modeled as long as the shape is a continuous curve and its curvature function can be expressed or calculated. Once the curvature function is defined, the initial generalized coordinates can be determined using multiple linear regression. Subsequently, the CoSCME can be employed to model various types of beams, such as Bezier curves and other complex shapes. This approach allows for a broader range of potential application scenarios beyond the commonly studied cosine-shaped and circular arc beams, significantly expanding the versatility and scope of beam modeling in practical applications.

4.3 Discussion

4.3.1 Discussion of Modeling Results

The results obtained using the CoSCME demonstrate strong agreement with FEA simulation results, confirming its accuracy in modeling large-deformation behavior in compliant mechanisms. However, certain deviations from FEA results occur in specific cases, particularly under extreme deformations. These deviations, as well as the model's strengths and limitations, are analyzed below in the order of the case studies.

The CoSCME model accurately predicts beam buckling behavior, capturing both the critical buckling load and pre-buckling deformation. The predicted Euler buckling load deviates by only 1.01% from theoretical and FEA results. The pre-buckling stage is well approximated due to the incorporation of axial deformation, which was absent in previous

SCME. However, post-buckling deviations arise where large deformations introduce strong geometric nonlinearities. The largest normalized relative error in force prediction is 0.28% for compresural beams, where polynomial fitting may struggle to capture sharp changes in curvature. The Poisson effect is expected to have a tiny influence here since buckling is dominated by bending instability. These results confirm CoSCME's applicability for stability and buckling analysis of slender beams.

The modeling results for BPMs and CBPMs demonstrate CoSCME's capability to handle axially stretched compliant structures. CoSCME successfully predicts force-displacement relationships of BPMs, with FEA validation showing less than 0.03% error in force predictions. The model also accurately captures the parasitic motion of BPMs, where lateral deflection predictions align well with FEA results. For CBPMs, where axial stretch is more pronounced, the largest deviation in force prediction occurs at highest beam elongation ($\Delta L_{\text{tip}} = 0.5mm$), which might due to the influence by Poisson effect, which is neglected in the model but contributes to additional lateral contraction, affecting force predictions. Overall, the results confirm that axial elongation effects are well captured, but future work incorporating the Poisson effect would further improve accuracy, particularly for highly tensile structures.

The CoSCME successfully models snap-through behavior in bistable mechanisms, accurately predicting force-displacement relationships with an error below 1.33%. Near the transition point, the deviation does not increase even with strong nonlinear behavior, where the error is less than 0.37%. The energy barrier is predicted, confirming that the model captures equilibrium configurations well. In preloaded rotational bistable mechanisms, CoSCME correctly predicts rotational bistability, with error less than 0.15%. Despite these minor deviations, CoSCME maintains high modeling accuracy for bistable mechanisms.

The multiple beam modeling capability of CoSCME is validated through the general lumped-compliance beam case study, where it successfully predicts load response relationship with high accuracy, while error is less than 0.02% compared to FEA. Different structural configurations are well captured, confirming its adaptability across a wide range of boundary conditions. The model effectively handles coordinate transformation effects, showing high accuracy even in complex layouts. Overall, CoSCME proves versatile and accurate in modeling multi-beam compliant mechanisms.Besides, the case study of initially curved beam demonstrates CoSCME's ability to model various initially curved shaped beams, including cosine, circular-arc, and arbitrary shapes. The nonlinear force-displacement behavior is also well captured with maximum error of 0.69%. The main sources of error

include limitations in multiple linear regression for initial curvature fitting, which could be improved by using a higher-order fitting function. Despite these limitations, CoSCME effectively captures the behavior of initially curved beams.

In summary, CoSCME achieves high accuracy across all case studies, validating its effectiveness for modeling large-deformation compliant mechanisms. The largest deviations arise in cases with significant deformations, particularly when axial elongation is pronounced. To further improve the model, future work should focus on incorporating Poisson effects to capture lateral contraction and improve axial deformation accuracy, enhancing post-buckling modeling through higher-order curvature fitting, and extending the method to include material nonlinearity, allowing for applications beyond linear-elastic materials. In addition, future studies may explore the use of wide Bézier curve equations to describe the beam neutral axis instead of polynomial representations, which could potentially improve modeling accuracy [232, 233].

4.3.2 Method Comparison

To evaluate the performance of the proposed CoSCME method, the proposed method is compared with CPRBM, CBCM, and high-order SCME using a translational bistable mechanism with straight beams as the modeling target, as described in section 4.2.3. The inclined angle (θ) of the translational bistable mechanism is set to 80 degrees to achieve significant large deformation. The geometric parameters of the beam are as follows: $T = 0.8$ mm, $L = 100$ mm, $W = 10$ mm, and the vertical displacement is set to $\Delta y = 155$ mm. The material properties are the same as those used in the case studies. The CBCM and CPRBM models use 10 and 20 beam elements, respectively, where the number of beam elements is denoted as n_{FEA}. The comparison considers key factors such as modeling error (normalized relative error e_n), time cost (modeling time in seconds), bending and axial deformation, and the number of variables and beam elements. The step tolerance (*StepTolerance*) and optimality tolerance (*OptimalityTolerance*) for these methods are all specified as 1×10^{-10}, ensuring that the optimization process achieves a satisfactory precision. All other parameters are kept at their default values in fmincon. Time cost is measured using the embedded function in MATLAB. The computer used for this comparison analysis is a desktop equipped with an Intel Core i7-9700 3.0 GHz processor, 32 GB of DDR4 RAM, and an AMD Radeon RX 550 graphics card. The MATLAB version is R2022b, running on Windows 11 Enterprise Edition. The comparison results are presented in Table 4.3.

Tab. 4.3.: Comparison of different modeling methods for a translational bistable mechanism. The comparison includes modeling error (normalized relative error E_n), time cost (modeling time in seconds), consideration of bending and axial deformation, and the number of variables and beam elements.

	E_n (max)	Time cost (s)	Bending deformation	Axial deformation	Variables count	Beam element count
FEA simulation	-	125	✓	✓	-	100
CPRBM(n_b=10)	6.209%	4.54	✓		10	10
CPRBM(n_b=20)	4.785%	7.17	✓		20	20
CBCM(n_b=10)	2.451%	7.62	✓	✓	30	10
CBCM(n_b=20)	0.125%	18.23	✓	✓	60	20
SCME (5th-order)	2.072%	0.0375	✓		6	1
CoSCME (5th-order)	1.003%	7.39	✓	✓	12	1

The modeling error results show that CBCM ($n_b = 20$) achieves the highest accuracy, with an error as low as 0.125%. The proposed CoSCME (5th-order) achieves 1.003%, which is significantly lower than SCME (2.072%) and CPRBM (ranging from 4.785% to 6.209%). In terms of time cost, SCME (5th-order) is the fastest, with a modeling time of 0.0375 seconds, but it sacrifices accuracy and does not account for axial deformation. Although CBCM ($n_b = 20$) provides the highest accuracy, it requires the longest modeling time at 18.23 seconds. CoSCME offers a balanced performance, maintaining relatively high accuracy with a moderate modeling time of 7.39 seconds.

All models capture bending deformation, but only CBCM ($n_b = 10, 20$) and CoSCME account for both bending and axial deformation. In terms of complexity, FEA has the highest computational cost, with 100 beam elements. CoSCME (5th-order) reduces the number of variables to 12 while using only a single beam element, achieving a balance between accuracy and time cost. Overall, CBCM ($n_b = 20$) is the most accurate but computationally demanding, while SCME is the fastest but less accurate. CoSCME achieves a favorable trade-off between accuracy and efficiency, making it a promising approach for compliant mechanism modeling.

4.4 Chapter Summary

In this chapter, the CoSCME was proposed and thoroughly reviewed, particularly highlighting its consideration of axial deformation compared to the original high-order SCME. The significant contributions of the CoSCME lie in its successful application to model various distinct mechanisms, demonstrating its versatility and effectiveness in accurately capturing the behavior of complex compliant structures. By incorporating the effects of

axial deformation, the CoSCME expands the application scenarios and makes it a valuable tool in the analysis and design of compliant mechanisms.

Despite its advantages, the CoSCME has certain limitations that need to be acknowledged. Firstly, the current method neglects spatial deformation, which can impact the accuracy when dealing with three-dimensional structures or those subjected to significant out-of-plane forces. Secondly, the plane stress assumption limits the applicability of the method to specific loading conditions, potentially reducing its accuracy in complex stress environments. Lastly, the CoSCME does not account for the response behavior under both displacement and force simultaneously, which restricts its ability to fully capture the mechanical response in certain scenarios. These limitations suggest that while CoSCME is effective, there is room for improvement to enhance its modeling capabilities.

5 Bi-level optimization framework: Tailoring kinetostatic behavior of bistable mechanisms

Although research interest in compliant bistable mechanisms has increased in recent years, a critical review of the literature indicates that most existing studies are primarily application oriented, with limited attention given to the systematic optimization of the structural performance of the bistable mechanisms themselves [234]. For example, in applications where bistable mechanisms function as mechanical switches, the force thresholds required for forward and backward transitions are often asymmetric. This asymmetry compromises reliability, as the system may more easily revert to the lower-energy state unintentionally [235]. Several earlier works have proposed solutions such as applying prestress or using multiple materials to balance switching thresholds [236, 237]. However, these methods often increase design complexity and hinder miniaturization, thereby limiting their applicability in compact scenarios such as MEMS. Therefore, proposing an integrated optimization approach for single degree-of-freedom bistable mechanisms is of critical importance.

To address the absence of systematic optimization in compliant bistable mechanism design, this study proposes a bi-level optimization framework aimed at tailoring their kinetostatic performance using a single-material design without prestress. Bi-level optimization refers to a hierarchical optimization structure in which one optimization problem (the upper level optimization) contains another optimization problem (the lower level optimization) as a subproblem or constraint [238].

Designs of compliant bistable mechanisms can be broadly categorized into three types: distributed-compliance bistable mechanisms, lumped-compliance bistable mechanisms, and topology-optimized bistable mechanisms. These types differ significantly in their structural composition, design flexibility, computational cost, and manufacturing feasibility. A comparative analysis of the three types is presented in Table 5.1.

Distributed-compliance bistable mechanisms typically consist of a single continuous flexible beam in which deformation is distributed along the entire structure [239]. Owing to their structural simplicity, these mechanisms are easy to fabricate using conventional

techniques. However, the tunability is significantly limited by small number of design variables, typically only the beam length and inclination angle, which restricts their ability to achieve complex or highly customized kinetostatic responses. Consequently, their design flexibility is inherently limited. Besides, the deformation range of such mechanism within allowable stress range is relatively small as well.

In addition, topology-optimized bistable mechanisms represent the other extreme, wherein the material distribution within a design domain is optimized to achieve desired response [240]. This approach provides extremely high design freedom, enabling the customization of complex force-displacement behaviors and tailored responses. Nevertheless, such advantages come at the cost of high computational complexity and significant manufacturing difficulty, as the resulting geometries are often highly intricate and incompatible with traditional fabrication methods.

In contrast, lumped-compliance bistable mechanisms offer a favorable trade-off between flexibility and practicality [106, 207]. These mechanisms consist of two flexible beams connected by an intermediate rigid frame, which concentrates deformation in designated regions while maintaining overall structural clarity. This configuration introduces additional design variables, including the lengths and inclination angles of both beams, as well as the dimensions of the rigid frame, resulting in a moderate total variable count. This expanded design space significantly enhances the potential for performance optimization compared with distributed-compliance designs, while still maintaining a structure that is easy to analyze and fabricate. Although they do not reach the theoretical design freedom of topology-optimized mechanisms, lumped-compliance mechanisms avoid the excessive structural complexity and manufacturing constraints associated with the latter. It is worth noting that, when the dimension of the rigid frame is reduced to zero, the lumped-compliance model degenerates into a distributed-compliance beam. Therefore, the design domain of the lumped-compliance model inherently includes that of the distributed-compliance counterpart.

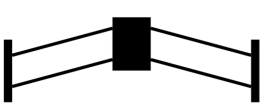
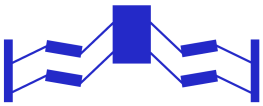
In addition, the lumped-compliance mechanism offers several distinct structural and functional advantages beyond its suitability for optimization. First, the inclusion of an intermediate rigid frame enables enhanced primary stiffness, which can contribute to a reduced footprint and improved load-bearing capacity. Second, the rigid frame can serve as a contact interface with other components, supporting applications such as mechanical stoppers or variable stiffness elements. Third, it provides a convenient location for direct actuation, simplifying integration with external actuators or control mechanisms.

Furthermore, it facilitates internal connectivity with other counterparts, allowing for performance enhancements such as increased bearing stiffness and reduced parasitic motion. Importantly, this configuration extends the design space by introducing additional intermediate parameters, offering greater flexibility for fine-tuning the mechanism's behavior according to specific functional requirements.

At the current stage, the proposed configuration employs a basic lumped-compliance configuration consisting of two compliant beams and one intermediate rigid frame. However, the framework is not limited to this specific topology. Building upon the underlying principles and theoretical foundation established in this work, future designs can incorporate more complex architectures featuring additional beams and rigid frames. Such extensions would introduce a further greater number of adjustable geometric parameters, thereby further enhancing the flexibility and applicability of the optimization framework. Moreover, the beam-to-frame connection types are not restricted to fixed or rigid joints; alternative connections such as pin joints or other compliant interfaces can also be considered. These variations would further enrich the design space, allowing for tailored mechanical behavior to meet diverse functional requirements across a wide range of applications.

Based on these considerations, the lumped-compliance bistable mechanism emerges as the most suitable configuration for optimization-driven design. It strikes a balance between structural complexity and customizability, enabling effective bistable behavior to be achieved through geometry-level parameter tuning, without resorting to computationally intensive topology optimization or sacrificing manufacturability. In this work, the upper-level problem determines the geometric parameters of the mechanism, while the lower-level problem solves for the equilibrium configuration and evaluates mechanical performance based on the analytical model.

Tab. 5.1.: Comparison of single-beam, lumped-compliance, and topology-optimized bistable mechanisms across multiple aspects, including structural complexity, design variables, customizability, and manufacturing difficulty. All three compared bistable mechanisms are based on single-material configurations. Among them, the lumped-compliance bistable mechanism is selected for integration into the proposed bi-level optimization framework.

	Distributed-compliance bistable mechanism	**Lumped-compliance bistable mechanism**	**Topology-optimized bistable mechanism**
Schematic diagram			
Component type	Single straight compliant beam	**Two straight compliant beams connected by intermediate rigid frame**	Discretized structural elements
Structural complexity	Low	**Moderate**	High
Design variables	Beam length and inclination angle	**Each beam's length and inclination angle; size of rigid frame**	Material distribution
Variable count	2	**6**	-
Customizability	Low	**Moderate**	High
Manufacturing sensitivity	Insensitive	**Insensitive**	Sensitive
Modeling methods	FEA, CoSCME, CBCM, CPRBM, etc.	**FEA, CoSCME, CBCM, CPRBM, etc.**	FEA, SIMP, LSM, ESO, etc. [241]

At the upper level, the optimization is primarily responsible for determining the geometric configuration of the compliant mechanism by selecting key design variables, such as beam lengths, inclination angles, and the position of the intermediate rigid frame. Serving as the macro-level decision-making layer, it governs the overall structural layout and directly influences the performance of the system. By decoupling geometric design from physical behavior modeling, the upper level simplifies the optimization problem and significantly reduces computational complexity. It treats the lower-level modeling process as a black-box evaluator, relying solely on performance metrics returned from the lower level to guide the search process. A global optimization algorithm, i.e. the Genetic Algorithm, is employed to explore the design space efficiently without requiring gradient information, making it suitable for non-convex and high-dimensional problems. This hierarchical structure enables modular, flexible, and scalable optimization, enhancing the effectiveness and generalizability of the overall design framework. The optimization variables are listed in Tab. 5.2.

In this study, a uniform beam thickness is assumed throughout the optimization framework. This choice is motivated by both practical and modeling considerations. From a fabrication

perspective, compliant mechanisms with uniform thickness are easier to manufacture, particularly when constructed by cutting flat sheet materials and assembling them with rigid components. From a modeling point, the effect of thickness on beam stiffness can be compensated by adjusting other geometric parameters, such as beam length, thus allowing the design objectives to be achieved without explicitly including thickness as an optimization variable.

Tab. 5.2.: Optimization variables and their corresponding symbols.

Variable name	Symbol	Unit
Beam A length	L_A	mm
Beam B length	L_B	mm
Inclination angle of Beam A	θ_A	deg
Inclination angle of Beam B	θ_B	deg
Lateral size of rigid frame	x_{fr}	mm
Vertical size of rigid frame	y_{fr}	mm

At the lower level, the optimziation objective is to determine the kinetostatic behavior of compliant bistable mechanisms through displacement-driven analytical modeling. It is worth mentioning that transitions between stable configurations typically involve snap-through behavior, which is a rapid configuration change when the applied load exceeds a critical threshold. This abrupt motion is governed by a complex coupling between geometric parameters and kinetostatic response. Force-driven modeling techniques are particularly challenging for capturing bistable responses due to the presence of snap-through behavior. Numerous previously proposed methods have demonstrated the capability to resolve such displacement-driven problems, and each can be integrated into the proposed lower-level optimization [242, 95, 99, 124]. In this specific work, the analytical model employed is the comprehensive energy method based on the smooth curvature model (CoSCME) [125]. CoSCME is a nonlinear large-deformation modeling approach that extends the smooth curvature model by incorporating the principle of minimum strain energy while accounting for both bending and axial deformations. It provides a reliable way to characterize the equilibrium and force-displacement response of compliant mechanisms.

In summary, the objective of this optimization framework is to design bistable mechanisms composed of lumped-compliance beams. The performance is evaluated using the CoSCME method, which captures nonlinear large deformations, aiming to enable tailored kinetostatic responses for various design tasks. Compared to conventional bistable mechanisms, the proposed lumped-compliance bistable mechanism offers more tunable parameters and improved controllability of the kinetostatic behavior. In contrast to topology-optimized

structures, it features geometrically regular beams, making it more suitable for practical manufacturing. The key features and novelties of the proposed bi-level optimization framework are summarized as follows:

1. **Featuring a modular bi-level optimization structure:**
   The separation of geometry exploration (upper level) and mechanical evaluation (lower level) allows efficient search in complex design spaces, while maintaining modeling flexibility.

2. **Employing high-fidelity displacement-driven modeling method:**
   The framework employs the CoSCME-based analytical model that accurately captures both bending and axial effects, enabling high-fidelity simulation of nonlinear responses under prescribed displacements.

3. **Focusing on geometry-driven optimization:**
   By eliminating the reliance on prestress or multi-material construction, the framework achieves advanced mechanical behaviors through single-material, fabrication-friendly configurations.

4. **Supporting various optimization objectives:**
   The framework supports both single and multiple optimization objectives, allowing it to address various functional requirements such as achieving symmetric forces and enhancing the linearity of the kinetostatic response.

5. **Exhibiting strong extensibility through methodological extensions:**
   The proposed bi-level optimization framework exhibits strong extensibility, with potential to be expanded toward topology-level configuration search, boundary and load condition optimization, and surrogate-assisted multi-stage strategies for enhanced computational efficiency.

Two representative case studies are conducted in this paper to investigate the potential for functional effectiveness of the proposed bi-level optimization framework.

For the first case study, in bistable mechanisms, achieving equal forward and backward switching forces allows bistable units to maintain stable equilibrium in both states, improving the robustness of large-scale assemblies and enhancing their practical applicability. Achieving equal switching force in a bistable compliant mechanism is a significant op-

timization objective. In classical bistable systems, the forward and backward switching forces, corresponding to transitions from the first to second stable state and vice versa, are often unequal due to structural asymmetry or energy landscape imbalance. This asymmetry can complicate actuation control and limit the practical utility of bistable components in applications requiring reversible and repeatable switching, such as soft robotics, mechanical memory, and deployable systems [243]. In addition, a bistable mechanism with symmetric switching force is generally considered more robust in its second equilibrium position, which is crucial for structural stability. For example, in multi-mode morphing wing designs composed of bistable units, asymmetric force responses of individual units have been shown to compromise overall stability and limit practical applicability [244].

For the second case study, the bistable mechanisms exhibit inherent negative stiffness during configuration transitions. This characteristics is often utilized by combining them with components that have positive linear stiffness to design constant-force or zero-force mechanisms [245, 246, 247]. Such constant stiffness systems are highly valuable in compliant constant force grippers [50, 54] for protecting gripping objectives and harvesting energy from the environment [248, 249]. Conventional bistable mechanisms suffer from two major limitations: (1) the negative stiffness region often deviates from linearity, resulting in reduced control accuracy; and (2) designs with stronger linearity typically exhibit limited motion range. This case study conducts an multi-objective optimization to deal with this problem, further demonstrating the scaleability of proposed bi-level optimization framework.

With the motivations and novelties clarified, the remainder of this chapter is organized as follows: Section 5.1 introduces the proposed bi-level optimization framework, detailing both the upper-level geometric optimization and the lower-level kinetostatic modeling based on the CoSCME method. Section 5.2 presents two representative case studies to demonstrate the effectiveness of the framework in achieving distinct performance objectives, including symmetric switching force and constant negative stiffness. Section 5.3 discusses the application scope, limitations, and potential methodological extensions of the proposed framework. Finally, Section 5.4 concludes the chapter and outlines future research directions.

5.1 Bi-level Optimization Framework

To better illustrate the interaction between design exploration and kinetostatic behavior evaluation, a detailed flowchart is presented in Figure 5.1. In this framework, a set of geometric parameters that guiding the structural configuration of the general lumped compliant beam is determined first. These parameters are then passed to the lower-level solver, where the CoSCME method is used to determine the equilibrium configuration by minimizing the total strain energy subject to kinematic constraints. The resulting kinetostatic response is then evaluated against the specified performance objectives, such as force–displacement relationship or energy-displacement relationship. The obtained results are returned to the upper-level optimization as performance indicators. At the upper level, the main objective is to continuously search for optimal parameter vectors that yield better performance. This modular and hierarchical structure enables integration of mechanical modeling and optimization, supporting extensibility across various design tasks.

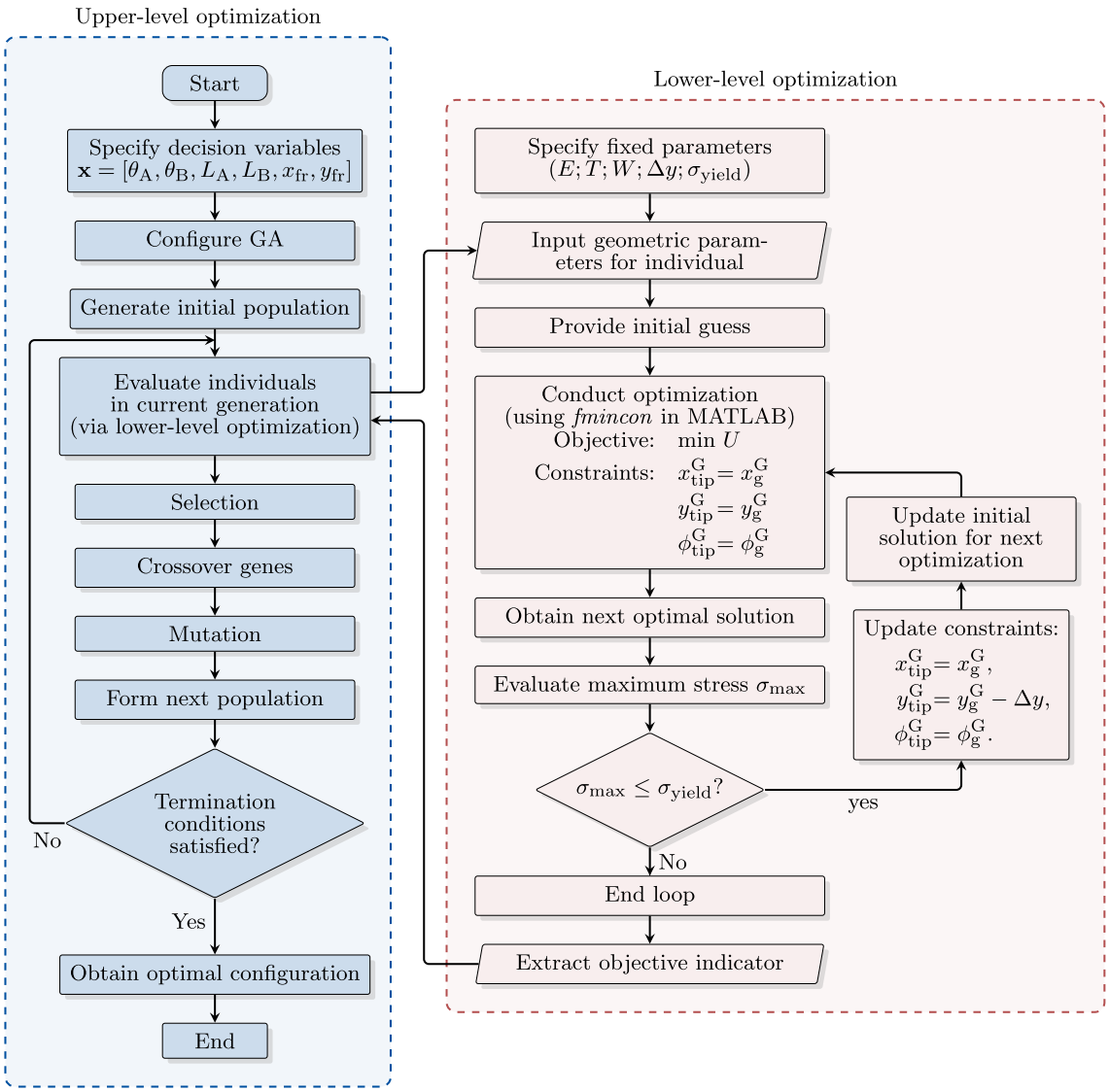


Fig. 5.1.: The flowchart of bi-level optimization.

The remaining content of this chapter provides a detailed introduction to both the upper and lower levels of the optimization framework. The lower-level formulation is introduced first, outlining the CoSCME-based modeling procedure for obtaining equilibrium configurations. This is followed by the upper-level optimization, which focuses on the selection and adjustment of geometric design variables to achieve target performance metrics. These sections collectively provide an overview of the hierarchical strategy employed in the design of compliant bistable mechanisms.

5.1.1 Lower-level optimization

The main focus of this section is the modeling procedure for the kinetostatic behavior of general lumped-compliance beams defined by specific geometric design variables. The kinetostatic model used in this study builds upon the formulation previously introduced in chapter 4, i.e. the CoSCME method, where it was applied to model the deformation of compliant mechanisms composed of serially connected beam segments. In the original formulation, beam A was assumed to be anchored at the origin, which limited the flexibility in representing more general planar configurations. To overcome this limitation, an additional coordinate transformation is introduced to allow beam A to rotate arbitrarily within the plane. This enhancement enables the modeling of more diverse spatial arrangements between connected beam segments, thereby improving the generality and expanding the design space for optimization. The coordinate systems and key notations defined for modeling general lumped-compliance beams are illustrated in Figure 5.2.

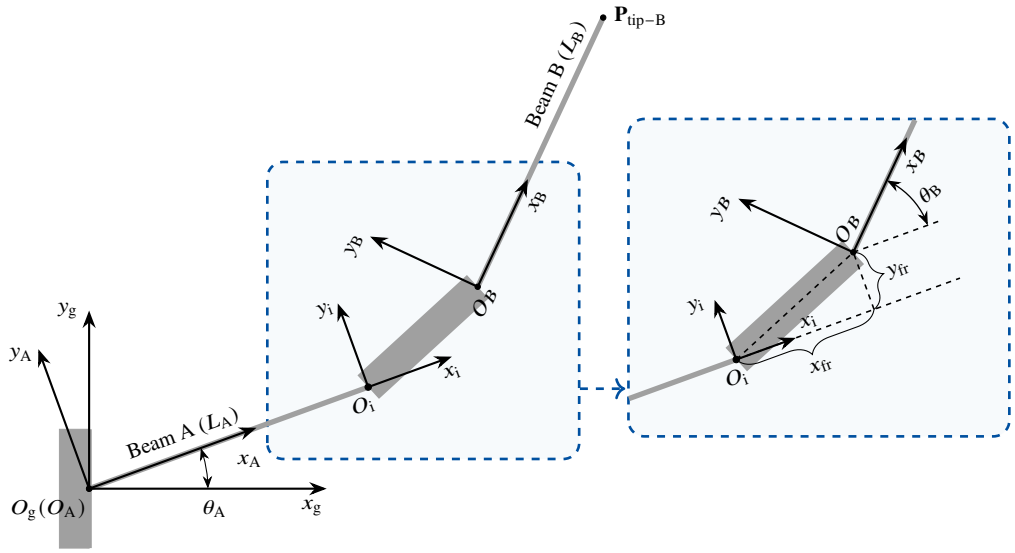


Fig. 5.2.: Definition of geometric layout and coordinate systems of lumped-compliance beam. The beams are rigidly connected to each other without hinges.

As demonstrated in Figure 5.2, four coordinate systems are defined to describe the deformation of the general lumped-compliance beam: the global coordinate system ($\mathcal{R}^{\mathrm{G}} - O_{\mathrm{g}} x_{\mathrm{g}} y_{\mathrm{g}}$), the local coordinate system for beam A ($\mathcal{R}^{\mathrm{A}} - O_{\mathrm{A}} x_{\mathrm{A}} y_{\mathrm{A}}$), the intermediate coordinate system ($\mathcal{R}^{\mathrm{I}} - O_{\mathrm{i}} x_{\mathrm{i}} y_{\mathrm{i}}$), and the local coordinate system of beam B ($\mathcal{R}^{\mathrm{B}} - O_{\mathrm{B}} x_{\mathrm{B}} y_{\mathrm{B}}$). The global coordinate system $\mathcal{R}^{\mathrm{G}}$ is fixed to the ground. The local coordinate system of beam A ($\mathcal{R}^{\mathrm{A}}$) is defined based on the initial inclination angle θ_{A} of beam A in the global frame. Specifically, the x_{A}-axis is aligned with the axial direction of beam A in its

undeformed configuration. This formulation allows the initial orientation of beam A to be adjusted, thereby improving the model's generality. An intermediate coordinate system $\mathcal{R}^{\mathrm{I}}$ is introduced to describe the geometric relationship between beam A and beam B. Its origin is located at the tip of beam A, and the x_{i}-axis is aligned with the tip deflection direction of beam A. The position and orientation of the local coordinate system $\mathcal{R}^{\mathrm{B}}$ of beam B with respect to $\mathcal{R}^{\mathrm{I}}$ is denoted by $(x_{\mathrm{fr}}, y_{\mathrm{fr}})$ and an angle θ_{B}. These quantities remain constant during deformation, reflecting the rigid connection between the two beams. The tip position of beam B in its own coordinate system is denoted as $\mathbf{P}^{\mathrm{B}}_{\text{tip-B}}$.

The tip position of the beam B expressed in the global coordinate system, denoted as $\mathbf{P}^{\mathrm{G}}_{\text{tip-B}}$, is obtained through a sequence of coordinate transformations. Specifically, the transformation follows:

$$\begin{bmatrix} x^{\mathrm{G}}_{\text{tip-B}} \\ y^{\mathrm{G}}_{\text{tip-B}} \\ 1 \end{bmatrix} = T^{\mathrm{G}}_{\mathrm{A}} \cdot T^{\mathrm{A}}_{\mathrm{I}} \cdot T^{\mathrm{I}}_{\mathrm{B}} \cdot \begin{bmatrix} x^{\mathrm{B}}_{\text{tip-B}} \\ y^{\mathrm{B}}_{\text{tip-B}} \\ 1 \end{bmatrix}, \tag{5.1}$$

where, $x^{\mathrm{G}}_{\text{tip-B}}$ and $y^{\mathrm{G}}_{\text{tip-B}}$ denote the tip position of beam B within global coordinate system $\mathcal{R}^{\mathrm{G}}$. The aforementioned transformation matrices are defined as follows:

- $T^{\mathrm{I}}_{\mathrm{B}}$ transforms coordinates from local coordinate system of beam B ($\mathcal{R}^{\mathrm{B}}$) to the intermediate coordinate system $\mathcal{R}^{\mathrm{I}}$.

$$T^{\mathrm{I}}_{\mathrm{B}} = \begin{bmatrix} \cos\theta_B & -\sin\theta_B & x_{\mathrm{fr}} \\ \sin\theta_B & \cos\theta_B & y_{\mathrm{fr}} \\ 0 & 0 & 1 \end{bmatrix} \tag{5.2}$$

- $T^{\mathrm{A}}_{\mathrm{I}}$ transforms coordinates from the intermediate coordinate system $\mathcal{R}^{\mathrm{I}}$ to the local coordinate system of beam A ($\mathcal{R}^{\mathrm{A}}$).

$$T^{\mathrm{A}}_{\mathrm{I}} = \begin{bmatrix} \cos\phi^{\mathrm{A}}_{\text{tip-A}} & -\sin\phi^{\mathrm{A}}_{\text{tip-A}} & x^{\mathrm{A}}_{\text{tip-A}} \\ \sin\phi^{\mathrm{A}}_{\text{tip-A}} & \cos\phi^{\mathrm{A}}_{\text{tip-A}} & y^{\mathrm{A}}_{\text{tip-A}} \\ 0 & 0 & 1 \end{bmatrix} \tag{5.3}$$

- $T_{\mathrm{A}}^{\mathrm{G}}$ transforms coordinates from the local coordinate system of beam A ($\mathcal{R}^{\mathrm{A}}$) to the global coordinate system $\mathcal{R}^{\mathrm{G}}$.

$$T_{\mathrm{A}}^{\mathrm{G}} = \begin{bmatrix} \cos\theta_{\mathrm{A}} & -\sin\theta_{\mathrm{A}} & 0 \\ \sin\theta_{\mathrm{A}} & \cos\theta_{\mathrm{A}} & 0 \\ 0 & 0 & 1 \end{bmatrix} \tag{5.4}$$

At this stage, the tip coordinates $x_{\text{tip-B}}^{\mathrm{G}}$ and $y_{\text{tip-B}}^{\mathrm{G}}$ have been determined through coordinate transformation. To fully describe the beam tip configuration in the global coordinate system, the orientation of beam tip with respect to the global frame is formulated as follows:

$$\phi_{\text{tip}-\mathrm{B}}^{\mathrm{G}} = \theta_{\mathrm{A}} + \phi_{\text{tip}-\mathrm{A}}^{\mathrm{A}} + \theta_{\mathrm{B}} + \phi_{\text{tip}-\mathrm{B}}^{\mathrm{B}}, \tag{5.5}$$

where, $\phi_{\text{tip}-\mathrm{B}}^{\mathrm{G}}$ denotes the orientation of beam tip in the global coordinate system.

The method used to determine the equilibrium configuration is based on the principle of minimum strain energy, which states that equilibrium is achieved when the strain energy reaches its minimum. Accordingly, the strain energy in the compliant beam is required to be formulated, as expressed in:

$$\begin{aligned} U = {} & \frac{EI}{2}\int_0^{L_{\mathrm{A}}} \omega^{\mathrm{A}}(\boldsymbol{\alpha}^{\mathrm{A}}, s)^2 ds + \frac{EI}{2}\int_0^{L_{\mathrm{B}}} \omega^{\mathrm{B}}(\boldsymbol{\alpha}^{\mathrm{B}}, s)^2 ds \\ & + \frac{EA}{2}\int_0^{L_{\mathrm{A}}} \varepsilon_a^{\mathrm{A}}(\boldsymbol{\beta}^{\mathrm{A}}, s)^2 ds + \frac{EA}{2}\int_0^{L_{\mathrm{B}}} \varepsilon_a^{\mathrm{B}}(\boldsymbol{\beta}^{\mathrm{B}}, s)^2 ds \end{aligned} \tag{5.6}$$

At this stage, all the kinetostatic formulations required for the lower-level optimization have been derived. For each design instance, the specified beam tip position and orientation serve as position constraints, while the strain energy minimization serves as the optimization objective. The overall objective function of the lower-level optimization problem is:

$$\underset{\boldsymbol{\alpha},\boldsymbol{\beta} \in \mathbb{R}}{\text{minimize}} \qquad U(\boldsymbol{\alpha}^{\mathrm{A}}, \boldsymbol{\alpha}^{\mathrm{B}}, \boldsymbol{\beta}^{\mathrm{A}}, \boldsymbol{\beta}^{\mathrm{B}})$$

$$
\begin{aligned}
\text{Subject to} \quad & x^{\mathrm{G}}_{\mathrm{tip-B}}(\boldsymbol{\alpha}^{\mathrm{A}}, \boldsymbol{\alpha}^{\mathrm{B}}, \boldsymbol{\beta}^{\mathrm{A}}, \boldsymbol{\beta}^{\mathrm{B}}) = x^{\mathrm{G}}_{\mathrm{g}}, \\
& y^{\mathrm{G}}_{\mathrm{tip-B}}(\boldsymbol{\alpha}^{\mathrm{A}}, \boldsymbol{\alpha}^{\mathrm{B}}, \boldsymbol{\beta}^{\mathrm{A}}, \boldsymbol{\beta}^{\mathrm{B}}) = y^{\mathrm{G}}_{\mathrm{g}}, \\
& \phi^{\mathrm{G}}_{\mathrm{tip-B}}(\boldsymbol{\alpha}^{\mathrm{A}}, \boldsymbol{\alpha}^{\mathrm{B}}, \boldsymbol{\beta}^{\mathrm{A}}, \boldsymbol{\beta}^{\mathrm{B}}) = \phi^{\mathrm{G}}_{\mathrm{g}},
\end{aligned} \tag{5.7}
$$

where, $x^{\mathrm{G}}_{\mathrm{g}}$, $y^{\mathrm{G}}_{\mathrm{g}}$ and $\phi^{\mathrm{G}}_{\mathrm{g}}$ denote the given beam tip position within global coordinate system, serve as target beam tip position. In general lumped-compliance beams, straight beam elements are employed as the fundamental structural units. Therefore, the initial tip position in its undeformed configuration can be directly derived from geometric relationships, which is provided as:

$$
x^{\mathrm{G}}_{\mathrm{g}} = L_{\mathrm{A}} \cos\theta_{\mathrm{A}} + \sqrt{x^2_{\mathrm{fr}} + y^2_{\mathrm{fr}}} \cos\left(\theta_{\mathrm{A}} + \arctan\frac{y_{\mathrm{fr}}}{x_{\mathrm{fr}}}\right) + L_{\mathrm{B}} \cos\left(\theta_{\mathrm{A}} + \arctan\frac{y_{\mathrm{fr}}}{x_{\mathrm{fr}}} + \theta_{\mathrm{B}}\right) \tag{5.8}
$$

$$
y^{\mathrm{G}}_{\mathrm{g}} = L_{\mathrm{A}} \sin\theta_{\mathrm{A}} + \sqrt{x^2_{\mathrm{fr}} + y^2_{\mathrm{fr}}} \sin\left(\theta_{\mathrm{A}} + \arctan\frac{y_{\mathrm{fr}}}{x_{\mathrm{fr}}}\right) + L_{\mathrm{B}} \sin\left(\theta_{\mathrm{A}} + \arctan\frac{y_{\mathrm{fr}}}{x_{\mathrm{fr}}} + \theta_{\mathrm{B}}\right) \tag{5.9}
$$

$$
\phi^{\mathrm{G}}_{\mathrm{g}} = \theta_{\mathrm{A}} + \theta_{\mathrm{B}} \tag{5.10}
$$

The applied load is a prescribed displacement along the negative direction of y-axis in global coordinate system. Accordingly, in the kinetostatic modeling process, the target beam tip position is defined as that the $x^{\mathrm{G}}_{\mathrm{g}}$ and orientation $\phi^{\mathrm{G}}_{\mathrm{g}}$ remain fixed, while the $y^{\mathrm{G}}_{\mathrm{g}}$ incrementally moves in the negative y-axis direction. Specifically, after each iteration, the target value of $y^{\mathrm{G}}_{\mathrm{g}}$ is updated as $y^{\mathrm{G}}_{\mathrm{g}} - \Delta y$. Following each updated configuration, the maximum stress in each beam is evaluated. If the stress remains within the allowable limit, the iteration proceeds. Otherwise, the process is terminated and all relevant data are stored.

To solve the constrained optimization problem described in (5.7), the *fmincon* solver from MATLAB's Optimization Toolbox was employed. The optimization was conducted using the interior-point algorithm with the following settings: maximum number of iterations set to 10^4, function evaluations capped at 10^{10}, and a convergence tolerance of 10^{-8} for the design variables. The optimization procedure was iteratively executed while the maximum stress remained below the yield limit. In each iteration, the beam tip position along the y-axis in global coordinate system was incrementally updated in the negative direction, while the position and orientation constraints were enforced through a nonlinear constraint

function. For each optimization step, the resulting structural configuration was analyzed to extract the maximum stress.

The aforementioned procedure describes the kinetostatic modeling process used to determine the equilibrium configurations of the general lumped-compliance beam. Through iterative solving, the kinetostatic response corresponding to a given geometric configuration can be obtained, including the reaction force–displacement and strain energy–displacement relationships. These reaction forces are extracted from the Lagrange multipliers associated with the position constraints, leveraging their physical interpretation as constraint forces. It is important to note that several independent parameters are required to be predefined and remain constant throughout this lower-level optimization process. These include the beam's width W, thickness T (which are not considered as decision variables in the geometric optimization process), Young's modulus E, yield strength σ_{yield}, and the displacement increment Δy. These parameters are fixed and not subject to updates during the iteration.

Once the complete kinetostatic response is obtained, various performance metrics or penalty functions can be defined based on the specific design objectives. These penalty functions serve as the output of the lower-level optimization and are used as the objective function in the upper-level optimization framework. Since the design goals may vary, the formulation of the penalty function is problem-dependent. The upper-level optimization then aims to minimize the selected penalty function to guide the design towards improved performance.

5.1.2 Upper-level optimization

In the bi-level optimization framework, the upper-level geometric optimization is responsible for exploring and selecting design variables, which directly determine the overall configuration and potential performance of the structure or system. Compared to traditional single-level approaches, the bi-level structure effectively mitigates computational burdens arising from high-dimensional and tightly coupled design spaces by decomposing the problem into two hierarchically organized layers. The upper level governs the geometric parameters, serving as the principal decision-making stage of the entire optimization process.

From a modeling perspective, the lower-level optimization can be encapsulated as a function that takes the geometric parameters of the beam as input and returns objective values

defined by various performance metrics. In this sense, the lower-level optimization acts as an 'individual evaluator' within the bi-level scheme, providing fitness values to guide the search process at the upper level. This encapsulated design allows the upper level to remain agnostic to the internal details of modeling and solving in the lower level, focusing solely on the evaluation outcomes for decision-making. The modular nature of this architecture enhances the flexibility of the overall optimization process. As geometric parameters often play a decisive role in structural performance, the effectiveness of the upper-level search significantly influences the quality of the final design. By separating geometric variables from physical behavior-related variables, the bi-level structure reduces the complexity of the optimization problem and decouples the variable sets. The upper level governs macro-level decisions such as shape and size, while the lower level is dedicated to performance analysis.

To achieve a globally optimal design of the structural geometric parameters, this study adopts the Genetic Algorithm (GA) as the upper-level optimization strategy [250]. Inspired by natural selection and genetic inheritance in biological evolution, GA performs efficient global searches in complex design spaces by simulating the processes of reproduction and evolution within a population. A notable advantage of GA is that it does not require gradient information and possesses strong global search capabilities, compared with gradient-based optimization strategies.

In this study, the design variables consist of the following geometric parameters:

$$\mathbf{d} = [\theta_{\mathrm{A}}, \theta_{\mathrm{B}}, L_{\mathrm{A}}, L_{\mathrm{B}}, x_{\mathrm{fr}}, y_{\mathrm{fr}}], \tag{5.11}$$

where each variable is assigned appropriate lower and upper bounds to ensure the feasibility and physical relevance of the design. The primary steps of the genetic algorithm are as follows:

1. **Initial population generation:**
   A diverse initial population is created by randomly sampling the design space. This diversity helps ensure broad coverage of the search domain.

2. **Evaluating individuals:**
   Each individual in the current generation is evaluated using a predefined objective function, which models kinetostatic behavior through the CoSCME method. The

fitness value quantifies the design quality and typically incorporates structural performance indicators and constraint conditions to ensure engineering validity.

3. **Selection:**
   MATLAB's *ga* function employs the *selectionstochunif* method by default [251]. This stochastic uniform selection arranges individuals on a line according to scaled fitness values, then steps uniformly along the line to choose parents. Compared to roulette wheel selection, this method offers lower sampling variance and ensures more stable propagation of individuals that better satisfy the optimization objective [252].

4. **Crossover:**
   Crossover-generated individuals are obtained by combining pairs of parents from the current population. For each coordinate of the child vector, the default crossover function randomly selects a gene from the corresponding coordinate of one of the two parents.

5. **Mutation:**
   Mutation offspring are created by introducing random changes to the genes of parent individuals. In unconstrained problems, this typically involves adding a random vector drawn from a Gaussian distribution.

6. **Form next population:**
   A new generation is formed based on the results of selection, crossover, and mutation, while maintaining a fixed population size.

7. **Termination condition check:**
   Execution stops once the maximum number of generations, time limit, or convergence threshold is reached. The best solution found is then returned.

Throughout the optimization process, real-time monitoring of the fitness curve of upper-level optimization, i.e. tracking the best and average fitness values, facilitates the assessment of convergence behavior and solution stability. By tightly coupling the genetic algorithm with the lower-level numerical model (CoSCME method), this framework achieves global optimization of complex geometric parameters. It offers strong adaptability and extensibility, making it suitable for a wide range of multi-objective and multi-constraint structural optimization problems, and serves as a powerful tool for compliant mechanism design.

5.2 Case Studies

To demonstrate the effectiveness and flexibility of the proposed bi-level optimization framework, two representative case studies are presented in this section. Both examples focus on the design of bistable compliant mechanisms with distinct mechanical behaviors. The first case aims to design a bistable mechanism with symmetric switching force, where the required forces for snap through between the two stable states are equal in magnitude. This task highlights the framework's ability to precisely control force response characteristics through structural optimization. The second case targets the design of a bistable mechanism exhibiting approximately constant negative stiffness, which is desirable for energy absorption and passive damping applications. Together, these two cases illustrate the framework's capability to explore complex design objectives involving nonlinear force-displacement responses.

5.2.1 Bistable Mechanism with Symmetric Switching Forces

The purpose of this case study is to investigate how geometric configuration influences the symmetry of switching forces, and to evaluate whether the proposed bi-level optimization framework can identify designs that achieve this objective. The switching force ratio (R_s), defined as the ratio between the backward and forward switching forces, and calculated as:

$$R_s(\mathbf{d}) = \frac{|F_{\text{backward}}|}{|F_{\text{forward}}|}, \tag{5.12}$$

where, the forward switching force, denoted by F_{forward}, refers to the critical force required to transition the structure from its first stable configuration (the manufactured state) to the second. Conversely, the backward switching force, F_{backward}, is the force needed to return the mechanism from the second stable configuration back to the first. The definitions of the forward and backward switching forces are illustrated in Figure 5.3 (a) and (b). In Figure 5.3 (a), the light blue shape indicates the initial configuration, and the dark blue shape represents the deformed configuration after snap-through. In Figure 5.3 (b) Forward switching force refers to the critical force that leads to forward snap through behavior; while the backward switching force refers to the critical force that leads to backward snap through behavior.

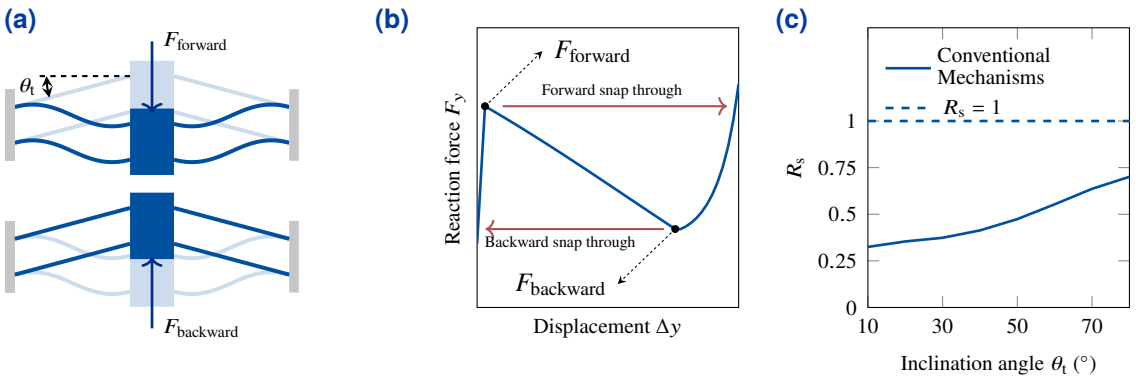


Fig. 5.3.: Forward and backward switching force analysis for conventional distributed-compliance bistable mechanisms. (a) Schematic of forward and backward switching forces, with beam inclination angle denoted by θ_t. (b) Illustration of forward and backward switching force from the force-displacement relationship. (c) Relationship between inclination angle θ_t and switching force ratio R_s.

It is worth noting that prior studies have proposed bistable structures with approximately equal switching forces [253, 254, 237]. However, these designs often rely on prestressed configurations or multi-material assemblies. In addition, a prestress-free approach was explored in [255], but it was based on a limited and non-generalizable design framework, restricting both the diversity of achievable configurations and the overall optimization potential. In contrast, the optimized design proposed in this study achieves equal switching forces without relying on prestress or material heterogeneity. Notably, the structure exhibits asymmetric energy barriers in the forward and backward directions while maintaining a symmetric switching force profile. This confirms that balanced force transitions can be realized purely through geometric optimization, offering a simpler, fully passive, and fabrication-friendly solution. These findings highlight the capability of the bi-level optimization framework to uncover non-intuitive yet practically advantageous designs beyond conventional approaches.

To rigorously demonstrate the fundamental limitation of conventional distributed compliance bistable mechanisms in achieving symmetric switching forces, a set of models with identical beam lengths and varying inclination angles is analyzed. The switching force ratio (R_s) is evaluated over an inclination angle range from 10° to 80°. The resulting curve is shown in Figure 5.3 (c), with the corresponding numerical data summarized in Table 5.3. The results clearly reveal that the desired switching force ratio of 1 is unattainable across the entire range considered. This confirms that it is virtually impossible to achieve symmetric switching behavior using conventional distributed-compliance designs. The main limitation arises from the extremely narrow design space, as only two geometric parameters, the

Tab. 5.3.: Switching force ratios of conventional distributed-compliance bistable mechanisms with distinct inclination angles.

Inclination angle	Switching force ratio
10°	0.324
20°	0.354
30°	0.373
40°	0.413
50°	0.474
60°	0.553
70°	0.636
80°	0.700

beam length and inclination angle, are available for tuning. In this study, the beam length is fixed at 100 mm, the thickness at 0.8 mm, and the selected material has a Young's modulus of 2800 MPa.

The above mentioned results highlight the need for a more general design framework with an expanded yet tractable design space. The general lumped-compliance beam model meets this requirement by enabling control over a moderate number of geometric parameters, sufficiently rich to allow exploration of diverse configurations, yet not so excessive as to compromise convergence. This balance provides greater flexibility for shaping force-displacement behavior and achieving targeted mechanical performance. To fully leverage this capability, the objective function in the upper-level optimization is formulated to drive the switching force ratio toward 1, thereby enabling the discovery of geometrically driven designs with symmetric switching behavior.

To evaluate the performance of each configuration, a penalty-based objective function is formulated with the primary goal of minimizing the absolute difference between the backward and forward switching forces. To ensure that the resulting design exhibits physically valid bistable behavior, three penalty terms are incorporated. First, a large penalty is applied if the force–displacement curve obtained from the lower-level optimization does not exhibit two distinct extreme values, specifically, one local maximum and one local minimum, as this indicates the absence of bistability. Second, an additional penalty is imposed if the minimum force is not negative, since a negative force is a fundamental requirement for a bistable transition. Another penalty is that the lateral dimension must be small enough to be printable by the Ultimaker S5 printer. These constraints guide the optimization toward not only achieving symmetric switching forces but also ensuring

$$
\begin{aligned}
\underset{\mathbf{d}\in\mathbb{R}}{\text{minimize}} \quad & |R_{\mathrm{s}}(\mathbf{d}) - 1| + P(\mathbf{d}), \\
\text{subject to} \quad & 10\ \text{mm} \le L_{\mathrm{A}} \le 80\ \text{mm}, \\
& 10\ \text{mm} \le L_{\mathrm{B}} \le 80\ \text{mm}, \\
& 0^\circ \le \theta_{\mathrm{A}} \le 360^\circ, \\
& 0^\circ \le \theta_{\mathrm{B}} \le 360^\circ, \\
& -100\ \text{mm} \le x_{\mathrm{fr}} \le 100\ \text{mm}, \\
& -100\ \text{mm} \le y_{\mathrm{fr}} \le 100\ \text{mm}, \\
& P(\mathbf{d}) = \begin{cases} 10^8 & \text{if the following conditions are not satisfied:} \\ & \quad \text{(i) force–displacement curve has exactly two extrema,} \\ & \quad \text{(ii) local maximum} > 0 \text{ while local minimum} < 0, \\ & \quad \text{(iii) lateral dimension} < 140\ \text{mm}, \\ 0 & \text{otherwise,} \end{cases}
\end{aligned}
\tag{5.13}
$$

that the resulting configurations possess true bistability. Thus, the objective function is summarized in Eq. (5.13):

The penalty function is denoted by $P(\mathbf{d})$. If any of the outlined conditions are not satisfied, a large penalty is added to the objective value. As previously introduced the decision variable $\mathbf{d}$ involves six geometric parameters. These decision variables are bounded within physically meaningful limits, as introduced in the objective function.

The genetic algorithm (GA) is implemented using MATLAB's built-in solver. The GA was configured with a population size of 100 and a maximum of 50 generations. To prevent unnecessary evaluations beyond convergence, the optimization was set to terminate once the improvement in objective value fell below a threshold of 10^{-4}. The initial seed is selected as $\mathbf{d} = [15^\circ, 0^\circ, 50\ \text{mm}, 50\ \text{mm}, 20\ \text{mm}, 0\ \text{mm}]$ to ensure reproducibility and to accelerate early-stage convergence. In addition, parallel computing was enabled to expedite the evaluation of the objective function. The above-described optimization procedure has been implemented and converges to a numerical optimum:

$$
\mathbf{d} = [357.849844^\circ, 193.405356^\circ, 37.085252\text{mm}, 40.831394\text{mm}, 93.811297\text{mm}, 34.644826\text{mm}].
\tag{5.14}
$$

The high numerical precision reported for the optimized geometric parameters reflects the continuous nature of the optimization process rather than the intended manufacturing accuracy. In practice, these parameters can be rounded to realistic fabrication tolerances with negligible influence on the predicted mechanical response. During the iterative process, the optimal solution of each generation is recorded. These results are provided in Appendix A.1, which includes the optimal value at each generation and its corresponding geometric parameters.

The optimum design of the bistable mechanism is demonstrated in Figure. 5.4 (a). The result is verified through FEA simulation conducted in Strand7, as shown in Figure. 5.4 (c). The FEA simulation is conducted with beam element and each beam is subdivided into 100 beam elements to maintain accuracy. In addition, the convergence and accuracy of the proposed 2D FEA approach for analyzing planar compliant mechanisms have been discussed and demonstrated in [125], thereby confirming its effectiveness. Furthermore, an experimental test was conducted using a texture analyzer (TA.XT plus Texture Static Test System) to verify the accuracy of the modeling results. The experimental setup is shown in Figure 5.4 (b). As shown in Figure 5.4 (c), the experimental results exhibit some deviation, primarily due to the limited manufacturing accuracy of the 3D-printed prototype.

Table 5.4 summarizes the maximum and minimum values of force and displacement obtained from modeling, finite element analysis (FEA), and experimental measurements. These values are extracted from the corresponding force-displacement curves derived through each approach.

Tab. 5.4.: Maximum and minimum values of force and displacement obtained from modeling, finite element analysis (FEA), and experimental results, extracted from their respective force-displacement curves.

	F_{forward} (N)	F_{backward} (N)
Analytical model	1.118	-1.118
FEA simulation	1.118	-1.117
Experiment	1.441	-1.270

The above-mentioned optimization procedure introduces the process of designing a compliant bistable mechanism with symmetric switching force in detail. By integrating the CoSCME model, bi-level optimization, and a genetic algorithm, the resulting mechanism achieves nearly identical forward and backward switching forces, as confirmed by FEA simulations. The result further demonstrates the effectiveness of the proposed optimization framework. This case validates the capability of the framework in handling single-objective optimization problems with high precision.

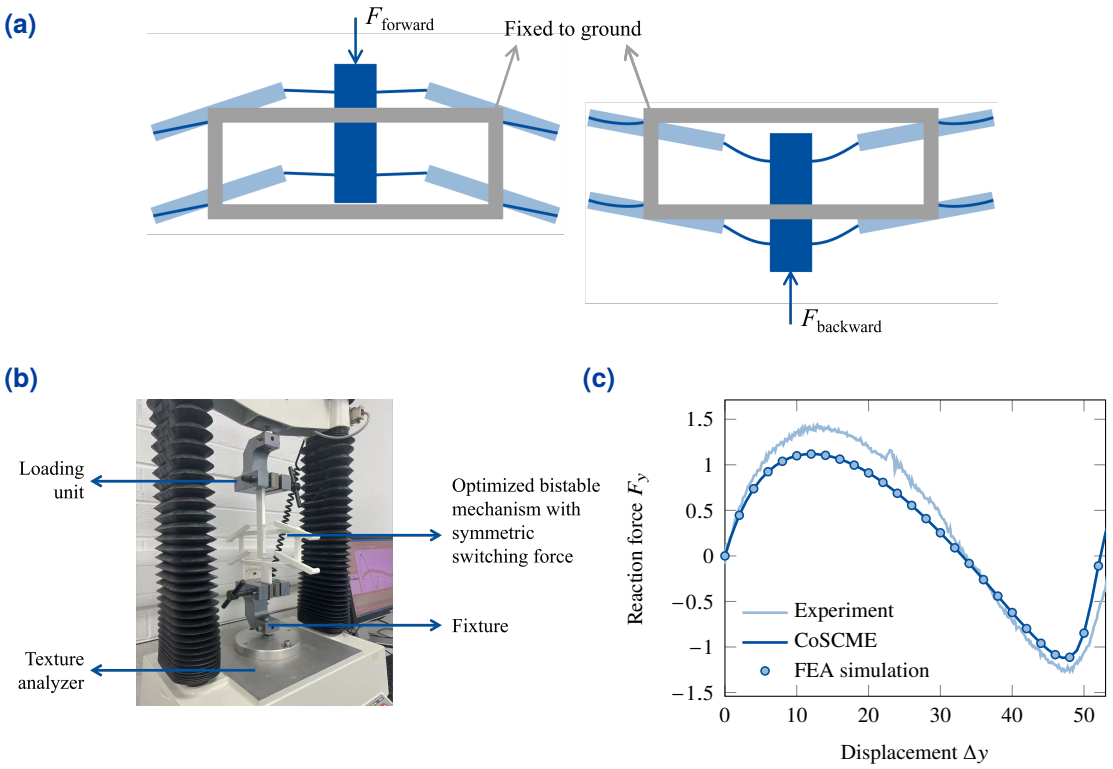


Fig. 5.4.: Optimal design of the bistable mechanism with symmetric switching force. A double-layer design is adopted to more effectively reduce the geometric size of the prototype. (a) The first and second stable configurations of the optimized mechanism. The grey block indicates the fixed part attached to the ground. The directions of the forward and backward forces are marked. (b) Force–displacement curve of a single lumped-compliance beam, validated by FEA simulation and experiment. (c) Experimental setup for testing the static behavior of the optimized mechanism.

To evaluate the effectiveness of the proposed optimization framework in achieving symmetric switching forces, a comparative analysis is conducted against other optimization methods. The comparison focuses specifically on the symmetry between the forward and backward switching forces in the optimized mechanisms. For each method, the forward and backward switching forces are extracted, and the relative error between them is used as a quantitative indicator. The relative error e_s is calculated using the Eq. (5.15).

$$e_s = \frac{|F_{\text{forward}}| - |F_{\text{backward}}|}{F_{\text{forward}}} \tag{5.15}$$

The extracted switching forces used for this comparative analysis are presented in Table 5.5.

Tab. 5.5.: Comparison of positive and negative switching forces from several previous studies, including their associated errors.

Source	$F_{\text{forward}}(mN)$	$F_{\text{backward}}(mN)$	e_s
[255]	1540.0	-1498.0	2.73%
[256]	2734.4	-2723.7	0.39%
[113]	2048.0	-2032.0	0.78%
This work	1118.644	-1118.645	0.000098%

As shown in Table 5.5, the proposed optimization method demonstrates a remarkable improvement in achieving symmetric switching forces compared to existing approaches. Among the previous methods, the best recorded relative error is 0.39% [256]. In contrast, the proposed bi-level optimization framework achieves a relative error of only 0.000098%, representing an improvement of nearly three orders of magnitude. This highlights the method's suitability for the design of bistable mechanisms requiring highly symmetric switching behavior. Moreover, the method proposed in [255] yields a much larger error of 2.73%, further underscoring the advantage of the present approach in controlling switching force symmetry.

It should be emphasized that the reported errors quantify numerical deviations within the CoSCME-based formulation rather than the practically achievable experimental accuracy. In practice, the observed switching-force symmetry is additionally influenced by manufacturing tolerances, boundary-condition uncertainties, non-linear material properties, and other experimental factors. Nevertheless, the ability to achieve near-perfect symmetry in the ideal model provides a sufficient design margin, which is particularly beneficial for the optimization and design of bistable mechanisms requiring robust symmetric switching behavior.

5.2.2 Bistable Mechanism with Approximately Constant Negative Stiffness

In this case study, the proposed bi-level optimization framework is employed to identify bistable configurations that exhibit a highly constant negative stiffness region, while ensuring that this region is sufficiently wide. To effectively address this bi-objective optimization problem, a multi-objective optimization strategy is necessary to be employed. One approach is transforming multiple objectives into a single scalar function through the introduction of penalty terms as implemented in 5.2.1. However, in the present optimization problem, these two objectives differ significantly in both magnitude and physical units. Consequently, determining the appropriate objective function becomes challenging, often requiring multiple rounds of parameter tuning, which introduces uncertainty and increases the complexity of the design process.

An alternative and more systematic approach to implementing such optimization problems is to employ dedicated multi-objective optimization algorithms. Common strategies include Pareto-based direct search methods, such as *paretosearch*, and evolutionary algorithms, such as *gamultiobj*. Both are built-in functions provided by MATLAB's Global Optimization Toolbox, specifically designed for solving multi-objective optimization problems [257]. Through iterative optimization, a set of optimal solutions, known as the Pareto front, is ultimately obtained.

The Pareto front refers to the set of non-dominated solutions in a multi-objective optimization problem. A solution is considered non-dominated if no other feasible solution performs better across all objectives. In other words, improving one objective necessarily results in the degradation of at least one other. The Pareto front therefore represents an optimal set of trade-offs among competing objectives. Unlike single-objective optimization, which typically yields a single global optimum, multi-objective optimization naturally results in a set of equally valid solutions, each representing a different compromise. This allows decision-makers to select the solution that best aligns with their specific performance priorities.

The two aforementioned methods differ in terms of their optimization strategies and search scope. *paretosearch* is a derivative-free, pattern-based local search algorithm that explores the design space near a given set of initial points. It is well suited for smooth, low-dimensional problems where local refinement is of primary interest. In contrast, *gamultiobj* employs a global, population-based evolutionary strategy that enables broad

exploration of complex design spaces. Owing to its heuristic nature, the algorithm is particularly effective at discovering non-intuitive and structurally diverse configurations, while being less sensitive to the choice of initial design.

Given the complexity and nonlinearity inherent in the bistable mechanism optimization problem, *gamultiobj* is preferred due to its superior global search capability. The algorithm is based on the well-established Non-dominated Sorting Genetic Algorithm-II (NSGA-II) framework, which maintains a diverse population of candidate solutions and evolves them through crossover and mutation operations [258]. At each generation, solutions are ranked by their level of non-domination, and diversity within each front is preserved using a crowding-distance metric. This ensures that the resulting Pareto front contains not only high-quality trade-off solutions but also spans a broad region of the objective space. Candidate designs can then be selected from the Pareto set based on specific performance criteria or further refined through local optimization techniques.

To quantitatively identify the negative stiffness region in the obtained force–displacement curve, a regression-based approach is employed to detect regions exhibiting negative stiffness. This method systematically examines all the continuous regions $[\Delta y_i, \Delta y_j]$ with a minimum distance of $5\Delta y$, i.e., $\Delta y_j - \Delta y_i \geq 5\Delta y$. The reaction forces corresponding to the vertical displacements at Δy_i and Δy_j are denoted by F_{yi} and F_{yj}, respectively. For each defined displacement region, a regression line connecting these two boundary points is formulated using the following function:

$$\hat{F}_y(\Delta y) = \frac{\Delta y_i F_{yi} - \Delta y_i F_{yj}}{\Delta y_j - \Delta y_i} \Delta y + F_{yi} \tag{5.16}$$

where, $\hat{F}_y(\Delta y)$ denotes the estimated vertical reaction force at a given displacement Δy and $\Delta y \in [\Delta y_i, \Delta y_j]$. The lines identified with a positive slope $((\Delta y_i F_{yi} - \Delta y_i F_{yj})/(\Delta y_j - \Delta y_i) \geq 0)$ are excluded, as they indicate in this region, the mechanism has positive stiffness. Furthermore, the linearity of stiffness in the region is evaluated and measured using the root mean square error (RMSE) between the estimated reaction force and CoSCME derived reaction force, which is formulated as:

$$\text{RMSE} = \sqrt{\frac{1}{j-i} \sum_{k=i}^{j} (f_k - \hat{f}_k)^2}, \tag{5.17}$$

where f_k denotes the reaction force predicted by the CoSCME model at the kth displacement sample (k ranges from i to j), and $\hat{f}_k$ denotes the corresponding value on the ideal linear regression line constructed between the two boundary points $(\Delta y_i, f_i)$ and $(\Delta y_j, f_j)$.

RMSE is used because the goal of maximizing the constant stiffness region is not only to match the slope at the two endpoints, but also to keep the entire force displacement curve close to a straight line over the prescribed displacement range. RMSE provides a single scalar measure of the overall deviation between the simulated force response and the target linear interpolation by considering all sampling points in the region. In addition, RMSE penalizes local fluctuations, which is important for achieving stable and practically usable constant stiffness behavior. Therefore, minimizing RMSE directly promotes a more uniformly linear response in the constant stiffness region and is well suited for optimization.

Only regions satisfying RMSE < 0.005 are retained, ensuring that the negative stiffness is approximately constant. In this case study, two objectives are defined: maximizing the length of the constant region and minimizing the RMSE. Since the optimization is carried out using a minimization strategy, the first objective is reformulated as minimizing the width of the region, i.e., $-(j-i)\Delta y$. The complete formulation of the bi-objective optimization problem is given in (5.18).

$$
\begin{aligned}
\underset{L_A, L_B, \theta_A, \theta_B, x_{fr}, y_{fr} \in \mathbb{R}}{\text{minimize}} \quad & \{\text{RMSE} + P(\mathbf{d}), -(j-i)\Delta y + P(\mathbf{d})\}, \\
\text{subject to} \quad & 10 \text{ mm} \le L_A \le 80 \text{ mm}, \\
& 10 \text{ mm} \le L_B \le 80 \text{ mm}, \\
& 0^\circ \le \theta_A \le 360^\circ, \\
& 0^\circ \le \theta_B \le 360^\circ, \\
& -100 \text{ mm} \le x_{fr} \le 100 \text{ mm}, \\
& -100 \text{ mm} \le y_{fr} \le 100 \text{ mm}, \\
& P(\mathbf{d}) = \begin{cases} 10^8 & \text{if the following conditions are not satisfied:} \\ & \quad \text{(i) stiffness in region } [\Delta y_i, \Delta y_j] \text{ is negative,} \\ & \quad \text{(ii) local maximum} > 0 \text{ while local minimum} < 0, \\ & \quad \text{(iii) lateral dimension} < 140 \text{ mm,} \\ 0 & \text{otherwise,} \end{cases}
\end{aligned}
\tag{5.18}
$$

The optimization process described above is implemented to obtain a set of optimal solutions. During the optimization, the algorithm is configured to display iteration information, utilize

parallel computation, and visualize the evolution of the Pareto front. The total runtime is limited to 360000 seconds. Each generation contains 100 individuals, and the maximum number of generations is set to 50. The convergence criterion is defined using a function tolerance of 1×10^{-3}. The optimization starts from a predefined initial population and uses an output function to save the Pareto front at each generation. As a result, a Pareto front consisting of nine non-dominated solutions is obtained. The corresponding data are provided in Appendix A.2. A comparison of each solution in terms of RMSE and the width of the constant negative stiffness region is conducted, and the results are listed in Table 5.6. Among these, solution 4 is selected with the optimized design variables: $\mathbf{d}$ = [117.1000°, 2.8278°, 70.3449 mm, 59.7228 mm, 52.3085 mm, 49.9021 mm].

Tab. 5.6.: Optimization variables and their corresponding symbols.

Solution	RMSE	Width
1	0.00368868	32 mm
2	0.00461749	34 mm
3	0.00494399	72 mm
4	0.00495061	88 mm
5	0.00493980	45 mm
6	0.00494943	84 mm
7	0.00499963	93 mm
8	0.00499977	103 mm
9	0.00499977	106 mm

The compliant mechanism derived from this set of design variables is illustrated in Figure 5.5 (a). In this figure, the original manufactured configuration is labeled, along with the configurations corresponding to the beginning and end of the constant negative stiffness region. Figure 5.5 (b) provides a visual explanation of the multi-objective optimization objectives including maximize the constant negative stiffness region and minimize the RMSE. Figure 5.5 (c) the experimental setup used to test the static behavior of the optimized mechanism. Figure 5.5 (d) presents a comparison between the modeling results, FEA simulation and experimental results of the selected optimal design. The optimal solution 1 exhibits constant negative stiffness but over a limited range. In contrast, solution 4 shows a significantly broader region of constant negative stiffness while maintaining a satisfactory level of linearity. Thus, the solution 4 is selected as the optimal design.

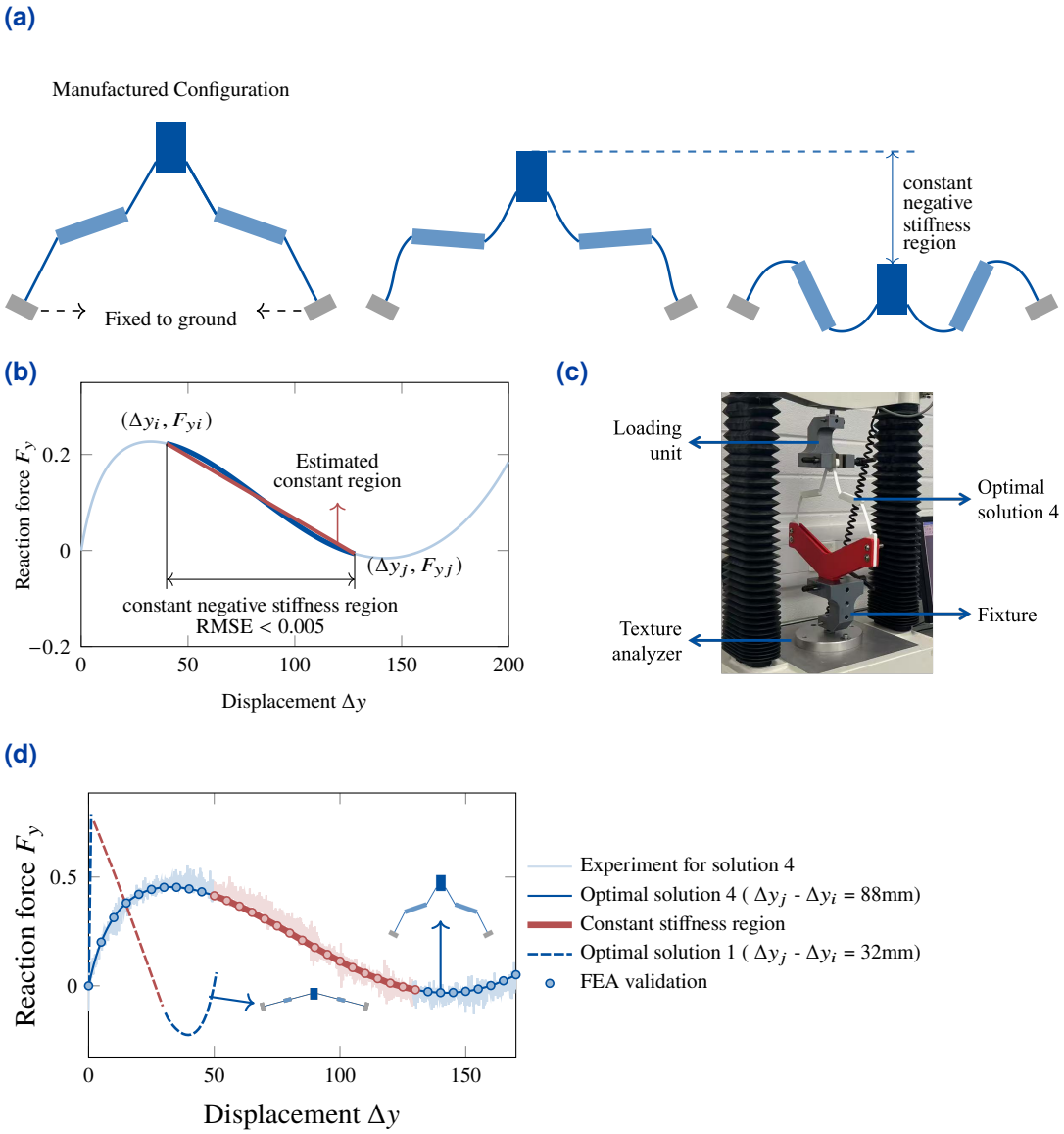


Fig. 5.5.: Illustration and validation of the optimized mechanism with constant negative stiffness. (a) Optimized configuration with labels indicating the original design and the constant negative stiffness region. (b) Visualization of optimization objectives. (c) Experimental setup for static testing. (d) Force–displacement curves of optimal solutions 1 and 4. Kinetostatic behavior of optimal solution 4 is validated through FEA simulations and experiment.

5.3 Discussion

This section provides a critical evaluation of the proposed bi-level optimization framework, highlighting its potential for broader application and future development. Beyond the demonstrated case studies, the framework exhibits strong adaptability for a wide range of design tasks. The following discussion elaborates on its applicability, extensibility, and current limitations, offering insights into potential improvements and directions for future work.

5.3.1 Application Scope

The two case studies presented in this work illustrate the application of the proposed bi-level optimization framework to the structural design of compliant bistable mechanisms. However, they do not capture the full scope of the framework's capabilities. As discussed below, it can also be extended to optimize a broader range of mechanisms beyond those explicitly explored here.

1. Path-guided compliant mechanism design

   The framework could be applied to design mechanisms whose output follows a prescribed trajectory under deformation, such as vertical, horizontal, or curved motion paths. This is particularly useful in applications involving motion transmission, biomimetic joints, or compliant robotics, where specific output paths are essential for functionality.

2. Constant-force and zero-force mechanisms

   By leveraging constant negative stiffness behavior, the proposed framework can assist in designing structures that exhibit nearly constant output force or zero-force resistance over a range of displacements. Such mechanisms are valuable in precision positioning stages, energy harvester and passive vibration isolation systems.

3. Adaptive grippers

   The optimization framework is well-suited for designing soft or flexible actuators with programmable deformation behavior. By shaping the force–displacement profile

and mechanical stability, it can help develop compliant robotic grippers or adaptive structures capable of safe interaction with soft or delicate objects.

In addition to the three potential application scenarios discussed above, there are other practical scenarios where the proposed optimization framework may also be applicable. These scenarios include, but are not limited to, deployable structures, energy-dissipative metamaterials, and shape-programmable systems. The full range of applicability remains to be further explored as the framework continues to evolve. While the proposed framework demonstrates promising applicability across various compliant mechanism design tasks, it is important to critically investigate its current limitations. A deeper understanding of these limitations not only highlights the boundaries of the current implementation but also provides valuable insights for future refinement and broader adoption.

5.3.2 Limitations

Despite the demonstrated versatility of the proposed bi-level optimization framework, several limitations constrain its current implementation. These limitations stem from both the modeling assumptions and the algorithmic strategies employed, and recognizing them is essential for guiding future improvements.

First, the current framework operates within a fixed structural configuration composed of two serially connected compliant beams. While this allows for a focused study on geometric optimization, it inherently restricts the diversity of possible designs. Without the capability to automatically explore or generate new topological configurations, the framework may overlook structurally novel or functionally superior solutions. This limitation reduces the exploratory power of the method, especially in applications demanding unconventional configurations or multifunctionality.

Second, the upper-level optimization process relies on heuristic algorithms such as genetic algorithms. Although these algorithms provide global search capabilities, they are inherently prone to being trapped in local minima, particularly in complex or high-dimensional design spaces. This susceptibility to local minima may lead to suboptimal design outcomes and highlights the need for more robust global search strategies or hybrid optimization approaches that combine global and local refinement. A potential strategy to avoid being trapped in local minima is to increase the population size and the number of generations;

however, this improvement in search robustness comes at the cost of a substantial increase in computational expense.

Third, the computational cost of the framework remains a significant challenge. The lower-level optimization is conducted using the CoSCME method, which ensures high-fidelity modeling by capturing both bending and axial deformations. However, this increased accuracy comes at the expense of computational efficiency. Compared to simplified alternatives such as the high-order SCME model, CoSCME evaluations are considerably more time-consuming. As the design space expands, the overall optimization process becomes increasingly slow, potentially limiting its scalability to larger or more complex design problems.

These limitations collectively underscore the trade-offs between modeling accuracy, search robustness, and computational efficiency. Several potential strategies to address these challenges are discussed in the following subsection.

5.3.3 Potential methodological extensions

To address the aforementioned limitations and enhance the generality of the framework, several promising directions for methodological extension are outlined below.

1. Topology-level configuration search via graph theory

   A natural extension of the proposed bi-level optimization framework involves elevating the design space from geometry-level parameter tuning to topology-level configuration search, thus construct a tri-level optimization framework. While the current framework operates within a fixed structural layout and optimizes continuous geometric parameters, many functional requirements in compliant mechanism design, such as multi-stability, motion amplification, or spatial adaptation, can benefit from exploring diverse structural topologies. By representing mechanisms as graph-based models, where nodes denote connection points and edges represent compliant elements, the design process can be reformulated to allow automated generation and evaluation of alternative configurations. In this extended framework, topological variables, such as the presence, connectivity, or type of beam elements, can be incorporated into the upper-level optimization. For instance, introducing a connectivity matrix enables the search algorithm to explore not only the shape

but also the structural layout of the mechanism. Coupling this with graph-theoretic operations, such as graph expansion, merging, or pruning, opens the door to a rule-based or data-driven structural growth process, where novel configurations are synthesized and tested iteratively. This expansion from parametric to topological exploration significantly enhances the generative capacity of the framework, enabling it to address more design challenges.

2. Boundary and load condition optimization

   In practical design scenarios, boundary conditions and loading configurations play a critical role in shaping the mechanical response of compliant mechanisms. While the current framework optimizes geometry under fixed external conditions, further improvements can be achieved by treating support locations, displacement directions and magnitudes, and actuation types (such as single-point or multi-point displacement input) as additional design variables. Parameterizing these factors allows the framework to optimize both structural configuration and its interaction with the surrounding environment, leading to more adaptive and application-specific designs. This is particularly beneficial when actuator placement, space constraints, or loading limitations are present in real-world implementations.

3. Surrogate-assisted strategy for enhancing optimization efficiency

   While the proposed framework employs CoSCME as the core modeling tool to ensure high-fidelity representation of beam-based compliant mechanisms, its computational cost remains a limiting factor, particularly when scaling up to large configuration spaces or structurally complex designs. Compared to CoSCME, the high-order SCME model offers significantly higher computational efficiency. However, SCME does not account for axial deformation, which can lead to notable accuracy loss in certain deformation regimes. To address this trade-off between speed and accuracy, a promising extension is to adopt a two-stage optimization strategy: first, employ high-order SCME as a fast surrogate model to perform a coarse global search using heuristic algorithms such as genetic algorithms, thereby identifying approximate yet functionally feasible configurations; then, refine these candidates through local optimization algorithms, such as gradient-based optimization or pattern search, within a small geometric neighborhood. This hybrid approach has the potential to significantly improve optimization efficiency without sacrificing solution

quality, making it especially attractive for high-dimensional or topology-level design problems.

In summary, the proposed bi-level optimization framework offers a modular and adaptable strategy for the design of compliant mechanisms. Its effectiveness in optimizing compliant bistable mechanisms has been demonstrated through representative case studies. Furthermore, the framework holds strong potential for extension to topology-level configuration search and high-efficiency multi-stage optimization, positioning it as a promising foundation for future advancements in functional structure synthesis.

5.4 Chapter Summary

This chapter presents a bi-level geometrical optimization framework for the design of compliant bistable mechanisms with tailored kinetostatic performance. The proposed framework integrates a modular upper-level geometric optimizer with a displacement-driven lower-level solver based on the CoSCME model, enabling accurate modeling of large deformations, including both bending and axial effects. Through two representative case studies, achieving symmetric switching forces and designing approximately constant negative stiffness, the framework demonstrates its capability to identify high-performance, fabrication-friendly configurations.

The optimization results are validated through finite element analysis and physical experiment, confirming both the accuracy of the CoSCME-based modeling and the effectiveness of the hierarchical optimization strategy. Compared with conventional bistable designs, the framework offers significantly enhanced flexibility in shaping the force–displacement response, thereby enabling broader application potential in domains such as soft robotics, mechanical metamaterials, and deployable systems.

Despite its demonstrated performance, the current implementation is limited by its fixed topology and the computational cost of lower-level evaluations. Future work will explore topology-level configuration search, boundary condition optimization, and surrogate-assisted strategies to enhance design diversity and efficiency. Overall, the proposed framework establishes a promising foundation for behavior-driven mechanism design and offers extensibility toward more complex multistable and programmable mechanical systems.

6 Conclusion

6.1 Conclusion

This thesis has systematically advanced the modeling and optimization of compliant mechanisms, focusing on addressing the challenges of capturing nonlinear large-deformation behavior and enabling efficient yet accurate design strategies. The research has bridged the gap between classical simplified models and computationally expensive finite element analysis, providing a set of methods that balance modeling accuracy and computational efficiency.

Chapter 1 introduces the research background and motivation of this thesis, highlighting the challenges in modeling and optimizing compliant mechanisms undergoing large nonlinear deformations. It identifies the limitations of existing analytical models and numerical approaches, thereby clearly defining the research gaps and objectives addressed in this work.

Chapter 2 presents the theoretical background underlying the proposed modeling and optimization frameworks. It reviews the kinematics of large deformations, strain energy formulations, and existing smooth curvature-based modeling approaches, establishing the necessary theoretical foundation for the developments introduced in subsequent chapters.

Chapter 3 introduces the high-order SCME for modeling compliant mechanisms undergoing large deformations. By employing high-order curvature representations, this chapter demonstrates that high-order SCME significantly improves modeling accuracy compared with classical simplified approaches while achieving substantially reduced computational cost relative to finite element analysis. The results confirm that high-order SCME provides an effective balance between accuracy and efficiency, making it well suited for iterative design and analysis of compliant bistable mechanisms.

Chapter 4 further extends this modeling framework by proposing the Comprehensive SCME. By incorporating both bending and axial deformations, together with their coupling effects, the Comprehensive SCME substantially enhances modeling fidelity under strong

geometric nonlinearity. The case studies in this chapter demonstrate that Comprehensive SCME enables accurate prediction of complex nonlinear responses that are difficult to capture using existing analytical models.

Chapter 5 builds upon the proposed modeling methods by introducing a bi-level optimization framework for compliant mechanism design. By integrating nonlinear modeling into a hierarchical optimization strategy, this chapter enables systematic exploration of the design space while balancing performance objectives, computational cost, and manufacturability. The results show that the proposed framework can achieve tailored kinetostatic behavior and discover mechanism configurations that are not readily attainable using conventional single-level optimization approaches.

Collectively, these chapters establish a coherent and progressive framework that advances both the modeling and optimization of compliant mechanisms. By introducing advanced curvature-based formulations and embedding them within a hierarchical optimization framework, this thesis contributes both theoretical advancements in nonlinear mechanics and practical tools for engineering applications. The contributions are not only validated through finite element simulations but also benchmarked against existing methods, ensuring robustness, reliability, and broader applicability. Overall, this thesis demonstrates that advanced analytical and optimization frameworks can significantly enhance the design capability of compliant mechanisms, paving the way for high-performance applications in precision engineering, robotics, and biomedical devices.

6.2 Future Work

Looking forward, the work presented in this thesis establishes a solid foundation for advancing the modeling and optimization of compliant mechanisms. The development of high-order SCME, CoSCME, and the bi-level optimization framework not only fills critical gaps in capturing nonlinear large-deformation behavior with high efficiency and accuracy, but also opens up a wide range of opportunities for both theoretical research and practical engineering applications. On the theoretical side, the proposed methods provide a systematic way to integrate nonlinear mechanics with optimization, which can be further extended to multi-physics, multi-scale, and data-driven modeling paradigms. On the practical side, the methodologies developed here pave the way for next-generation designs of compliant structures and devices that combine lightweight construction, high performance, and functional adaptability. These future directions are outlined as follows:

- **Mechanical metamaterials and adaptive structures:** Applying SCME and CoSCME to design architected materials and deployable systems with tailored nonlinear responses (e.g., bistability, negative stiffness, morphing) for vibration isolation, energy absorption, and aerospace applications.

- **Soft robotics and biomedical devices:** Leveraging accurate nonlinear modeling and bi-level optimization to develop efficient compliant actuators, manipulators, and patient-specific biomedical tools and implants.

- **Micro/nano and multifunctional systems:** Extending the methods to MEMS/NEMS and integrating coupled physical fields (piezoelectric, thermal, magnetic) for smart compliant systems with sensing, actuation, and energy conversion capabilities.

Bibliography

[1] T. L. Thomas, V. K. Venkiteswaran, G. K. Ananthasuresh, S. Misra, Surgical applications of compliant mechanisms: A review, Journal of Mechanisms and Robotics (2021) 020801. https://doi.org/10.1115/1.4049491.

[2] L. L. Howell, S. P. Magleby, B. M. Olsen (Eds.), Handbook of Compliant Mechanisms, John Wiley & Sons Ltd, 2013. https://doi.org/10.1002/9781118516485.

[3] X. Markl, Technical perspective: The flexure revolution – compliant mechanisms applied to watchmaking (2023).
URL https://monochrome-watches.com/technical-perspective-flexure-revolution-compliant-mechanisms-applied-watchmaking/

[4] J. Zhu, G. Hao, S. Li, X. Kong, A compact mirror-symmetrical xy compliant parallel manipulator for minimizing parasitic rotations, Journal of Mechanical Design (2022) 073303. https://doi.org/10.1115/1.4053818.

[5] J. Jovanova, A. Nastevska, M. Frecker, M. E. Aguirre, Analysis of a functionally graded compliant mechanism surgical grasper, in: 2018 International Conference on Reconfigurable Mechanisms and Robots (ReMAR), 2018, pp. 1–8. https://doi.org/10.1109/REMAR.2018.8449868.

[6] P. A. Halverson, Modeling, design, and testing of contact-aided compliant mechanisms in spinal arthroplasty, Ph.D. thesis, Brigham Young University, Provo, Utah (Jul. 2010).
URL https://scholarsarchive.byu.edu/etd/2168

[7] O. Piccin, N. Kumar, L. Meylheuc, L. Barbé, B. Bayle, Design, development and preliminary assessment of grasping devices for robotized medical applications, in: Proceedings of the ASME 2012 International Design Engineering Technical Conferences and Computers and Information in Engineering Conference, 2012, pp. 65–73. https://doi.org/10.1115/DETC2012-70634.

[8] S. A. Zirbel, K. A. Tolman, B. P. Trease, L. L. Howell, Bistable mechanisms for space applications, PLOS ONE (2016) 1–18. https://doi.org/10.1371/journal.pone.0168218.

[9] H. Pruett, N. Coleman, S. Magleby, Preliminary concepts for magnetic actuation and stabilization of origami-based arrays, in: Proceedings of the ASME 2023 International Design Engineering Technical Conferences and Computers and Information in Engineering Conference, 2023, p. V008T08A051. https://doi.org/10.1115/DETC2023-116615.

[10] P. Crnjak, Compliant robotic gripper (2020).
URL https://hackaday.io/project/174555-compliant-robotic-gripper

[11] C.-M. Chang, L. Gerez, N. Elangovan, A. Zisimatos, M. Liarokapis, On alternative uses of structural compliance for the development of adaptive robot grippers and hands, Frontiers in Neurorobotics (2019) 91. https://doi.org/10.3389/fnbot.2019.00091.

[12] S. Li, S. Abdelaziz, L. Wang, G. Hao, Design and kinetostatic analysis of a tip-stiffness improved compliant continuum robot using anti-buckling universal joints, The International Journal of Robotics Research (0) 02783649251344328. https://doi.org/10.1177/02783649251344328.

[13] E. Pernette, S. Henein, I. Magnani, R. Clavel, Design of parallel robots in micro-robotics, Robotica (1997) 417–420. https://doi.org/10.1017/S0263574797000519.

[14] E. Thalmann, S. Henein, Triple crossed flexure pivot based on a zero parasitic center shift kinematic design, Journal of Mechanisms and Robotics (2022) 045001. https://doi.org/10.1115/1.4053471.

[15] C.-X. Li, G.-Y. Gu, M.-J. Yang, L.-M. Zhu, Design, analysis and testing of a parallel-kinematic high-bandwidth xy nanopositioning stage, Review of Scientific Instruments (2013) 125111. https://doi.org/10.1063/1.4848876.

[16] L.-J. Lai, G.-Y. Gu, L.-M. Zhu, Design and control of a decoupled two degree of freedom translational parallel micro-positioning stage, Review of Scientific Instruments (2012) 045105. https://doi.org/10.1063/1.3700182.

[17] X. Zhu, X. Xu, Z. Wen, J. Ren, P. Liu, A novel flexure-based vertical nanopositioning stage with large travel range, Review of Scientific Instruments (2015) 105112. https://doi.org/10.1063/1.4932963.

[18] J. Qu, W. Chen, J. Zhang, A parallelogram-based compliant remote-center-of-motion stage for active parallel alignment, Review of Scientific Instruments (2014) 095112. https://doi.org/10.1063/1.4895680.

[19] J. Shang, Y. Tian, Z. Li, F. Wang, K. Cai, A novel voice coil motor-driven compliant micropositioning stage based on flexure mechanism, Review of Scientific Instruments (2015) 095001. https://doi.org/10.1063/1.4929867.

[20] Z. Shi, X. Li, Z. Zhu, Design, optimization, and characterization of an xy nanopositioning stage with multi-level spatial flexure hinges for high-precision large-stroke motion guidance, Review of Scientific Instruments (2023) 125007. https://doi.org/10.1063/5.0173722.

[21] P. Gräser, S. Linß, F. Harfensteller, M. Torres, L. Zentner, R. Theska, High-precision and large-stroke xy micropositioning stage based on serially arranged compliant mechanisms with flexure hinges, Precision Engineering (2021) 469–479. https://doi.org/j.precisioneng.2021.02.001.

[22] F. Wang, X. Zhao, Z. Huo, B. Shi, C. Liang, Y. Tian, D. Zhang, A 2-dof nanopositioning scanner with novel compound decoupling-guiding mechanism, Mechanism and Machine Theory (2021) 104066. https://doi.org/10.1016/j.mechmachtheory.2020.104066.

[23] S. Polit, J. Dong, Design of high-bandwidth high-precision flexure-based nanopositioning modules, Journal of Manufacturing Systems (2009) 71–77. https://doi.org/10.1016/j.jmsy.2010.01.001.

[24] Y. Li, Q. Xu, A totally decoupled piezo-driven xyz flexure parallel micropositioning stage for micro/nanomanipulation, IEEE Transactions on Automation Science and Engineering (2011) 265–279. https://doi.org/10.1109/TASE.2010.2077675.

[25] P. Wang, Q. Xu, Design of a flexure-based constant-force xy precision positioning stage, Mechanism and Machine Theory (2017) 1–13. https://doi.org/10.1016/j.mechmachtheory.2016.10.007.

[26] Q. Meng, K. Harrington, J. Stirling, R. Bowman, The openflexure block stage: sub-100 nm fibre alignment with a monolithic plastic flexure stage, Opt. Express (2020) 4763–4772. https://doi.org/10.1364/OE.384207.

[27] M. I. Frecker, K. M. Powell, R. Haluck, Design of a multifunctional compliant instrument for minimally invasive surgery, Journal of Biomechanical Engineering (2005) 990–993. https://doi.org/10.1115/1.2056560.

[28] P. A. Halverson, A. E. Bowden, L. L. Howell, A compliant-mechanism approach to achieving specific quality of motion in a lumbar total disc replacement, International Journal of Spine Surgery (2012) 78–86. https://doi.org/10.1016/j.ijsp.2012.02.002.

[29] J. Arata, S. Kogiso, M. Sakaguchi, R. Nakadate, S. Oguri, M. Uemura, C. Byunghyun, T. Akahoshi, T. Ikeda, M. Hashizume, Articulated minimally invasive surgical instrument based on compliant mechanism, International Journal of Computer Assisted Radiology and Surgery (2015) 1837–1843. https://doi.org/10.1007/s11548-015-1159-4.

[30] M. Zanaty, T. Fussinger, A. Rogg, A. Lovera, D. Lambelet, I. Vardi, T. J. Wolfensberger, C. Baur, S. Henein, Programmable multistable mechanisms for safe surgical puncturing, Journal of Medical Devices (2019) 021002. https://doi.org/10.1115/1.4043016.

[31] D. Shin, H.-U. Kim, A. Kulkarni, Y.-H. Kim, T. Kim, Development of force sensor system based on tri-axial fiber bragg grating with flexure structure, Sensors (2022). https://doi.org/10.3390/s22010016.

[32] P. Kumar, C. Schmidleithner, N. B. Larsen, O. Sigmund, Topology optimization and 3d printing of large-deformation compliant mechanisms for straining biological tissues, Structural and Multidisciplinary Optimization (2021) 1351–1366. https://doi.org/10.1007/s00158-020-02764-4.

[33] G. Molinari, M. Quack, A. F. Arrieta, M. Morari, P. Ermanni, Design, realization and structural testing of a compliant adaptable wing, Smart Materials and Structures (2015) 105027. https://doi.org/10.1088/0964-1726/24/10/105027.

[34] G. Molinari, A. F. Arrieta, M. Guillaume, P. Ermanni, Aerostructural performance of distributed compliance morphing wings: Wind tunnel and flight testing, AIAA Journal (2016) 3859–3871. https://doi.org/10.2514/1.J055073.

[35] I. K. Kuder, A. F. Arrieta, M. Rist, P. Ermanni, Aeroelastic response of a selectively compliant morphing aerofoil featuring integrated variable stiffness bi-stable lam-

inates, Journal of Intelligent Material Systems and Structures (2016) 1949–1966. https://doi.org/10.1177/1045389X15620038.

[36] F. Previtali, G. Molinari, A. F. Arrieta, M. Guillaume, P. Ermanni, Design, manufacturing and testing of a morphing wing with enhanced corrugations, Journal of Intelligent Material Systems and Structures (2016) 278–292. https://doi.org/10.1177/1045389X15595296.

[37] F. Runkel, U. Fasel, G. Molinari, A. F. Arrieta, P. Ermanni, Wing twisting by elastic instability: A purely passive approach, Composite Structures (2018) 750–761. https://doi.org/10.1016/j.compstruct.2018.07.095.

[38] S. Henein, P. Spanoudakis, S. Droz, L. I. Myklebust, E. Onillon, Flexure pivot for aerospace mechanisms, in: Proceedings of the 10th European Space Mechanisms and Tribology Symposium, Vol. 524, San Sebastián, Spain, 2003, pp. 285–288.

[39] H. M. Y. C. Mallikarachchi, S. Pellegrino, Quasi-static folding and deployment of ultrathin composite tape-spring hinges, Journal of Spacecraft and Rockets (2011) 187–198. https://doi.org/10.2514/1.47321.

[40] H. M. Y. C. Mallikarachchi, S. Pellegrino, Deployment dynamics of ultrathin composite booms with tape-spring hinges, Journal of Spacecraft and Rockets (2014) 604–613. https://doi.org/10.2514/1.A32401.

[41] H. M. Y. C. Mallikarachchi, S. Pellegrino, Design of ultrathin composite self-deployable booms, Journal of Spacecraft and Rockets (2014) 1811–1821. https://doi.org/10.2514/1.A32815.

[42] S. A. Zirbel, K. A. Tolman, B. P. Trease, L. L. Howell, Bistable mechanisms for space applications, PLOS ONE (2016) e0168218. https://doi.org/10.1371/journal.pone.0168218.

[43] A. F. Arrieta, O. Bilgen, M. I. Friswell, P. Hagedorn, Modelling and configuration control of wing-shaped bi-stable piezoelectric composites under aerodynamic loads, Aerospace Science and Technology (2013) 453–461. https://doi.org/10.1016/j.ast.2013.05.004.

[44] E. H. Llanos, B. Corves, M. Huesing, A. Saxena, Systematic mapping of synthesis methods for compliant grippers using prisma, Mechanism and Machine Theory (2025) 105900. https://doi.org/10.1016/j.mechmachtheory.2024.105900.

[45] J. Gan, J. Zhang, M.-F. Ge, X. Tu, Designs of compliant mechanism-based force sensors: A review, IEEE Sensors Journal (2022) 8282–8294. https://doi.org/10.1109/JSEN.2022.3161963.

[46] R. Niiyama, Soft actuation and compliant mechanisms in humanoid robots, Current Robotics Reports (2022) 111–117. https://doi.org/10.1007/s43154-022-00084-7.

[47] Z. Samadikhoshkho, E. Saive, M. G. Lipsett, A review of compliant mechanisms for contact robotics applications, Robotics and Autonomous Systems (2025) 104902. https://doi.org/10.1016/j.robot.2024.104902.

[48] X. Zhou, S. Bi, A survey of bio-inspired compliant legged robot designs, Bioinspiration & Biomimetics (2012) 041001. https://doi.org/10.1088/1748-3182/7/4/041001.

[49] S. Henein, C. Aymon, S. Bottinelli, R. Clavel, Articulated structures with flexible joints dedicated to high precision robotics, in: Proceedings of the International Advanced Robotics Programme Workshop on Micro Robots, Machines and Systems, 1999.
URL https://infoscience.epfl.ch/handle/20.500.14299/202071

[50] J.-Y. Wang, C.-C. Lan, A constant-force compliant gripper for handling objects of various sizes, Journal of Mechanical Design (2014) 071008. https://doi.org/10.1115/1.4027285.

[51] D. Petković, N. D. Pavlović, S. Shamshirband, N. Badrul Anuar, Development of a new type of passively adaptive compliant gripper, Industrial Robot: the international journal of robotics research and application (2013) 610–623. https://doi.org/10.1108/IR-12-2012-452.

[52] D. Petkovic, M. Issa, N. D. Pavlovic, L. Zentner, Passively adaptive compliant gripper, Applied Mechanics and Materials (2012) 316–325. https://doi.org/10.4028/www.scientific.net/amm.162.316.

[53] P. Liu, J. Qian, P. Yan, Y. Liu, Design, analysis and evaluation of a self-lockable constant-force compliant gripper, Sensors and Actuators A: Physical (2022) 113354. https://doi.org/10.1016/j.sna.2021.113354.

[54] J. Gan, H. Xu, X. Zhang, H. Ding, Design of a compliant adjustable constant-force gripper based on circular beams, Mechanism and Machine Theory (2022) 104843. https://doi.org/10.1016/j.mechmachtheory.2022.104843.

[55] G. Hao, H. Li, A. Nayak, S. Caro, Design of a compliant gripper with multimode jaws, Journal of Mechanisms and Robotics (2018) 031005. https://doi.org/10.1115/1.4039498.

[56] X. Sun, S. Yang, Y. Li, W. Chen, Y. Jin, A low-cost underactuated compliant gripper with multifunctional jaws for precision manipulation, Sensors and Actuators A: Physical (2024) 115047. https://doi.org/10.1016/j.sna.2024.115047.

[57] Q. Xu, Design and development of a novel compliant gripper with integrated position and grasping/interaction force sensing, IEEE Transactions on Automation Science and Engineering (2017) 1415–1428. https://doi.org/10.1109/TASE.2015.2469108.

[58] Q. Xu, Structure design of a new compliant gripper based on scott-russell mechanism, in: 2013 IEEE International Conference on Robotics and Biomimetics (ROBIO), 2013, pp. 1623–1628. https://doi.org/10.1109/ROBIO.2013.6739699.

[59] J. Zhu, G. Hao, Design and test of a compact compliant gripper using the scott–russell mechanism, Archives of Civil and Mechanical Engineering (2020) 81. https://doi.org/10.1007/s43452-020-00085-3.

[60] G. Hao, R. B. Hand, Design and static testing of a compact distributed-compliance gripper based on flexure motion, Archives of Civil and Mechanical Engineering (2016) 708–716. https://doi.org/10.1016/j.acme.2016.04.011.

[61] P.-L. Chang, I.-T. Chi, N. D. K. Tran, D.-A. Wang, Design and modeling of a compliant gripper with parallel movement of jaws, Mechanism and Machine Theory (2020) 103942. https://doi.org/10.1016/j.mechmachtheory.2020.103942.

[62] W. Wang, H. Rodrigue, H.-I. Kim, M.-W. Han, S.-H. Ahn, Soft composite hinge actuator and application to compliant robotic gripper, Composites Part B: Engineering (2016) 397–405. https://doi.org/10.1016/j.compositesb.2016.05.030.

[63] M. Lofroth, E. Avci, Development of a novel modular compliant gripper for manipulation of micro objects, Micromachines (2019). https://doi.org/10.3390/mi10050313.

[64] Y. Gao, X. Huang, I. S. Mann, H.-J. Su, A novel variable stiffness compliant robotic gripper based on layer jamming, Journal of Mechanisms and Robotics (2020) 051013. https://doi.org/10.1115/1.4047156.

[65] C.-H. Liu, T.-L. Chen, C.-H. Chiu, M.-C. Hsu, Y. Chen, T.-Y. Pai, W.-G. Peng, Y.-P. Chiang, Optimal design of a soft robotic gripper for grasping unknown objects, Soft Robotics (2018) 452–465. https://doi.org/10.1089/soro.2017.0121.

[66] O. Shiryayev, N. Vahdati, F. F. Yap, H. Butt, Compliant mechanism-based sensor for large strain measurements employing fiber optics, Sensors (2022). https://doi.org/10.3390/s22113987.

[67] Z. Wang, H. Hu, Analysis and optimization of a compliant mechanism-based digital force/weight sensor, IEEE Sensors Journal (2005) 1243–1250. https://doi.org/10.1109/JSEN.2005.859286.

[68] G. Krishnan, G. K. Ananthasuresh, Evaluation and design of displacement-amplifying compliant mechanisms for sensor applications, Journal of Mechanical Design (2008) 102304. https://doi.org/10.1115/1.2965599.

[69] F. Chen, Y. Zhou, L. Zhong, W. Yang, J. Gan, Design of a strain gauge-based force sensor with three ranges based on compliant mechanisms, IEEE Transactions on Instrumentation and Measurement (2025) 1–10. https://doi.org/10.1109/TIM.2025.3529078.

[70] L. Clark, B. Shirinzadeh, Y. Tian, B. Yao, Development of a passive compliant mechanism for measurement of micro/nanoscale planar 3-dof motions, IEEE/ASME Transactions on Mechatronics (2016) 1222–1232. https://doi.org/10.1109/TMECH.2015.2503728.

[71] G. S. Baichapur, H. Gugale, A. Maheshwari, S. D. B. Bhargav, G. K. Ananthasuresh, A vision-based micro-newton static force sensor using a displacement-amplifying compliant mechanism (dacm), Mechanics Based Design of Structures and Machines (2014) 193–210. https://doi.org/10.1080/15397734.2013.864938.

[72] Z. Gao, D. Zhang, Design, analysis and fabrication of a multidimensional acceleration sensor based on fully decoupled compliant parallel mechanism, Sensors and Actuators A: Physical (2010) 418–427. https://doi.org/10.1016/j.sna.2010.08.021.

[73] G. Hao, M. Murphy, X. Luo, Development of a compliant-mechanism-based compact three-axis force sensor for high-precision manufacturing, in: Proceedings of the ASME 2015 International Design Engineering Technical Conferences and Computers and Information in Engineering Conference, 2015, p. V009T07A082. https://doi.org/10.1115/DETC2015-46166.

[74] A. Gao, R. J. Murphy, H. Liu, I. I. Iordachita, M. Armand, Mechanical model of dexterous continuum manipulators with compliant joints and tendon/external force interactions, IEEE/ASME Transactions on Mechatronics (2017) 465–475. https://doi.org/10.1109/TMECH.2016.2612833.

[75] X. Dong, M. Raffles, S. Cobos-Guzman, D. Axinte, J. Kell, A novel continuum robot using twin-pivot compliant joints: Design, modeling, and validation, Journal of Mechanisms and Robotics (2015) 021010. https://doi.org/10.1115/1.4031340.

[76] F. Feng, W. Hong, L. Xie, Design of 3d-printed flexible joints with presettable stiffness for surgical robots, IEEE Access (2020) 79573–79585. https://doi.org/10.1109/ACCESS.2020.2991092.

[77] K. Xu, N. Simaan, An investigation of the intrinsic force sensing capabilities of continuum robots, IEEE Transactions on Robotics (2008) 576–587. https://doi.org/10.1109/TRO.2008.924266.

[78] M. D. Kutzer, S. M. Segreti, C. Y. Brown, M. Armand, R. H. Taylor, S. C. Mears, Design of a new cable-driven manipulator with a large open lumen: Preliminary applications in the minimally-invasive removal of osteolysis, in: 2011 IEEE International Conference on Robotics and Automation, 2011, pp. 2913–2920. https://doi.org/10.1109/ICRA.2011.5980285.

[79] P. Qi, C. Qiu, H. Liu, J. S. Dai, L. D. Seneviratne, K. Althoefer, A novel continuum manipulator design using serially connected double-layer planar springs, IEEE/ASME Transactions on Mechatronics (2016) 1281–1292. https://doi.org/10.1109/TMECH.2015.2498738.

[80] X. Dong, M. Raffles, S. C. Guzman, D. Axinte, J. Kell, Design and analysis of a family of snake arm robots connected by compliant joints, Mechanism and Machine Theory (2014) 73–91. https://doi.org/10.1016/j.mechmachtheory.2014.01.017.

[81] T. L. Thomas, V. K. Venkiteswaran, G. K. Ananthasuresh, S. Misra, A monolithic compliant continuum manipulator: A proof-of-concept study, Journal of Mechanisms and Robotics (2020) 061006. https://doi.org/10.1115/1.4046838.

[82] P. Bilancia, G. Berselli, An overview of procedures and tools for designing nonstandard beam-based compliant mechanisms, Computer-Aided Design (2021) 103001. https://doi.org/10.1016/j.cad.2021.103001.

[83] L. U. Odhner, A. M. Dollar, The Smooth Curvature Model: An Efficient Representation of Euler–Bernoulli Flexures as Robot Joints, IEEE Transactions on Robotics (2012) 761–772. https://doi.org/10.1109/TRO.2012.2193232.

[84] L. L. Howell, A. Midha, T. W. Norton, Evaluation of Equivalent Spring Stiffness for Use in a Pseudo-Rigid-Body Model of Large-Deflection Compliant Mechanisms, Journal of Mechanical Design (1996) 126–131. https://doi.org/10.1115/1.2826843.

[85] S. Sen, Beam constraint model: Generalized nonlinear closed-form modeling of beam flexures for flexure mechanism design., Ph.D. thesis, University of Michigan (2013).
URL https://deepblue.lib.umich.edu/handle/2027.42/97856

[86] S. Sen, S. Awtar, A closed-form nonlinear model for the constraint characteristics of symmetric spatial beams, Journal of Mechanical Design (2013) 031003. https://doi.org/10.1115/1.4023157.

[87] G. L. Holst, G. H. Teichert, B. D. Jensen, Modeling and Experiments of Buckling Modes and Deflection of Fixed-Guided Beams in Compliant Mechanisms, Journal of Mechanical Design (2011) 051002. https://doi.org/10.1115/1.4003922.

[88] A. Saxena, S. N. Kramer, A simple and accurate method for determining large deflections in compliant mechanisms subjected to end forces and moments, Journal of Mechanical Design (1998) 392–400. https://doi.org/10.1115/1.2829164.

[89] S. M. Lyon, L. L. Howell, A simplified pseudo-rigid-body model for fixed-fixed flexible segments, International Design Engineering Technical Conferences and Computers and Information in Engineering Conference, 2002, pp. 23–33. https://doi.org/10.1115/DETC2002/MECH-34203.

[90] H.-J. Su, A Pseudorigid-Body 3R Model for Determining Large Deflection of Cantilever Beams Subject to Tip Loads, Journal of Mechanisms and Robotics (2009) 021008. https://doi.org/10.1115/1.3046148.

[91] G. Chen, B. Xiong, X. Huang, Finding the optimal characteristic parameters for 3R pseudo-rigid-body model using an improved particle swarm optimizer, Precision Engineering (2011) 505–511. https://doi.org/10.1016/j.precisioneng.2011.02.006.

[92] V. K. Venkiteswaran, H.-J. Su, A Versatile 3R Pseudo-Rigid-Body Model for Initially Curved and Straight Compliant Beams of Uniform Cross Section, Journal of Mechanical Design (2018) 092305. https://doi.org/10.1115/1.4040628.

[93] Y.-Q. Yu, Z.-L. Feng, Q.-P. Xu, A pseudo-rigid-body 2R model of flexural beam in compliant mechanisms, Mechanism and Machine Theory (2012) 18–33. https://doi.org/10.1016/j.mechmachtheory.2012.04.005.

[94] Y.-Q. Yu, S.-K. Zhu, 5R pseudo-rigid-body model for inflection beams in compliant mechanisms, Mechanism and Machine Theory (2017) 501–512. https://doi.org/10.1016/j.mechmachtheory.2017.06.016.

[95] M. Jin, Z. Yang, C. Ynchausti, B. Zhu, X. Zhang, L. L. Howell, Large-Deflection Analysis of General Beams in Contact-Aided Compliant Mechanisms Using Chained Pseudo-Rigid-Body Model, Journal of Mechanisms and Robotics (2020) 031005. https://doi.org/10.1115/1.4045425.

[96] L. Qiu, C. Li, S. Dai, Y. Yu, Research on the line-arc-line constant-torque flexure hinge (LAL-CTFH) based on improved pseudo-rigid-body model (PRBM), Mechanism and Machine Theory (2022) 104878. https://doi.org/10.1016/j.mechmachtheory.2022.104878.

[97] S. Dai, L. Qiu, Y. Yu, C. Li, On the numerical synthesis of a contact-aided branch hinge (CABH) with variable stiffness, Mechanism and Machine Theory (2023) 105167. https://doi.org/10.1016/j.mechmachtheory.2022.105167.

[98] L. Qiu, S. Dai, Y. Li, C. Li, Design and analysis of a contact-aided leaf hinge (CALH) with continuous variable stiffness, Mechanism and Machine Theory (2022) 104653. https://doi.org/10.1016/j.mechmachtheory.2021.104653.

[99] G. Chen, F. Ma, Kinetostatic modeling of fully compliant bistable mechanisms using timoshenko beam constraint model, Journal of Mechanical Design (2015) 022301. https://doi.org/10.1115/1.4029024.

[100] P. Liu, P. Yan, Kinetostatic modeling of bridge-type amplifiers based on timoshenko beam constraint model, International Journal of Precision Engineering and Manufacturing (2018) 1339–1345. https://doi.org/10.1007/s12541-018-0158-0.

[101] F. Ma, G. Chen, Bi-bcm: A closed-form solution for fixed-guided beams in compliant mechanisms, Journal of Mechanisms and Robotics (2016) 014501. https://doi.org/10.1115/1.4035084.

[102] P. Bilancia, M. Baggetta, G. Hao, G. Berselli, A variable section beams based Bi-BCM formulation for the kinetostatic analysis of cross-axis flexural pivots, International Journal of Mechanical Sciences (2021) 106587. https://doi.org/10.1016/j.ijmecsci.2021.106587.

[103] L. Meng, R. Kang, D. Gan, G. Chen, L. Chen, D. T. Branson, J. S. Dai, A Mechanically Intelligent Crawling Robot Driven by Shape Memory Alloy and Compliant Bistable Mechanism, Journal of Mechanisms and Robotics (2020) 061005. https://doi.org/10.1115/1.4046837.

[104] J. Zhu, G. Hao, H. Tang, Design and Modelling of a Generic Compliant Mechanism with Bi-stability and Static Balancing, in: 2022 IEEE International Conference on Manipulation, Manufacturing and Measurement on the Nanoscale (3M-NANO), 2022, pp. 172–177. https://doi.org/10.1109/3M-NANO56083.2022.9941512.

[105] G. Hao, Extended nonlinear analytical models of compliant parallelogram mechanisms: third-order models, Transactions of the Canadian Society for Mechanical Engineering (2015) 71–83. https://doi.org/10.1139/tcsme-2015-0006.

[106] J. Zhu, G. Hao, Modelling of a general lumped-compliance beam for compliant mechanisms, International Journal of Mechanical Sciences (2024) 108779. https://doi.org/10.1016/j.ijmecsci.2023.108779.

[107] M. Ling, L. Yuan, X. Zhang, Geometrically nonlinear analysis of compliant mechanisms using a dynamic beam constraint model (DBCM), Mechanism and Machine Theory (2024) 105489. https://doi.org/10.1016/j.mechmachtheory.2023.105489.

[108] F. Ma, G. Chen, Modeling Large Planar Deflections of Flexible Beams in Compliant Mechanisms Using Chained Beam-Constraint-Model, Journal of Mechanisms and Robotics (2015) 021018. https://doi.org/10.1115/1.4031028.

[109] G. Chen, F. Ma, G. Hao, W. Zhu, Modeling Large Deflections of Initially Curved Beams in Compliant Mechanisms Using Chained Beam Constraint Model, Journal of Mechanisms and Robotics (2018) 011002. https://doi.org/10.1115/1.4041585.

[110] F. Ma, G. Chen, H. Wang, Large-stroke constant-force mechanisms utilizing second buckling mode of flexible beams: Evaluation metrics and design approach, Journal of Mechanical Design (2020) 103303. https://doi.org/10.1115/1.4046242.

[111] K. Kong, G. Chen, G. Hao, Kinetostatic Modeling and Optimization of a Novel Horizontal-Displacement Compliant Mechanism, Journal of Mechanisms and Robotics (2019) 064502. https://doi.org/10.1115/1.4044334.

[112] W. Zeng, G. Xu, H. Jiang, C. Huang, F. Gao, S. Yang, Design of a variable-diameter wheel with a novel distributed compliant mechanism, Mechanism and Machine

Theory (2023) 105450. https://doi.org/10.1016/j.mechmachtheory.2023.105450.

[113] I.-T. Chi, T. H. Ngo, P.-L. Chang, N. D. K. Tran, D.-A. Wang, Design of a bistable mechanism with b-spline profiled beam for versatile switching forces, Sensors and Actuators A: Physical (2019) 173–184. https://doi.org/10.1016/j.sna.2019.05.028.

[114] G. Chen, R. Bai, Modeling large spatial deflections of slender bisymmetric beams in compliant mechanisms using chained spatial-beam constraint model, Journal of Mechanisms and Robotics (2016) 041011. https://doi.org/10.1115/1.4032632.

[115] R. Bai, G. Chen, S. Awtar, Closed-form solution for nonlinear spatial deflections of strip flexures of large aspect ratio considering second order load-stiffening, Mechanism and Machine Theory (2021) 104324. https://doi.org/10.1016/j.mechmachtheory.2021.104324.

[116] B. Todd, B. D. Jensen, S. M. Schultz, A. R. Hawkins, Design and Testing of a Thin-Flexure Bistable Mechanism Suitable for Stamping From Metal Sheets, Journal of Mechanical Design (2010) 071011. https://doi.org/10.1115/1.4001876.

[117] J. Zhao, J. Jia, X. He, H. Wang, Post-buckling and Snap-Through Behavior of Inclined Slender Beams, Journal of Applied Mechanics (2008) 041020. https://doi.org/10.1115/1.2870953.

[118] A. Zhang, G. Chen, A Comprehensive Elliptic Integral Solution to the Large Deflection Problems of Thin Beams in Compliant Mechanisms, Journal of Mechanisms and Robotics (2013) 021006. https://doi.org/10.1115/1.4023558.

[119] N. Iwatsuki, T. Kosaki, Large deformation analysis and synthesis of elastic closed-loop mechanism made of a certain spring wire described by free curves, Chinese Journal of Mechanical Engineering (2015) 756–762. https://doi.org/10.3901/CJME.2015.0506.067.

[120] P. Kuresangsai, M. O. T. Cole, G. Hao, Grasp stability and design analysis of a flexure-jointed gripper mechanism via efficient energy-based modeling, IEEE Robotics and Automation Letters (2022) 12499–12506. https://doi.org/10.1109/LRA.2022.3220152.

[121] O. A. Turkkan, H.-J. Su, A general and efficient multiple segment method for kinetostatic analysis of planar compliant mechanisms, Mechanism and Machine Theory (2017) 205–217. https://doi.org/10.1016/j.mechmachtheory.2017.02.010.

[122] S. Wu, Z. Shao, H. Su, H. Fu, An energy-based approach for kinetostatic modeling of general compliant mechanisms, Mechanism and Machine Theory (2019) 103588. https://doi.org/10.1016/j.mechmachtheory.2019.103588.

[123] G. Chen, F. Ma, R. Bai, W. Zhu, S. P. Magleby, L. L. Howell, An Energy-Based Framework for Nonlinear Kinetostatic Modeling of Compliant Mechanisms Utilizing Beam Flexures, Journal of Computing and Information Science in Engineering (2021) 064501. https://doi.org/10.1115/1.4050472.

[124] T. Liu, G. Hao, J. Zhu, P. Kuresangsai, S. Abdelaziz, E. Wehrle, Modeling compliant bistable mechanisms: An energy method based on the high-order smooth curvature

model, International Journal of Mechanical Sciences (2024) 109315. https://doi.org/10.1016/j.ijmecsci.2024.109315.

[125] T. Liu, G. Hao, Comprehensive SCME: A nonlinear large-deformation modeling approach for planar compliant mechanisms, Mechanism and Machine Theory (2025) 106070. https://doi.org/10.1016/j.mechmachtheory.2025.106070.

[126] M. Y. Wang, S. Chen, Compliant mechanism optimization: Analysis and design with intrinsic characteristic stiffness, Mechanics Based Design of Structures and Machines (2009) 183–200. https://doi.org/10.1080/15397730902761932.

[127] N. Olhoff, J. E. Taylor, On structural optimization, Journal of Applied Mechanics (1983) 1139–1151. https://doi.org/10.1115/1.3167196.

[128] P. W. Christensen, A. Klarbring, An Introduction to Structural Optimization, 1st Edition, Solid Mechanics and Its Applications, Springer Dordrecht, 2009. https://doi.org/10.1007/978-1-4020-8666-3.

[129] M. Z. Cohn, A. S. Dinovitzer, Application of structural optimization, Journal of Structural Engineering (1994) 617–650. https://doi.org/10.1061/(ASCE)0733-9445(1994)120:2(617).

[130] C. N. Wang, K. P. Truong, N. T. Huynh, H. Nguyen, Optimization on effects of design parameter on displacement amplification ratio of 2 dof working platform employing bridge-type compliant mechanism flexure hinge using taguchi method, Journal of Physics: Conference Series (2019) 012053. https://doi.org/10.1088/1742-6596/1303/1/012053.

[131] J. A. Hetrick, S. Kota, Size and Shape Optimization of Compliant Mechanisms: An Efficiency Formulation, in: Proceedings of the ASME Design Engineering Technical Conferences, 1998, p. V01BT01A049. https://doi.org/10.1115/DETC98/MECH-5943.

[132] F. De Bona, M. G. Munteanu, Optimized flexural hinges for compliant micromechanisms, Analog Integrated Circuits and Signal Processing (2005) 163–174. https://doi.org/10.1007/s10470-005-2597-7.

[133] B. H. V. Topping, Shape optimization of skeletal structures: A review, Journal of Structural Engineering (1983) 1933–1951. https://doi.org/10.1061/(ASCE)0733-9445(1983)109:8(1933).

[134] R. T. Haftka, R. V. Grandhi, Structural shape optimization — a survey, Computer Methods in Applied Mechanics and Engineering (1986) 91–106. https://doi.org/10.1016/0045-7825(86)90072-1.

[135] S. Bhavikatti, C. Ramakrishnan, Shape optimization of structural systems using finite elements and sequential linear programming, in: Large Engineering Systems, 1977, pp. 224–235. https://doi.org/10.1016/B978-0-08-021295-1.50022-5.

[136] R. Yang, D. Dewhirst, J. Allison, A. Lee, Shape optimization of connecting rod pin end using a generic model, Finite Elements in Analysis and Design (1992) 257–264. https://doi.org/10.1016/0168-874X(92)90056-I.

[137] D. A. Tortorelli, J. A. Tomasko, T. E. Morthland, J. A. Dantzig, Optimal design of nonlinear parabolic systems. part ii: Variable spatial domain with applications to casting optimization, Computer Methods in Applied Mechanics and Engineering (1994) 157–172. https://doi.org/10.1016/0045-7825(94)90216-X.

[138] J. A. Hetrick, S. Kota, An energy formulation for parametric size and shape optimization of compliant mechanisms, Journal of Mechanical Design (1999) 229–234. https://doi.org/10.1115/1.2829448.

[139] H. Zhou, K.-L. Ting, Geometric optimization of spatial compliant mechanisms using three-dimensional wide curves, Journal of Mechanical Design (2009) 051002. https://doi.org/10.1115/1.3086792.

[140] H. Zhou, K.-L. Ting, Wide curve based geometric optimization of compliant mechanisms, Vol. Volume 7: 29th Mechanisms and Robotics Conference, Parts A and B of International Design Engineering Technical Conferences and Computers and Information in Engineering Conference, 2005, pp. 35–41. https://doi.org/10.1115/DETC2005-84605.

[141] H. Zhou, K.-L. Ting, Geometric modeling and optimization of multimaterial compliant mechanisms using multilayer wide curves, Journal of Mechanical Design (2008) 062303. https://doi.org/10.1115/1.2902278.

[142] M. P. Dang, H. G. Le, N. L. Chau, T.-P. Dao, A multi-objective optimization design for a new linear compliant mechanism, Optimization and Engineering (2020) 673–705. https://doi.org/10.1007/s11081-019-09469-8.

[143] Y. Tummala, M. Frecker, A. Wissa, J. Hubbard, James E., Design and optimization of a bend-and-sweep compliant mechanism, Vol. Volume 6A: 37th Mechanisms and Robotics Conference of International Design Engineering Technical Conferences and Computers and Information in Engineering Conference, 2013, p. V06AT07A023. https://doi.org/10.1115/DETC2013-12338.

[144] B. Zhu, X. Zhang, H. Zhang, J. Liang, H. Zang, H. Li, R. Wang, Design of compliant mechanisms using continuum topology optimization: A review, Mechanism and Machine Theory (2020) 103622. https://doi.org/10.1016/j.mechmachtheory.2019.103622.

[145] O. Sigmund, On the design of compliant mechanisms using topology optimization, Mechanics of Structures and Machines (1997) 493–524. https://doi.org/10.1016/10.1080/08905459708945415.

[146] T. E. Bruns, D. A. Tortorelli, Topology optimization of non-linear elastic structures and compliant mechanisms, Computer Methods in Applied Mechanics and Engineering (2001) 3443–3459. https://doi.org/10.1016/S0045-7825(00)00278-4.

[147] X. Huang, Y. Li, S. Zhou, Y. Xie, Topology optimization of compliant mechanisms with desired structural stiffness, Engineering Structures (2014) 13–21. https://doi.org/10.1016/j.engstruct.2014.08.008.

[148] Z. Luo, L. Chen, J. J. Yang, Y. Zhang, K. Abdel-Malek, Compliant mechanism design using multi-objective topology optimization scheme of continuum structures, Structural and Multidisciplinary Optimization (2005) 142–154. https://doi.org/10.1007/s00158-004-0512-y.

[149] J. Lin, Z. Luo, L. Tong, A new multi-objective programming scheme for topology optimization of compliant mechanisms, Structural and Multidisciplinary Optimization (2010) 241–255. https://doi.org/10.1007/s00158-008-0355-z.

[150] D. M. D. Leon, J. Alexandersen, J. S. O. Fonseca, O. Sigmund, Stress-constrained topology optimization for compliant mechanism design, Structural and Multidisci-

plinary Optimization (2015) 929–943. https://doi.org/10.1007/s00158-015-1279-z.

[151] R. Ansola, E. Veguería, J. Canales, J. A. Tárrago, A simple evolutionary topology optimization procedure for compliant mechanism design, Finite Elements in Analysis and Design (2007) 53–62. https://doi.org/10.1016/j.finel.2007.09.002.

[152] Q. Xia, T. Shi, Topology optimization of compliant mechanism and its support through a level set method, Computer Methods in Applied Mechanics and Engineering (2016) 359–375. https://doi.org/10.1016/j.cma.2016.03.017.

[153] N. Kogiso, W. Ahn, S. Nishiwaki, K. Izui, M. Yoshimura, Robust topology optimization for compliant mechanisms considering uncertainty of applied loads, Journal of Advanced Mechanical Design, Systems, and Manufacturing (2008) 96–107. https://doi.org/10.1299/jamdsm.2.96.

[154] B. K. Stanford, P. Beran, Conceptual design of compliant mechanisms for flapping wings with topology optimization, AIAA Journal (2011) 855–867. https://doi.org/10.2514/1.J050940.

[155] J. Liang, X. Zhang, B. Zhu, H. Zhang, R. Wang, Topology optimization method for designing compliant mechanism with given constant force range, Journal of Mechanisms and Robotics (2023) 061008. https://doi.org/10.1115/1.4056379.

[156] M. Jin, X. Zhang, A new topology optimization method for planar compliant parallel mechanisms, Mechanism and Machine Theory (2016) 42–58. https://doi.org/10.1016/j.mechmachtheory.2015.08.016.

[157] S. Rahmatalla, C. C. Swan, Sparse monolithic compliant mechanisms using continuum structural topology optimization, International Journal for Numerical Methods in Engineering (2005) 1579–1605. https://doi.org/10.1002/nme.1224.

[158] S. Xia, N. Wang, B. Chen, X. Zhang, W. Chen, Topology optimization of compliant mechanisms including links, supports and material distribution, Computers & Structures (2024) 107210. https://doi.org/10.1016/j.compstruc.2023.107210.

[159] Y. Lu, L. Tong, Topology optimization of compliant mechanisms and structures subjected to design-dependent pressure loadings, Structural and Multidisciplinary Optimization (2021) 1889–1906. https://doi.org/10.1007/s00158-020-02786-y.

[160] Y. Wang, Z. Luo, J. Wu, N. Zhang, Topology optimization of compliant mechanisms using element-free galerkin method, Advances in Engineering Software (2015) 61–72. https://doi.org/10.1016/j.advengsoft.2015.03.001.

[161] M.-H. Lin, J.-F. Tsai, C.-S. Yu, A review of deterministic optimization methods in engineering and management, Mathematical Problems in Engineering (2012) 756023. https://doi.org/10.1155/2012/756023.

[162] M. Cavazzuti, Deterministic Optimization, Springer Berlin Heidelberg, 2013, pp. 77–102. https://doi.org/10.1007/978-3-642-31187-1_4.

[163] J. C. Meza, Steepest descent, Wiley Interdisciplinary Reviews: Computational Statistics (2010) 613–619. https://doi.org/10.1002/wics.117.

[164] J. Fliege, B. F. Svaiter, Steepest descent methods for multicriteria optimization, Mathematical Methods of Operations Research (2000) 479–494. https://doi.org/10.1007/s001860000043.

[165] L. G. Drummond, B. Svaiter, A steepest descent method for vector optimization, Journal of Computational and Applied Mathematics (2005) 395–414. https://doi.org/10.1016/j.cam.2004.06.018.

[166] H.-K. Xu, T. H. Kim, Convergence of hybrid steepest-descent methods for variational inequalities, Journal of Optimization Theory and Applications (2003) 185–201. https://doi.org/10.1023/B:JOTA.0000005048.79379.b6.

[167] B. Widrow, J. McCool, A comparison of adaptive algorithms based on the methods of steepest descent and random search, IEEE Transactions on Antennas and Propagation (1976) 615–637. https://doi.org/10.1109/TAP.1976.1141414.

[168] J. R. Shewchuk, An introduction to the conjugate gradient method without the agonizing pain (1994). https://dl.acm.org/doi/10.5555/865018.

[169] S. P. S., I. Branislav, M. Haifeng, M. Dijana, A survey of gradient methods for solving nonlinear optimization, Electronic Research Archive (2020) 1573–1624. https://doi.org/10.3934/era.2020115.

[170] L. Lasdon, S. Mitter, A. Waren, The conjugate gradient method for optimal control problems, IEEE Transactions on Automatic Control (1967) 132–138. https://doi.org/10.1109/TAC.1967.1098538.

[171] A. Galántai, The theory of newton's method, Journal of Computational and Applied Mathematics (2000) 25–44. https://doi.org/10.1016/S0377-0427(00)00435-0.

[172] B. Polyak, Newton's method and its use in optimization, European Journal of Operational Research (2007) 1086–1096. https://doi.org/10.1016/j.ejor.2005.06.076.

[173] C. T. Kelley, Solving Nonlinear Equations with Newton's Method, Society for Industrial and Applied Mathematics, 2003. https://doi.org/10.1137/1.9780898718898.

[174] J. Fliege, L. M. G. n. Drummond, B. F. Svaiter, Newton's method for multiobjective optimization, SIAM Journal on Optimization (2009) 602–626. https://doi.org/10.1137/08071692X.

[175] D. P. Bertsekas, Projected newton methods for optimization problems with simple constraints, SIAM Journal on Control and Optimization (1982) 221–246. https://doi.org/10.1137/0320018.

[176] J. Goodman, Newton's method for constrained optimization, Mathematical Programming (1985) 162–171. https://doi.org/10.1007/BF01582243.

[177] B. C. Truong, N. V. Thuan, N. H. Hau, M. McAleer, Applications of the newton-raphson method in decision sciences and education, Advances in Decision Sciences (December 2019). https://pure.eur.nl/en/publications/applications-of-the-newton-raphson-method-in-decision-sciences-an.

[178] S. Hartmann, A remark on the application of the newton-raphson method in non-linear finite element analysis, Computational Mechanics (2005) 100–116. https://doi.org/10.1007/s00466-004-0630-9.

[179] R. L. Rardin, R. Uzsoy, Experimental evaluation of heuristic optimization algorithms: A tutorial, Journal of Heuristics (2001) 261–304. https://doi.org/10.1023/A:1011319115230.

[180] A. Saxena, Synthesis of compliant mechanisms for path generation using genetic algorithm, Journal of Mechanical Design (2005) 745–752. https://doi.org/10.1115/1.1899178.

[181] R. Parsons, S. L. Canfield, Developing genetic programming techniques for the design of compliant mechanisms, Structural and Multidisciplinary Optimization (2002) 78–86. https://doi.org/10.1007/s00158-002-0216-0.

[182] J. A. Cabrera, A. Simon, M. Prado, Optimal synthesis of mechanisms with genetic algorithms, Mechanism and Machine Theory (2002) 1165–1177. https://doi.org/10.1016/S0094-114X(02)00051-4.

[183] S. Erkaya, Investigation of balancing problem for a planar mechanism using genetic algorithm, Journal of Mechanical Science and Technology (2013) 2153–2160. https://doi.org/10.1007/s12206-013-0530-z.

[184] K. Deb, S. Tiwari, Multi-objective optimization of a leg mechanism using genetic algorithms, Engineering Optimization (2005) 325–350. https://doi.org/10.1080/03052150500066695.

[185] J. Lampinen, Cam shape optimisation by genetic algorithm, Computer-Aided Design (2003) 727–737. https://doi.org/10.1016/S0010-4485(03)00004-6.

[186] G. N. N. Naik, S. Gopalakrishnan, R. Ganguli, Design optimization of composites using genetic algorithms and failure mechanism based failure criterion, Composite Structures (2008) 354–367. https://doi.org/10.1016/j.compstruct.2007.05.005.

[187] S. Y. Wang, M. Y. Wang, K. Tai, An enhanced genetic algorithm for structural topology optimization, International Journal for Numerical Methods in Engineering (2006) 18–44. https://doi.org/10.1002/nme.1435.

[188] N. Sikalo, O. Hasemann, C. Schulz, A. M. Kempf, I. Wlokas, A genetic algorithm–based method for the optimization of reduced kinetics mechanisms, International Journal of Chemical Kinetics (2015) 695–723. https://doi.org/10.1002/kin.20942.

[189] T. Bhoskar, O. K. Kulkarni, N. K. Kulkarni, S. L. Patekar, G. M. Kakandikar, V. M. Nandedkar, Genetic algorithm and its applications to mechanical engineering: A review, Materials Today: Proceedings (2015) 2624–2630. https://doi.org/10.1016/j.matpr.2015.07.219.

[190] B.-R. Ding, X.-H. Qu, Y.-L. Chen, Application and research of mechanical design optimization based on genetic algorithm kinematics simulation technology, Journal of Intelligent & Fuzzy Systems (2018) 871–878. https://doi.org/10.3233/JIFS-169380.

[191] S. Phelps, P. McBurney, S. Parsons, Evolutionary mechanism design: a review, Autonomous Agents and Multi-Agent Systems (2010) 237–264. https://doi.org/10.1007/s10458-009-9108-7.

[192] R. Storn, K. V. Price, Differential evolution – a simple and efficient heuristic for global optimization over continuous spaces, Journal of Global Optimization (1997) 341–359. https://doi.org/10.1023/A:1008202821328.

[193] J. Kennedy, R. Eberhart, Particle swarm optimization, in: Proceedings of ICNN'95 - International Conference on Neural Networks, Vol. 4, 1995, pp. 1942–1948 vol.4. https://doi.org/10.1109/ICNN.1995.488968.

[194] A. Bedford, K. M. Liechti, Mechanics of Materials, 2nd Edition, Springer Cham, 2020. https://doi.org/10.1007/978-3-030-22082-2.

[195] J. Jiang, S. Lin, H. Wang, Task-driven geometric synthesis method of a bistable compliant mechanism for the rigid guidance problem, Mechanical Sciences (2024) 515–529. https://doi.org/10.5194/ms-15-515-2024.

[196] J. Shen, Efficient spectral-galerkin method i. direct solvers of second- and fourth-order equations using legendre polynomials, SIAM Journal on Scientific Computing (1994) 1489–1505. https://doi.org/10.1137/0915089.

[197] P. N. Swarztrauber, On computing the points and weights for gauss–legendre quadrature, SIAM Journal on Scientific Computing (2003) 945–954. https://doi.org/10.1137/S1064827500379690.

[198] R. V. Southwell, Castigliano' s principle of minimum strain-energy, Proceedings of the Royal Society of London. Series A - Mathematical and Physical Sciences (1936) 4–21. https://doi.org/10.1098/rspa.1936.0033.

[199] C. M. Sourkounis, D. S. Garcia Morales, T. Kwasnitschka, A. Raatz, Exploring the deep sea: Combining a bistable mechanism with origami-inspired soft actuators, in: 2024 IEEE 7th International Conference on Soft Robotics (RoboSoft), 2024, pp. 115–120. https://doi.org/10.1109/RoboSoft60065.2024.10521929.

[200] Z. Wu, B. Zhu, R. Wang, X. Zhang, Design of mechanical metamaterial for energy absorption using a beam with a variable cross-section, Mechanism and Machine Theory (2022) 105027. https://doi.org/10.1016/j.mechmachtheory.2022.105027.

[201] J. Shi, H. Mofatteh, A. Mirabolghasemi, G. Desharnais, A. Akbarzadeh, Programmable multistable perforated shellular, Advanced Materials (2021) 2102423. https://doi.org/10.1002/adma.202102423.

[202] K. Bertoldi, V. Vitelli, J. Christensen, M. van Hecke, Flexible mechanical metamaterials, Nature Reviews Materials (2017) 17066. https://doi.org/10.1038/natrevmats.2017.66.

[203] H. Yang, L. Ma, Multi-stable mechanical metamaterials by elastic buckling instability, Journal of materials science (2019) 3509–3526. https://doi.org/10.1007/s10853-018-3065-y.

[204] H. Yang, L. Ma, 1D to 3D multi-stable architected materials with zero poisson's ratio and controllable thermal expansion, Materials & Design (2020) 108430. https://doi.org/10.1016/j.matdes.2019.108430.

[205] J. U. Surjadi, L. Gao, H. Du, X. Li, X. Xiong, N. X. Fang, Y. Lu, Mechanical metamaterials and their engineering applications, Advanced Engineering Materials (2019). https://doi.org/10.1002/adem.201800864.

[206] M. Zanaty, I. Vardi, S. Henein, Programmable multistable mechanisms: Synthesis and modeling, Journal of Mechanical Design (2018) 042301. https://doi.org/10.1115/1.4038926.

[207] T. Liu, G. Hao, Design of deployable structures by using bistable compliant mechanisms, Micromachines (2022). https://doi.org/10.3390/mi13050651.

[208] Y. Song, R. M. Panas, S. Chizari, L. A. Shaw, J. A. Jackson, J. B. Hopkins, A. J. Pascall, Additively manufacturable micro-mechanical logic gates, Nature communications (2019). https://doi.org/10.1038/s41467-019-08678-0.

[209] R. T. Rockafellar, Lagrange multipliers and optimality, SIAM Review (1993) 183–238. https://doi.org/10.1137/1035044.

[210] D. Spring, On the second derivative test for constrained local extrema, The American Mathematical Monthly (1985) 631–643.

[211] L. Tissot-Daguette, H. Schneegans, E. Thalmann, S. Henein, Analytical modeling and experimental validation of rotationally actuated pinned-pinned and fixed-pinned buckled beam bistable mechanisms, Mechanism and Machine Theory (2022) 104874. https://doi.org/10.1016/j.mechmachtheory.2022.104874.

[212] H. Karabulut, The physical meaning of Lagrange multipliers, European Journal of Physics (2006) 709. https://doi.org/10.1088/0143-0807/27/4/003.

[213] Strand7 Pty Ltd., Strand7 Finite Element Analysis Software, Strand7 Pty Ltd., Sydney, Australia, version R2.4.4 (2024).
URL https://www.strand7.com

[214] UltiMaker, UltiMaker Tough PLA Material Datasheet, UltiMaker, accessed 2025 (2024).
URL https://ultimaker.com/materials/tough-pla

[215] L. Mendo, Estimation of a probability with guaranteed normalized mean absolute error, IEEE Communications Letters (2009) 817–819. https://doi.org/10.1109/LCOMM.2009.091128.

[216] Y. K. Yong, T.-F. Lu, Kinetostatic modeling of 3-rrr compliant micro-motion stages with flexure hinges, Mechanism and Machine Theory (2009) 1156–1175. https://doi.org/10.1016/j.mechmachtheory.2008.09.005.

[217] S. Šalinić, A. Nikolić, A new pseudo-rigid-body model approach for modeling the quasi-static response of planar flexure-hinge mechanisms, Mechanism and Machine Theory (2018) 150–161. https://doi.org/10.1016/j.mechmachtheory.2018.02.011.

[218] J. Wu, Y. Zhang, S. Cai, J. Cui, Modeling and analysis of conical-shaped notch flexure hinges based on nurbs, Mechanism and Machine Theory (2018) 560–568. https://doi.org/10.1016/j.mechmachtheory.2018.07.005.

[219] S. Awtar, Synthesis and analysis of parallel kinematic xy flexure mechanisms, Ph.D. thesis, Massachusetts Institute of Technology (2003). http://hdl.handle.net/1721.1/17945.

[220] G. Hao, H. Li, S. Kemalcan, G. Chen, J. Yu, Understanding coupled factors that affect the modelling accuracy of typical planar compliant mechanisms , Frontiers of Mechanical Engineering (2016) 129–134. https://doi.org/10.1007/s11465-016-0392-z.

[221] T. Liu, G. Hao, Precision polishing platform based on a flexure-based constant force mechanism, in: Proceedings of the 24th International Conference and Exhibition of the European Society for Precision Engineering and Nanotechnology (euspen), Dublin, Ireland, 2024.

[222] J. Jiang, S. Lin, H. Wang, N. Modler, Modeling method for static large deflection problem of curved planar beams in compliant mechanisms based on a novel

governing equation, Journal of Mechanisms and Robotics (2023) 031014. https://doi.org/10.1115/1.4062916.

[223] A. I. Lurie, A. Belyaev, Theory of Elasticity, Springer, 2005. https://doi.org/10.1007/978-3-540-26455-2.

[224] T. Weller, H. Abramovich, R. Yaffe, Dynamic buckling of beams and plates subjected to axial impact, Computers & Structures (1989) 835–851. https://doi.org/10.1016/0045-7949(89)90368-4.

[225] A. Bedford, K. M. Liechti, Mechanics of Materials, 2nd Edition, Springer, 2020. https://doi.org/10.1007/978-3-030-22082-2.

[226] G. Hao, J. Mullins, On the infinitely-stable rotational mechanism using the off-axis rotation of a bistable translational mechanism, Mechanical Sciences (2015) 75–80. https://doi.org/10.5194/ms-6-75-2015.

[227] H. Li, G. Hao, R. C. Kavanagh, Position-space-based compliant mechanism reconfiguration approach and its application in the reduction of parasitic motion, Journal of Mechanical Design (2016) 092301. https://doi.org/10.1115/1.4033988.

[228] H. Li, G. Hao, Position-space-based design of a symmetric spatial translational compliant mechanism for micro-/nano-manipulation, Micromachines (2018). https://doi.org/10.3390/mi9040189.

[229] J. Qiu, J. Lang, A. Slocum, A curved-beam bistable mechanism, Journal of Microelectromechanical Systems (2004) 137–146. https://doi.org/10.1109/JMEMS.2004.825308.

[230] Y.-S. Wu, C.-C. Lan, Linear Variable-Stiffness Mechanisms Based on Preloaded Curved Beams, Journal of Mechanical Design (2014) 122302. https://doi.org/10.1115/1.4028705.

[231] L. U. Odhner, A. M. Dollar, The Smooth Curvature Model: An Efficient Representation of Euler–Bernoulli Flexures as Robot Joints, IEEE Transactions on Robotics (2012) 761–772. https://doi.org/10.1109/TRO.2012.2193232.

[232] H. Nair Prakashah, H. Zhou, Synthesis of constant torque compliant mechanisms, Journal of Mechanisms and Robotics (2016) 064503. https://doi.org/10.1115/1.4034885.

[233] C.-C. Lan, J.-Y. Wang, Design of adjustable constant-force forceps for robot-assisted surgical manipulation, in: 2011 IEEE International Conference on Robotics and Automation, 2011, pp. 386–391. https://doi.org/10.1109/ICRA.2011.5979556.

[234] Y. Cao, M. Derakhshani, Y. Fang, G. Huang, C. Cao, Bistable structures for advanced functional systems, Advanced Functional Materials (2021) 2106231. https://doi.org/10.1002/adfm.202106231.

[235] N. D. Masters, L. L. Howell, A self-retracting fully compliant bistable micromechanism, Journal of Microelectromechanical Systems (2003) 273–280. https://doi.org/10.1109/JMEMS.2003.811751.

[236] H. Liang, H. Fu, G. Hao, A miniaturized statically balanced compliant mechanism for on-chip ultralow wide-bandwidth vibrational energy harvesting, Mechanical Sciences (2024) 159–168. https://doi.org/10.5194/ms-15-159-2024.

[237] T. Chen, J. Mueller, K. Shea, Integrated Design and Simulation of Tunable, Multi-State Structures Fabricated Monolithically with Multi-Material 3D Printing, Scientific Reports (2017) 45671. https://doi.org/10.1038/srep45671.

[238] B. Colson, P. Marcotte, G. Savard, An overview of bilevel optimization, Annals of operations research (2007) 235–256. https://doi.org/10.1007/s10479-007-0176-2.

[239] J. Zhao, Y. Yang, K. Fan, P. Hu, H. Wang, A bistable threshold accelerometer with fully compliant clamped-clamped mechanism, IEEE Sensors Journal (2010) 1019–1024. https://doi.org/10.1109/JSEN.2010.2042712.

[240] Q. Chen, X. Zhang, H. Zhang, B. Zhu, B. Chen, Topology optimization of bistable mechanisms with maximized differences between switching forces in forward and backward direction, Mechanism and Machine Theory (2019) 131–143. https://doi.org/10.1016/j.mechmachtheory.2019.04.012.

[241] S. Liu, Q. Li, J. Hu, W. Chen, Y. Zhang, Y. Luo, Q. Wang, A survey of topology optimization methods considering manufacturable structural feature constraints for additive manufacturing structures, Additive Manufacturing Frontiers (2024) 200143. https://doi.org/10.1016/j.amf.2024.200143.

[242] F. Ma, G. Chen, Modeling large planar deflections of flexible beams in compliant mechanisms using chained beam-constraint-model1, Journal of Mechanisms and Robotics (2015) 021018. https://doi.org/10.1115/1.4031028.

[243] R. Xu, C. Chen, J. Sun, Y. He, X. Li, M.-H. Lu, Y. Chen, The design, manufacture and application of multistable mechanical metamaterials-a state-of-the-art review, International Journal of Extreme Manufacturing (2023) 042013. https://doi.org/10.1088/2631-7990/acf96a.

[244] J. Wang, Y. Wang, Y. Tian, G. Hao, F. Xi, Y. Zhao, Design of Multi-Mode Morphing Wings Based on Multi-Stable Beam-Type Metastructures, in: Intelligent Robotics and Applications, Springer Nature Singapore, 2025, pp. 139–153.

[245] B. Ding, X. Li, Y. Li, Configuration design and experimental verification of a variable constant-force compliant mechanism, Robotica (2022) 3463–3475. https://doi.org/10.1017/S0263574722000340.

[246] X. Qin, S. Lu, P. Liu, P. Yan, Design and testing of a novel nested, compliant, constant-force mechanism with millimeter-scale strokes, Micromachines (2023). https://doi.org/10.3390/mi14020480.

[247] Q. Xu, Design of a large-stroke bistable mechanism for the application in constant-force micropositioning stage, Journal of Mechanisms and Robotics (2016) 011006. https://doi.org/10.1115/1.4035220.

[248] H. Liang, G. Hao, O. Z. Olszewski, V. Pakrashi, Ultra-low wide bandwidth vibrational energy harvesting using a statically balanced compliant mechanism, International Journal of Mechanical Sciences (2022) 107130. https://doi.org/10.1016/j.ijmecsci.2022.107130.

[249] H. Liang, G. Hao, O. Z. Olszewski, A review on vibration-based piezoelectric energy harvesting from the aspect of compliant mechanisms, Sensors and Actuators A: Physical (2021) 112743. https://doi.org/10.1016/j.sna.2021.112743.

[250] A. Lambora, K. Gupta, K. Chopra, Genetic algorithm- a literature review, in: 2019 International Conference on Machine Learning, Big Data, Cloud and Parallel

Computing (COMITCon), 2019, pp. 380–384. https://doi.org/10.1109/COMITCon.2019.8862255.

[251] The MathWorks, Inc., Genetic Algorithm, The MathWorks, Inc., Natick, MA, USA, accessed 2025 (2024).
URL https://www.mathworks.com/help/gads/genetic-algorithm.html

[252] A. Shukla, H. M. Pandey, D. Mehrotra, Comparative review of selection techniques in genetic algorithm, in: 2015 International Conference on Futuristic Trends on Computational Analysis and Knowledge Management (ABLAZE), 2015, pp. 515–519. https://doi.org/10.1109/ABLAZE.2015.7154916.

[253] X. Liu, F. Lamarque, E. Dore, P. Pouille, Multistable wireless micro-actuator based on antagonistic pre-shaped double beams, Smart Materials and Structures (2015) 075028. https://doi.org/10.1088/0964-1726/24/7/075028.

[254] Y. Gou, G. Chen, L. L. H. and, A design approach to fully compliant multistable mechanisms employing a single bistable mechanism, Mechanics Based Design of Structures and Machines (2021) 986–1009. https://doi.org/10.1080/15397734.2019.1707685.

[255] N. D. K. Tran, D.-A. Wang, Design of a crab-like bistable mechanism for nearly equal switching forces in forward and backward directions, Mechanism and Machine Theory (2017) 114–129. https://doi.org/10.1016/j.mechmachtheory.2017.05.005.

[256] L. Hu, H. Wang, W. Liang, G. Wang, Symmetry optimization of a three-segment fully compliant bistable mechanism for switching forces in forward and backward directions, Iranian Journal of Science and Technology, Transactions of Mechanical Engineering (2024) 1607. https://doi.org/10.1007/s40997-023-00747-6.

[257] The MathWorks, Inc., Global Optimization Toolbox, The MathWorks, Inc., Natick, MA, USA, accessed 2025 (2024).
URL https://www.mathworks.com/help/gads/global-optimization.html

[258] K. Deb, A. Pratap, S. Agarwal, T. A. M. T. Meyarivan, A fast and elitist multiobjective genetic algorithm: Nsga-ii, IEEE Transactions on Evolutionary Computation (2002) 182–197. https://doi.org/10.1109/4235.996017.

Optimization Results

A

This appendix presents the optimization results for the case studies in Chapter 5, which focuses on the bi-level optimization framework. It provides detailed convergence histories for both the single-objective optimization (symmetric switching force), aiming to minimize the objective function, and the multi-objective optimization (constant stiffness region), aiming to identify an optimal set of Pareto candidates. The results are reported in detail, together with the corresponding numerical values.

A.1 Convergence history of optimization case study 1

This appendix presents the convergence history for case studies in chapter 5 optimization. The convergence history for the case study 1, optimizing bistable mechanism with symmetric switching force is plotted in Fig. A.1 and the corresponding objective values and decision variables are recorded in Tab. A.1.

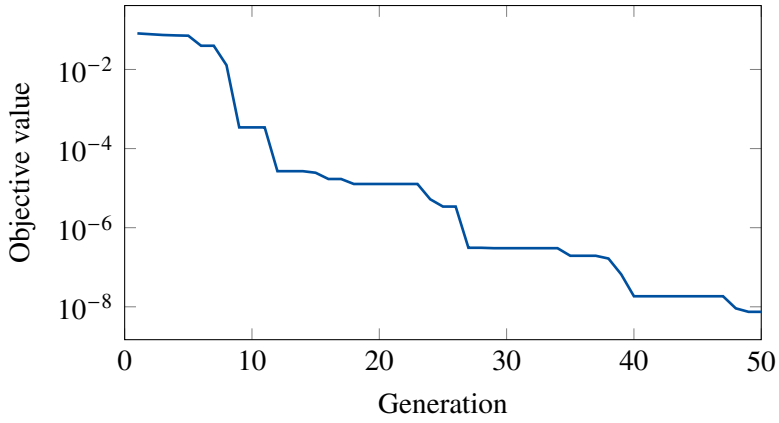


Fig. A.1.: Convergence history of the optimization for bistable mechanism with symmetric switching force.

Tab. A.1.: Optimal solution at each generation for bistable mechanism with symmetric switching force.

Generation	Objective	θ_A	θ_B	L_A	L_B	x_{fr}	y_{fr}
1	8.1671×10^{-02}	359.268789	29.047632	46.342761	40.578867	92.809298	35.392690
2	7.7960×10^{-02}	359.268789	30.047632	47.342761	40.578867	94.809298	35.392690
3	7.4498×10^{-02}	358.268789	30.047632	47.342761	40.578867	94.809298	35.392690
4	7.2696×10^{-02}	358.268789	30.047632	48.342761	40.578867	93.809298	35.392690
5	7.1425×10^{-02}	358.268789	30.047632	48.342761	39.578867	93.809298	35.392690
6	3.9803×10^{-02}	358.268789	193.154909	48.342761	40.578867	93.809298	35.392690
7	3.9803×10^{-02}	358.268789	193.154909	48.342761	40.578867	93.809298	35.392690
8	1.2819×10^{-02}	358.268789	193.154909	37.070710	40.578867	93.809298	35.392690
9	3.4340×10^{-04}	357.768789	193.154909	37.070710	40.578867	93.809298	34.392690
10	3.4340×10^{-04}	357.768789	193.154909	37.070710	40.578867	93.809298	34.392690
11	3.4340×10^{-04}	357.768789	193.154909	37.070710	40.578867	93.809298	34.392690
12	2.6819×10^{-05}	357.831289	193.279909	37.070710	40.766367	93.809298	34.642690
13	2.6819×10^{-05}	357.831289	193.279909	37.070710	40.766367	93.809298	34.642690
14	2.6819×10^{-05}	357.831289	193.279909	37.070710	40.766367	93.809298	34.642690
15	2.4491×10^{-05}	357.768789	193.154909	37.070710	40.828867	93.809298	34.642690
16	1.7023×10^{-05}	357.831289	193.389284	37.070710	40.828867	93.809298	34.642690
17	1.7023×10^{-05}	357.831289	193.389284	37.070710	40.828867	93.809298	34.642690
18	1.2734×10^{-05}	357.831289	193.404909	37.070710	40.828867	93.809298	34.642690
19	1.2734×10^{-05}	357.831289	193.404909	37.070710	40.828867	93.809298	34.642690
20	1.2734×10^{-05}	357.831289	193.404909	37.070710	40.828867	93.809298	34.642690
21	1.2734×10^{-05}	357.831289	193.404909	37.070710	40.828867	93.809298	34.642690
22	1.2734×10^{-05}	357.831289	193.404909	37.070710	40.828867	93.809298	34.642690
23	1.2734×10^{-05}	357.831289	193.404909	37.070710	40.828867	93.809298	34.642690
24	5.2351×10^{-06}	357.846914	193.409304	37.082917	40.833750	93.809542	34.642690
25	3.4198×10^{-06}	357.831289	193.404909	37.070710	40.855234	93.778048	34.642690
26	3.4198×10^{-06}	357.831289	193.404909	37.070710	40.855234	93.778048	34.642690
27	3.1060×10^{-07}	357.846914	193.404909	37.082917	40.828867	93.809542	34.642690
28	3.1060×10^{-07}	357.846914	193.404909	37.082917	40.828867	93.809542	34.642690
29	3.0316×10^{-07}	357.846914	193.404909	37.082917	40.828867	93.809298	34.642690
30	3.0316×10^{-07}	357.846914	193.404909	37.082917	40.828867	93.809298	34.642690
31	3.0316×10^{-07}	357.846914	193.404909	37.082917	40.828867	93.809298	34.642690
32	3.0316×10^{-07}	357.846914	193.404909	37.082917	40.828867	93.809298	34.642690
33	3.0316×10^{-07}	357.846914	193.404909	37.082917	40.828867	93.809298	34.642690
34	3.0316×10^{-07}	357.846914	193.404909	37.082917	40.828867	93.809298	34.642690
35	1.9513×10^{-07}	357.850347	193.406862	37.084035	40.828867	93.813876	34.646394
36	1.9513×10^{-07}	357.850347	193.406862	37.084035	40.828867	93.813876	34.646394
37	1.9513×10^{-07}	357.850347	193.406862	37.084035	40.828867	93.813876	34.646394
38	1.6607×10^{-07}	357.846914	193.402399	37.083417	40.828978	93.807345	34.642690
39	6.6235×10^{-08}	357.846914	193.404909	37.082917	40.828978	93.807345	34.642690
40	1.8476×10^{-08}	357.849844	193.405356	37.085252	40.831389	93.811541	34.644826
41	1.8476×10^{-08}	357.849844	193.405356	37.085252	40.831389	93.811541	34.644826
42	1.8476×10^{-08}	357.849844	193.405356	37.085252	40.831389	93.811541	34.644826
43	1.8476×10^{-08}	357.849844	193.405356	37.085252	40.831389	93.811541	34.644826
44	1.8476×10^{-08}	357.849844	193.405356	37.085252	40.831389	93.811541	34.644826
45	1.8476×10^{-08}	357.849844	193.405356	37.085252	40.831389	93.811541	34.644826
46	1.8476×10^{-08}	357.849844	193.405356	37.085252	40.831389	93.811541	34.644826
47	1.8476×10^{-08}	357.849844	193.405356	37.085252	40.831389	93.811541	34.644826
48	9.1352×10^{-09}	357.846987	193.405378	37.082917	40.831400	93.811541	34.644826
49	7.4608×10^{-09}	357.849844	193.405356	37.085252	40.831394	93.811297	34.644826
50	7.4608×10^{-09}	357.849844	193.405356	37.085252	40.831394	93.811297	34.644826

A.2 Convergence history of optimization case study 2

This appendix showcases the optimization results of Case Study 2 in Chapter 5, i.e. optimizing a bistable mechanism with approximately constant negative stiffness, which includes a Pareto front scatter plot (Figure A.2) that illustrates the distribution of non-dominated solutions in the bi-objective space, as well as a table (Table A.2) that records the corresponding decision variables for each optimal design.

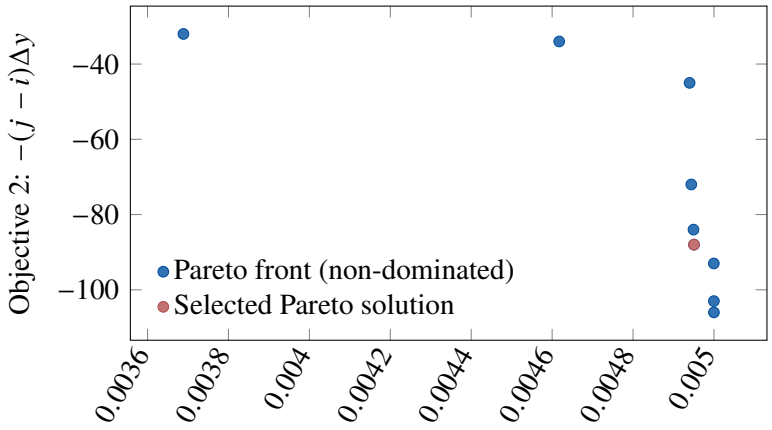


Fig. A.2.: Pareto front obtained from multi-objective optimization for a bistable mechanism with approximately constant negative stiffness. Scatter plot of the Pareto front showing non-dominated solutions in the objective space, where Objective 1 represents the RMSE and Objective 2 corresponds to the vertical displacement difference $-(j-i)\Delta y$. The red dot indicates the selected Pareto-optimal solution.

Tab. A.2.: Geometric parameters corresponding to each Pareto-optimal solution in the case study of optimizing a bistable mechanism with approximately constant negative stiffness. The term width refers to the length of constant negative stiffness region.

Solution	RMSE	Width(mm)	θ_1	θ_2	L_1	L_2	x_{fr}	y_{fr}
1	0.00368868	32	15.0206	0.0000	50.5310	50.2060	20.4855	0.0060
2	0.00461749	34	15.3537	0.0024	51.0944	49.0519	20.7746	0.1669
3	0.00494399	72	111.7998	1.4980	58.9928	69.4817	36.4274	34.0484
4	0.00495061	88	117.1000	2.8278	70.3449	59.7228	52.3085	49.9021
5	0.00493980	45	22.9991	0.0577	52.5346	49.1771	37.5883	-0.6239
6	0.00494943	84	123.4002	3.3238	67.5709	60.5960	51.7800	42.4672
7	0.00499963	93	119.6063	2.9857	70.5282	70.0944	50.7008	37.0442
8	0.00499977	103	115.8255	4.5979	70.8945	76.1186	52.0048	52.6197
9	0.00499977	106	113.3639	4.7032	72.2182	77.5495	52.3774	53.0506

End of Thesis